Geodätisch-geophysikalische Arbeiten in der Schweiz

(Fortsetzung der Publikationsreihe
«Astronomisch-geodätische Arbeiten in der Schweiz»)

herausgegeben von der

Schweizerischen Geodätischen Kommission
(Organ der Akademie der Naturwissenschaften Schweiz)

Achtzigster Band
Volume 80

Sea Surface Topography and Marine Geoid by Airborne Laser Altimetry and Shipborne Ultrasound Altimetry

Philippe Limpach

2010

Adresse der Schweizerischen Geodätischen Kommission:

Institut für Geodäsie und Photogrammetrie
ETH Zürich
CH-8093 Zürich, Switzerland

Internet: http://www.sgc.ethz.ch

ISBN 978-3-908440-24-6

Redaktion des 80. Bandes:
Dr. Ph. Limpach, Prof. Dr. A. Geiger,
J. Müller-Gantenbein

Druck: Print-Atelier ADAG, Zürich

VORWORT

Ein wichtiger Aspekt des viel diskutierten Klimawandels sind Meeresspiegeländerungen und ihre Auswirkungen auf küstennahe Gebiete. Radargestützte Altimetrie-Satelliten sind geeignet, Klimasignale sowie Anomalien des Schwerefeldes der Erde zu erfassen. Es ist daher von Bedeutung, die Satellitenmessungen zu validieren und zu kalibrieren. Das Hauptziel der vorliegenden Forschungsarbeit bestand darin, dafür Methoden zu entwickeln und zu erproben. Sie beinhalten Airborne Laser Altimetrie, marines Ultraschallmonitoring, sowie GPS Bojen- und Schiffsmessungen.

Von Bedeutung für die Airborne Laser-Altimetrie ist die Georeferenzierung. Mit differenziellen GPS Phasenmessungen war es möglich, Genauigkeiten von besser als 5 cm zu erreichen. Unter extremen Wetterbedingungen wurden Schwierigkeiten bei den troposphärischen Korrekturen aufgezeigt, die den limitierenden Faktor darstellten. Zur Bestimmung der Neigungen der Messplattform, hat Herr Limpach ein Multi-Antennensystem sowie ein Inertialsystem nutzbar gemacht. Erwähnenswert ist auch die von ihm entwickelte Laser-Selbstkalibration, mit der man auf mehrfache Überflüge verzichten kann. Gezeitenwirkungen erreichen in der Ägäis mehrere dm. Herr Limpach hat verschiedene Gezeitenmodelle analysiert, einbezogen und auch eigene Pegelmessungen für die Korrekturen berücksichtigt. Die Effekte des Luftdrucks lagen während der Messkampagnen in derselben Grössenordnung wie die Gezeiten und mussten entsprechend berücksichtigt werden. Die Messungen konzentrierten sich auf das Meeresgebiet um Kreta, sowie auf Schiffsmessungen in der Nord-Ägäis.

Im letzten Teil des Berichtes interpretiert Philippe Limpach die erhaltene Meerestopographie im Hinblick auf geophysikalische Phänomene. Das Relief des Kretischen Meeres ist stark beeinflusst vom Hellenischen Tiefseegraben. Der Horizontalgradient der Meeresoberfläche erreicht beachtliche Werte von bis zu 22 cm/km. Sie stehen mit den dortigen geodynamischen Prozessen im Zusammenhang. Ähnliche Anomalien wurden auch für den Nordägäischen Graben nachgewiesen und interpretiert.

Das Projekt hat dank Herrn Limpachs hervorragender Forschungsarbeit sehr gute Resultate erbracht. Die Thematik ist fachübergreifend und öffnet den Weg für neue Validierungs- und Kalibrationsmöglichkeiten der Satellitenradar-Altimetrie im Offshore Bereich. Herr Limpach hat die komplexe geodätische Fragestellung wissenschaftlich ausserordentlich kompetent bearbeitet und weit über den eigentlichen Fachbereich hinaus diskutiert. Internationale Bemühungen, die Meeresoberfläche räumlich hochaufgelöst bestimmen zu können, belegen die Bedeutung der Arbeit. Im Rahmen von Radaraltimetrie-Missionen werden die entwickelten Methoden einen bedeutenden Stellenwert erhalten.

Philippe Limpach hat dieses Projekt mit beispiellosem Einsatz nicht nur in der Theorie, sondern auch in nächtelangen Messfahrten erfolgreich bearbeitet und international grosse Anerkennung gefunden. Die Schweizerische Geodätische Kommission gratuliert Herrn Limpach zu seiner Leistung und dankt ihm für diesen wertvollen Beitrag. Wir danken dem Schweizerischen Nationalfonds für die Unterstützung dieses Projektes sowie der Schweizerischen Akademie für Naturwissenschaften für die Übernahme der Druckkosten.

Prof. Dr. Hans-Gert Kahle
Institut für Geodäsie und Photogrammetrie
ETH Zürich

Prof. Dr. Alain Geiger
ETH Zürich
Präsident der SGK

PREFACE

Les variations de la surface des mers et leurs effets dans les zones côtières sont un des aspects importants des changements climatiques. Les satellites altimétriques radar sont des instruments adaptés pour la détection des signaux climatiques et des anomalies gravifiques. Il est par conséquent très important de valider et de calibrer leurs mesures. Le principal objectif du travail présenté ici fût de développer et de tester des méthodes destinées à cette validation et à cette calibration. Ces méthodes comprennent l'altimétrie laser aéroportée, l'altimétrie ultrasonique marine et l'utilisation de bouées équipées de récepteurs GPS.

Le référencement géographique est un des problèmes clefs de l'altimétrie laser aéroportée. Dans des conditions de mauvais temps troposphérique, les corrections de réfraction se sont montrées comme un facteur limitant la précision finale. Un dispositif multi-antennes GPS et une station inertielle furent utilisés pour les corrections de l'attitude de l'avion ainsi que du bateau utilisé pour les mesures altimétriques. Un aspect important de cette recherche a été le développement d'une méthode d'auto-calibration qui a permit d'éviter la répétition de multiples survols. Les effets des marées peuvent atteindre plusieurs décimètres dans la mer Egée. Monsieur Limpach a, d'une façon critique, analysé différents modèles de marées et a intégré ceux-ci dans la procédure de correction. De même, des marégraphes ont été installés. Les effets des variations de la pression atmosphérique ont montrés être du même ordre de grandeur et ont été pris en considération. Les mesures aéroportées ont été conduites autour de l'île de Crète alors que les mesures marines le furent dans la partie nord de la mer Égée.

Dans la partie finale du présent travail la topographie de la surface de la mer a été interprétée en termes de structures géophysiques. La surface de la mer Crétoise est fortement influencée par la zone de subduction Hellénique. Le gradient horizontal de la surface marine atteint des valeurs allant jusqu'à 22 cm/km. Ces valeurs sont associées à des processus géodynamiques actuels. Des gradients d'amplitudes similaires ont aussi été trouvés dans la partie septentrionale de la mer Egée. Des modélisations complètes du champ gravifique ont révélé des anomalies significatives pouvant être associées à la structure tectonique du fossé nord-Égéen.

Ce projet, grâce à l'excellent travail de Monsieur Limpach, a apporté de remarquables résultats. Des méthodes innovatrices pour la calibration et la validation des données altimétriques par satellites ont été développées, aussi bien en termes d'ingénierie de „hardware" que de „software". Monsieur Limpach a travaillé et discuté les problèmes géodésiques compliqués bien au-delà du domaine du sujet proprement dit. Les efforts internationaux pour déterminer la topographie de la surface de la mer à haute définition spatiale et temporelle donnent du crédit à l'important travail accompli. Ces réalisations donneront certainement encore plus de crédit aux missions d'altimétrie spatiale futures et en cours.

Monsieur Philippe Limpach a poursuivi ce projet avec de minutieux efforts non seulement théoriques, mais aussi sur le terrain. La poursuite du satellite Jason a été faite durant de nombreuses nuits en mer, souvent dans des conditions météorologiques adverses. Les campagnes de mesures n'auraient pas été possibles sans un engagement tenace dans tous les aspects des activités marines.

L'institut de géodésie et photogrammétrie de l'EPF-Z et la commission géodésique suisse, membre de l'académie suisse des sciences naturelles, désirent remercier le Dr. Limpach pour cette contribution de grande valeur. Nous sommes redevable à la fondation nationale suisse pour la science du financement de ce projet de recherche et à l'académie des sciences du financement des coûts d'impression du présent fascicule.

Prof. Dr. Hans-Gert Kahle
Institut de Géodésie et Photogrammétrie
ETH Zürich

Prof. Dr. Alain Geiger
ETH Zurich
Président de la CGS

FOREWORD

Sea surface variability and its effects in near coastal areas are an important aspect of climate change. Radar based altimetry satellites are best suited for the detection of climate signals and gravity anomalies. It is, therefore, important to validate and calibrate the satellite measurements. The main objective of the research work presented was to develop and test corresponding methods. These include airborne laser altimetry, ship-borne ultrasound altimetry as well as GPS-equipped buoys.

Georeferencing is one of the key problems in airborne laser altimetry. Accuracies of better than 5 cm were achieved by applying differential GPS phase measurements. In bad weather tropospheric refraction corrections were found to be a limiting factor for the final accuracy. A multi-antenna GPS array and inertial systems were used for control and correction of the attitude of the aircraft and the ship. An important aspect was also the development of a method for self-calibration of boresight misalignment which saved repetitions of multiple overflights. Tidal effects amount to several dm in the Aegean Sea. Philippe Limpach has critically analyzed different tidal models and integrated these in the correction procedure. Also own tide gauges were installed and taken into account. Air pressure effects were found to be in the same order of magnitude and had to be considered as well. Airborne measurements were made around the island of Crete. Shipborne campaigns were carried out in the North Aegean Sea.

In the final part of this report the sea surface topography obtained was interpreted in terms of geophysical structures. The sea surface of the Cretan Sea is strongly influenced by the Hellenic subduction zone. The horizontal gradient of the sea surface attains values of up to 22 cm/km. These are associated with ongoing geodynamic processes. Gradients in similar size were also found in the North Aegean sea. Comprehensive modelling of the potential field revealed significant gravity anomalies which can be associated with the tectonic structure of the North Aegean trough.

Important results were achieved thanks to Philippe Limpach's outstanding research work which is truly interdisciplinary. Innovative methods for calibration and validation of satellite altimetry have been successfully worked out, both in terms of hardware engineering and software development. A complex geodetic task has been performed and discussed far in excess of the subject area. International efforts to determine the sea surface topography at high spatio-temporal resolution account for the importance of the work accomplished. The achievements will certainly be given credit in the frame of ongoing and future spaceborne radar altimetry missions.

Philippe Limpach has pursued this project with painstaking endeavour, not only theoretically but also in the field. Tracing the Jason Satellite numerous night-time campaigns had to be carried out at sea also in adverse weather conditions. The expeditions would not have been possible without his persistent commitment in all aspects of marine activities.

The Institute of Geodesy and Photogrammetry of the ETH Zürich and the Swiss Geodetic Commission (SGC) of the Swiss Academy of Natural Sciences would like to thank Dr. Limpach for his highly valuable contribution. We are grateful to the Swiss National Science Foundation for funding the research project and to the Swiss Academy of Sciences for financing the printing costs.

Prof. Dr. Hans-Gert Kahle
Institute of Geodesy and Photogrammetry
ETH Zurich

Prof. Dr. Alain Geiger
ETH Zurich
President of SGC

Abstract

The aim of this project was to contribute to the improvement of sea level monitoring and to provide local-scale information on the short-wavelength structure of the marine gravity field, by developing enhanced methods for offshore sea surface height observations. The methods include airborne laser altimetry, shipborne ultrasound altimetry and GPS-equipped buoys.

In a first step, instrumental aspects of sea surface height observations by airborne and shipborne altimetry were analyzed. Precise position and attitude of the range sensor are crucial for an accurate sea surface height computation. For this purpose, the survey aircraft and boat were equipped with a multi-antenna GPS array and inertial systems. Sea surface heights were computed from the range data by direct georeferencing. Important aspects are the influences of errors in the differential kinematic GPS positioning and in the attitude determination, as well as the calibration of boresight misalignments. In a second step, the obtained sea surface heights were reduced to mean sea surface by applying corrections for geophysical effects, including waves, tides, atmospheric pressure and wind forcing.

In the framework of this work, several regional campaigns for sea surface height surveys based on airborne and shipborne altimetry were carried out in the Eastern Mediterranean Sea. Dedicated surveys, including deployments of GPS buoys, were performed along Jason-1 radar altimetry ground tracks. Airborne laser altimetry data was acquired along densely spaced flight tracks covering an area of 200 by 200 km around the western part of the island of Crete, Greece, in the vicinity of the Hellenic Trench. The objective was the determination of a detailed regional geoid and sea surface topography model in the framework of the GAVDOS project, funded by the European Union. Furthermore, several shipborne campaigns for sea surface height observations were carried out in the North Aegean Sea, in the vicinity of the North Aegean Trough.

Based on the airborne and shipborne altimetry data, a high-resolution sea surface topography of the survey areas was computed, with an accuracy of better than 10 cm. Geoid undulations were derived from the sea surface heights by subtracting the mean dynamic ocean topography induced by oceanic currents. Around western Crete, the geoid obtained from airborne laser altimetry is characterized by very large gradients, with an average height difference of 20 m along a distance of only 200 km and maximum local gradients of 22 cm/km. These gradients are a clear indication for significant gravity effects caused by the bathymetry and the geodynamic system of the Hellenic Trench. In the survey area in the North Aegean Sea, the geoid obtained from shipborne altimetry shows a distinct depression of 1.5 m, indicating a connection with the bathymetry and the geodynamic features of the North Aegean Trough.

The high resolution and accuracy of the sea surface and geoid heights obtained were verified by comparisons with mean sea surface models from multi-mission satellite radar altimetry, as well as with global and regional geoid models. The reduction of the geoid heights for modeled mass effects of topography, bathymetry, marine sedimentary deposits and crust-mantle boundary revealed pronounced gravity anomalies related to the geodynamic processes in the survey areas.

Zusammenfassung

Ziel dieser Arbeit ist die genaue Bestimmung der Meeresoberfläche als Beitrag zur Verbesserung der Beobachtung des Meeresspiegels und zur lokalen Bestimmung der kurzwelligen Strukturen des Schwerefeldes. Zu diesem Zweck wurden mehrere Methoden zur präzisen und flächendeckenden Vermessung der Meeresoberfläche untersucht, weiterentwickelt und eingesetzt. Es handelt sich hierbei um flugzeuggestützte Laser-Altimetrie, schiffsgestützte Ultraschall-Altimetrie und GPS Bojen-Messungen.

In einem ersten Schritt werden die instrumentellen Aspekte von Meereshöhenbeobachtungen mittels flugzeug- und schiffsgestützter Altimetrie analysiert und diskutiert. Für die genaue Berechnung der Meereshöhen ist die präzise Kenntnis von Position und Lage der Messplattform von entscheidender Bedeutung. Zu diesem Zweck wurden Flugzeug und Schiff mit mehreren GPS-Antennen und einem Inertialsystem ausgerüstet. Die momentanen Meereshöhen wurden mittels direkter Georeferenzierung aus den Altimeterdaten berechnet. Die wichtigsten Aspekte sind hierbei die Einflüsse von Fehlern in der differentiellen kinematischen GPS-Positionierung, Fehlern in der Lagebestimmung, sowie Orientierungsfehler der Sensoren. In einem zweiten Schritt wurden zeitabhängige Variationen der Meereshöhe, verursacht durch geophysikalische Einflüsse wie Wellen, Gezeiten, Luftdruck und Wind, korrigiert.

Im Rahmen dieser Arbeit wurden mehrere regionale Messkampagnen im östlichen Mittelmeer durchgeführt. Die Messgebiete beinhalten Ground-Tracks des Radar-Altimeter Satelliten Jason-1. Entlang dieser Tracks wurden Messungen während Überflügen von Jason-1 durchgeführt. In einem Gebiet von 200 auf 200 km rund um die Insel Kreta wurde die Meeresoberfläche mittels flugzeuggestützte Laser-Altimetrie vermessen. Das Gebiet umfasst einen Teil des Hellenischen Grabens. Ziel dieser Messkampagne war die Bestimmung eines detaillierten Geoid- und Meeresoberflächenmodells im Rahmen des GAVDOS-Projektes, unterstützt von der Europäischen Union. Des Weiteren wurden mehrere Messkampagnen mittels schiffsgestützter Ultraschall-Altimetrie in der Nord-Ägäis durchgeführt. Ein besonderes geodynamisches Merkmal dieser Region ist der Nordägäische Graben.

Mit Hilfe der Flugzeug- und Schiffsdaten konnte eine hochauflösende Meerestopographie mit einer Genauigkeit unter 10 cm bestimmt werden. Durch Abzug der dynamischen Meerestopographie, welche durch Meeresströmungen verursacht wird, wurden aus den beobachteten Meereshöhen Geoidhöhen abgeleitet. Das resultierende Geoid rund um Kreta zeigt sehr starke Gradienten, mit einem durchschnittlichen Gefälle von 20 m auf 200 km und maximalen Gradienten von 22 cm/km. Diese Gradienten sind ein klarer Hinweis auf signifikante Schwerefeldeffekte, verursacht durch die Bathymetrie und das geodynamische System des Hellenischen Grabens. Das Geoid im untersuchten Gebiet in der Nord-Ägäis zeigt eine ausgeprägte Depression von 1.5 m, welche mit der Bathymetrie und den geodynamischen Eigenschaften des Nordägäischen Grabens in Verbindung gebracht werden kann.

Die hohe Auflösung und Genauigkeit der berechneten Meeres- und Geoidhöhen konnten durch Vergleiche mit Modellen der mittleren Meereshöhe aus Satelliten-Radar-Altimetrie, sowie mit globalen und regionalen Geoidmodellen, aufgezeigt werden. Des Weiteren wurden durch die Reduktion von modellierten Masseneffekten, verursacht durch Topographie, Bathymetrie, marinen Sedimenten und Kruste-Mantel-Grenze, starke Anomalien im Schwerefeld detektiert, welche mit den geodynamischen Prozessen in den Messgebieten in Verbindung stehen.

Contents

1 Introduction **1**
- 1.1 Motivation and Goals . . . 1
- 1.2 Geophysical Characteristics of the Eastern Mediterranean . . . 3
- 1.3 Former Work by the GGL in Related Fields of Research . . . 5
- 1.4 Research Tasks and Project Outline . . . 6

2 Geoid, Sea Surface and Dynamic Ocean Topography **9**
- 2.1 Introduction . . . 9
- 2.2 Geoid . . . 9
  - 2.2.1 Gravity Potential, Geoid and Gravity Anomalies . . . 9
  - 2.2.2 Gravitational Mass Effect and Mass Reduction . . . 13
  - 2.2.3 Gravitational Models . . . 15
- 2.3 Mean Sea Surface . . . 15
- 2.4 Sea Level Anomaly . . . 17
- 2.5 Dynamic Ocean Topography . . . 19
  - 2.5.1 Absolute and Mean Dynamic Topography . . . 19
  - 2.5.2 Geostrophic Flow Fields from Dynamic Ocean Topography . . . 20
  - 2.5.3 Mean Dynamic Topography of the Mediterranean Sea . . . 20
- 2.6 Permanent Tide . . . 22
  - 2.6.1 Permanent Tidal Effects on Gravitational Potential and Earth's Crust . . . 22
  - 2.6.2 Mean-Tide, Zero-Tide and Tide-Free Systems . . . 23
  - 2.6.3 Conversion between Permanent Tide Systems . . . 24
  - 2.6.4 Conversion of Sea Surface Heights between Permanent Tide Systems . . . 26

3 Geophysical Effects on Sea Surface Heights **29**
- 3.1 Introduction . . . 29
- 3.2 Ocean Waves . . . 29
- 3.3 Tides . . . 30
  - 3.3.1 Characteristics of Tides . . . 30
  - 3.3.2 Ocean Tide . . . 30
  - 3.3.3 Solid Earth Tide . . . 34
  - 3.3.4 Ocean Loading Tide and Pole Tide . . . 37
- 3.4 Atmospheric Pressure and Wind Forcing . . . 37
  - 3.4.1 Inverse Barometer Effect . . . 37
  - 3.4.2 Dynamic Atmospheric Correction . . . 38

4 Airborne Laser Altimetry **39**
- 4.1 Introduction . . . 39
- 4.2 Instumental Setup . . . 39
  - 4.2.1 Overview . . . 39
  - 4.2.2 Laser Profiler . . . 40
  - 4.2.3 Laser Scanner . . . 40
  - 4.2.4 Multi-Antenna GPS Configuration . . . 41
  - 4.2.5 Inertial Navigation System . . . 41
- 4.3 Laser Ranging . . . 42

4.3.1 Basic Principle . . . 42
4.3.2 Atmospheric Refraction of Light . . . 42
4.3.3 Atmospheric Refraction Models . . . 44
4.3.4 Impact of Atmospheric Refraction in Airborne Laser Altimetry . . . 45
4.4 Laser Backscatter from Sea Surface . . . 46
4.4.1 Reflection and Refraction at Air-Water Boundary . . . 46
4.4.2 Specular and Diffuse Reflection . . . 48
4.4.3 Impact of Sea Surface Geometry . . . 49
4.4.4 Absorption, Scattering, Penetration Depth and Backscattering . . . 49
4.4.5 Optical Properties of Water . . . 51
4.4.6 Case Study: Backscatter Intensity and Return Rate from Sea Surface . . . 51

5 Shipborne Ultrasound Altimetry 55
5.1 Introduction . . . 55
5.2 Instrumental Setup . . . 55
5.2.1 Overview . . . 55
5.2.2 Ultrasonic Distance Sensors . . . 55
5.2.3 GPS Antenna Configuration . . . 56
5.2.4 Inertial Attitude and Heading Reference System . . . 56
5.3 Ultrasound Ranging . . . 57
5.3.1 Basic Principles . . . 57
5.3.2 Atmospheric Influences . . . 59
5.3.3 Ultrasonic Target Reflection . . . 60
5.4 Sensor Synchronization . . . 61
5.4.1 Self-Synchronization between Ultrasonic Sensors . . . 61
5.4.2 Synchronization of Ultrasonic Sensors with GPS . . . 61

6 Direct Georeferencing 63
6.1 Introduction . . . 63
6.2 Basic Principle . . . 63
6.2.1 Direct Georeferencing Equation . . . 63
6.2.2 Vertical Component of Direct Georeferencing Equation . . . 65
6.2.3 Impact of Attitude Error onto Ground Point Height . . . 66
6.2.4 Required Attitude Accuracy . . . 67
6.3 Kinematic GPS Positioning . . . 68
6.3.1 Basic Principle . . . 68
6.3.2 Atmospheric Influences . . . 68
6.3.3 Case Study: Impact of Troposphere on Airborne GPS Solutions . . . 69
6.4 Multi-Antenna GPS Attitude Determination . . . 74
6.4.1 Basic Principle . . . 74
6.4.2 Processing of Moving GPS Baselines . . . 75
6.4.3 Algorithm for Multi-Antenna GPS Attitude Determination . . . 75
6.4.4 Accuracy of Multi-Antenna GPS Attitude Determination . . . 77
6.4.5 Case Study: Airborne Multi-Antenna GPS vs. Tactical-Grade INS . . . 78
6.4.6 Case Study: Shipborne Multi-Antenna GPS vs. MEMS-Based AHRS . . . 80
6.5 Boresight Misalignment Calibration in Airborne Altimetry . . . 83
6.5.1 Introduction . . . 83
6.5.2 Impact of Boresight Misalignment on Ground Point Height . . . 83
6.5.3 Impact of Simplification for Small Boresight Misalignment Angles . . . 83
6.5.4 Self-Calibration Based on Piecewise Polynomial Fit of Water Surfaces . . . 84
6.5.5 Case Study: Airborne Laser Profiler Calibration . . . 86

7 Sea Surface Heights by Airborne Laser Altimetry around Western Crete 91
7.1 GAVDOS Airborne Laser Altimetry Campaign . . . 91

7.2 Instantaneous Sea Surface Height Profiles . . . 92
7.2.1 Sea Surface Height Profiles . . . 92
7.2.2 Calibration of Airborne Altimetry Data with GPS Buoys . . . 95
7.2.3 Significant Wave Heights . . . 97
7.3 Sea Surface Height Corrections . . . 97
7.3.1 Ocean Wave Correction . . . 97
7.3.2 Ocean Tide Correction . . . 97
7.3.3 Correction for Atmospheric Pressure and Wind Forcing . . . 97
7.3.4 Validation of Tidal and Atmospheric Corrections with Tide-Gauge . . . 100
7.3.5 Sea Level Anomaly Correction . . . 101
7.4 Repeatability Analysis . . . 103
7.4.1 Analysis of Repeated Tracks . . . 103
7.4.2 Crosspoints Analysis . . . 104
7.4.3 LSQ Adjustment Based on Crosspoints . . . 106
7.5 Time-Independent Sea Surface Topography . . . 106

8 Sea Surface Heights by Shipborne Ultrasound Altimetry in the North Aegean Sea 111
8.1 Shipborne Ultrasound Altimetry Campaigns . . . 111
8.2 Instantaneous Sea Surface Height Profiles . . . 111
8.3 Sea Surface Height Corrections . . . 112
8.3.1 Ocean Wave Correction . . . 112
8.3.2 Ocean Tide Correction . . . 112
8.3.3 Correction for Atmospheric Pressure and Wind Forcing . . . 113
8.3.4 Validation of Tidal and Atmospheric Corrections with Tide-Gauge . . . 117
8.3.5 Sea Level Anomaly Correction . . . 118
8.4 Repeatability Analysis . . . 121
8.4.1 Crosspoints Analysis . . . 121
8.4.2 LSQ Adjustment Based on Crosspoints . . . 121
8.5 Time-Independent Sea Surface Topography . . . 123

9 Validation of Satellite Radar Altimetry Data 129
9.1 Introduction . . . 129
9.2 Validation of Jason-1 Data with Airborne Laser Altimetry . . . 130
9.3 Validation of Mean Sea Surface from Radar Altimetry . . . 131
9.3.1 Validation with Airborne Laser Altimetry around Western Crete . . . 131
9.3.2 Validation with Shipborne Altimetry in the North Aegean Sea . . . 133

10 Geoscientific Exploitation of Airborne Altimetry Data around Western Crete 135
10.1 Marine Geoid, Gravity Anomalies and Deflections of the Vertical from Sea Surface Heights . . . 135
10.2 Local Altimetric Geoid vs. Existing Models . . . 135
10.3 Mean Dynamic Topography Estimation . . . 138
10.4 Modeled Mass Effects on Geoid Heights and Gravity . . . 141
10.4.1 Introduction . . . 141
10.4.2 Mass Effect of Topography and Bathymetry . . . 143
10.4.3 Mass Effect of Sediments . . . 143
10.4.4 Mass Effect of Moho Depths . . . 143
10.4.5 Mass Effect of Isostatic Moho Depths . . . 143
10.4.6 Combined Mass Effects . . . 144
10.4.7 Cuboids vs. Point Mass Modeling . . . 144
10.5 Mass Reduction of Local Altimetric Geoid . . . 150
10.5.1 Introduction . . . 150
10.5.2 Topography-Bathymetry Cogeoid . . . 150
10.5.3 Topography-Bathymetry-Sediments Cogeoid . . . 150

10.5.4 Topography-Bathymetry-Sediments-Moho Cogeoid . . . 151
10.5.5 Topography-Bathymetry-Sediments-Isostasy Cogeoid . . . 151

11 Geoscientific Exploitation of Shipborne Altimetry Data in the North Aegean Sea 155
11.1 Marine Geoid, Gravity Anomalies and Deflections of the Vertical from Sea Surface Heights . . . 155
11.2 Local Altimetric Geoid vs. Existing Models . . . 155
11.3 Mean Dynamic Topography Estimation . . . 161
11.4 Modeled Mass Effects on Geoid Heights and Gravity . . . 162
11.4.1 Introduction . . . 162
11.4.2 Mass Effect of Topography and Bathymetry . . . 162
11.4.3 Mass Effect of Sediments . . . 162
11.4.4 Mass Effect of Moho Depths . . . 162
11.4.5 Mass Effect of Isostatic Moho Depths . . . 164
11.4.6 Combined Mass Effects . . . 164
11.4.7 Cuboids vs. Point Mass Modeling . . . 164
11.5 Mass Reduction of Local Altimetric Geoid . . . 170
11.5.1 Introduction . . . 170
11.5.2 Topography-Bathymetry Cogeoid . . . 170
11.5.3 Topography-Bathymetry-Sediments Cogeoid . . . 170
11.5.4 Topography-Bathymetry-Sediments-Moho Cogeoid . . . 170
11.5.5 Topography-Bathymetry-Sediments-Isostasy Cogeoid . . . 171

12 Summary and Conclusions 175

Bibliography 179

A Models of Atmospheric Refraction of Light 189
A.1 Barrell and Sears Model (1939) . . . 189
A.2 Barrell Model (1951) . . . 190
A.3 Edlén Model (1966) . . . 190
A.4 Birch and Downs Model (1994) . . . 191

B Standard Atmosphere Model 193

C GPS-Equipped Buoys 195
C.1 Introduction . . . 195
C.2 GPS-Equipped Buoys Developed by the GGL . . . 195
C.3 Case Study: Ocean Tide Observations with GPS Buoys . . . 196

D Rotation Matrices 197
D.1 General Formulation . . . 197
D.2 Rotation from Local Level to Geocentric System . . . 198

E Differential Clock Bias in Moving Baseline GPS Processing 199

F ECMWF Atmospheric Pressure 201

G Dynamic Atmospheric Correction over the Mediterranean Sea 205

Abbreviations

A/D	Analog-to-Digital
AHRS	Attitude and Heading Reference System
ADT	Absolute Dynamic ocean Topography
AUTH	Aristotle University of Thessaloniki
AVISO	Archiving, Validation and Interpretation of Satellite Oceanographic data
CLS	Collecte Localisation Satellites
CLS01	Mean sea surface model 2001 by CLS Space Oceanography Division
CNES	Centre National d'Etudes Spatiales
CNRS	Centre National de la Recherche Scientifique
DAC	Dynamic Atmospheric Correction
DNSC	Danish National Space Center
DORIS	Détermination d'Orbite et de Radiopositionnement Intégrés par Satellite
DOT	Dynamic Ocean Topography
DOV	Deflection of the Vertical
DT	Delayed-Time
DUACS	Data Unification and Altimeter Combination System
ECMWF	European Centre for Medium-Range Weather Forecasts
EDM	Electronic Distance Measurement
EGM	Earth Geopotential Model
ESA	European Space Agency
ESC	European Seismological Commission
ETH(Z)	Eidgenössische Technische Hochschule (Zürich)
EU	European Union
FFT	Fast Fourier Transformation
FIR	Flight Information Region
GDR	Geophysical Data Records
GFZ	GeoForschungsZentrum Postdam
GGL	Geodesy and Geodynamics Laboratory
GLOSS	Global Sea Level Observing System
GNSS	Global Navigation Satellite System
GPS	Global Positioning System
GOCE	Gravity Field and Steady-State Ocean Circulation Explorer
GRGS	Groupe de Recherche de Geodésie Spatiale
GRS80	Geodetic Reference System 1980
GSFC	Goddard Space Flight Center (NASA)
HNHS	Hellenic Navy Hydrographic Service
IAG	International Association of Geodesy
IB	Inverse Barometer
IERS	International Earth Rotation and Reference Systems Service
IGS	International GNSS Service
INS	Inertial Navigation System
IMU	Inertial Measurement Unit
ITS	International Temperature Scale
ITRF	International Terrestrial Reference Frame
IUGG	International Union of Geodesy and Geophysics

KMS	National Survey and Cadastre of Denmark (Kort & Matrikelstyrelsen)
LAGEOS	Laser Geodynamics Satellite
LEGOS	Laboratoire d'Études en Géophysique et Océanographie Spatiale
LSQ	Least-Squares
MDT	Mean Dynamic ocean Topography
MEMS	Micro-Electro-Mechanical Systems
MOG2D	2D Gravity Wave Model
MSS	Mean Sea Surface
NASA	National Aeronautics and Space Administration
NAT	North Aegean Trough
NED	North, East, Down coordinate system
NGA	National Geospatial-Intelligence Agency
NIMA	National Imagery and Mapping Agency
NOAA	National Oceanic and Atmospheric Administration
OSTM	Ocean Surface Topography Mission
PODAAC	Physical Oceanography Distributed Active Archive Center
POL	Proudman Oceanographic Laboratory
RMS	Root-Mean-Square
SELF	Sea Level Fluctuation Project
SLA	Sea Level Anomaly
SLR	Satellite Laser Ranging
SMDT	Synthetic Mean Dynamic ocean Topography
SSALTO	CNES multimission ground-segment
SSH	Sea Surface Height
SST	Sea Surface Topography
UT	Universal Time
UTC	Universal Time Coordinated
WGS84	World Geodetic System 1984
WMO	World Meteorological Organization
ZPD	Zenith Path Delay

1 Introduction

1.1 Motivation and Goals

Concerns of the future are associated with the fact that non-natural processes have begun to influence life on our planet at a global scale. Global change has become of major interest, raising the need to describe the Earth as a changing system. One of the internationally widely accepted scientific focuses is pointed upon the sea level and its variability. Since the sea surface reflects the integral of both the amount of water and the heat content of the oceans, it is a key quantity that responds to climate change and short-term variability. With an increasing understanding of the processes involved in sea surface variability, precise sea surface height observations will provide long-term benefits in environment management, safety and protection, and contribute to the assessment of global change. Interdisciplinary studies of climatic interactions in the Mediterranean area are important for the surrounding countries. Sea-level fluctuations in the region have long history and can result in tremendous economic losses, regarding the present distribution of coastal cities.

On a global scale, satellite radar altimetry missions are the basic means for sea surface height monitoring over the deep sea, with dense and homogeneous coverage in space and time. For the past decades, Europe has invested in several radar altimetry space missions (ERS-1, ERS-2, and ENVISAT, operated by ESA), as well as in the joint participation of the French Space Agency CNES and the United States NASA in the missions TOPEX/Poseidon (AVISO, 1996) and its follow-on mission Jason-1 (Picot et al., 2003). In June 2008, Jason-2, also called Ocean Surface Topography Mission (OSTM), was launched as another follow-on mission (OSTM, 2008). Important outputs of satellite radar altimetry missions are information on the short- and long-term variability of the sea surface. A result of major concern is the evidence of global sea level rise of 3.3 mm/yr detected by continuous radar altimetry observations since 1992 (Fig. 1.1). Half of this rise is most likely due to the dilatation of the water associated with global ocean temperature increase. The global image of sea level variations provided by radar altimetry shows the large geographical variability of sea level trends (Fig. 1.2). Furthermore, radar altimetry missions allowed to captured the evolution of El Niño/La Niña events and broadened our understanding of these phenomena like no other source of information has done before. In addition, they provide a major source for improvement in the knowledge of the short- and mid-wave structure of the marine geoid.

Due to the increasing requirements in accuracy and long-term integrity of spatio-temporal monitoring, it has become mandatory to validate and calibrate satellite radar altimetry system. Hence, the availability of ground-truth data have become a major target for current and future altimeter missions, leading to an international effort to establish calibration sites (Bonnefond et al., 2003; Haines et al., 2003; Pavlis et al., 2004). Common methods applied are tide gauge observations and deployments of GPS-equipped buoys underneath satellite tracks. With such calibration facilities, the accuracy of the oceanographic products is being improved. What is often missing, however, is offshore calibration data in the open sea.

The major aim of this project was to contribute to the improvement of sea level monitoring by developing enhanced methods for offshore regional sea surface height observations. The methods investigated included airborne laser altimetry, shipborne ultrasound altimetry and GPS-equipped buoys. By deploying these methods adjacent to radar altimetry sub-satellite tracks, they can contribute to the validation and calibration of spaceborne radar altimetry missions. In addition, these methods can be used to provide a link between offshore radar altimetry data and onshore

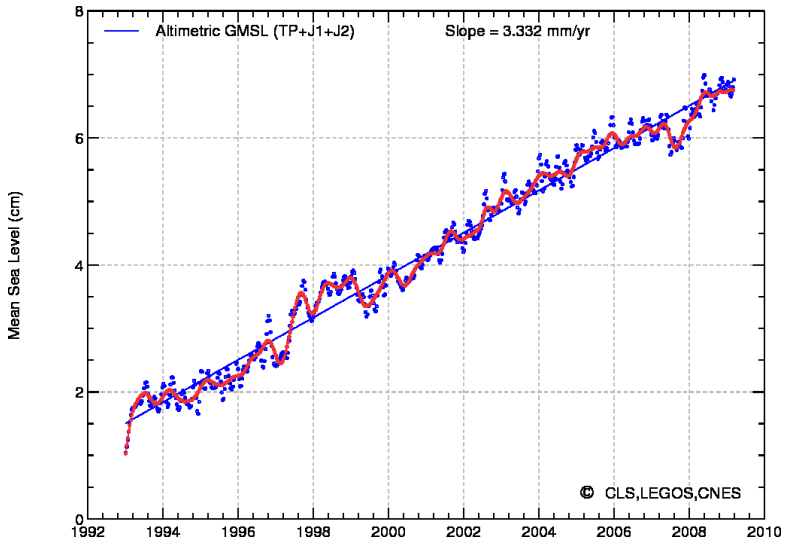

Figure 1.1: Global mean sea level (1992 to 2009) from the combination of data from TOPEX/Poseidon, Jason-1 and Jason-2. Seasonal variations have been removed. (Credits: CNES, CLS, LEGOS).

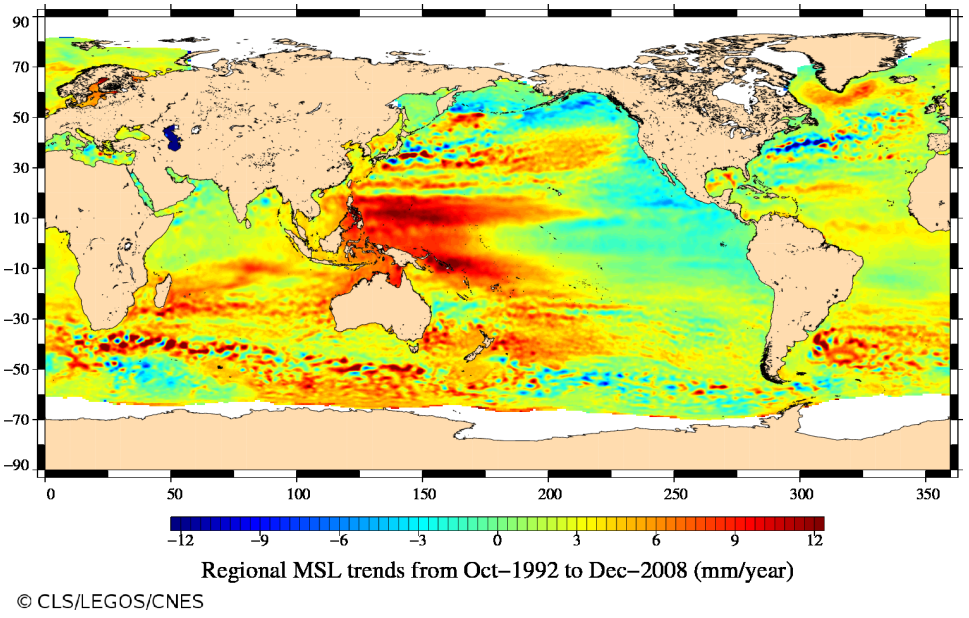

Figure 1.2: Sea level variation trends since 1992. (Credits: CNES, CLS, LEGOS).

tide-gauge stations. The final goal of this project was the analysis of the obtained regional sea surface topography and derived geoid heights in connection with geodynamic processes. The mean sea surface corresponds in a very good approximation to an equipotential surface of the Earth's gravity field. Thus, the gathered sea surface height data provides local-scale information on the short-wave structure of the marine geoid and related gravity field and can be used to improve local geoid solutions. Since the geoid is an equipotential surface of the Earth's gravity field, it depends on the mass distribution of the Earth's interior. The knowledge of mass distribution is of major importance for geophysical and geodynamical research. With the inversion of mean sea surface and geoid data, models of mass distribution can be constrained.

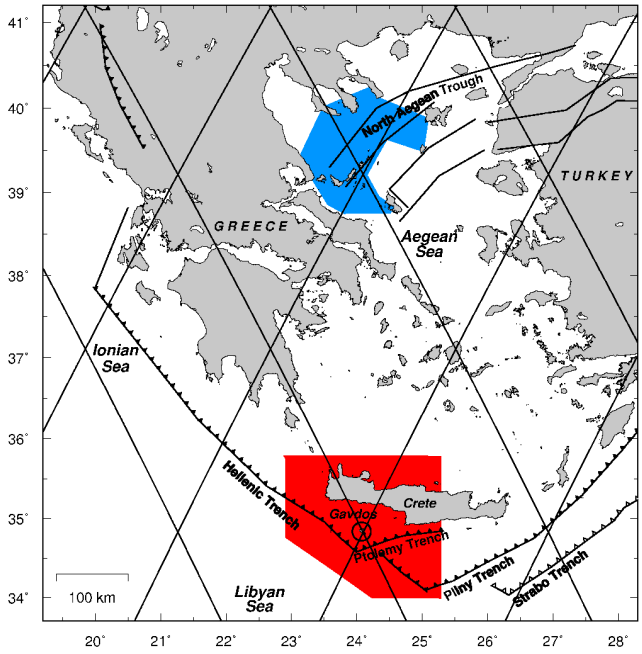

Figure 1.3: Survey areas in the Eastern Mediterranean Sea, with survey area for airborne laser altimetry around western Crete and survey area for shipborne ultrasound altimetry in the North Aegean Sea. Diagonal gridlines: Jason-1 ground tracks.

The area of investigation is the Eastern Mediterranean Sea, where two regional survey areas were chosen adjacent to Jason-1 radar altimetry ground tracks (Fig. 1.3). A detailed airborne laser altimetry campaign was carried out around the western part of the island of Crete, in the vicinity of the Hellenic Trench and the Hellenic subduction zone. Several campaigns for shipborne sea surface height surveys were carried out in the North Aegean Sea, in the vicinity of the North Aegean Trough. The sea surface height observations were concentrated on these areas in order to contribute to the improvement of the knowledge of the local gravity field, which could improve the understanding of the complex geodynamic processes related to the Hellenic subduction zone and the North Aegean Trough.

1.2 Geophysical Characteristics of the Eastern Mediterranean

The Mediterranean Sea is located between Africa and Europe and has a surface of $2.5 \cdot 10^6\,\mathrm{km}^2$, with a limited access to the Atlantic Ocean at the Strait of Gibraltar. Due to its semi-closed nature, the sea surface height of the Mediterranean Sea is strongly influenced by the seasonal atmospheric variations over Europe and North Africa, like wind tension, surface heat flow, rainfall and evaporation. A second forcing is formed by the mass flow through the Strait of Gibraltar.

The Eastern Mediterranean region is located in the slope region between the geoid high in the North Atlantic and the low in the Indian Ocean, associated with values of 40 m in the North Aegean down to 1 m in the Libyan Sea, south of Crete (Fig. 1.4). The Eastern Mediterranean is a region of high geodynamic activity, exposed to considerable earthquake and tsunami risks related to different types of active plate-tectonic boundaries. The region is mainly characterized by the collision between the Eurasian and African lithospheric plates (Fig. 1.5) (Kahle and Mueller, 1998). This collision is closely related to continental subduction and formation of the Hellenic Arc and Hellenic Trench system (Fig. 1.3). Superimposed on the relatively slow motion of the African

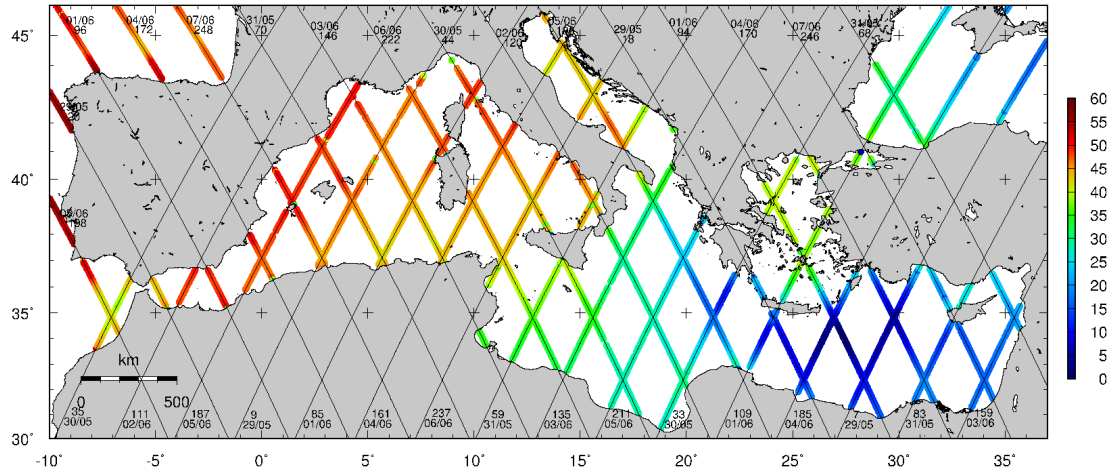

Figure 1.4: Jason-1 ground tracks in the Mediterranean Sea, with sea surface heights (in m) above the reference ellipsoid. A pronounced regional slope of the sea surface is observed, ranging from 50 m in the Balearic Sea down to 5 m in the Southern Aegean Sea.

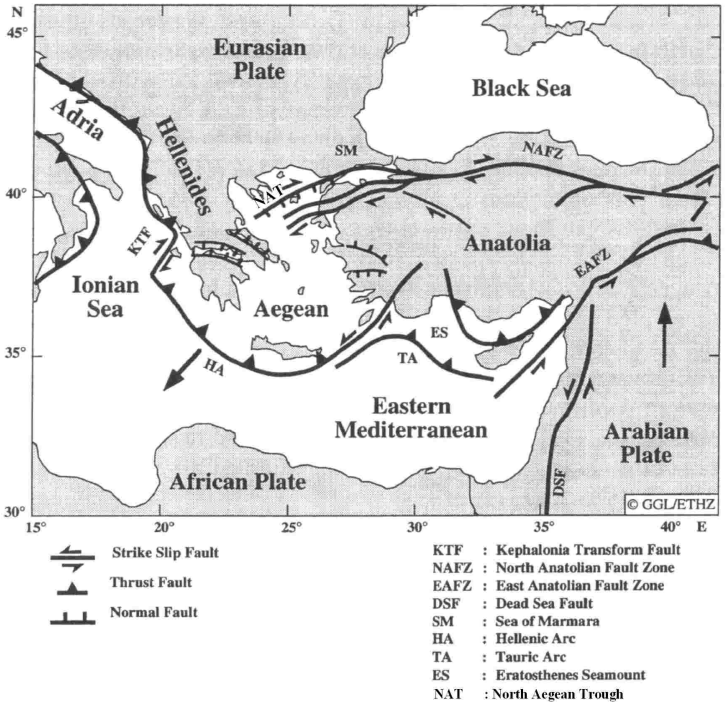

Figure 1.5: Simplified tectonic setting of the Eastern Mediterranean. From (Kahle and Mueller, 1998).

plate, complex dynamic processes affect the lithospheric blocks between the two major plates (Kahle et al., 2000). The most prominent kinematic feature is the rapid motion of the Anatolia and Aegean regions to the west and south-west, reaching velocities of up to 4 cm/yr, relative to Eurasia (McClusky et al., 2000; Hollenstein, 2006). The Hellenic Trench zone south of Crete is characterized by strong normal compression strain (Fig. 1.6). It is commonly accepted that the subduction and large-scale motion of the lithospheric blocks are associated with crustal and upper mantle mass anomalies causing pronounced geoid undulations which are also reflected in the sea surface topography.

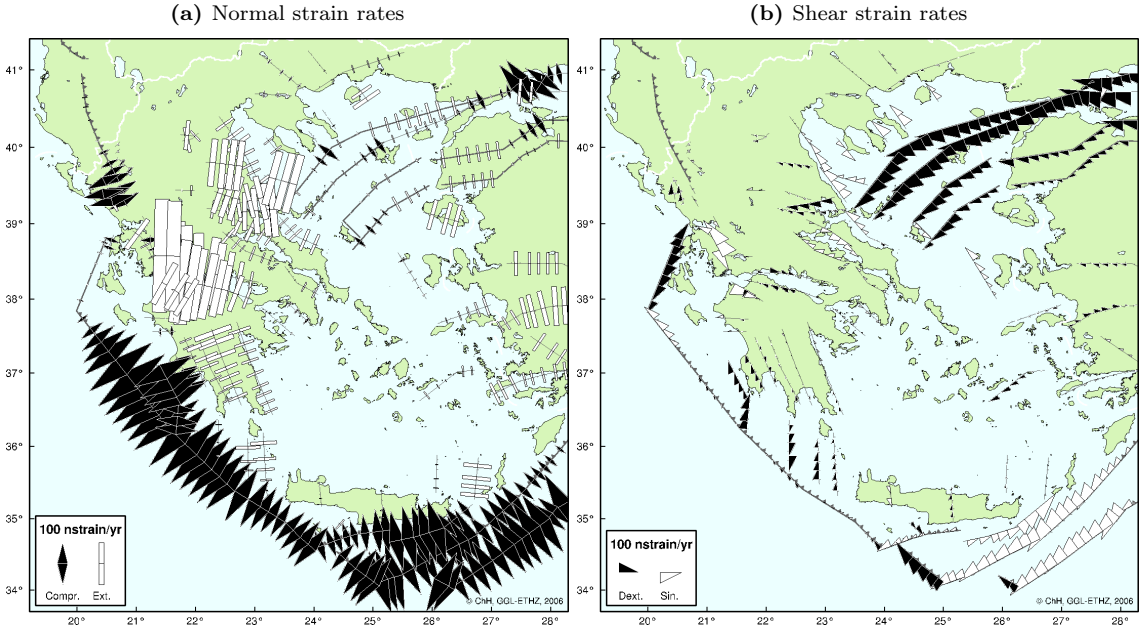

Figure 1.6: Normal **(a)** and shear **(b)** strain rates in the Eastern Mediterranean, derived from GPS observations (Hollenstein, 2006).

Besides the Hellenic Trench, another important geodynamic feature in the Eastern Mediterranean is the North Aegean Trough (NAT), situated in the North Aegean Sea (Fig. 1.5). The NAT is a tectonic graben-like feature characterized by a deep water zone reaching 1500 m and trending from north-east to south-west. It is considered to form the western continuation of the seismically active North Anatolian Fault Zone (NAFZ). The area of the NAFZ and NAT is identified as a major strike-slip boundary characterized by high seismicity, separating the Anatolia-Aegean plate from Eurasia (McNeill et al., 2004). It is accompanied with dextral shear strain rates of up to 170 nstrain/yr, combined with normal extension and isolated normal compression (Fig. 1.6) (Hollenstein, 2006). Compared to other strike slip boundaries between major tectonic plates, the GPS derived strain rates found along the NAFZ-NAT are of similar magnitude as those of the San Andreas fault zone (Kahle et al., 1999).

1.3 Former Work by the GGL in Related Fields of Research

The Geodesy and Geodynamics Lab (GGL) of ETH Zurich collaborated in several international projects covering the Mediterranean and Black Sea regions, such as the sea level fluctuation projects SELF–I and SELF–II (Zerbini et al., 1996; Becker et al., 2002), and a WEGENER study (Plag et al., 1998). The GGL has been active in the field of airborne laser altimetry since 1994. The technique was used for geoid determination in the Ionian and Aegean Seas, Greece (Cocard et al., 2002), as well as at the Lakes of Geneva (Favey and Schlatter, 1998) and Constance, Switzerland. Airborne laser altimetry surveys were conducted at the Unteraar glacier, Switzerland, with the goal to generate repeated surface models of the glacier used for mass balance determination and glacier monitoring (Favey, 2001; Favey et al., 2002). Airborne gravimetry was another main research area of the GGL (Verdun et al., 2003; Baumann, 2003). Satellite geodesy and GPS technology are other important research fields. Apart from high-precision static GPS applications, kinematic aspects and dynamic positioning are investigated. Different tests and feasibility studies have been carried out, leading to the development of a software for kinematic GPS positioning (Cocard, 1995).

1.4 Research Tasks and Project Outline

The project is structured in four main research tasks (Fig. 1.7):

1. Determination of instantaneous sea surface heights (SSH)

   This task focuses on the precise determination of instantaneous SSH profiles by airborne laser altimetry and shipborne ultrasound altimetry. For accurate SSH determination, the datasets have to be corrected for instrumental errors, like ranging errors due to atmospheric refraction and boresight misalignment. GPS-equipped buoys are used to provide ground-truth SSH data, for the calibration of the airborne and shipborne altimetry systems.

2. Transformation from instantaneous SSH to time-independent sea surface topography (SST)

   Based on the instantaneous SSH from research task 1, a time-independent SST is generated, by applying corrections for time-dependent geophysical effects, including ocean waves, tides, atmospheric pressure (inverse barometer effect) and wind forcing.

3. Validation of satellite radar altimetry missions

   This research task concentrates on the comparison of the detailed SST from airborne laser altimetry and shipborne ultrasound altimetry with the ones obtained from spaceborne radar altimetry missions, especially Jason-1.

4. Geoscientific exploitation

   This research task includes the modeling of local mass effects and the interpretation of sea surface height anomalies over the Hellenic Trench and the North Aegean Trough.

Based on the research tasks presented above, this work is organized in the following chapters:

Chapter 2: *Geoid, Sea Surface and Dynamic Ocean Topography* gives an overview of the theoretical background concerning these three geophysical quantities, as well as their interrelationship. The basic definitions and equations of gravitational potential, geoid, gravity anomalies, modeling of mass effects, mean sea surface, sea level anomalies, absolute and mean dynamic ocean topography and permanent tides are presented.

Chapter 3: *Geophysical Effects on Sea Surface Heights* gives an overview of the theoretical background of geophysical effects influencing the height of the sea surface on a time-dependent basis. The effects covered in this chapter are ocean waves, tides, atmospheric pressure and wind forcing.

Chapter 4: *Airborne Laser Altimetry* describes the instrumental setup used during the airborne altimetry surveys, as well as the theoretical background of laser ranging onto water surfaces.

Chapter 5: *Shipborne Ultrasound Altimetry* describes the instrumental setup used during the shipborne altimetry surveys, as well as the theoretical background of ultrasound ranging.

Chapter 6: *Direct Georeferencing* presents an approach for direct georeferencing, valid for both airborne laser and shipborne ultrasound altimetry. The GPS based trajectory and attitude recovery is discussed, and comparisons with attitude solutions from inertial units are made. In addition, a calibration method for boresight misalignment in airborne laser altimetry is presented.

Chapter 7: *Sea Surface Heights by Airborne Laser Altimetry around Western Crete* gives a description of the airborne laser altimetry surveys. Instantaneous sea surface height results are presented. The obtained sea surface heights are corrected for geophysical effects, including ocean tides, atmospheric pressure and wind forcing. A repeatability analysis and least-squares adjustment based on crosspoints is carried out, and the finally obtained time-independent sea surface topography is presented.

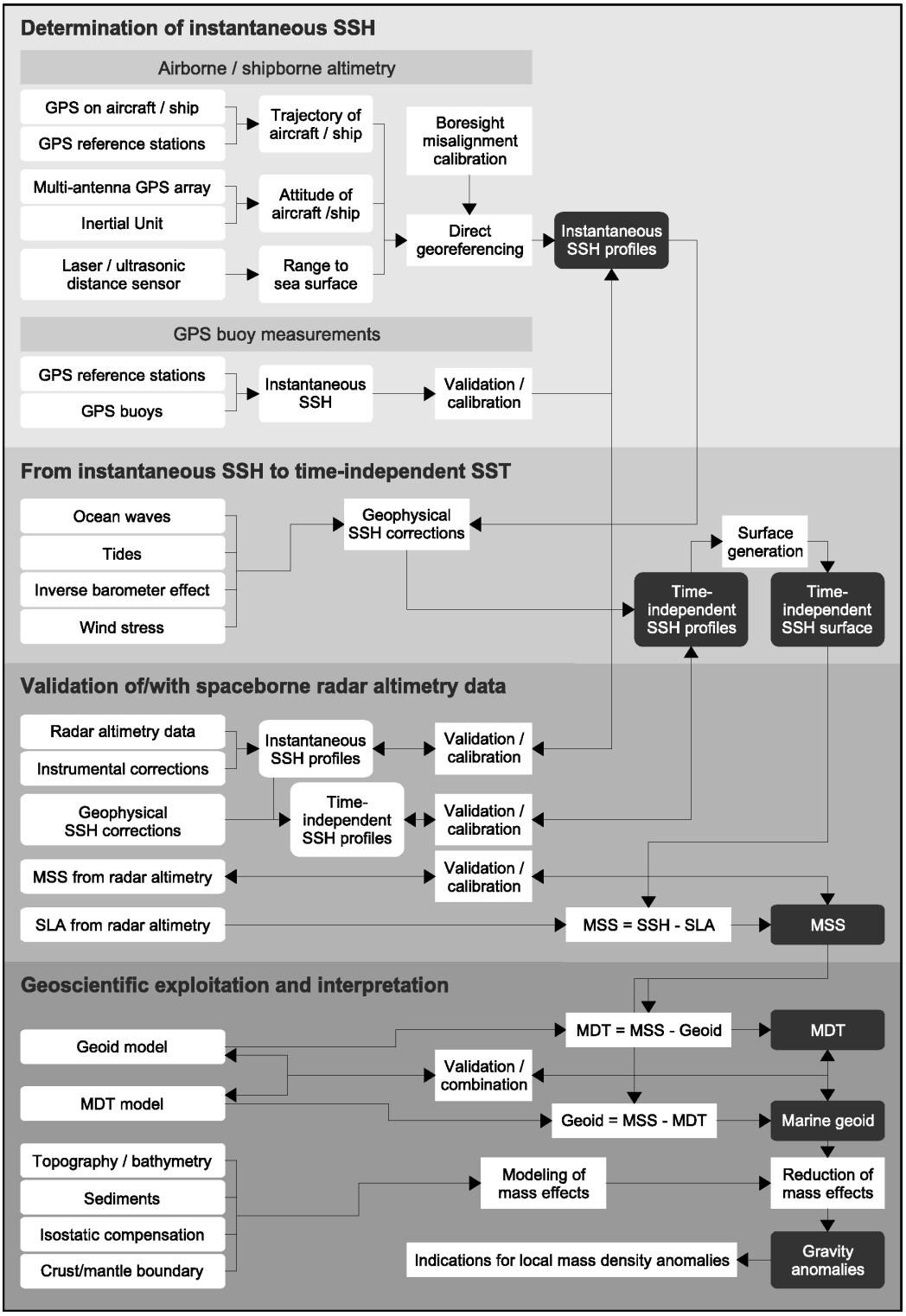

Figure 1.7: Flow diagram showing the four research tasks and the main results and outcomes (in black).

Chapter 8: *Sea Surface Heights by Shipborne Ultrasound Altimetry in the North Aegean Sea* is equivalent to Chapter 7 for shipborne ultrasound altimetry in the North Aegean Sea.

Chapter 9: *Validation of Satellite Radar Altimetry Data* presents a comparison between sea surface heights from airborne laser altimetry and Jason-1. Furthermore, a validation of mean sea surfaces from CLS01 and DNSC08 from multi-mission satellite radar altimetry with airborne and shipborne altimetry results is carried out.

Chapter 10: *Geoscientific Exploitation of Airborne Altimetry Data around western Crete* presents marine geoid heights, gravity anomalies, geoid gradients and deflections of the vertical derived from airborne laser altimetry around western Crete. A comparison of the obtained local altimetric geoid heights with existing models is carried, namely with the global models EGM96, EGM2008, EIGEN-5S, EIGEN-5C. Attempts to determine the mean dynamic topography are presented. Finally, mass effects are modeled for the survey areas and used to reduce the obtained geoid heights, for the detection and interpretation of geoid anomalies and mass anomalies.

Chapter 11: *Geoscientific Exploitation of Shipborne Altimetry Data in the North Aegean* is equivalent to Chapter 10 for shipborne ultrasound altimetry in the North Aegean Sea.

Chapter 12: *Summary and Conclusions* draws a summary and the major conclusions of this research project.

2 Geoid, Sea Surface and Dynamic Ocean Topography

2.1 Introduction

Techniques like satellite radar altimetry, airborne laser altimetry and shipborne ultrasound altimetry provide observations of the instantaneous sea surface height SSH_i above the reference ellipsoid (Fig. 2.1). After correcting SSH_i for geophysical effects like tides and atmospheric pressure, contributing to the relief of the sea surface on a time-dependent basis, time-independent sea surface heights SSH are obtained (Chapter 3).

The geoid forms the main permanent part of the sea surface topography, while ocean currents form both a permanent and a variable part. The permanent part is usually called mean dynamic topography MDT, whereas the sum of the permanent and the variable part is called absolute dynamic topography ADT. The SSH above the reference ellipsoid, provided by altimetry, is the sum of the geoid height N above the same ellipsoid and the ADT:

$$SSH \;=\; N \;+\; ADT \tag{2.1}$$

The mean sea surface MSS above the reference ellipsoid, the geoid undulations N above the same ellipsoid and the mean dynamic topography MDT are related by the following equation:

$$MSS \;=\; N \;+\; MDT \tag{2.2}$$

In the following sections, the constituents of the above equations will be described in more detail.

2.2 Geoid

2.2.1 Gravity Potential, Geoid and Gravity Anomalies

The gravity potential W of the Earth, at a point $P(x, y, z)$ on or outside the Earth's surface, is the sum of the gravitational potential V and the potential V_c of the centrifugal force:

$$W(P) \;=\; V(P) \;+\; V_c(P) \tag{2.3}$$

The gravitational potential V is given by Newton's integral:

$$V(P) \;=\; G \iiint_v \frac{dm}{l} \;=\; G \iiint_v \frac{\rho}{l}\, dv \tag{2.4}$$

where $G = 6.6742 \cdot 10^{-11}$ [$\mathrm{m^3\,kg^{-1}\,s^{-2}}$] is Newton's gravitational constant, dm is an element of mass, dv is an element of volume, ρ is the mass density of the element and l is the distance between the mass element dm and the attracted point P.

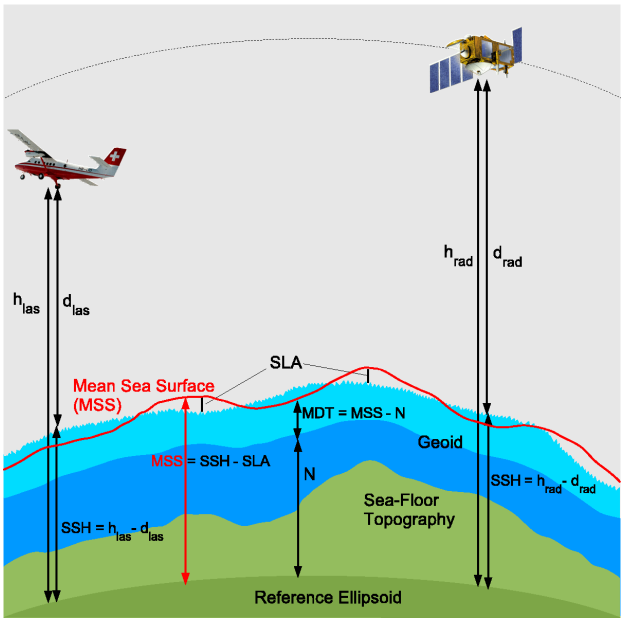

Figure 2.1: Altimetric sea surface height observations and relations between sea surface height, geoid and dynamic ocean topography.

The geoid is an equipotential surface of the Earth's gravity field that is closely associated with the location of the mean sea surface (Picot et al., 2003). The constant gravity potential on the geoid is defined by:

$$W(P) \;=\; W_0 \;=\; \text{constant} \tag{2.5}$$

The normal gravity potential U is given by:

$$U(Q) \;=\; V_e(Q) \;+\; V_c(Q) \tag{2.6}$$

where Q is a point on the ellipsoid, $V_e(Q)$ is the gravitational potential of the reference ellipsoid representing the best approximation of the geoid and $V_c(Q)$ is the potential of the centrifugal force. The reference ellipsoid is defined in a way that its gravity potential on its surface is equal to the potential of the geoid:

$$U(Q) \;=\; W_0 \;=\; \text{constant} \tag{2.7}$$

The vector gravitational acceleration, or gravity vector, $\overrightarrow{g}$ is the gradient of W:

$$\overrightarrow{g} \;=\; grad\ W \;=\; \left(\frac{\partial W}{\partial x}, \frac{\partial W}{\partial y}, \frac{\partial W}{\partial z}\right) \tag{2.8}$$

$\overrightarrow{g}$ is always perpendicular to the equipotential surface, meaning that there are no lateral gravitational forces along the geoid. Analogous, the normal gravity vector $\overrightarrow{\gamma}$ is the gradient of U:

$$\overrightarrow{\gamma} \;=\; grad\ U \;=\; \left(\frac{\partial U}{\partial x}, \frac{\partial U}{\partial y}, \frac{\partial U}{\partial z}\right) \tag{2.9}$$

The magnitude of the normal gravity vector $\overrightarrow{\gamma}$ on the surface of the ellipsoid can be obtained by the closed formula:

$$\gamma \;=\; \gamma_e \,\frac{1 + k \sin^2 \phi}{\sqrt{1 - e^2 \sin^2 \phi}} \tag{2.10}$$

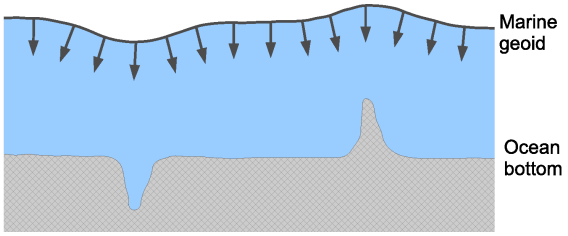

Figure 2.2: Schematic diagram of a bump and a depression at the ocean bottom and the corresponding marine geoid. Vectors indicate the gravitational acceleration along the geoid.

where $k = \frac{b \cdot \gamma_p}{a \cdot \gamma_e} - 1$, a and b are the semi-major and semi-minor axes of the ellipsoid, γ_e and γ_p are the theoretical gravity at the equator and poles, e is the first ellipsoid eccentricity and ϕ is the geodetic latitude. Definitions and values of the ellipsoidal parameters of the WGS84 reference ellipsoid can be found in (NIMA, 2000).

The anomalous or disturbing gravity potential T is given by the difference between the real gravity potential $W(P)$ and the normal gravity potential $U(P)$:

$$T(P) \; = \; W(P) \; - \; U(P) \tag{2.11}$$

The surface of the geoid is generally described in terms of geoid undulations N, which are the heights of the geoid with respect to the reference ellipsoid. The geoid height N is related to the anomalous gravity potential T by Brun's formula:

$$N \; = \; \frac{T}{\gamma} \tag{2.12}$$

where γ is the normal gravity related to the reference ellipsoid (2.10). The most negative geoid undulations of -106 m are found in the Indian Ocean, whereas the most positive geoid heights are encountered over Indonesia (85 m) and in the Northern Atlantic Ocean (61 m). On a global scale, the geoid is usually defined using spherical harmonic expansions of the Earth's gravity potential.

As stated above, the geoid is an equipotential surface of the Earth's gravity field that is closely associated with the location of the mean sea surface (Picot et al., 2003). In the absence of other forcing (e.g. pressure gradients, wind forcing or tides), the sea surface would be a surface of constant gravity potential, corresponding the marine geoid (Chelton, 1988). Variations in gravitational acceleration over the Earth's surface result in an uneven distribution of water mass in the oceans (Chelton, 1988) and in deformations of the sea surface. Although geoid undulations are primarily long-wavelength phenomena, short-wavelength changes in the geoid undulation are seen over seamounts, trenches and ridges in the oceans (Picot et al., 2003). The gravitational acceleration at the sea surface is slightly stronger over bumps on the ocean bottom and slightly weaker over depressions in the bathymetry (Chelton, 1988). The gravitational acceleration is locally deflected towards the bump and away from the depression and is perpendicular to the geoid (Fig. 2.2). The amount of the deflection depends on the composition of the bathymetric feature and decreases with the distance to the feature. Thus, a feature in the far field has essentially no effect on the local gravitational acceleration. The marine geoid over a bump is also a bump, but smoothed due to the inverse dependency on the distance to the bump. Similarly, the marine geoid over a depression in the bathymetry (e.g. a trench) is also depressed (Chelton, 1988). In a first approximation, the marine geoid can be considered as a low-pass filtered image of the bathymetry (Fig. 2.2).

The deflection of the vertical is the angle between the normal to the geoid and the normal to the ellipsoid. The east and north components (η, ξ) of the deflection of the vertical, corresponding to

the slope of the geoid in east and north direction, are given by (Heiskanen and Moritz, 1967):

$$\eta \;=\; -\frac{\partial N}{\partial x}\;, \quad \xi \;=\; -\frac{\partial N}{\partial y} \tag{2.13}$$

and with the spherical approximation:

$$\eta \;=\; -\frac{1}{a\cos\phi}\frac{\partial N}{\partial \lambda}\;, \quad \xi \;=\; -\frac{1}{a}\frac{\partial N}{\partial \phi} \tag{2.14}$$

where ϕ is the geodetic latitude, λ is the longitude and a is the mean radius of the Earth.

The gravity anomaly vector $\Delta\overrightarrow{g}$ is the difference between the gravity vector $\overrightarrow{g}$ (2.8) and the normal gravity vector $\overrightarrow{\gamma}$ (2.9). Analogous, the difference in magnitude is the gravity anomaly Δg:

$$\Delta g \;=\; g(P) \;-\; \gamma(Q) \tag{2.15}$$

where P is a point on the geoid and Q is the projection of P onto the ellipsoid along the ellipsoidal normal. The gravity anomaly can also be computed as (Hofmann-Wellenhof and Moritz, 2006):

$$\Delta g \;=\; -\frac{\partial T}{\partial z} \;+\; \frac{\partial \gamma}{\partial z}\,N \tag{2.16}$$

where z denotes the vertical direction, normal to the ellipsoid. In (2.16), the first term on the right-hand side is the gravity disturbance δg at the point P on the geoid:

$$\delta g(P) \;=\; g(P) \;-\; \gamma(P) \;=\; -\frac{\partial T}{\partial z} \tag{2.17}$$

The second term of (2.16) accounts for the gravity change between the point P on the geoid and the point Q on the ellipsoid. In practice, e.g. in free-air gravity reduction, the vertical gradient of the normal gravity is usually approximated by:

$$\frac{\partial \gamma}{\partial z} \;=\; -\;0.3086\;\;[\text{mGal/m}] \tag{2.18}$$

Anomalies of the marine gravity field can be derived from the marine geoid using Laplace's equation:

$$\frac{\partial^2 T}{\partial x^2} \;+\; \frac{\partial^2 T}{\partial y^2} \;+\; \frac{\partial^2 T}{\partial z^2} \;=\; 0 \tag{2.19}$$

Substitution of (2.12), (2.16) and (2.13) in Laplace's equation (2.19), and considering that $\frac{\partial^2 \gamma}{\partial z^2} = 0$, yields the following relation between the vertical gravity gradient and the curvature of the geoid (Sandwell and Smith, 1997):

$$\frac{\partial \Delta g}{\partial z} \;=\; \gamma\left(\frac{\partial^2 N}{\partial x^2} + \frac{\partial^2 N}{\partial y^2}\right) \;=\; -\gamma\left(\frac{\partial \eta}{\partial x} + \frac{\partial \xi}{\partial y}\right) \tag{2.20}$$

The differential equation (2.20) can be solved in the frequency domain by Fourier transformation of gridded geoid heights (Sandwell and Smith, 1997). The use of Laplace's equation (2.19) implies that there are no masses outside the geoid. For the marine geoid, this condition is always verified, except for coastal areas, where the marine gravity field and geoid are influenced by topographic masses outside the geoid.

Table 2.1: Density values used in the modeling of mass effects and isostatic compensation.

Layer	Density [10^3 kg/m^3]
Sea water	1.03
Light sediments	2.30
Upper crust (topography)	2.67
Lower crust (above crust-mantle boundary)	2.90
Upper mantle	3.30

More details on the theory of gravity potential, geoid and gravity anomalies can be found in many textbooks on physical geodesy, e.g. (Heiskanen and Moritz, 1967; Moritz, 1980; Hofmann-Wellenhof and Moritz, 2006).

2.2.2 Gravitational Mass Effect and Mass Reduction

Regional anomalies of the gravity potential are mainly caused by mass anomalies from topography, bathymetry, sedimentary deposits, crust-mantle boundary and lithosphere structures like subducting slabs. These mass effects can be modeled and used to reduce observed geoid heights or gravity. The effect of a mass element on the gravitational potential is given by Newton's integral (2.4). Denoting the coordinates of the attracted point P by (x_p, y_p, z_p) and the coordinates of the mass element dm by (x, y, z), the disturbing potential T caused by the mass elements is given by:

$$T(x_p, y_p, z_p) \;=\; G \iiint_v \frac{\rho\ (x, y, z)}{l}\ dx\ dy\ dz \tag{2.21}$$

where $l = \sqrt{(x - x_p)^2 + (y - y_p)^2 + (z - z_p)^2}$ is the distance between the mass element of density ρ and the attracted point P. Typical values of mass densities ρ are given in Tab. 2.1. The effect of mass elements on the geoid height N at the computation point P is obtained from (2.21) using Brun's formula (2.12):

$$N(x_p, y_p, z_p) \;=\; \frac{T}{\gamma} = \;\frac{G}{\gamma} \iiint_v \frac{\rho(x, y, z)}{l}\ dx\ dy\ dz \tag{2.22}$$

Based on (2.16), the effect of mass elements on the gravity anomaly Δg at the computation point P is obtained from (2.21), by first order derivation along the vertical z direction:

$$\Delta g(x_p, y_p, z_p) \;=\; -\frac{\partial T}{\partial z} \;=\; -\ G \iiint_v \frac{\rho(x, y, z)\ (z - z_p)}{l^3}\ dx\ dy\ dz \tag{2.23}$$

Note that in (2.23), the term $\frac{\partial \gamma}{\partial z} N$ of (2.16) was omitted. Hence the gravity anomaly Δg in (2.23) is more precisely a gravity disturbance δg as defined in (2.17). Due to the $1/l^3$ dependency of the gravity anomaly Δg on the distance l between the mass element and the attracted point P (2.23), the influence of a mass element on gravity decreases much faster with increasing distance than its influence on the geoid height N (2.22). Hence, as compared to geoid heights, gravity anomalies are less affected by the long-wavelength part of the gravitational potential and are therefore better suited for the analysis of local gravitational anomalies.

A method to compute mass effects on geoid heights or on gravity based on (2.22) or (2.23) consists in dividing the present masses into mass cuboids. The derivation of the complete formulas for the potential of a finite cuboid and the derivations of the potential to the third degree can be found

in (Mader, 1951). The following formula gives the gravitational potential T of a finite cuboid, obtained by solving the integral in (2.21) for a finite cuboid (Mader, 1951):

$$\begin{aligned}\frac{1}{G\,\rho}\,T(P) \;=\; &\{x_2y_2z_2\} - \{x_1y_2z_2\} - \{x_2y_2z_1\} + \{x_1y_2z_1\} \\ &- \{x_2y_1z_2\} + \{x_1y_1z_2\} + \{x_2y_1z_1\} - \{x_1y_1z_1\}\end{aligned} \tag{2.24}$$

with e.g.

$$\begin{aligned}\{x_2y_2z_2\} \;= \; &y_2\;z_2\;\log(x_2+r_{222}) \;+\; x_2\;y_2\;\log(z_2+r_{222}) \;+\; x_2\;z_2\;\log(y_2+r_{222}) \\ &-\;\frac{x_2^2}{2}\;\arctan\left(\frac{y_2\;z_2}{x_2\;r_{222}}\right) \;-\;\frac{y_2^2}{2}\;\arctan\left(\frac{x_2\;z_2}{y_2\;r_{222}}\right) \;-\;\frac{z_2^2}{2}\;\arctan\left(\frac{x_2\;y_2}{z_2\;r_{222}}\right)\end{aligned}$$

where $x_1, x_2, y_1, y_2, z_1, z_2$ are the coordinates of the edges of the cuboid and e.g. $r_{222} = \sqrt{x_2^2 + y_2^2 + z_2^2}$ is the distance between the point (x_2, y_2, z_2) and the computation point $P(0, 0, 0)$. Geoid heights are obtained from (2.24) using Brun's formula (2.12). Similar to (2.24), the gravity anomaly Δg are obtained by solving the integral in (2.23) for a finite cuboid, or by first order derivation of (2.24) along the vertical z direction (Mader, 1951):

$$\begin{aligned}\frac{1}{G\,\rho}\,\Delta g(P) \;=\; -\frac{1}{G\,\rho}\,\frac{\partial T(P)}{\partial z} \;=\; &\{x_2y_2z_2\} - \{x_1y_2z_2\} - \{x_2y_2z_1\} + \{x_1y_2z_1\} \\ &- \{x_2y_1z_2\} + \{x_1y_1z_2\} + \{x_2y_1z_1\} - \{x_1y_1z_1\}\end{aligned} \tag{2.25}$$

with e.g.

$$\{x_2y_2z_2\} \;=\; y_2\;\log(x_2+r_{222}) \;+\; x_2\;\log(y_2+r_{222}) \;-\; z_2\;\arctan\left(\frac{x_2\;y_2}{z_2\;r_{222}}\right)$$

Since the computation of the effects of cuboid masses using (2.24) and (2.25) can be very CPU-intensive, a simplified method to compute approximate mass effects on geoid heights and on gravity based on (2.22) and (2.23) consists in concentrating the mass of each cuboid at its center of mass (point mass). In order to assess the impact of this approximation, the effects on geoid heights computed based on cuboid masses and on point masses were compared in Sections 10.4.7 and 11.4.7.

With the mass reduction, the mass effects computed with (2.22) or (2.23) are removed from the geoid heights or gravity anomalies. The residual geoid heights or gravity anomalies represent the effects caused by unmodeled masses. Hence, the mass reduction allows to detect anomalous mass distributions. Positive residuals indicate an existing mass excess with respect to the modeled masses or an underestimation of the mass effect in the model. On the other hand, negative residuals indicate an existing mass deficiency with respect to the modeled masses or an overestimation of the mass effect in the model.

In Sections 10.4 and 11.4, mass effects of topography, bathymetry, sediments and crust-mantle boundary (Moho) on geoid heights and on gravity anomalies were computed using (2.22) and (2.23), respectively (2.24) and (2.25). In Sections 10.5 and 11.5, the modeled mass effects were used to reduce the geoid heights and gravity anomalies derived from the sea surface heights obtained from airborne and shipborne altimetry, in the area of Crete and in the North Aegean Sea, respectively.

More details on the theory of mass effects can be found in textbooks on physical geodesy, e.g. (Heiskanen and Moritz, 1967; Moritz, 1980; Hofmann-Wellenhof and Moritz, 2006).

2.2.3 Gravitational Models

A brief description of the gravitational models used in Sections 10.2 and 11.2 for comparison with the geoid heights obtained from airborne and shipborne altimetry, is given below:

- The Earth Gravitational Model **EGM96** was developed by the NASA GSFC and NIMA (Lemoine et al., 1998). The data used to derive the EGM96 include orbital perturbations from over 20 satellites, surface and airborne gravimetric surveys from different regions and sea surface heights from radar altimetry missions GEOSAT, ERS-1 and TOPEX/Poseidon. The EGM96 is complete to spherical harmonics degree and order 360, corresponding to a spatial resolution of approximately 55 km (half-wavelength).
- The Earth Gravitational Model **EGM2008** was publicly released by the U.S. NGA EGM Development Team in April 2008 (Pavlis et al., 2008). It combines gravity information from the GRACE mission with a global gravity anomaly database of $5' \times 5'$ resolution from surface gravity data and altimetry data. The EGM2008 does not incorporate any GPS/leveling data or astronomic deflections of the vertical. It is complete to spherical harmonics degree and order 2159, and contains additional coefficients extending to degree 2190 and order 2159, corresponding to a spatial resolution of approximately 10 km (half-wavelength). Geoid heights computed from EGM2008 over the Mediterranean Sea are shown in Fig. 2.3a.
- The **EIGEN-5C** is a combined gravity field model computed by the GFZ-GRGS cooperation (Foerste et al., 2008). It is a combination of GRACE data from Feb. 2003 to Jan. 2007 and LAGEOS data from Jan. 2002 to Dec. 2006, as well as $0.5^\circ \times 0.5^\circ$ surface gravimetric and altimetric data. The EIGEN-5C is complete to spherical harmonics degree and order 360, corresponding to a spatial resolution of approximately 55 km (half-wavelength).
- The **EIGEN-5S** is a satellite-only model associated with the EIGEN-5C. It includes only GRACE and LAGEOS data, and is independent of surface data and radar altimetry data. Since missions like GRACE and LAGEOS do not resolve short-wavelength signals, the EIGEN-5S is only complete to spherical harmonics degree and order 150, corresponding to a spatial resolution of approximately 130 km (half-wavelength).
- The **AUTH2008** is a gravimetric geoid model based on free-air gravity anomaly data, covering the area of Greece. It was computed by the Aristotle University of Thessaloniki (AUTH), Greece (Tziavos and Andritsanos, 1999; Vergos et al., 2004; Grigoriadis, 2009). For the area of Crete, the model is partly based on airborne gravimetric data collected during the combined airborne gravimetry-altimetry campaign in the framework of the GAVDOS project (Tziavos et al., 2004) (Section 7.1).

2.3 Mean Sea Surface

The mean sea surface MSS represents the position of the ocean surface averaged over an appropriate time period to remove annual, semi-annual, seasonal and spurious sea surface height signals (Picot et al., 2003). The MSS is a height above a reference ellipsoid. It corresponds to the sum of the geoid undulation N and the mean dynamic topography MDT averaged over a selected time period (Hernandez and Schaeffer, 2001), according to (2.2). MSS models are essentially based on satellite radar altimetry data. They are used for various purposes, such as the computation of along-track and cross-track geoid gradients, needed as corrections in the repeat orbit method, for the computation of gridded gravity anomalies, for the operational computation of sea level anomalies SLA (Section 2.4) and to provide a common reference for distinct satellite missions. The MSS models used in this project to validate the sea surface heights obtained by airborne and shipborne altimetry are the CLS01 and DNSC08 (Sections 9.3.1 and 9.3.2):

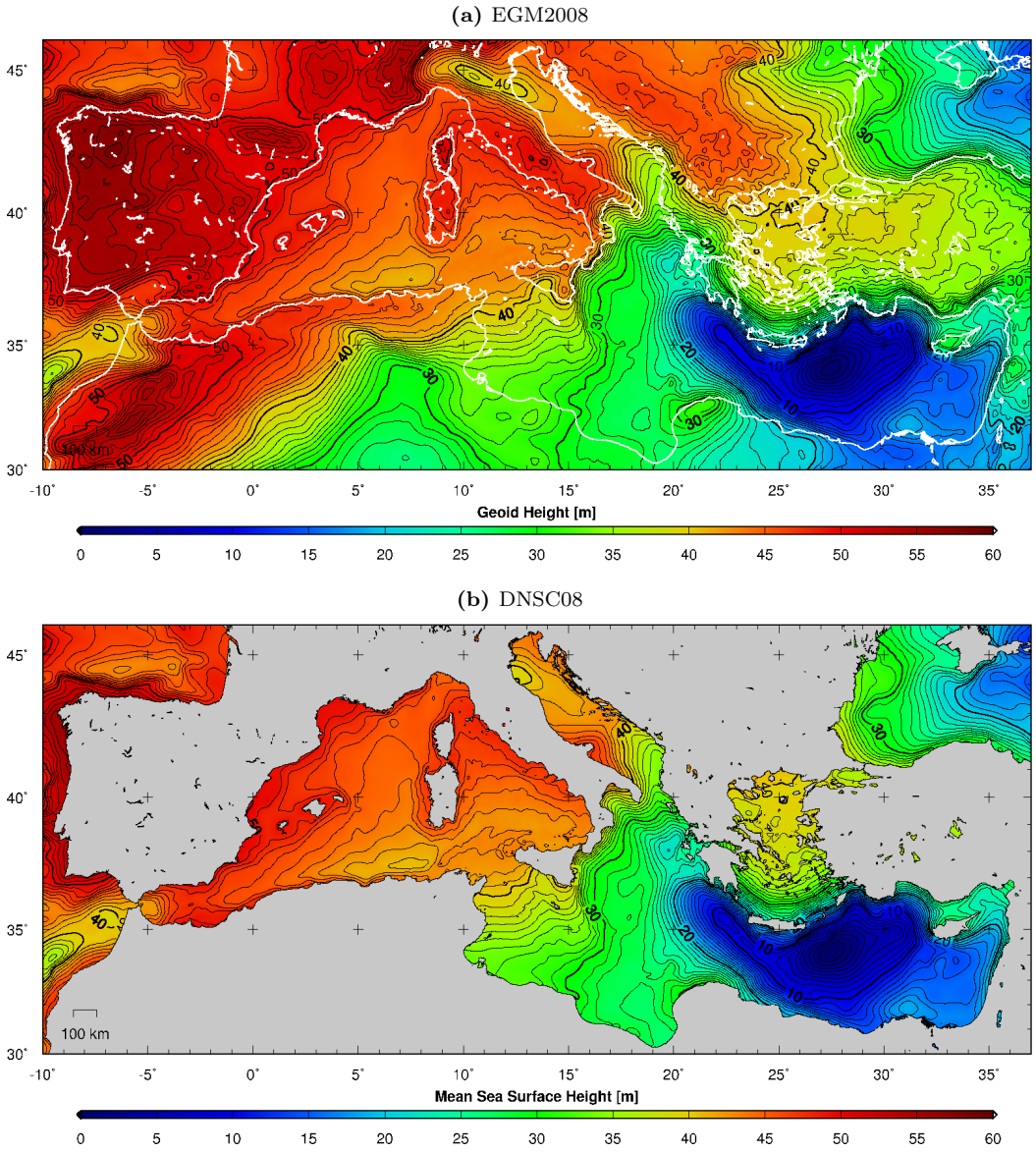

Figure 2.3: **(a)** EGM2008 geoid heights and **(b)** DNSC08 mean sea surface heights above the WGS84 reference ellipsoid in the Mediterranean Sea. The pronounced regional slopes of the marine geoid and the sea surface range from 50 m in the Balearic Sea in the Western Mediterranean down to 0 m in the Eastern Mediterranean. Contour intervals: 1 m.

- The **CLS01** was produced by CLS Space Oceanography Division and distributed by AVISO, with support from CNES (Hernandez and Schaeffer, 2000). The reference time period of the CLS01 is from 1993 to 1999 (7 years). It was computed using TOPEX/Poseidon mean profiles over 7 years, ERS-1/2 mean profiles over 5 years, GEOSAT mean profiles over 2 years and ERS-1 data. The CLS01 is determined oceanwide between 80°S and 82°N. Over continents, it is based on the EGM96 geoid, with a smooth transition in coastal areas. The CLS01 is provided on a regular grid with a spatial resolution of 2'×2' ($\simeq$ 4 km). However, the inherent resolution of along-track radar altimetry data is limited to about 10 km by their footprint diameter. In addition, ground track spacing between multi-mission data can reach even higher values. Furthermore, the CLS01 is based on a local least square collocation, using

altimetric data in a radius of 200 km (Hernandez and Schaeffer, 2001). Hence, the CLS01 can resolve wavelengths down to 10 - 20 km.

- The **DNSC08** is the most recent MSS released by the Danish National Space Center (DNSC) (Andersen et al., 2007; Andersen and Knudsen, 2008). An extract of the DNSC08 in the Mediterranean Sea is shown in Fig. 2.3b. It is based on multi-mission radar altimetry data from TOPEX/Poseidon, Jason-1, ERS-1/2, ENVISAT, GFO and GEOSAT, as well as ICESAT data. The DNSC08 is provided on a regular grid with a spatial resolution of 1'×1' ($\simeq 2$ km). The coverage is global (90°S to 90°N). Similar to the remarks concerning the CSL01 above, the DNSC08 can resolve wavelengths down to 10 - 20 km.

The MSS from CLS01 and DNSC08 are both referenced to the TOPEX/Poseidon Earth ellipsoid ($a = 6378136.3$ m, $1/f = 298.257$, $GM = 398600.4415\,\mathrm{km}^3/\mathrm{s}^2$). For comparison purposes with the sea surface heights from airborne and shipborne altimetry determined in this project, the MSS heights were transformed to the WGS84 reference ellipsoid. This transformation corresponds to a mean vertical shift of -0.705 m at the latitudes of the Mediterranean Sea.

2.4 Sea Level Anomaly

The sea level anomaly SLA is the difference between the time-independent sea surface height SSH from (3.1) and the mean sea surface MSS from (2.2):

$$SLA \;=\; SSH \;-\; MSS \tag{2.26}$$

The only means to observe SLA on a global and regional scale is satellite radar altimetry, since repeated observations of the sea surface at the same location over time periods of several years are needed. In (2.26), the MSS can either be a multi-mission mean sea surface (Section 2.3) or a mono-mission mean sea surface profile computed along repeated tracks of the same mission. The SLA always refers to the reference height MSS used to compute it.

The SLA products used in this project are delayed-time SSALTO/DUACS SLA (AVISO, 2008). They are produced by SSALTO/DUACS and distributed by AVISO, with support from CNES. DUACS (Data Unification and Altimeter Combination System) is part of the CNES multi-mission ground segment SSALTO. The SSALTO/DUACS are multi-mission products from TOPEX/-Poseidon, Jason-1, ENVISAT, GFO, ERS-1/2 and GEOSAT. Delayed-time SLA products from SSALTO/DUACS are provided as along-track data for each altimetry mission, as well as gridded products merging data from all missions. Altimetry observations are resampled along a theoretical ground track (or mean track) associated to each mission. Then, a mean profile is subtracted from the resampled data to obtain along-track SLA, using (2.26). The mean profile is a time average of similarly resampled data over a long period. For example, the mean profiles used for TOPEX/Poseidon and Jason-1 were computed with TOPEX/Poseidon data from January 1993 to December 1999, using the new 2008 GDR standards. The gridded products are provided on a global 1/3° Mercator grid and on regional grids, e.g. a 1/8° regular grid for the Mediterranean Sea, based on one week of altimeter data.

An example of gridded weekly SLA from multi-mission SSALTO/DUACS over the Mediterranean Sea is shown in Fig. 2.4, corresponding to the time period of the GAVDOS airborne campaign (Section 7.1). A high spatial variability was observed, with SLA values ranging from -15 to 25 cm. The average sea surface of the Mediterranean was higher than the reference height, with positive mean SLA values of 8.6 and 2.8 cm for 08/01/2003 and 15/01/2003, respectively. The rapid decrease of the mean SLA by 5.8 cm during only one week, as well as local SLA variations of up to 15 cm (Fig. 2.4, bottom), underline the highly dynamic behavior of sea level variations in time.

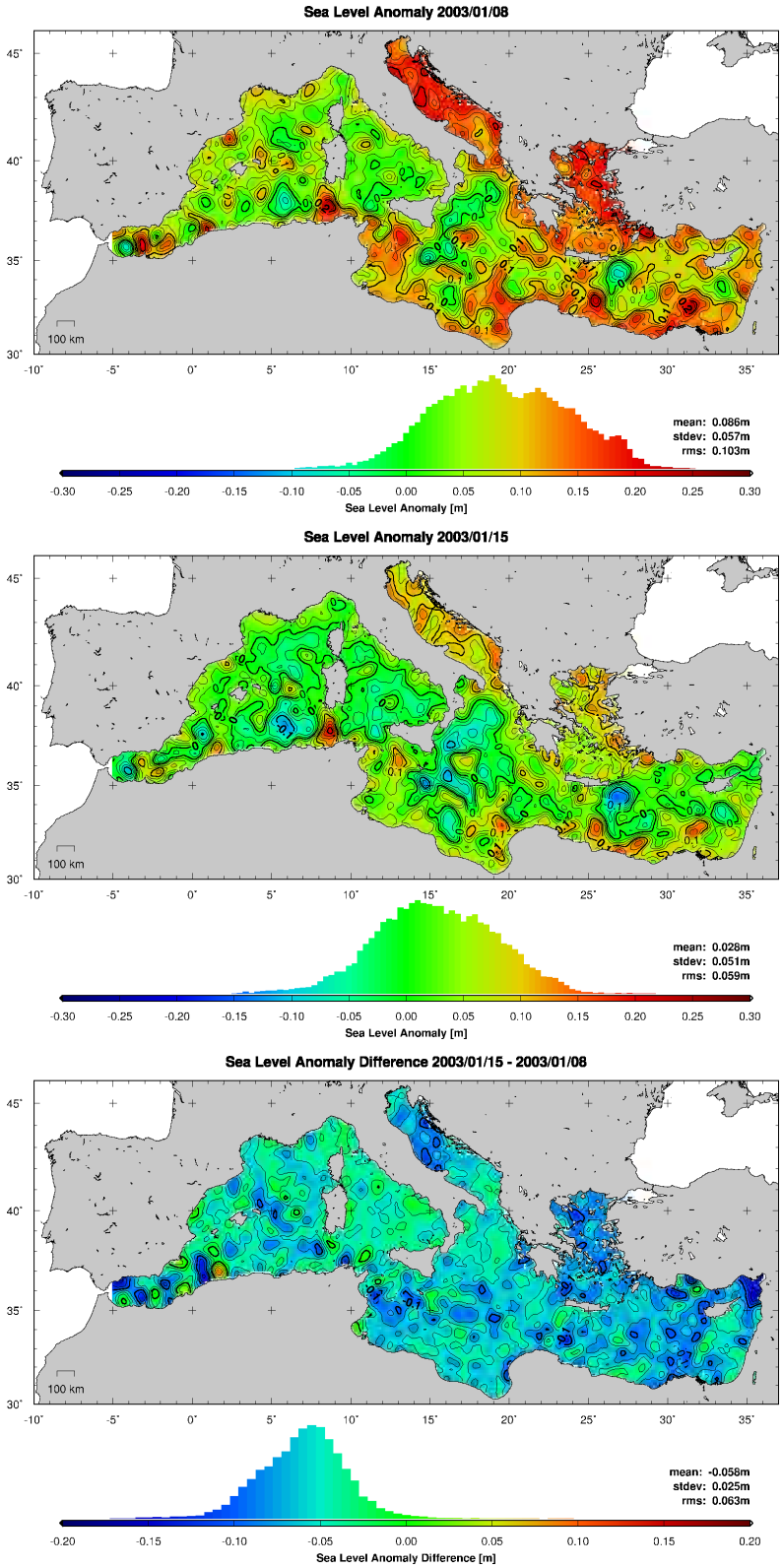

Figure 2.4: Weekly sea level anomalies (SLA) from SSALTO/DUACS merged multi-mission altimetric data in the Mediterranean Sea, on 08/01/2003 (top) and 15/01/2003 (center), as well as difference between the two consecutive weekly datasets (bottom). Contour intervals: 2.5 cm

2.5 Dynamic Ocean Topography

2.5.1 Absolute and Mean Dynamic Topography

The dynamic ocean topography is an important indicator in the study of ocean dynamics (Dobslaw, 2007). From an oceanographic perspective, the primary purpose of sea surface height observations is the determination of the sea surface elevation induced by ocean currents. This sea surface elevation is called absolute dynamic topography ADT of the ocean. Based on (2.1), the ADT is given by the difference between the sea surface height SSH, corrected for geophysical effects like tides and atmospheric pressure (3.1), and the geoid height N:

$$ADT = SSH - N \tag{2.27}$$

The major application of ADT signals from radar altimetry is their assimilation into general circulation models, which is crucial for the development of operational forecasting systems (Rio et al., 2007). Analogous to (2.27), the mean dynamic topography MDT of the ocean is obtained from (2.2) as the residual surface between the mean sea surface MSS and the geoid height N:

$$MDT = MSS - N \tag{2.28}$$

The MDT is the part of the MSS produced by permanent ocean currents. In (2.28), MSS can either be a gridded multi-mission MSS or a mono-mission MSS profile along repeated tracks of the same mission. The ADT and MDT are orthometric sea surface heights above the geoid. Equations (2.27) and (2.28) are called direct method for the computation of the absolute and mean dynamic topography. The direct method requires that the accuracy and spatial resolution of the marine geoid and sea surface height information comply with the amplitudes and wavelengths of the effects produced by ocean currents. Important features of the oceanic circulation typically contain wavelengths as short as 100 - 200 km (Rio and Hernandez, 2004). The altimetric MSS resolves spatial scales down to 10 - 20 km (Section 2.3), while geoid models are usually only available at lower resolutions (Section 2.2.3), especially over oceans. In this case, the MSS has to be low-pass filtered to make it compatible with the resolution of the geoid model. Hence, the resolution of the marine geoid model is generally the limiting factor for the resolution of the dynamic ocean topography determined with the direct method. As demonstrated in (Rio et al., 2006), combined geoid solutions, enhancing the satellite-only solutions by introducing in situ gravimetric and altimetric data to better estimate the shortest scales of the geoid, produce better MDT results. However, since they rely on altimetric sea surface height data, the combined solutions intrinsically include information on the mean ocean circulation, and the obtained MDT is therefore not independent of this a priori information. It was shown in (Rio et al., 2006) that using the most recent satellite-only geoid models from GRACE (at that time the EIGEN-GL04S), the MDT could only be estimated with sufficient accuracy at spatial scales of 300 - 400 km. However, the MDT contains scales shorter than 130 km (Rio et al., 2006). Hence, geoid models resolving such small wavelengths, independently of altimetric data, are needed. Such a geoid model is expected from the GOCE mission, who's launch is scheduled for March 2009. GOCE aims to provide geoid heights with cm-level accuracy at a resolution better than 100 km.

In order to bypass the geoid uncertainties, altimetric missions were designed with repeated orbits, allowing to compute accurate along-track MSS profiles and to deduce SLA at cm-level accuracy. In theory, the SLA represents the change of the sea surface height related to effects that are not considered during the correction for geophysical effects like tides and atmospheric pressure (3.1). The major part of these residual effects are changing ocean currents. By inserting (2.27) and (2.28)

in (2.26), the SLA can be defined as:

$$SLA \;=\; ADT \;-\; MDT \tag{2.29}$$

Thus, by neglecting all other residual effects, the SLA corresponds to the variable part of the dynamic ocean topography, or the deviation of the absolute dynamic topography ADT from the mean dynamic topography MDT. This is the so-called repeat-track method, providing the variable part of the dynamic topography with 3 - 4 cm accuracy (Rio and Hernandez, 2004). The analysis of the SLA has led to numerous progresses in the knowledge of ocean dynamics, but the inference of the ADT and MDT from altimetric observations remains a challenge (Rio et al., 2006).

A method used to estimate the MDT independently of the geoid and its uncertainties is the so-called synthetic method. Based on (2.29), it allows to locally estimate the MDT by subtracting the SLA, as observed by altimetry (2.26), from in situ ADT observations, obtained from satellite-tracked drifting buoys (Rio and Hernandez, 2004; Rio et al., 2007).

In reality, however, the SLA is not only produced by changing ocean currents, but also by apparent or true sea surface height variations related to unconsidered or mismodeled effects in (3.1), as well as uncorrected measurement errors. The SLA can e.g. be affected by uncertainties in the tidal model and in the model of the response to atmospheric pressure and wind. Residual measurement errors can be produced by altimeter ranging errors, orbit errors, errors in the sea state bias correction, tropospheric correction, ionospheric correction and skewness of the sea surface. In addition, steric sea level changes, produced by the volume change of water molecules related to temperature change, are not considered and are therefore also included in the SLA signal. One of the major challenges in satellite radar altimetry is therefore to reduce the model errors on the instrumental and geophysical correction levels, in order that their impacts on the SLA become negligible as compared to the effect of changing ocean currents, so that (2.29) applies.

2.5.2 Geostrophic Flow Fields from Dynamic Ocean Topography

Ocean currents can be derived from the ADT and MDT, on an instantaneous and permanent basis, respectively. These flow fields are of great importance for hydrological and oceanographic research. Under the assumption of the geostrophic equilibrium, the ocean circulation can be derived from gradients of the vertical deviation of the ocean topography with respect to its position of rest. The position of rest, observed in the hypothetic case of complete absence of ocean circulation, is an equipotential surface of the Earth's gravity field, the geoid (Section 2.2.1). Aside from the equator and on timescales longer than a few days, the ADT of height H above the geoid is linked to the geostrophic part of the ocean circulation (u_g, v_g) by the geostrophic equilibrium equation (Fu and Chelton, 2001; Le Traon and Morrow, 2001; Rio and Hernandez, 2004):

$$u_g \;=\; -\frac{g}{f}\,\frac{\partial H}{\partial y} \qquad\qquad v_g \;=\; \frac{g}{f}\,\frac{\partial H}{\partial x} \tag{2.30}$$

where u_g and v_g are the horizontal East (zonal) and North (meridian) components of the geostrophic circulation velocity, x and y are the East and North directions, g is gravity and $f = 2\,\omega \sin\phi$ is the Coriolis parameter, with $\omega = 7.292115 \cdot 10^{-5}\,[\mathrm{rad} \cdot \mathrm{s}^{-1}]$ the mean angular velocity of the Earth's rotation and ϕ the geographic latitude. Geostrophic mean velocities and geostrophic velocity anomalies can be obtained from (2.30), by inserting the MDT or the SLA of (2.29) as H, respectively.

2.5.3 Mean Dynamic Topography of the Mediterranean Sea

The mean circulation in the Mediterranean Sea is largely unknown. It is characterized by smaller scales and less intensity than in the open ocean, making the interpretation of the variability ob-

served from altimetric SLA rather difficult. The accurate knowledge of the Mediterranean MDT should help to correctly interpret the altimetric observations and therefore to remove many remaining ambiguities on the Mediterranean variability (Rio et al., 2007). An inventory of the main Mediterranean features from basin scale to mesoscale, mainly based on the analysis of sea surface temperature images, is given e.g. in (Millot, 1999) for the western Mediterranean basin and in (Hamad et al., 2005) for the eastern basin. Despite the fact that a correlation exists between the dynamic height and the surface temperature, such images are not always easy to interpret as they only contain surface information and therefore do not reflect the ocean dynamics (Rio et al., 2007).

The mean dynamic topography used in this project is the RioMed (Fig. 2.5a). RioMed was produced by CLS Space Oceanography Division and distributed by AVISO, with support from CNES (Rio et al., 2007). It is based on the Rio07 synthetic MDT of the Mediterranean Sea computed for the period 1993-1999. Values are given on a $1/8°$ regular grid. Besides the MDT, the RioMed

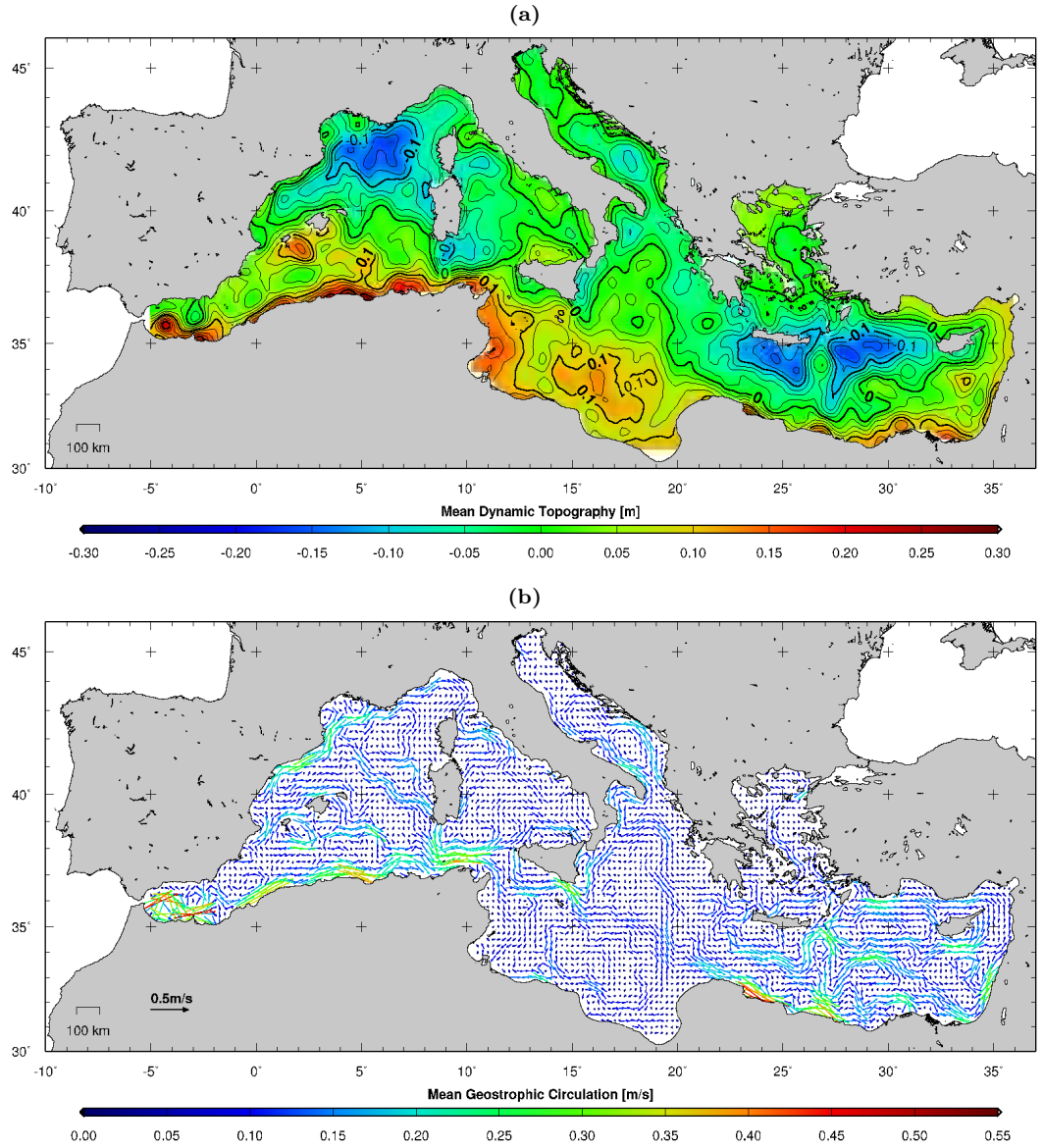

Figure 2.5: **(a)** RioMed mean dynamic topography of the Mediterranean Sea. Contour interval: 0.025 m. **(b)** RioMed mean geostrophic circulation.

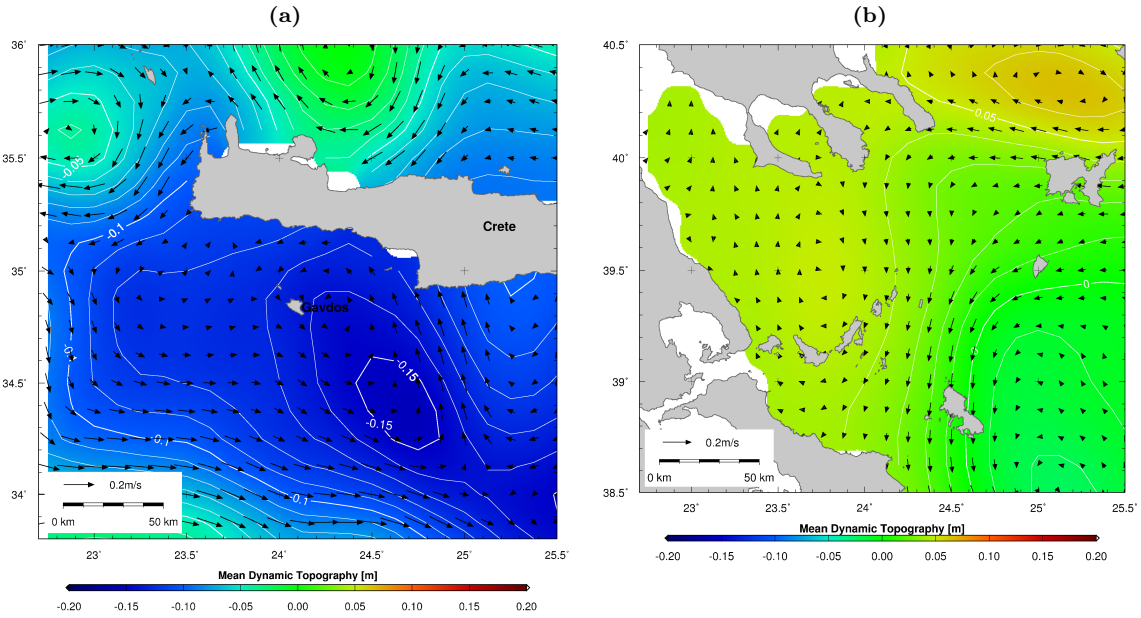

Figure 2.6: Extracts of the RioMed mean dynamic topography (surface) and mean geostrophic circulation (arrows) shown in Fig. 2.5 around Crete **(a)** and in the North Aegean Sea **(b)**. Contour interval: 0.01 m

product includes zonal and meridian components of the geostrophic mean circulation derived from to the MDT (Fig. 2.5b). The accuracy of the synthetic mean field obtained in areas covered by drifting buoys is directly linked to the number of buoy velocity observations used for the estimation (Rio et al., 2007). The smallest errors are found in the Ionian and Adriatic Seas, while larger errors affect areas like the Balearic Sea or the Levantine basin. Inversely, where no buoy observations are available (mainly in the northern Levantine Sea and the North Aegean Sea), the accuracy is linked to the a priori model errors.

The Riomed MDT ranges from -0.17 to 0.27 m over the entire Mediterranean Sea (Fig. 2.5a). The Cretan area is characterized by a cyclonic (counter clockwise) circulation cell of the Cretan cyclone, centered at 25°E, 35°N (Fig. 2.5b). In the survey area around western Crete, the maximum effect of the MDT reaches -0.15 m (Fig. 2.6a). In the survey area in the North Aegean Sea, the effect of the MDT is small, with a maximum of only 0.05 m (Fig. 2.6b). The order of magnitude of the gradients of the RioMed MDT in the North Aegean Sea is in accordance with values found by other author, e.g. (Kourafalou and Tsiaras, 2007).

2.6 Permanent Tide

2.6.1 Permanent Tidal Effects on Gravitational Potential and Earth's Crust

A considerable part of the tides does not vary periodically with time but is permanent (Ekman, 1989). This permanent deformation of the Earth caused by the presence of the Sun and the Moon is called permanent tide. The permanent tide complicates the definition of the geoid and the mean sea surface. The Earth's own gravitational potential is perturbed by the action of the external tidal potential. The observed gravitational potential $V(t)_{obs}$ in the vicinity of the Earth is a combination of the Earth's own potential $V(t)_E$ and the tidal gravitational potential of external bodies (i.e. the Moon, the Sun and the planets) (McCarthy and Petit, 2004). The external tidal potential contains both permanent and periodic parts (V_{ext} and $V(t)_{ext}$), and so does the tide-induced part of the

Earth's own potential (V_{def} and $V(t)_{def}$):

$$V(t)_{obs} = V(t)_E + V_{ext} + V(t)_{ext} + V_{def} + V(t)_{def} \tag{2.31}$$

where

$V(t)_{obs}$	observed gravitational potential at a given position and time t
$V(t)_E$	gravitational potential of the Earth (not induced by tidal effects)
V_{ext}	permanent external tidal gravitational potential caused by external bodies (Moon, Sun and planets)
$V(t)_{ext}$	periodic external tidal gravitational potential caused by external bodies (Moon, Sun and planets)
V_{def}	permanent tide-induced gravitational potential, related to the permanent deformation of the Earth caused by the permanent external tidal potential V_{ext}
$V(t)_{def}$	periodic tide-induced gravitational potential, related to the periodic deformation of the Earth (solid-Earth tide) caused by the periodic external tidal potential $V(t)_{ext}$

Similar to the gravitational potential in (2.31), the observed site position is affected by displacements associated with crustal deformations produced by the tidal potential (McCarthy and Petit, 2004). Considering only the vertical site position $h(t)_{obs}$:

$$h(t)_{obs} = h(t)_E + dh_{def} + dh(t)_{def} \tag{2.32}$$

where

$h(t)_{obs}$	observed site height at time t
$h(t)_E$	site height without crustal deformation caused by external tidal potential
dh_{def}	permanent vertical deformation of the crust caused by the permanent part of the external tidal potential V_{ext} (permanent solid Earth tide)
$dh(t)_{def}$	periodic vertical deformation of the crust caused by the periodic part of the external tidal potential $V(t)_{ext}$ (periodic solid Earth tide)

2.6.2 Mean-Tide, Zero-Tide and Tide-Free Systems

Consideration of the permanent tidal effects described in (2.31) has led to the definition of three types of gravitational potentials: mean-tide, zero-tide and tide-free (Lemoine et al., 1998). The mean-tide potential $V(t)_m$, zero-tide potential $V(t)_z$ and tide-free potential $V(t)_f$ are derived from (2.31) using the following equation:

$$V(t)_m = V(t)_{obs} - V(t)_{ext} - V(t)_{def} = V(t)_E + V_{ext} + V_{def} \tag{2.33}$$

$$V(t)_z = V(t)_m - V_{ext} = V(t)_E + V_{def} \tag{2.34}$$

$$V(t)_f = V(t)_z - V_{def} = V(t)_E \tag{2.35}$$

The mean-tide potential is obtained from (2.31) by removing the periodic parts of the tidal contributions from the observed potential (2.33). Hence, the mean-tide potential includes the permanent external tidal potential V_{ext} and the permanent potential V_{def}, associated with the permanent tidal deformation of the crust, and is free of periodic variations due to tidal forces. The removal of the permanent external potential V_{ext} from the mean-tide potential in (2.33) results in the zero-tide

potential (2.34), which is strictly a geopotential (Lemoine et al., 1998). The removal of the permanent potential V_{def}, related to the permanent tidal deformation, from the zero-tide potential in (2.34) results in the tide-free potential (2.35). In a tide-free quantity (e.g. potential), all tidal effects have been removed. Because the perturbing bodies are always present, a truly tide-free quantity cannot be observed (McCarthy and Petit, 2004). Similar to the gravitational potential in (2.33), (2.34) and (2.35), the mean-tide, zero-tide and tide-free gravity are given by:

$$g(t)_m = g(t)_{obs} - g(t)_{ext} - g(t)_{def} = g(t)_E + g_{ext} + g_{def} \quad (2.36)$$
$$g(t)_z = g(t)_m - g_{ext} = g(t)_E + g_{def} \quad (2.37)$$
$$g(t)_f = g(t)_z - g_{def} = g(t)_E \quad (2.38)$$

The mean-tide, zero-tide and tide-free geoid undulation are given by:

$$N(t)_m = N(t)_{obs} - N(t)_{ext} - N(t)_{def} = N(t)_E + N_{ext} + N_{def} \quad (2.39)$$
$$N(t)_z = N(t)_m - N_{ext} = N(t)_E + N_{def} \quad (2.40)$$
$$N(t)_f = N(t)_z - N_{def} = N(t)_E \quad (2.41)$$

The mean-tide geoid corresponds to the mean sea surface, exempt from non-gravitational disturbances (ocean currents, wind, air pressure, salinity, temperature), but including permanent tidal effects. The zero-tide geoid is obtained by removing the permanent direct effects of the Sun and Moon from the mean-tide geoid, while the indirect effects related to the elastic deformation of the Earth are retained. The tide-free geoid would exist for a tide-free Earth, with all (direct and indirect) effects of the Sun and Moon removed (Lemoine et al., 1998).

Analogous to the potential in (2.33), (2.34) and (2.35), the station height in the mean-tide, zero-tide and tide-free system can be derived from (2.32):

$$h(t)_m = h(t)_{obs} - dh(t)_{def} = h(t)_E + dh_{def} \quad (2.42)$$
$$h(t)_z = h(t)_m = h(t)_E + dh_{def} \quad (2.43)$$
$$h(t)_f = h(t)_m - dh_{def} = h(t)_E \quad (2.44)$$

When removing the periodic part of the tidal contributions from the observed station height in (2.32), the resulting station height $h(t)_m$ is on the mean-tide crust (2.42). The permanent part of the deformation produced by the tidal potential is still present in the mean-tide crust. The zero-tide crust $h(t)_z$ is identical to the mean-tide crust (2.43). If the permanent deformation due to the permanent tidal potential is removed from the mean-tide crust, the tide-free crust $h(t)_f$ is obtained (2.44).

2.6.3 Conversion between Permanent Tide Systems

The conversion between mean-tide gravity $g(t)_m$, zero-tide gravity $g(t)_z$ and tide-free gravity $g(t)_f$ is obtained from (2.36), (2.37) and (2.38) (Ekman, 1989):

$$g(t)_m - g(t)_z = g_{ext} = -\frac{\partial V_{ext}}{\partial r} = -30.4 + 91.2 \sin^2\phi \quad [\mu\text{gal}] \quad (2.45)$$

$$g(t)_z - g(t)_f = g_{def} = -(\delta - 1)\frac{\partial V_{ext}}{\partial r} = (\delta - 1)(-30.4 + 91.2 \sin^2\phi) \quad [\mu\text{gal}] \quad (2.46)$$

$$g(t)_m - g(t)_f = g_{ext} + g_{def} = -\delta \frac{\partial V_{ext}}{\partial r} = \delta(-30.4 + 91.2 \sin^2\phi) \quad [\mu\text{gal}] \quad (2.47)$$

with

$$\delta = 1 + \left(\frac{\partial V_{def}}{\partial r}\right) / \left(\frac{\partial V_{ext}}{\partial r}\right) \simeq 1.16 \quad (2.48)$$

where $\partial/\partial r$ is the radial derivative and ϕ is the geographic latitude. The difference between mean-tide gravity and zero-tide gravity (2.45) corresponds to the gravitation g_{ext} of the permanent external tidal potential. The difference between zero-tide gravity and tide-free gravity (2.46) corresponds to the gravitation g_{def} of the permanent potential, related to the permanent deformation of the Earth caused by the permanent external tidal potential V_{ext}. The difference between mean-tide gravity and tide-free gravity (2.47) is the sum of g_{ext} and g_{def}. Numerical expressions after (Ekman, 1989), associated with the permanent external tidal gravitational potential V_{ext} caused by the Moon and the Sun, are given on the right-hand side of (2.45), (2.46) (2.47). The numerical expressions are plotted in Fig. 2.7a as a function of latitude. The permanent external gravitation g_{ext} is more pronounced (factor of 6.25) than the gravitation g_{def} caused by the deformation due to the permanent solid Earth tide. The effect of the permanent tide on gravity is more pronounced at the poles and at the equator than at mid-latitude. The difference between mean-tide gravity and tide-free gravity varies between -35.3 μgal at the equator and 70.5 μgal at the poles. At the equator, the total gravity is decreased by the permanent tidal effects g_{ext} and g_{def}, while it is increased at the poles.

The conversion between mean-tide geoid $N(t)_m$, zero-tide geoid $N(t)_z$ and tide-free geoid $N(t)_f$ is obtained from (2.39), (2.40) and (2.41) (Ekman, 1989):

$$N(t)_m - N(t)_z = N_{ext} = \frac{V_{ext}}{g} = 9.9 - 29.6 \sin^2\phi \quad [\text{cm}] \quad (2.49)$$

$$N(t)_z - N(t)_f = N_{def} = k\frac{V_{ext}}{g} = k(9.9 - 29.6 \sin^2\phi) \quad [\text{cm}] \quad (2.50)$$

$$N(t)_m - N(t)_f = N_{ext} + N_{def} = (1 + k)\frac{V_{ext}}{g} = (1 + k)(9.9 - 29.6 \sin^2\phi) \quad [\text{cm}] \quad (2.51)$$

with

$$k = \frac{V_{def}}{V_{ext}} \simeq 0.30 \quad (2.52)$$

where k is the (fundamentally unknowable) zero frequency Love number, usually taken as 0.30 (e.g. for the EGM96), g is gravity and ϕ is the geographic latitude. The difference between mean-tide geoid and zero-tide geoid (2.49) corresponds to the geoid deformation N_{ext} caused by the permanent external tidal potential V_{ext}. The difference between zero-tide geoid and tide-free geoid (2.50) corresponds to the geoid deformation N_{def}, associated with the permanent solid Earth tide. The difference between mean-tide geoid and tide-free geoid (2.51) is the sum of N_{ext} and N_{def}. Numerical expressions after (Ekman, 1989), associated with the permanent external tidal gravitational potential V_{ext} caused by the Moon and the Sun, are given on the right-hand side of (2.49), (2.50) (2.51). The numerical expressions are plotted in Fig. 2.7b as a function of latitude. Similar equations can be found in (Rapp, 1989). The deformation N_{ext} of the geoid caused by

the permanent external potential is more pronounced (factor of 3.33) than the deformation N_{def} caused by the permanent solid Earth tide. The effect of the permanent tide on the deformation of the geoid is more pronounced at the poles and at the equator than at mid-latitude. The difference between mean-tide geoid and tide-free geoid varies between -25.6 cm at the poles and 12.9 cm at the equator. The positive values near the equator indicate that the permanent external potential V_{ext} and the potential caused by the permanent solid Earth tide V_{def} are increasing the geoid undulation near the equator. At the poles, they have a decreasing effect on the geoid undulation.

Finally, the conversion of GPS heights above the ellipsoid on the tide-free crust to GPS heights on the mean-tide (or zero-tide) crust can be derived from (2.42), (2.43) and (2.44) (Ekman, 1989):

$$h(t)_m \; - \; h(t)_f \; = \; dh_{def} \; = \; h \; \frac{V_{ext}}{g} \; = \; h \; (9.9 \; - \; 29.6 \; \sin^2 \phi) \quad [\text{cm}] \tag{2.53}$$

where the Love number $h \simeq 0.62$. The difference is equal to the deformation dh_{def} of the crust due to the permanent part of the solid Earth tide. A similar equation can be found in the IERS Conventions 2003 (McCarthy and Petit, 2004):

$$h(t)_m \; - \; h(t)_f \; = \; [\; -0.1206 \; + \; 0.0001 \; P_2(\sin \phi) \;] \; P_2(\sin \phi) \quad [\text{m}] \tag{2.54}$$

with $P_2(\sin \phi) = (3 \sin^2 \phi - 1)/2$. Similar results are obtained using (2.53) and (2.54), with values of -12.21 and -12.05 cm at the poles, and 6.14 and 6.03 cm at the equator, respectively. The deformation of the crust caused by the permanent tide, corresponding to the difference between mean-tide (or zero-tide) and the tide-free crust heights (2.53) is shown in Fig. 2.7c, as a function of latitude. The difference varies between -12.2 cm at the poles and 6.1 cm at the equator.

2.6.4 Conversion of Sea Surface Heights between Permanent Tide Systems

Most gravitational models and their associated geoid undulations are referenced to a tide-free system. On the other hand, the undisturbed sea surface is a representation of the geoid in a mean-tide system, because it includes all the effects of the permanent tide on the Earth's crust. Sea surface heights observed by satellite radar altimetry are therefore referenced to a mean-tide system. In order to make comparisons between geoid undulations and sea surface heights, they have both to be referenced to the same permanent tide system, e.g. the tide-free system. The deformation of the sea surface due to the permanent tide is a combination of the deformation of the Earth's crust (sea bottom) and the deformation of the water masses above it. It follows that the deformation of the sea surface due to permanent tide is similar to the deformation of the geoid due to the permanent tide.

As opposed to satellite radar altimetry, the sea surface heights determined in this project by airborne laser altimetry, shipborne ultrasound altimetry and GPS buoys all involve GPS observations, referenced to the tide-free ITRF reference frame. The GPS heights are therefore also related to the tide-free system. However, this definition only applies to the Earth's crust, but not to the sea surface. In a first step, in order to obtain consistent sea surface heights SSH_m in a mean-tide system, the observed heights SSH_{obs}, derived from GPS, have to be converted from the tide-free to the mean-tide system, using (2.53) or (2.54). Using (2.53), the following corrections are obtained for the survey areas of Crete and North Aegean Sea:

$$\text{Crete (35.0°N)} : \; SSH_m \; = \; SSH_{obs} \; + \; 0.001 \quad [\text{m}] \tag{2.55}$$

$$\text{North Aegean (39.5°N)} : \; SSH_m \; = \; SSH_{obs} \; - \; 0.013 \quad [\text{m}] \tag{2.56}$$

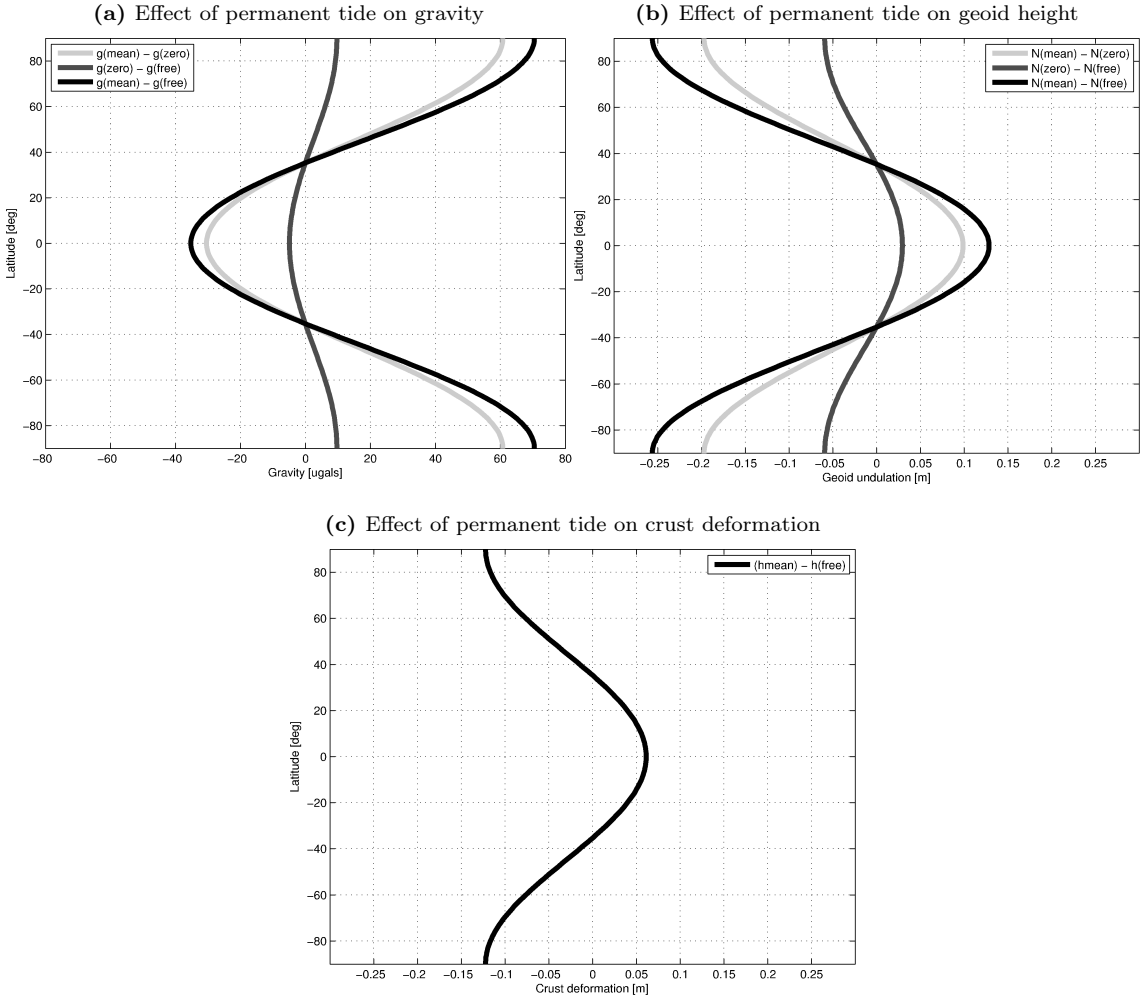

Figure 2.7: Effect of permanent tide, as a function of latitude, on **(a)** gravity ((2.45), (2.46), (2.47)), **(b)** geoid height ((2.49), (2.50), (2.51)) and **(c)** crust deformation (2.53).

Using the above equations, the sea surface heights determined in this project are made compatible with sea surface heights from satellite radar altimetry. The undisturbed sea surface heights in a mean-tide system are equivalent to geoid undulations N_m in a mean-tide system. In order to obtain sea surface heights SSH_f in a tide-free system, the mean-tide sea surface heights SSH_m have to be converted using (2.51):

$$\text{Crete (35.0°N)}: \; SSH_f = SSH_m - 0.002 = SSH_{obs} - 0.001 \;\; [\text{m}] \tag{2.57}$$

$$\text{North Aegean (39.5°N)}: \; SSH_f = SSH_m + 0.027 = SSH_{obs} + 0.014 \;\; [\text{m}] \tag{2.58}$$

These are the corrections that have to be applied to make the sea surface heights determined in this project using airborne laser altimetry, shipborne ultrasound altimetry and GPS buoys compatible with geoid heights in a tide-free system. The difference between the observed sea surface heights SSH_{obs} and sea surface heights SSH_f in a tide-free system are negligibly small, with values of 0.1 cm in the survey area around Crete and 1.4 cm in the North Aegean Sea.

3 Geophysical Effects on Sea Surface Heights

3.1 Introduction

Instantaneous sea surface heights SSH_i, as obtained by satellite radar altimetry, airborne laser altimetry, shipborne ultrasound altimetry and GPS buoys, are affected by time-dependent geophysical effects, including ocean waves, astronomical tides, atmospheric pressure (inverse barometer effect) and wind stress. By subtracting these effects from SSH_i, time-independent sea surface heights SSH are obtained:

$$\begin{aligned} SSH \;=\; SSH_i \;&-\; \text{ocean waves} \\ &-\; \text{tide effects} \\ &-\; \text{inverse barometer effect} \\ &-\; \text{high frequency wind response} \end{aligned} \tag{3.1}$$

This correction procedure is equivalent to the one applied by the official analysis centers of spaceborne radar altimetry data (Picot et al., 2003). The correction for tidal effects has nowadays generally reached centimeter accuracy, whereas the effects associated with the forcing of wind and atmospheric pressure are less well known. Other effects influencing sea surface heights, like precipitation, evaporation, river inflow, changing ocean currents, salinity and steric sea level variations due to the volume change of water molecules related to water temperature change, and in the case of the Mediterranean Sea the net flow at the strait of Gibraltar and from the Black Sea, are not considered directly (Fenoglio-Marc et al., 2006). The resulting time-independent sea surface heights SSH can be interpolated in order to obtain a surface representing the time-independent sea surface topography.

3.2 Ocean Waves

Ocean waves have typical amplitudes of half a meter to several meters in extreme cases. They are characterized by a succession of crests and troughs, The wave height H is the vertical distance between a trough and the next crest. The significant wave height $\bar{H}_{1/3}$ is given by the average height of the 1/3 highest waves in a record (WMO, 1998). It roughly approximates the visually estimated wave height. More details on waves can be found in (Coulson and Jeffrey, 1977; Lighthill, 1978; WMO, 1998).

The airborne and shipborne altimetry data, as well as the GPS buoy data, contain information on ocean waves. Wave characteristics (sea state) and significant wave heights can be derived from these data by signal filtering and wave modeling (Section 7.2.3, Fig. 7.6). Appropriate filter algorithms, based on cubic splines and windowed median, have been developed and applied in the framework of this project, allowing to separate the high-frequency wave component from the sea surface height signal (Sections 7.2.1 and 8.2).

3.3 Tides

3.3.1 Characteristics of Tides

Tidal effects are governed by Newton's law of gravitation, where the gravitational force $\vec{F}$ between two bodies of masses m and M, separated by a distance vector $\vec{r}$ is given by:

$$\vec{F} \;=\; G\,\frac{M\cdot m}{|\vec{r}|^3}\,\vec{r} \tag{3.2}$$

where G is Newton's universal gravitational constant. In the degree of approximation needed in the computation of tides, only the Moon and the Sun have an influence on the Earth: the Sun because of its enormous mass and the Moon because of its relatively small distance to the Earth. The tide generating force can be derived from the tide generating potential. In the case of the system formed by the three bodies Earth, Moon and Sun, the total astronomic tide generating potential can be separated into the sum of the lunar and the solar potential. The trajectories of the Moon and the Sun with respect to the Earth are highly complex. They have elliptic orbits contained in a plane which's inclination varies with respect to the terrestrial equatorial plane. In addition, interactions between the Moon, the Sun and the Earth are modifying the orbital trajectories. The tide generating force needs therefore to be separated into a sum of elementary forces (Tab. 3.1).

There are several contributions to the tidal effect influencing the sea surface height: ocean tide (with respect to the ocean bottom), ocean loading tide (of the ocean bottom), solid Earth tide and pole tide (Picot et al., 2003). The first three contributions are related to luni-solar forcing of the Earth (astronomical tides), either directly, in the case of the ocean tide and solid Earth tide, or indirectly, in the case of the ocean loading tide, since it is forced by the ocean tide. The sum of these tidal contributions is called the geocentric tide:

$$\text{geocentric tide} \;=\; \text{ocean tide} \;+\; \text{ocean loading tide} \;+\; \text{solid Earth tide} \;+\; \text{pole tide} \tag{3.3}$$

Tide-gauges directly observe the ocean tide, while satellite altimetry data includes the entire geocentric tide (3.3). The geocentric tide has therefore to be removed to correct altimetric data for tidal effects. The same applies for airborne and shipborne altimetry data, but with special considerations concerning the solid Earth tide (Section 3.3.3).

3.3.2 Ocean Tide

The ocean tide of astronomic origin is the periodic variation of the sea surface height resulting from the actions of the celestial bodies (in particular the Moon and the Sun) moving around the Earth. The relative movements of the Moon and the Sun with respect to the Earth, combined with the Earth's own rotation, are generating periodic gravitational forces. Each of these elementary forces generates a periodic displacement of the water masses on Earth, resulting in sinusoidal variations of the sea surface (tidal waves), called harmonic tidal components.

The tide generating force is the differential force between the gravitational force of the Moon and the Sun at a given point of the sea surface and the rotational centrifugal force of the Earth-Sun-Moon system (Fig. 3.1). The latter corresponds to the reciprocal of the gravitational force of the Moon and the Sun at the center of mass of the Earth, since the Earth is in equilibrium. Hence, at the center of the Earth, the gravitational force towards the Moon/Sun and the centrifugal force away from the Moon/Sun are perfectly in balance. Assuming that the sea surface instantaneously adopts the equilibrium position corresponding to the acting gravitational forces of the attraction of the Moon and the Sun on the water particles and on the center of mass of the Earth, the equilibrium tide is obtained based on the tide generating force.

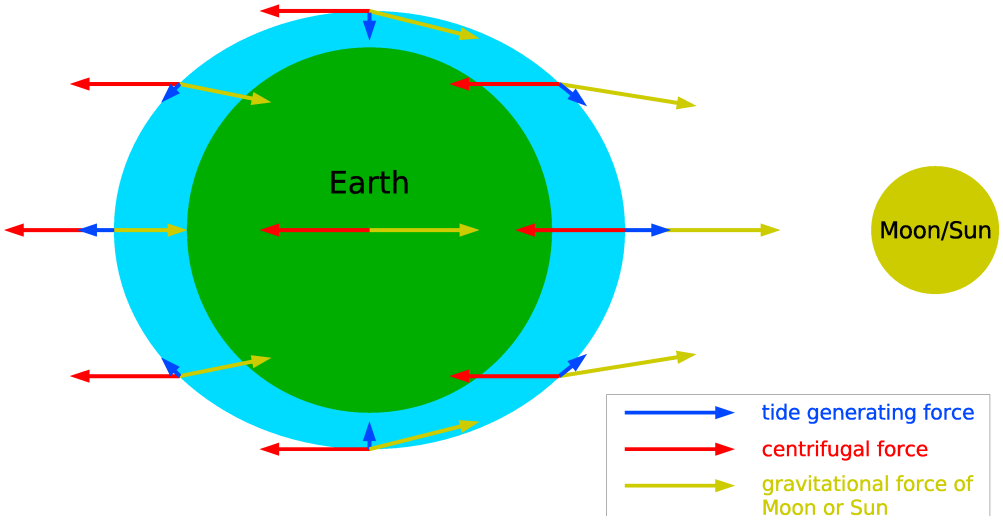

Figure 3.1: Schematic view of the forces governing the equilibrium ocean tide.

On the surface of the Earth nearest to the Moon/Sun, the gravitational force is stronger than the centrifugal force, resulting in a force towards the Moon/Sun causing a water bulge (Fig. 3.1). On the opposite side of the Earth, the gravitational force is weaker, since the Moon/Sun is further away, and the centrifugal force is dominant. Hence there is a resulting force away from the Moon/Sun, creating another water bulge (Fig. 3.1).

When the Earth, Moon and Sun are in line (during new and full Moon), the bulges of water caused by the Moon and the Sun occur in the same place on the Earth's surface. The lunar and solar tides are reinforcing each other, which leads to higher than average high tides, and lower than average low tides. These are called spring tides. When the Earth, Moon and Sun form a right angle, the high water caused by the lunar tide coincides with the low water of the solar tide. This produces lower than average high waters and higher than average low waters, which are called neap tides. They occur approximately seven days after spring tides (POL, 2009).

The tidal variation of the sea surface is constituted by the superposition of many oscillations generated by different phenomena (Le Provost, 2001). Laplace's theory of dynamic response of the ocean suggests that the tide generating force induces a response of the ocean in form of oscillations with the same frequencies than the tide generating force, characterized by an amplitude and a phase. Based on Laplace's theory, the variation of the sea surface height $h_t(x,t)$ at location x and time t caused by the ocean tide is given by:

$$h_t(x,t) \;=\; \sum_{k=1}^{N} A_k(x)\;\cos\;[\;\omega_k\;t\;+\;V_k\;-\;G_k(x)\;] \tag{3.4}$$

where k is the tidal component with oscillation period ω_k, astronomical phase V_k, amplitude $A_k(x)$ and Greenwich phase lag $G_k(x)$. The major components k have diurnal or semi-diurnal periods (Fig. 3.2 and Tab. 3.1). The semi-diurnal waves have a period of about 12 hours. The M2 wave (M for Moon and 2 for semi-diurnal) is the most important semi-diurnal wave, corresponding to the tide generated by the Moon uniformly moving around the Earth with a circular orbit in the equatorial plane. The S2 wave (S for Sun) corresponds to the same phenomena for the Sun. There are other semi-diurnal waves due to the ellipsoidal shape of the orbits. The diurnal waves have a period of about 24 hours. The principal diurnal waves are the lunar-solar declination wave K1 and the lunar wave O1. In addition, there are waves with longer periods, e.g. the annual wave Sa caused by the annual variation of the distance Sun-Earth.

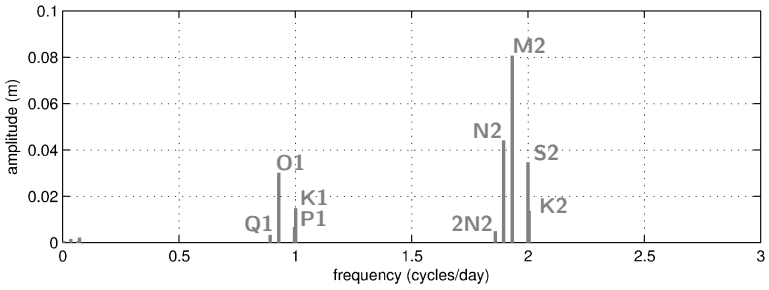

Figure 3.2: Tidal amplitudes as a function of frequency in the survey area in the North Aegean Sea.

Table 3.1: Major harmonic constituents of the astronomical tide.

Type	Name	Period	Origin
Semi-diurnal	M2	12h25	Mean movement of the Moon
	S2	12h00	Apparent mean movement of the Sun
	K2	11h59	Lunar-solar declination
	N2	12h39	Major lunar eccentricity effects
	L2	12h11	Minor lunar eccentricity effects
	2N2	12h54	Lunar eccentricity effects of 2^{nd} order
Diurnal	K1	23h56	Lunar-solar declination
	O1	25h49	Lunar declination
	P1	24h03	Solar declination
	Q1	26h56	Major lunar eccentricity effects
Long period	Mf	13.661 days	Semi-monthly lunar declination
	Mm	27.555 days	Monthly lunar declination
	Ssa	182.621 days	Semi-annual solar declination
	Sa	365.240 days	Annual variation of the distance Sun-Earth

If the Earth was covered by a uniform water layer, the dynamic prediction of ocean tides at any location would be easy, since the astronomical periods, amplitudes and phases of all tidal constituents are known precisely (Chelton, 1988). However, the propagation speed of these oscillations depends on the water depth. In addition, they are reflected on the continental shelf, refracted and dissipated (Roblou, 2001). Hence, ocean tides are strongly influenced by the continental boundaries, the submarine topography (bathymetry), the complex sea floor topography in coastal regions, the shape of the coastline and the eigenfrequency of oceanic basins (Le Provost, 2001). These influences, which can locally produce tidal amplitudes of several meters, are making purely dynamic predictions only marginally useful (Chelton, 1988). In practice, ocean tides are therefore determined empirically at selected locations, based e.g. on hourly observations of the sea level from tide-gauges, covering a period long enough (usually a few months to several years) to resolve the major tidal constituents by harmonic analysis of the observed tidal signal. The harmonic analysis yields amplitudes and phase lags of the harmonic constituents of the tidal signal at the observations site. Dynamic models of global ocean tides are then constrained by the tidal amplitudes and phases empirically determined at the tide-gauges (Chelton, 1988). Empirical tidal constituents can only be determined at locations where the sea level can be measured on a regular basis. Hence, satellite radar altimetry is a revolutionary technique, since it allows to observe the sea level at nearly every point on Earth.

The ocean tide is one of the most significant variations of the sea surface. Its amplitudes in the open ocean are typically 1 - 2 m. This means that the tidal amplitudes are often larger than the signals of interest in altimetric studies of ocean circulation or local geoid signals. Ocean tides need therefore to be removed from the observed sea surface heights. The variation of the sea surface due to ocean tides represents 80% of its variability in the open ocean (Le Provost, 2001), but much less in semi-enclosed seas like the Mediterranean (Fig. 3.3). In the Mediterranean Sea, tidal amplitudes

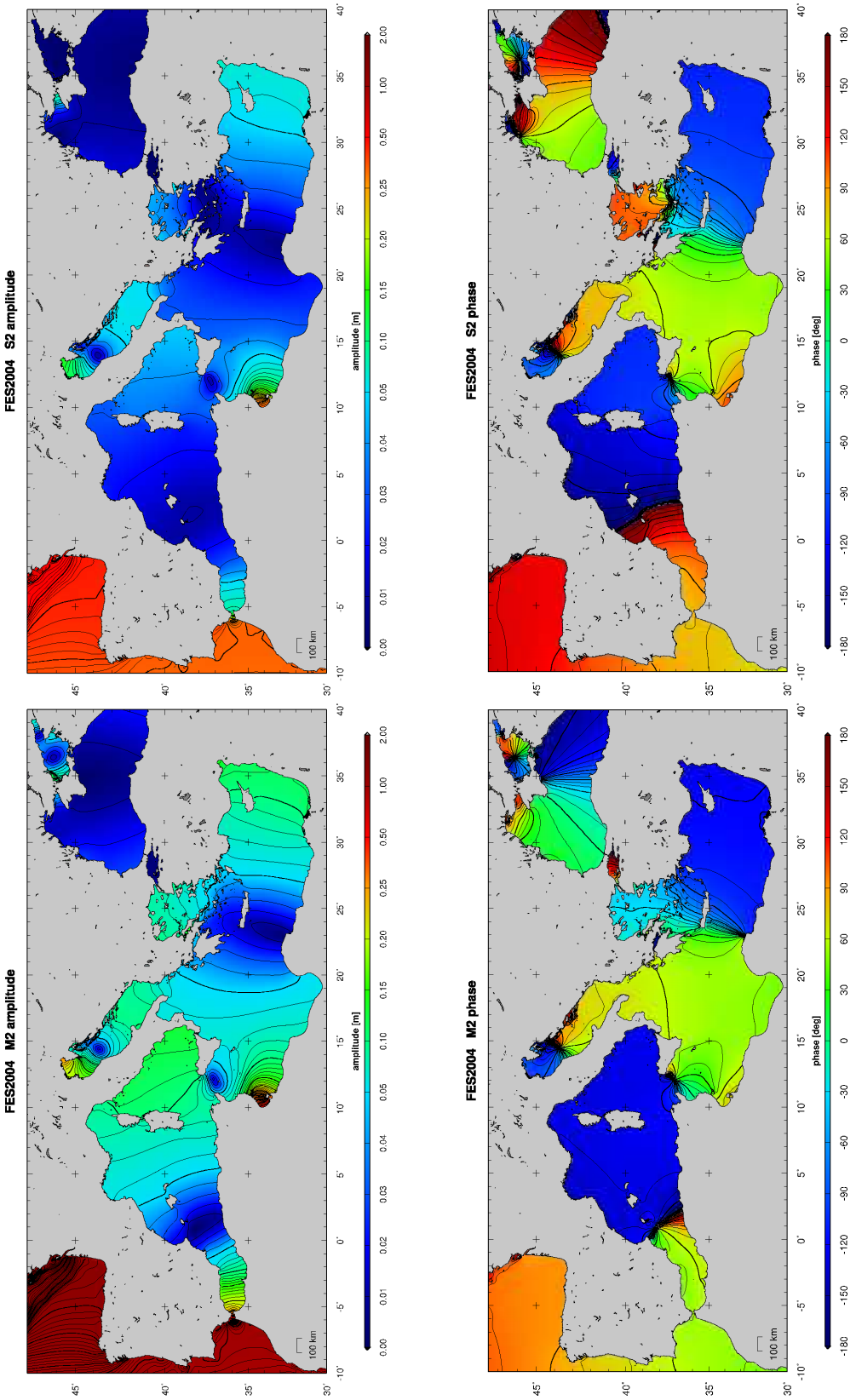

Figure 3.3: M2 and S2 ocean tide amplitude and phase from FES2004 in the Mediterranean Sea.

are small as compared to the open sea, as can be seen from the amplitudes in the Atlantic Ocean, adjacent to the Mediterranean Sea. The ocean tide models used in this project are the FES2004, GOT00.2 and POL models:

- The FES2004 tide model (Lyard et al., 2006; Letellier, 2004; Le Provost, 2001) is based on a finite element hydrodynamic model and the assimilation of tide-gauge data and observations from TOPEX/Poseidon and ERS-2. FES2004 was produced by LEGOS and CLS Space Oceanography Division and distributed by AVISO, with support from CNES. The hydrodynamic model is based on the resolution of the tidal barotropic equations on a global finite element grid of approx. 1 million nodes. It includes 14 tidal constituents (M2, S2, K2, N2, 2N2, O1, P1, K1, Q1, Mf, Mtm, Mm, Msqm, M4) distributed on global 1/8°×1/8°grids of amplitude and phase lag (Fig. 3.3). FES2004 is used as default correction model for the altimetric products of TOPEX/Poseidon and Jason-1.

- The GOT00.2 tide model (Ray, 1999) consists of independent near-global estimates of 8 major constituents (Q1, O1, K1, P1, N2, M2, S2, K2). FES94.1 was used as a priori hydrodynamic model, as well as several local hydrodynamic models. The tidal constituents are given on 0.5°×0.5°grids. GOT00.2 used 286 cycles of TOPEX/Poseidon data, supplemented in shallow seas and in polar seas (latitudes above 66°) by 81 cycles of ERS-1 and ERS-2 data.

- A local tide model for the Mediterranean Sea, developed by the Proudman Oceanographic Laboratory (POL) (Tsimplis et al., 1995). The POL model is a high-resolution two-dimensional hydrodynamic model forced by the equilibrium tide and the incoming tide at the Strait of Gibraltar. It is based on depth-averaged equations of continuity and motion in spherical polar coordinates and relies on the data of 63 coastal tide-gauges, including tide-gauges in the Aegean Sea and on Crete. It consists of the 4 most significant constituents (M2, S2, K1, O1) distributed on 1/12°×1/12°grids of amplitude and phase lag.

3.3.3 Solid Earth Tide

The solid Earth tide is the elastic periodic deformation of the Earth's crust, including the ocean bottom, due to luni-solar forcing. The solid Earth responds to external gravitational forces similar to the oceans (Picot et al., 2003). The response of the Earth is fast enough that it can be considered to be in equilibrium with the tide generating forces. Solid Earth tides have amplitudes of about 10 - 20 cm. Solid Earth tides occur at the same frequencies than the ocean tide, but can be modeled much more accurately (to approx. 1 cm) than ocean tides (Chelton, 1988). Since the movement of the ocean bottom due to solid Earth tides affects the height of the sea surface, it must be removed from spaceborne altimetric data.

In the case of sea surface height observations from airborne and shipborne altimetry, or from other techniques where the positioning of the altimetric sensor relies on differential GPS processing, the treatment of solid Earth tides has to be considered with care. Terrestrial GPS stations are affected by solid Earth tides. In classical differential processing of a GPS baseline between two terrestrial stations of height h_1 and h_2, the solid Earth tide correction is given by the difference between the solid Earth tide at the two stations (Fig. 3.4a):

$$h_2 \;=\; h_1 \;+\; \Delta h_{obs}(t_i) \;+\; tide_1(t_i) \;-\; tide_2(t_i) \tag{3.5}$$

where h_1 and h_2 are the heights of the reference station and roving station corrected for solid Earth tides, $\Delta h_{obs}(t_i)$ is the height difference between the two stations observed by differential GPS at time t_i, $tide_1(t_i)$ and $tide_2(t_i)$ are the solid Earth tides at the reference station and at the roving station at time t_i.

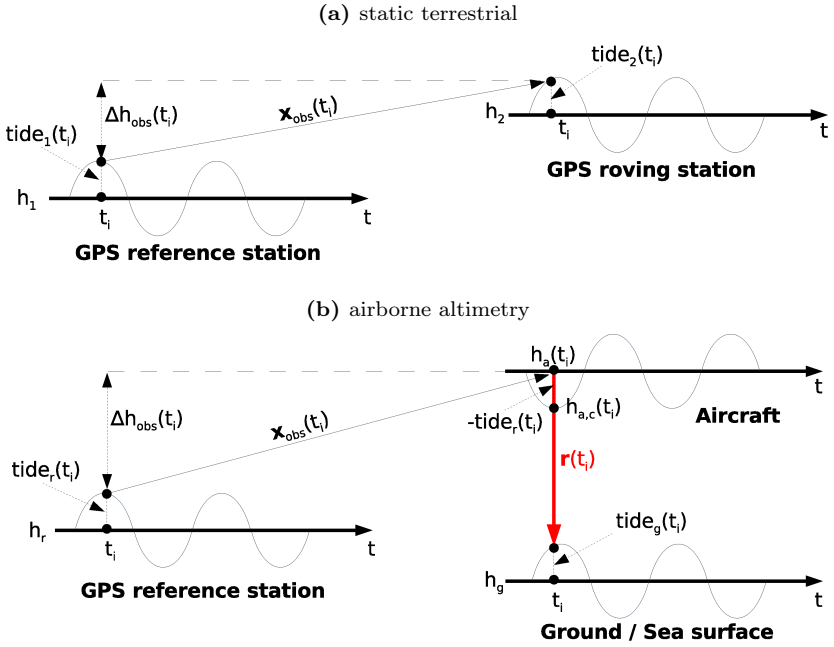

Figure 3.4: **(a)** Solid Earth tides in static differential GPS processing between two terrestrial stations. **(b)** Solid Earth tides in airborne altimetry and kinematic differential GPS processing between a terrestrial reference station and the aircraft, resp. the laser ground point.

In airborne altimetry, the height of the aircraft is not affected by solid Earth tides. In this case, the solid Earth tide correction that has to be applied to the laser ground point depends on how solid Earth tides were considered during kinematic GPS baseline processing between the terrestrial reference station and the aircraft. If the solid Earth tide at the reference station was considered, the real aircraft height $h_a(t_i)$ is obtained (Fig. 3.4b):

$$h_a(t_i) \;=\; h_r \;+\; \Delta h_{obs}(t_i) \;+\; tide_r(t_i) \tag{3.6}$$

where h_r is the height of the reference station corrected for solid Earth tides, $\Delta h_{obs}(t_i)$ is the height difference between the aircraft and the reference station observed by differential GPS at time t_i and $tide_r(t_i)$ is the solid Earth tide at the reference station at time t_i. In airborne altimetry, the laser sensor is measuring the range between the real position of the aircraft, not affected by solid Earth tides, and the ground surface (sea or land) affected by solid Earth tides. Hence, by subtracting the observed vertical range $r(t_i)$ from the aircraft height $h_a(t_i)$, the sum of the ground point height $h_g(t_i)$, corrected for solid Earth tides, and the solid Earth tide effect $tide_g(t_i)$ is obtained (Fig. 3.4b):

$$h_g(t_i) \;+\; tide_g(t_i) \;=\; h_a(t_i) \;-\; r(t_i) \tag{3.7}$$

This means that if the solid Earth tide on the GPS reference station was corrected during kinematic GPS processing, the surface height obtained by airborne altimetry includes the full effect of the solid Earth tide at the ground point position, analogous to spaceborne altimetry. However, most kinematic GPS software do not consider solid Earth tide corrections. In that case, by fixing the baseline origin to the a priori coordinates of the reference station h_r, the tidal deformation $tide_r(t_i)$ at the reference station propagates with opposite sign into the computed aircraft height $h_{a,c}(t_i)$ (Fig. 3.4b), yielding vertical errors of up to 20 cm:

$$h_{a,c}(t_i) \;=\; h_r \;+\; \Delta h_{obs}(t_i) \;=\; h_a(t_i) \;-\; tide_r(t_i) \tag{3.8}$$

By subtracting the observed vertical range $r(t_i)$ (3.7) from the aircraft height $h_{a,c}(t_i)$ falsified by the solid Earth tide effect $tide_r(t_i)$ at the reference station (3.8), the obtained surface height is the sum of the ground point height $h_g(t_i)$, corrected for solid Earth tides, and the differential solid Earth tide effect between the laser ground point and thereference station, analogous to the differential GPS positioning between terrestrial stations (3.5):

$$h_g(t_i) \; + \; tide_g(t_i) \; - \; tide_r(t_i) \; = \; h_{a,c}(t_i) \; - \; r(t_i) \tag{3.9}$$

During the kinematic differential processing of airborne GPS data used to compute sea surface heights from airborne laser altimetry, no correction for solid Earth tides was applied. Hence, the solid Earth tide correction to be applied to the obtained sea surface heights is given by the differential solid Earth tide between the laser ground point and the GPS reference station, according to (3.9). The solid Earth tides, computed for both the reference station and the laser ground points, show amplitudes in the order of 10 - 15 cm (Fig. 3.5). In the present case, with baseline lengths below 150 km (Fig. 7.1), the differential solid Earth tide between the laser ground points and the reference station ranges between -3 and 4 mm. This means that the major part of the effect of the solid Earth tide on the observed sea surface height was indirectly eliminated during the differential GPS processing, and that the remaining part can be considered negligible because it is about one order of magnitude smaller than the expected accuracy of the airborne laser altimetry system. On the other hand, removing the absolute value of the solid Earth tide computed at the laser ground points from the obtained sea surface heights would induce a vertical error of up to 20 cm. In general, the differential solid Earth tide correction becomes negligible for short baselines.

Sea surface height observations by shipborne altimetry and GPS buoys, involving differential GPS processing, are similar to the case of two terrestrial GPS station (Fig. 3.4a). The ship and the buoy are both directly affected by the solid Earth tide, in the same way as a terrestrial station. Hence, (3.5) applies, meaning that the obtained sea surface heights are affected by the differential solid Earth tide between the observation point and the reference station, unless solid Earth tides were considered during GPS processing. For baselines below 150 km (Fig. 8.1), similar to the case of airborne altimetry above, the differential solid Earth tide correction can be considered negligible, because it is about one order of magnitude smaller than the expected accuracy.

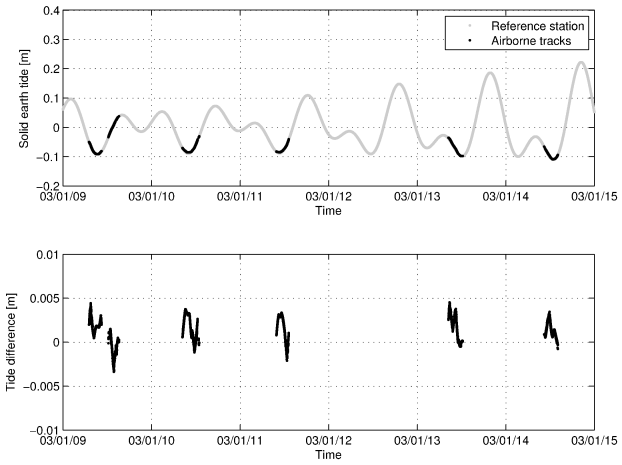

Figure 3.5: Top: Time series of solid Earth tide at the GPS reference station TUC1 and along airborne altimetry tracks (Fig. 7.1). Bottom: Difference between solid Earth tides along airborne tracks and at the GPS reference station, corresponding to the correction to be applied to the observed sea surface heights.

3.3.4 Ocean Loading Tide and Pole Tide

The ocean loading tide is the oscillation of the ocean bottom (and the adjacent continental shelf in coastal areas), caused by the tidal variations of the load of the water masses. Hence, the ocean loading tide is indirectly related to luni-solar forcing. The pole tide is unrelated to luni-solar forcing. Considering the sea surface, it is a tide-like motion of the ocean surface as a response of both the solid Earth and the oceans to the centrifugal potential that is generated by small perturbations to the Earth's rotation axis (Picot et al., 2003). These perturbations primarily occur at periods of 433 days, called the Chandler wobble, and annually. Modeling the pole tide requires knowledge of proportionality constants, the so-called Love numbers, and a time series of perturbations to the Earth's rotation axis, a quantity that is now measured routinely with space techniques (Picot et al., 2003). Ocean loading and pole tide values were computed for the region of Crete and the North Aegean Sea using the GOT00.2 tide model. Both effects were found to be below 1 cm in these survey areas, and were therefore not further considered.

3.4 Atmospheric Pressure and Wind Forcing

3.4.1 Inverse Barometer Effect

As atmospheric pressure increases and decreases, the sea surface tends to respond hydrostatically by falling or rising, respectively (Picot et al., 2003). This effect is referred to as the inverse barometer (IB) effect. The instantaneous IB effect on the sea surface height is given by (Dorandeu and Le Traon, 1999; Picot et al., 2003; Chelton, 1988):

$$IB \;=\; \frac{1}{\rho\, g}\,(\;P \;-\; P_{ref}\;) \;=\; -0.9948\;(\;P \;-\; P_{ref}\;) \tag{3.10}$$

where IB is the inverse barometer effect in cm, $\rho = 1.025\,\mathrm{g/cm^3}$ is the density of sea water, $g = 980.7\,\mathrm{cm/s^2}$ is gravity, P is the atmospheric pressure at the sea surface in hPa and P_{ref} is the time varying mean global surface atmospheric pressure over the oceans in hPa. In many applications, P_{ref} is assumed to be constant, e.g. 1013.3 hPa. However, using a constant P_{ref} creates unrealistic signals: the mean correction is no longer zero, which is not consistent with ocean mass conservation (Dorandeu and Le Traon, 1999). The scale factor of -0.9948 implies that a local increase of 1 hPa in atmospheric pressure locally depresses the sea surface by about 1 cm.

Since water is nearly incompressible, the variation of the sea surface elevation in relation with atmospheric pressure changes does not result from a compression of water, but from a horizontal redistribution of the water masses in response to horizontal variations of the atmospheric pressure (Chelton, 1988). If the atmospheric pressure would change uniformly over an entire ocean basin, there would be no change in the sea level, except for a negligible variation due to the small compressibility of seawater. The response of the sea surface to atmospheric pressure loading depends both on the spatial and temporal scale of the pressure forcing (Wunsch, 1972). The adjustment to a change in atmospheric pressure propagates relatively rapidly by means of long gravity waves. The detailed wavenumber-frequency characteristics of the transfer function between sea surface elevation and atmospheric pressure loading is not known (Chelton, 1988). It is likely that the transfer function varies geographically, with e.g. different behaviours in coastal and open ocean regions. The response is believed to be nearly isostatic for time scales between 2 days and 2 weeks (Wunsch, 1972). At shorter time scales, the response of the ocean is too slow to compensate for rapid pressure changes. At longer time scales, the ocean responds dynamically in the form of geostrophic currents and Rossby waves.

The IB correction is presently a major source of error in altimetric studies of dynamic ocean topography (Chelton, 1988). Its accuracy is limited by the uncertainties in the atmospheric surface

pressure field over the oceans and in the transfer function between sea surface elevation and atmospheric pressure loading. The uncertainty in the atmospheric pressure is typically about 3 hPa, corresponding to an uncertainty of 3 cm in the IB correction. This uncertainty may be higher by a factor of two or more in the case of intense storms and in the southern hemisphere, where atmospheric pressure fields are not well resolved by meteorological models (Chelton, 1988). A detailed review of the theoretical background on atmospheric loading and the oceanic inverted barometer effect is given in (Wunsch and Stammer, 1997).

3.4.2 Dynamic Atmospheric Correction

The ocean response to meteorological forcing is poorly accounted for by simply applying the inverse barometer (IB) correction (Wunsch and Stammer, 1997), described in Section 3.4.1. The classic IB correction formulates the static response of the ocean to atmospheric pressure forcing, while wind effects are totally ignored (Carrère and Lyard, 2003). The validity of the IB assumption depends on the temporal and spatial scales considered. The ocean has a dynamic response (differing from the IB response) to atmospheric pressure forcing at high frequencies (periods below 3 days) and at high latitudes. Thus, the high frequency variability needs to be corrected from an independent model. Wind effects prevail particularly around the 10 days period (Carrère and Lyard, 2003).

The corrections for atmospheric pressure and wind forcing used in this project are the dynamic atmospheric corrections (DAC) produced by CLS Space Oceanography Division using the MOG2D model from LEGOS and distributed by AVISO, with support from CNES. The corrections are composed of two parts. The correction of the low frequency (above 20 days) response of the ocean to atmospheric forcing is computed using an IB correction developed by CLS, assuming a static response and neglecting wind effects. The correction of the high frequency (below 20 days) ocean response to atmospheric pressure and wind forcing is computed using the MOG2D barotropic model (Carrère and Lyard, 2003) developed by LEGOS/CNRS.

MOG2D (2D Gravity Waves model) is a barotropic non-linear model derived from (Lynch and Gray, 1979). The model is governed by the classic shallow water continuity and momentum equations and it can include tides (Carrère and Lyard, 2003). It is based on a finite elements space discretization, which allows to increase the resolution in areas of interest with strong topographic gradients or shallow waters. The grid size ranges from 400 km in the deep sea to 20 km in coastal, shallow areas (Carrère and Lyard, 2003). In shallow water, the MOG2D model shows an oceanic response very different from the classic IB response (Carrère and Lyard, 2003). The simulation domain includes the Mediterranean Sea and other semi-enclosed seas. The model is forced by atmospheric pressure and 10 m wind speeds from ECMWF analysis data, with a temporal resolution of 6 hours and a spatial resolution of $0.25° \times 0.25°$. MOG2D dynamic atmospheric corrections are provided via the AVISO web site as global grids with a temporal resolution of 6 hours and a spatial sampling of $0.25° \times 0.25°$. An example of MOG2D correction grids during the airborne laser altimetry campaign around Crete is shown in Appendix G. Corresponding ECMWF atmospheric pressure fields at sea level are shown in Appendix F. More details on MOG2D can be found in (Carrère and Lyard, 2003; Letellier, 2004; Mourre, 2004; Roblou, 2001).

4 Airborne Laser Altimetry

4.1 Introduction

Airborne laser altimetry has become a powerful method serving a wide range of applications in remote sensing, geodesy, geophysics and geodynamics (Luthcke et al., 2002). These applications include the determination of digital terrain models and the monitoring of changing surfaces like landslides and glaciers. During the last decades, advances in airborne laser altimetry have enabled the production of precise digital surface models on an operational level, with accuracies better than 20 cm. The potential of airborne laser altimetry especially lies in regions where conventional methods encounter problems due to a lack of sufficient texture or fast deforming terrain, where the establishment of reliable ground control points is difficult or impossible. In oceanography-related projects, airborne laser altimetry is mainly aimed at sea level determination in coastal areas, to bridge the gap between deep sea satellite radar altimetry data and coastal tide-gauge stations.

Airborne laser altimetry provides 3D coordinates of ground surface points. It is based on range observations between an aircraft and the ground surface using a laser distance measurement device. Since the laser device measures the slant range between the aircraft and the ground surface, the position of the ground point can only be determined if the position and orientation of the laser system are permanently known with respect to an absolute coordinate system. Hence, precise knowledge of position and attitude are crucial for the production of accurate data. For the determination of ground surface points, the laser system has therefore to be supported by a positioning and orientation system, providing autonomous and accurate position and attitude of the aircraft without further ground information. Details on the computation of laser ground point coordinates based on direct georeferencing of airborne laser altimetry data are given in Chapter 6.

4.2 Instumental Setup

4.2.1 Overview

The airborne laser altimetry surveys were carried using the DeHavilland Twin-Otter of the Swiss Federal Office of Topography (swisstopo), operated by the Swiss airforce (Fig. 4.1). The aircraft was equipped with the following instruments:

- Optech 501 SA Rangefinder laser profiler, sampling rate 1 - 2 kHz (Fig. 4.2)
- Riegl LMS-Q140i-60 laser scanner (provided by KMS)
- 4 GPS receivers for position and attitude determination, sampling rate 2 Hz (Fig. 4.1)
- Honeywell H-764G INS (provided by KMS), sampling rate 50 Hz (Fig. 4.2a)
- LaCoste Romberg S-meter sea/air gravimeter (provided by the University of Bergen)

Since the aircraft is mainly used for photogrammetric missions, the laser sensors can be mounted in the photogrammetric camera shafts (Fig. 4.2). All instruments had to be integrated into the measuring system and synchronized with GPS time.

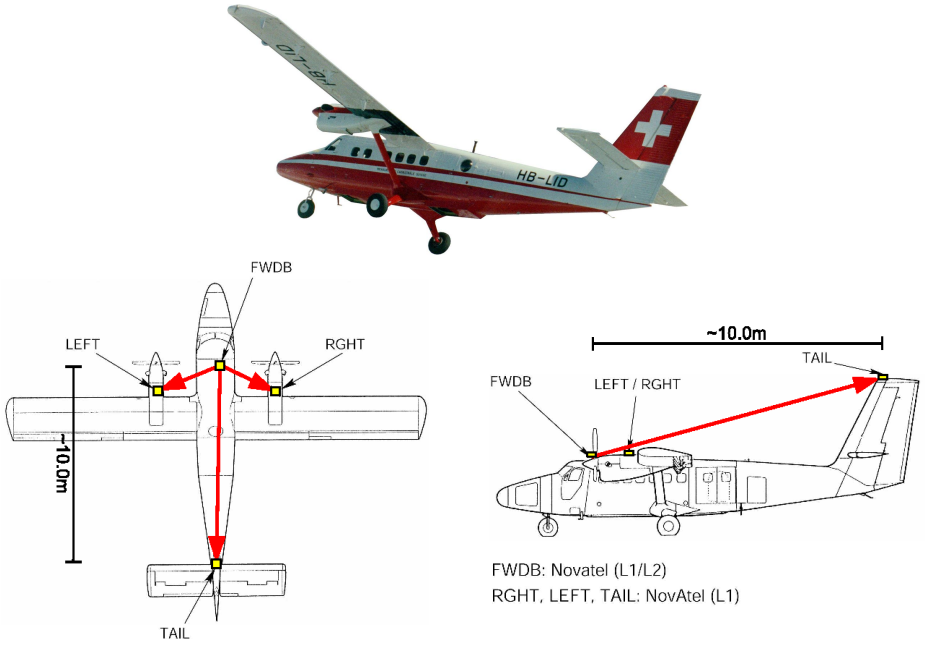

Figure 4.1: DeHavilland Twin-Otter survey aircraft owned by the Swiss Federal Office of Topography (swisstopo), with array of four GPS antennas and resulting baseline vectors for attitude determination.

4.2.2 Laser Profiler

The Optech 501 SA Rangefinder is a pulsed laser ranging instrument designed to give high accuracy readings on a single-shot basis (Fig. 4.2 and Tab. 4.1) (Optech, 1989). The unit uses a GaAs laser diode to generate optical pulses. A high precision time interval counter measures the time-of-flight of the laser pulse to and from the target. The time-of-flight is converted into range by a microprocessor. The GaAs diode in the transmitter module generates 15 - 20 ns wide optical pulses of near-infrared radiation at a wavelength of 904 nm. The laser beam has an initial diameter of 8 cm and a beam divergence of 0.25% (= 2.5 mrad = 0.143°). Hence, for a flight height of 200 m above ground, the laser footprint has a diameter of 58 cm. The instrument can be operated at pulse repetition rates up to 2 kHz, with a range resolution of 1 cm and an operating range of 10 - 500 m.

4.2.3 Laser Scanner

A Riegl LMS-Q140i-60 linear laser mirror scanner (Tab. 4.1), provided by KMS, was used as additional equipment. It is based on the principle of time-of-flight measurement of short laser pulses in the near-infrared (900 nm). An electrical pulse generator periodically drives a semiconductor laser diode sending out infrared light pulses.Via the receiver lens, part of the echo signal reflected by the target hits a photodiode which generates an electrical receiver signal. The time interval between transmitted and received pulses are counted by a quartz-stabilized clock frequency and processed by the internal microprocessor. The laser beam divergence is 0.30% (= 3 mrad = 0.172°). Hence, for a flight height of 200 m above ground, the laser footprint has a diameter of 60 cm. The nominal maximum range is 150 m and 350 m under a target reflectance of 10% and 80%, respectively. In bright sunlight, the operational range is considerably shorter than under overcast sky. The range resolution and nominal accuracy (1 σ) are 2.5 cm. The angular deflection of the laser beam is realized by a rotating polygon mirror wheel, rotated continuously at a fixed speed to provide repetitive unidirectional scans. The scanner has a scan angle range of 60°. It was operated at a scan speed of 40 scans/s and a pulse repetition rate of 25 kHz, leading to an angular step width of 0.288°.

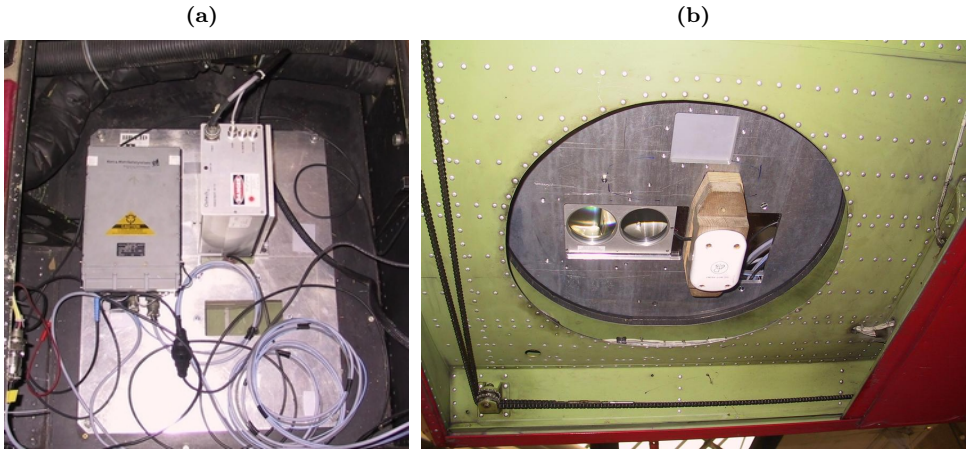

Figure 4.2: **(a)** Optech 501 SA laser profiler (right) and Honeywell H-764G INS (left), mounted on the same platform installed in the photogrammetric camera shaft of the aircraft. **(b)** Outside view of the photogrammetric camera shaft with downward-looking laser profiler optics.

Table 4.1: Technical specifications of Optech 501 SA laser profiler and Riegl LMS-Q140i-60 laser scanner.

	Optech 501 SA	Riegl LMS-Q140i-60
Wavelength	904 nm (near infrared)	900 nm (near infrared)
Range	10 - 500 m[1]	2 - 350 m[2]
Range resolution	0.01 m	0.025 m
Beam divergence	2.5 mrad (0.25%)	3.0 mrad (0.30%)
Pulse repetition rate	1 kHz (max. 2 kHz)	25 kHz (max. 30 kHz)
Scan angle range	-	60°
Scan speed	-	40 scans/s
Angular step width	-	0.288°
Angle readout accuracy	-	0.036°

[1] The maximum range of 500 m is based on a target reflectance of 20%.

[2] The maximum range is 150 m and 350 m under a target reflectance of 10% and 80%.

4.2.4 Multi-Antenna GPS Configuration

The aircraft was equipped with an array of four GPS antennas adequately mounted on the aircraft's top side (Fig. 4.1) and connected to four independent GPS receivers. One dual frequency receiver is used for trajectory recovery and as reference for moving baseline processing. The other three receivers are single frequency receivers, acting as remote receivers in the moving baseline processing, yielding three vectors used for attitude determination. The baseline lengths are 5.5 m between the engine antennas and 10 m between the front and rear antennas. This setup allows highly accurate 3D positioning (trajectography) of the aircraft in combination with terrestrial GPS reference stations, as well as autonomous attitude determination, both needed for georeferencing the laser ground point (Chapter 6).

4.2.5 Inertial Navigation System

A Honeywell H-764G Inertial Navigation System (INS), provided by KMS, allowed for attitude recovery at a sampling rate of 50 Hz, independent of the multi-antenna GPS system (Fig. 4.2a). It is a tactical-grade INS used on military aircrafts and helicopters. It is based on accelerometers and digital ring-laser gyros, and it is coupled with GPS.

4.3 Laser Ranging

4.3.1 Basic Principle

In laser ranging, two major principles exist: continuous wave lasers, which continuously emit light, and pulsed lasers (Wehr and Lohr, 1999). The continuous wave principle is based on measuring the phase difference between the transmitted signal and the received signal backscattered from the target surface. In current laser ranging systems, mostly pulsed lasers are used. The principle of pulsed lasers is based on determining the time-of-flight of a light pulse by measuring the traveling time t between the emitted and received pulse. The distance r between the ranging unit and the target is then given by:

$$r \;=\; c\,\frac{t}{2} \tag{4.1}$$

where c is the speed of light (299'792.458 km/s in the vacuum). The range determination is complicated by the atmospheric refraction of light, discussed in Section 4.3.2. From (4.1), the range resolution Δr, which is directly proportional to the time resolution Δt of the ranging unit, can be derived (Wehr and Lohr, 1999):

$$\Delta r \;=\; c\,\frac{\Delta t}{2} \tag{4.2}$$

To achieve a range resolution Δr of 1 cm in the vacuum, a time resolution Δt of 0.07 ns is required.

4.3.2 Atmospheric Refraction of Light

When traveling through the atmosphere, electromagnetic waves experience velocity changes and associated changes of their direction (bending), called refraction. These changes depend on the physical state of the gas quantities in the traversed atmosphere. The propagation velocity v in the atmosphere deviates from the velocity c in the vacuum by the refractive index n:

$$v \;=\; \frac{c}{n} \tag{4.3}$$

Since $n > 1$, v is always smaller than the velocity c in the vacuum. The refraction has a different behavior in the troposphere and the ionosphere. Since laser ranging in airborne altimetry is only affected by tropospheric effects, ionospheric effects are not considered here. The tropospheric refraction is caused by the neutral non-ionized part of the Earth's atmosphere. In the troposphere, the refractive index of air depends on temperature, pressure and water vapor content. The refractive index n is proportional to the density of air and therefore decreases with increasing altitude and becomes approx. 1 at an altitude of 40 km (Fig. 4.4a). Since the troposphere is a dispersive medium for optical frequencies, the refractive index also depends on the wavelength of the electromagnetic waves. The range r measured through air is given by the integral along the curved signal path (Hopfield, 1979):

$$r \;=\; \int_{path} n\; dr \tag{4.4}$$

In laser ranging, refraction due to the atmospheric effects results in a delay of the laser signal. This delay yields an range error Δs, given by the difference between the optical and geometrical distance between the laser site and the target (Hopfield, 1979):

$$\Delta s \;=\; r \;-\; s \;=\; \int_{path} n\; dr \;-\; \int_0^s ds \;=\; \int_0^s (n-1)\; ds \;+\; \int_{path} n\; dr \;-\; \int_0^s n\; ds \tag{4.5}$$

where r is the optical path length measured along the beam trajectory (optical range) and s is the slant distance between the initial and end point of the beam trajectory. The first integral on the right hand side is the range error produced by the reduced traveling speed in the atmosphere and the associated longer traveling time. The difference between the second and the third integral gives the geometrical effect of the bending of the beam trajectory on the measured length with respect to the slant distance. If the bending effect is negligible, the integral along the curved signal path in (4.4) can be taken along the slant range vector (Hopfield, 1979), yielding:

$$r \;=\; \int\limits_{path} n\; dr \;=\; \int_0^s n\; ds \tag{4.6}$$

Inserting (4.6) in (4.5), it follows that the range error Δs is only affected by the reduced traveling speed along the slant range vector:

$$\Delta s \;=\; \int_0^s (n-1)\; ds \tag{4.7}$$

Note that in applications like satellite laser ranging, signal bending is not negligible and equation (4.5) must be used. For short distances, the refractive index n can be considered as constant, and (4.6) and (4.7) yield the following formulas for the range error Δs and the real slant range s:

$$\Delta s \;=\; r \;-\; s \;=\; (n-1)\; s \;=\; \left(1 - \frac{1}{n}\right)\; r \tag{4.8}$$

$$s \;=\; r \;-\; \Delta s \;=\; \frac{1}{n}\; r \;=\; \frac{c}{n}\;\frac{t}{2} \tag{4.9}$$

where r is the optical range provided by an uncalibrated EDM (Electronic Distance Measurement) instrument (4.1) and t is the observed traveling time. Usually, EDM instruments are calibrated in order to provide correct distances under standard atmospheric conditions. The range r_0 given by a calibrated instrument, the range error Δs_0, caused by the deviation of the actual refraction n from the refraction during calibration n_0, and the slant range s are given by:

$$r_0 \;=\; \frac{c}{n_0}\;\frac{t}{2} = \;\frac{1}{n_0}\; r \tag{4.10}$$

$$\Delta s_0 \;=\; r_0 \;-\; s \;=\; \left(\frac{n}{n_0} - 1\right)\; s \;=\; \left(1 - \frac{n_0}{n}\right)\; r_0 \tag{4.11}$$

$$s \;=\; r_0 \;-\; \Delta s_0 \;=\; \frac{n_0}{n}\; r_0 \;=\; \frac{c}{n}\;\frac{t}{2} \tag{4.12}$$

Note that in of all the above equations, the distances s, r and r_0 correspond to the one-way range between the source and the target, covered during half the traveling time t. Instead of the refractive index n, the refractivity is often used to quantify the atmospheric refraction. The refractivity N is the difference of the refractive index n from unity, commonly multiplied by 10^6 to obtain N in units of ppm, corresponding to a delay or range error of 1 mm/km of range:

$$N\;[\text{ppm}] \;=\; (n-1)\cdot 10^6 \tag{4.13}$$

Most geodetic EDM instruments use intensity-modulated or pulsed light, which can be considered as a superposition of waves of different wavelengths forming short groups of waves. The velocity

v in (4.3) represents the phase velocity of a monochromatic carrier wave, whereas the center of a group of waves, as used by most EDM instruments, travels at the group velocity v_g. Therefore, knowledge of the group refractivity N_g, rather than the phase refractivity N, is required. The group velocity v_g is given by:

$$v_g \;=\; v \;-\; \lambda \, \frac{dv}{d\lambda} \tag{4.14}$$

where λ is the operational wavelength of the laser device. Since in a dispersive medium like the troposphere, the refractive index n, and hence the velocity v, depend on the wavelength, $\frac{dv}{d\lambda} \neq 0$. The group refractivity N_g is given by (Marini and Murray, 1973):

$$N_g \;=\; \frac{d\,(f\;N)}{df} \;=\; N \;-\; \lambda \, \frac{dN}{d\lambda} \tag{4.15}$$

where f is the operational frequency of laser beam, λ is the corresponding wavelength and N is the phase refractivity.

4.3.3 Atmospheric Refraction Models

In Appendix A, an non-exhaustive overview of models of atmospheric refraction at optical wavelengths is given, namely the (Barrell and Sears, 1939) model, the (Barrell, 1951) model, the (Edlén, 1966) model and the (Birch and Downs, 1994) model. In the 1990's, the International Association of Geodesy (IAG) established a working group to develop equations better suited to the very wide ranges of atmospheric conditions and wavelengths required in geodetic surveying (McCarthy and Petit, 2004). As part of that effort, a new set of equations was developed, based on more recent equations and recently reported measurements for density and dispersion in the visible and the near-infrared regions (Ciddor, 1996). In 1999, the IAG recommended (IUGG, 1999) that the group refractive index in the atmosphere, for EDM with visible and near infrared wavelengths, to better than 1 ppm should be computed using the procedure published by (Ciddor and Hill, 1999) and (Ciddor, 1996). Since this procedure is rather complex as compared to the former equations given in Appendix A, the IAG also recommended the following closed formulae be adopted for the computation of the group refractive index in the atmosphere, for EDM with visible and near infrared wavelengths, to within 1 ppm (IUGG, 1999):

$$N \;=\; (n-1)\cdot 10^6 \;=\; N_g \, \frac{273.15}{T} \, \frac{p}{1013.25} \;-\; \frac{11.27}{T} \, e \tag{4.16}$$

where

$$N_g \;=\; (n_g-1)\cdot 10^6 \;=\; 287.6155 \;+\; \frac{4.88660}{\lambda^2} \;+\; \frac{0.06800}{\lambda^4} \tag{4.17}$$

with

N	refractivity [ppm] of visible and near infrared light of wavelength λ in ambient air
n	corresponding refractive index
N_g	group refractivity [ppm] of standard air at $T = 273.15\,\mathrm{K}$ (0°C), $p = 1013.25\,\mathrm{hPa}$, $e = 0.0\,\mathrm{hPa}$ and 0.0375 % CO_2 content
n_g	corresponding group refractive index
T	temperature [K] at the laser site in the ITS-90, with $T = 273.15 + t\,[°\mathrm{C}]$
p	total atmospheric pressure [hPa] at the laser site
e	partial water vapor pressure [hPa] at the laser site
λ	carrier wavelength of the EDM signal in the vacuum [μm]

(4.16) and (4.17) reveal the dependency of the refractive index on the wavelength, temperature, air pressure and water vapor content (Fig. 4.3a). Under standard atmospheric conditions of 15°C,

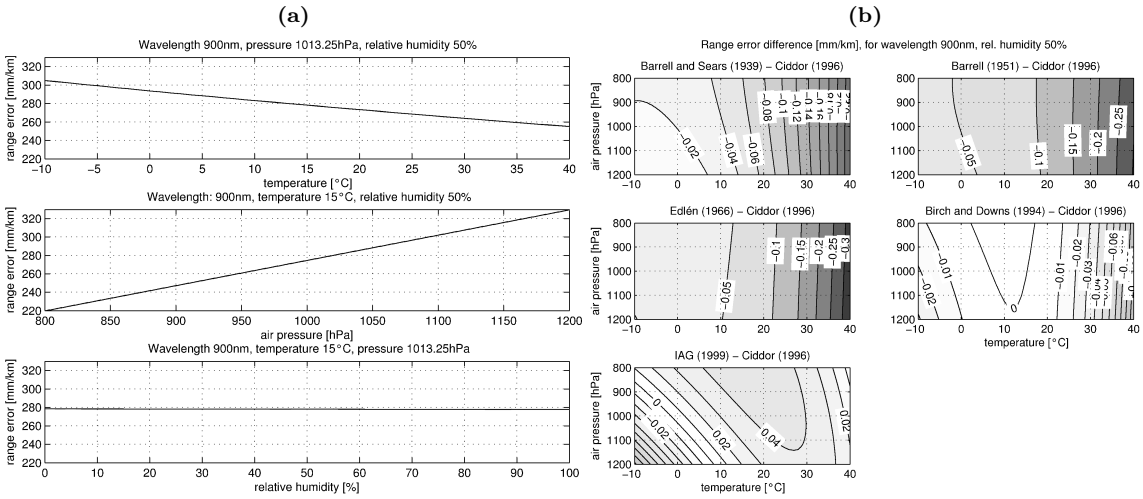

Figure 4.3: **(a)** Refractivity N (relative range error) in mm/km (ppm) for a wavelength of 900 nm (near infrared), computed from (4.16) and (B.1). Top: as a function of temperature. Center: as a function of atmospheric pressure. Bottom: as a function of relative humidity. **(b)** Refractivity (relative range error) differences in mm/km (ppm) with respect to the (Ciddor, 1996) model, as a function of temperature and atmospheric pressure, for a wavelength of 900 nm (near infrared) and a relative humidity of 50%.

1013.25 hPa and 50% relative humidity, the refractivity (relative range error) at a wavelength of 900 nm (near infrared) is about 280 mm/km. The average variation of the refractivity as a function of temperature and as a function of atmospheric pressure is -1 ppm/°C and 0.275 ppm/hPa, respectively. The variation of the refractivity as a function of relative humidity is negligible compared to the influence of temperature and pressure, with a decrease of only 0.6 ppm over the entire humidity range of 0 - 100%. The computation of the refractivity is complicated by atmospheric condition changing in space and time, depending e.g. on the time of day and the cloudiness. Especially the near-ground temperature can change rapidly. The input values in (4.16) for temperature, atmospheric pressure and water vapor pressure are usually measured in situ at the laser site.

The models considered in Appendix A and in this section produce similar refractivity values (Fig. 4.3b). Within the considered range of atmospheric conditions, the models are not deviating more than 0.35 mm/km from each other. Since in the models in Appendix A, the refractive indices of standard air were originally related to phase velocities, they had to be converted to group refractive indices using (4.15).

4.3.4 Impact of Atmospheric Refraction in Airborne Laser Altimetry

In airborne laser altimetry, vertical range observations are carried out between the aircraft and the ground. In case of long vertical distances, it might be necessary to consider the change of refractivity with altitude. In airborne laser altimetry, it is usually not possible to measure atmospheric parameters at the laser site. In that case, they can be derived from a standard atmosphere model, as a function of the altitude of the laser site (Appendix B). The decrease of refractivity with increasing altitude, computed from (4.16) and (B.1), is shown in Fig. 4.4a. In airborne laser altimetry, ranges are usually below 1000 m. In sea surface height applications, they are usually below 300 m because of the sparse to inexistent return from water surfaces in case of longer distances. For a flight altitude (vertical one-way distance covered by the laser signal) of 300 m, the variation of the refractivity is only 7.7 ppm, corresponding to 2.3 mm along the distance of 300 m.

The short ranges in airborne laser altimetry, as compared to e.g. ranges of several 1000 km in

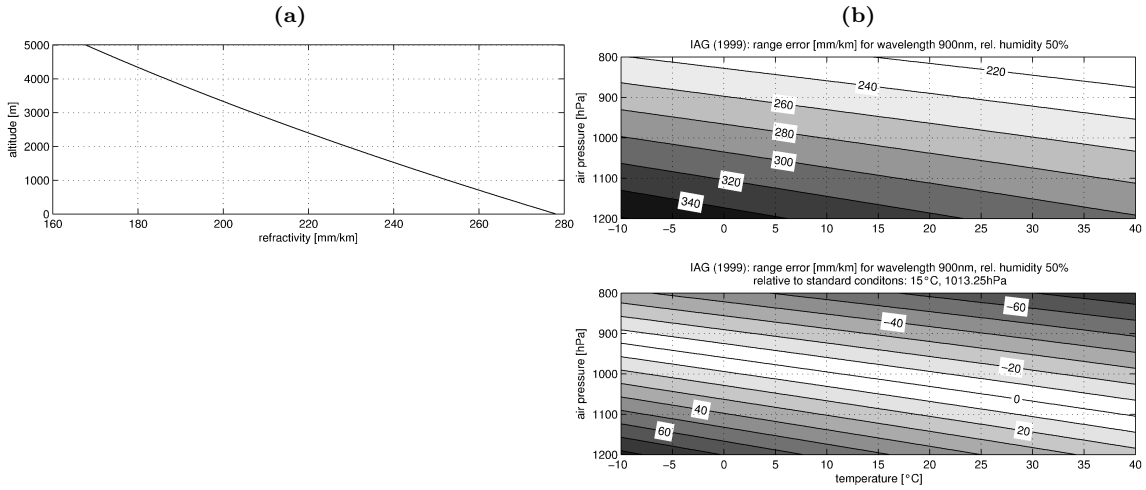

Figure 4.4: **(a)** Refractivity N in mm/km (ppm) as a function of altitude for a standard atmosphere and a wavelength of 900 nm (near infrared), computed from (4.16) and (B.1). **(b)** Top: Refractivity (relative range error) in mm/km (ppm) from the (IUGG, 1999) model, as a function of temperature and atmospheric pressure, for a wavelength of 900 nm (near infrared) and a relative humidity of 50%. Bottom: Same range error, but relative to standard atmospheric conditions (equivalent to the range error produced by an instrument calibrated under standard conditions).

satellite laser ranging (SLR), are reducing the impact of atmospheric refraction errors, since the range error Δs is proportional to the range s itself ((4.8) and (4.11)). For a range of 300 m, the maximum deviation of the refractivity (relative range error) of 0.3 mm/km (Fig. 4.3b) between the models considered in Section 4.3.3 corresponds to a range difference of 0.1 mm. The required absolute range accuracy in the airborne laser altimetry surveys conducted in this project is in the order of one to a few centimeters. Hence, it can be concluded that the models produce no noticeable difference in refractivity in the considered order of magnitude.

For a vertical range of 300 m, absolute range errors of 7 - 9 cm can be expected (Fig. 4.4b, top). These errors have to be considered if cm-accuracy is sought. However, if a calibrated instrument is used, the range error caused by refraction consists only of the deviation of the actual refraction from the reference refraction during calibration (4.11). In this case, the range error varies only between -2 and 2 cm over the wide range of atmospheric conditions considered (Fig. 4.4b, bottom). It can be concluded that in airborne laser altimetry applications for sea surface height observations, with ranges below 300 m and accuracy requirements of 1 - 5 cm, the application of additional refractivity corrections is not needed if the ranging instrument was calibrated under conditions similar to the operating conditions (where similar means ±100 hPa air pressure and ±20°C air temperature.

4.4 Laser Backscatter from Sea Surface

4.4.1 Reflection and Refraction at Air-Water Boundary

When light passes from a transparent medium (e.g. air) with refractive index n_1 into another transparent medium (e.g. water) with refractive index n_2, one part of the incident light is refracted and penetrates into the second medium, while the other part is reflected at the surface, due to the discontinuity of the refractive index at the medium boundary (Fig. 4.5a). This phenomena is called diffraction. The velocity of light changes depending on the refractive index of the medium. According to the law of specular reflection, the incident light is always reflected in a plane normal

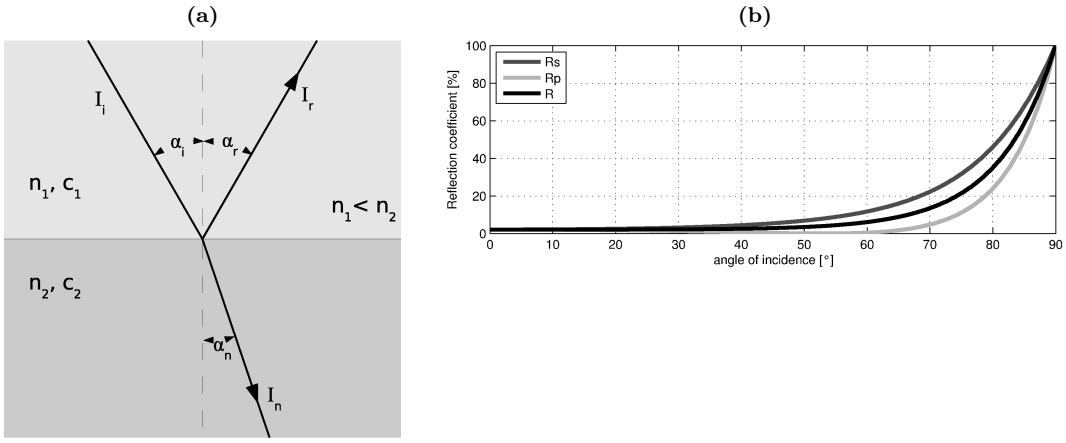

Figure 4.5: **(a)** Diffraction (reflection and refraction) at a medium boundary with refractive index $n_1 < n_2$. **(b)** Reflection coefficients ρ_s (labeled Rs) of light polarized in the plane perpendicular to the plane of incidence, ρ_p (labeled Rp) of light polarized in the plane of incidence and ρ (labeled R) of unpolarized light (4.21), as a function of the angle of incidence, at an air-seawater boundary ($n_1 = 1.000278$, $n_2 = 1.338$).

to the surface at an angle of reflection α_r opposite to the angle of incidence α_i (Fig. 4.5a):

$$a_i \;=\; -\,a_r \tag{4.18}$$

The relation between the angle of incidence α_i and the angle of refraction α_n is given by the law of diffraction, also called Snell's law (Fig. 4.5a):

$$\frac{\sin\alpha_i}{\sin\alpha_n} \;=\; \frac{n_2}{n_1} \;=\; \frac{c_1}{c_2} \tag{4.19}$$

where α_i is the angle of incidence and α_n is the angle of refraction, both relative to the normal of the medium boundary, n_1 and n_2 are the refractive indices of medium 1 and 2 and c_1 and c_2 are the speed of light in medium 1 and 2. The intensity distribution of the diffraction (Fig. 4.5a) is given by:

$$I_i \;=\; I_r \;+\; I_n \tag{4.20}$$

where I_i is the intensity of the incident light, I_r is the intensity of the reflected light and I_n is the intensity of the refracted light penetrating into the second medium. The relation between the intensity of the incident light and the intensity of the reflected light, called reflection coefficient ρ (or reflectivity, or reflectance), depends on the refractive indices, the angle of incidence and the polarization of the incident light. The reflection coefficient ρ of unpolarized light (containing an equal mix of s- and p-polarizations) is given by:

$$\rho \;=\; \frac{I_r}{I_i} \;=\; \frac{\rho_p \;+\; \rho_s}{2} \tag{4.21}$$

where ρ_p is the reflection coefficient for energy polarized in the plane of incidence and ρ_s is the reflection coefficient for energy polarized in the plane perpendicular to the plane of incidence. For a normal or near-normal angle of incidence ($\alpha_i < 20°$), ρ, ρ_p and ρ_s have similar values (Fig. 4.5b), and (4.21) yields the following simplified expression for the reflection coefficient ρ:

$$\rho = \rho_s = \rho_p = \frac{I_r}{I_i} = \left(\frac{n_1 - n_2}{n_1 + n_2}\right)^2 \tag{4.22}$$

The refractive index n is proportional to the density of the medium. The refractive index of dry air at 15℃ and 1013.25 hPa is $n_{air} = 1.000278$. The refractive index of water is affected by its temperature, as well as the concentration of dissolved and particulate matter. The refractive index increases with increasing salinity and turbidity but decreases with increasing temperature (Bufton et al., 1983). The refractive index of pure water at 20℃, 1013.25 hPa and 500 nm is $n_{water} = 1.336$, while the refractive index of uncontaminated seawater is 1.338 (Cox and Munk, 1954). Since $n_{air} < n_{water}$, the diffraction at an air-water boundary is characterized by Fig.4.5a. In the case of an air-water boundary, (4.22) yields a reflection coefficient $\rho = 2\%$ at normal incidence ($\alpha_i = 0°$), meaning that only 2% of the incident light is reflected by the water surface ($I_r = 0.02\, I_i$). The remaining 98% of incident light penetrate into the water medium, where absorption and scattering occurs (Section 4.4.4). The reflection coefficient has its minimum at normal incidence and is nearly constant for angles of incidence up to 40° (Fig. 4.5b). Beyond 40°, the reflectivity increases, but the probability of receiving a return signal from the water surface in airborne applications decreases rapidly (Section 4.4.6). From an optical point of view, the air-water boundary is comparable to an air-glass boundary, with $n_{glass} = 1.5$ and $I_r = 0.04\, I_i$. In the case of reflection at an $n_1 < n_2$ boundary (e.g. air-water), the reflected part of the incident wave incurs a phase jump of half its wavelength during reflection. This phenomena is important when using a continuous wave laser tracking the phase difference between the transmitted and received signal, but is not relevant for pulsed lasers relying on the time-of-flight.

4.4.2 Specular and Diffuse Reflection

In laser ranging, two types of reflection may occur at the target surface: specular (coherent, mirror) or diffuse reflection (Fig. 4.6). Specular reflection is the reflection without scattering or diffusion, as from a surface that is smooth in relation to the wavelength of the incident radiation. In the case of specular reflection, a laser beam is reflected following the law of specular reflection (4.18). Examples of specular surfaces include calm water, paved roads, mirrors and geodetic corner reflectors. Diffuse reflection is obtained from a relatively rough surface in terms of wavelength of the incident radiation, where the reflected rays are scattered in all directions (Fig. 4.6). Diffuse reflecting surfaces are e.g. forest canopies and agricultural fields. In reflector-less laser ranging applications, the target surface needs to have diffuse reflection properties, unless the surface is oriented perfectly normal to the laser beam. Even a narrow-width laser beam reflects from a diffuse surface at any angle. In airborne laser altimetry, the major factors that determine the type of reflection (specular or diffuse) of the incident radiation by the sea surface are (Zissis, 1993):

1. the surface geometry and wave slope distribution, influencing the surface reflection
2. the optical properties of water, influencing the subsurface reflection

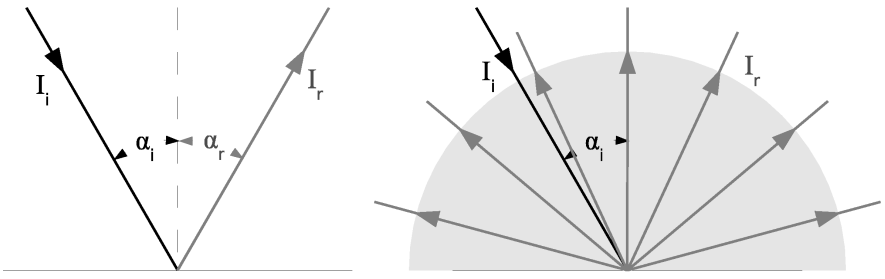

Figure 4.6: Specular (coherent) reflection (left) and diffuse reflection (right).

4.4.3 Impact of Sea Surface Geometry

In the theoretical case of a completely flat water surface, an incident laser beam is partly reflected at the surface as it would from a mirror (specular reflection), with an angle of reflection α_r opposite to the angle of incidence α_i (Fig. 4.5a). In order to receive a return signal from the water surface, the incident laser beam needs to be normal or very close to normal to the sea surface ($\alpha_i \simeq 0°$). The tolerance for the deviation of the angle of incidence from normal is in the order of half the beam divergence, corresponding to less than 0.09° (4.1), independently of the range. Hence, the probability that such a coherently-reflected laser beam reaches the receiver lens is virtually zero, underlining the necessity of diffuse reflection in laser ranging onto targets like water surfaces.

In most cases, the sea surface is affected by wind and waves, yielding a multitude of little facets at the surface, each of them acting like a small mirror with specular reflection. The slope of a small water facet in any direction is assumed to be independent of the wind direction and the cumulative probability distribution for slopes is approximated by a Gaussian distribution (Hooper and Gerber, 1983). If the surface of the laser footprint is large enough to contain a large number of facets, a multitude of specular reflections in many different directions occur. As a consequence, the larger the footprint, the higher the probability of signal returns. The resulting integral reflection can be considered as a pseudo-diffuse reflection, with a significantly higher probability of signal return to the receiver lens. Thus, the equivalent Lambertian reflection coefficient of water is strongly dependent on its surface state and varies from less than 1% when its surface is very smooth to more than 20% when it is rough (Optech, 1989). However, the inherent specular reflection coefficient of the water surface remains unchanged (e.g. 2% for an angle of incidence of 0°), regardless if the sea surface is flat or rough (Cox and Munk, 1954). On the other hand, if the laser footprint is smaller or of similar size than the surface facets, specular reflection occurs despite the faceted surface structure and the signal reception probability is drastically lowered. This can occur in the case of short distances between the laser source and the sea surface, e.g. in shipborne observations. The effects of wind stress on the optical properties of the sea surface have been studied for several decades (Tratt et al., 1996). In particular, the study of (Cox and Munk, 1954), linking sea surface wind fields to wave slope statistics provides a phenomenology by which the wind velocity at the sea surface can be estimated from direct measurements of the wave-modulated surface reflectance.

4.4.4 Absorption, Scattering, Penetration Depth and Backscattering

In laser ranging onto water surfaces, the major part of the incident light (about 98%) penetrates into the water volume (Section 4.4.1). When traveling through a medium (e.g. water), the intensity of a laser beam is continuously weakened by absorption and scattering. The optical transparency T of a medium at a given wavelength λ is given by:

$$T = \frac{I}{I_0} = e^{-d\,(a_\lambda + b_\lambda)} = e^{-d\,c_\lambda} \tag{4.23}$$

where I is the intensity of a laser beam after a traveling distance d in the medium, I_0 is the initial intensity of the laser beam, a_λ and b_λ are the absorption and scattering coefficients of the medium (both e.g. in m^{-1}), and c_λ is the attenuation coefficient regrouping absorption and scattering. Coefficients a_λ and b_λ, and hence the transparency T, are a function of the wavelength λ of the laser beam and the optical properties of the medium.

The penetration depth and the intensity of the light reemerging from the penetrated medium are depending on absorption and scattering, and thus on the wavelength λ and the optical properties of the medium. The penetration depth d_p is usually defined as the traveled distance at which the collimated beam has been attenuated by a factor of e^{-1} (= 37%) (Welch et al., 1989). Thus, (4.23)

yields:

$$d_p \;=\; \frac{1}{a_\lambda \;+\; b_\lambda} \;=\; \frac{1}{c_\lambda} \tag{4.24}$$

Natural water bodies contain both solutes and particulates in suspension. In this case, the attenuation coefficient c_λ is a measure of the decrease of downward-welling radiation from the combined effects of absorption of the solution and particulates, as well as scattering due to the particulates. Because of multiple absorption and scattering, the attenuation coefficient is not necessarily the simple sum of the absorption coefficient of the solution and the scattering coefficient of the particulates as assumed in (4.23) and (4.24) (Zissis, 1993). When the medium's absorptive capacity is very high relative to its scattering ability, the laser beam remains highly collimated and the penetration depth is given by the reciprocal of the absorption coefficient a_λ (Welch et al., 1989).

Backscattered laser radiation from the water volume must be considered in addition to surface backscatter for predicting pulse energy reaching the laser receiver (Bufton et al., 1983). A concise method for treating volume backscatter is obtained by defining the subsurface irradiance reflectivity for zero depth $R(0_-)$, depending on the ratio between the upwelling and downwelling irradiance just beneath the water surface at zero depth (Gordon, 1977). This enables the water volume to be handled as an hypothetical Lambertian reflector of reflectivity $R(0_-)$ located just beneath the surface. A simple relation for the subsurface irradiance reflectivity for zero depth $R(0_-)$ is given by (Morel and Prieur, 1977):

$$R(0_-) \;=\; 0.33\;\frac{b_\lambda}{a_\lambda} \tag{4.25}$$

Volume backscatter and hence $R(0_-)$ are strongly dependent on the wavelength λ of the laser and the inherent optical properties of water. Volume backscatter has a pronounced effect at 532 and 337 nm wavelengths, yielding $R(0_-) \simeq 1\%$, while it is negligible at 9.5 μm because of essentially no surface penetration due to strong absorption (Bufton et al., 1983). In airborne laser altimetry, the natural solar background is negligible compared to the laser backscatter. Hence, $R(0_-)$ only needs to be considered at the respective laser wavelength.

In laser ranging with a pulsed laser to a diffuse reflecting target, the power of the return signal P_r (or backscattered pulse energy), arriving at the receiver, is given by:

$$P_r \;=\; P_e\;\frac{S_r}{d^2}\;R\;e^{\;-2\;d\;c_\lambda} \tag{4.26}$$

where P_e is the power emitted by the pulsed laser, S_r is the effective surface of the receiver, d is the one way distance traveled by the laser beam, c_λ is the attenuation coefficient regrouping absorption and scattering of the medium at wavelength λ, e^{-2dc_λ} is the two-way atmospheric transmission (4.23) and R is the optical reflectivity of the target. The backscatter properties of the sea surface are modeled by the target term R, which is given by (Bufton et al., 1983):

$$R \;=\; \frac{\rho}{\Omega} \tag{4.27}$$

where ρ is the specular surface reflectivity (4.22) and Ω is a solid angle that models the pattern of reflected radiation for backscatter (Bufton et al., 1983). Both ρ and Ω are functions of the angle of incidence. The power P_r arriving at the receiver is proportional to the emitted power P_e and the surface S_r of the receiver (4.26). In order to maximize the exploitation of the intensity from diffuse reflection, the surface S_r has to be increased. The propagation of light after diffuse reflection follows Lambert's law. Hence, the intensity decreases with the square of the traveled distance d from the target to the receiver. Additionally, the attenuation in the atmosphere results in a large loss of intensity that can be counteracted using high-power laser sources.

4.4.5 Optical Properties of Water

In water, the attenuation of light by absorption and scattering is much higher than in the atmosphere. The absorption coefficient of pure water is relatively low (0.015 - $0.840\,\mathrm{m^{-1}}$) in the visible band between 0.4 and $0.7\,\mu$m (Fig. 4.7a). At these wavelengths, there is a good transmission of light through water. A broad absorption minimum is observed in the blue and green spectral range (0.44 - $0.54\,\mu$m). At these wavelengths, the amount of absorption and scattering is about equal, yielding considerable penetration depths (Fig. 4.7b). The absorption coefficient reaches its minimum of $0.015\,\mathrm{m^{-1}}$ at blue wavelengths between 0.46 and $0.48\,\mu$m, corresponding to a penetration depth of 67 m. For red and near-infrared wavelengths (0.63 - $1.40\,\mu$m), scattering is predominant. At 0.9 and $1.06\,\mu$m (near-infrared), the absorption coefficients of pure water are 6.55 and $17.70\,\mathrm{m^{-1}}$, corresponding to penetration depths of 0.15 and 0.06 m, respectively (Fig. 4.7b). At $1.06\,\mu$m, 30 - 50% of the light that penetrates into the water reemerges due to subsurface scattering (Welch et al., 1989). Due to the very high absorption coefficient and very small penetration depth of water at infrared wavelengths above $1.4\,\mu$m, any contribution to the total reflectance due to subsurface scatter can be neglected (Tratt et al., 1996). Seawater has similar optical properties than pure water. It also has its absorption minimum in the blue and green spectral range, although less pronounced due to solute salts, particulates and plankton. Consequently, blue and green radiations can penetrate deeply into seawater and scatter from suspended particulates or even be reflected by the bottom (Zissis, 1993).

4.4.6 Case Study: Backscatter Intensity and Return Rate from Sea Surface

A case study of backscatter intensity and return rate from the sea surface in airborne laser altimetry was carried out based on the data of the GAVDOS campaign (Section 7.1). With the laser profiler (Section 4.2.2), operated at a sampling rate of 1 - 2 kHz, a mean return rate of 70% was obtained during straight flight lines at or close to nadir (roll angle $\simeq 0°$) (Fig. 4.8b). For off-nadir (roll) angles of 5° and 10°, the return rate is reduced to 50% and 20%, resepectively. For off-nadir angles above 15°, the return rate is close to 0%. During turns, the return rate is thus drastically reduced and can reach 0%. In addition, the return rate depends on the sea state (Fig. 4.8a).

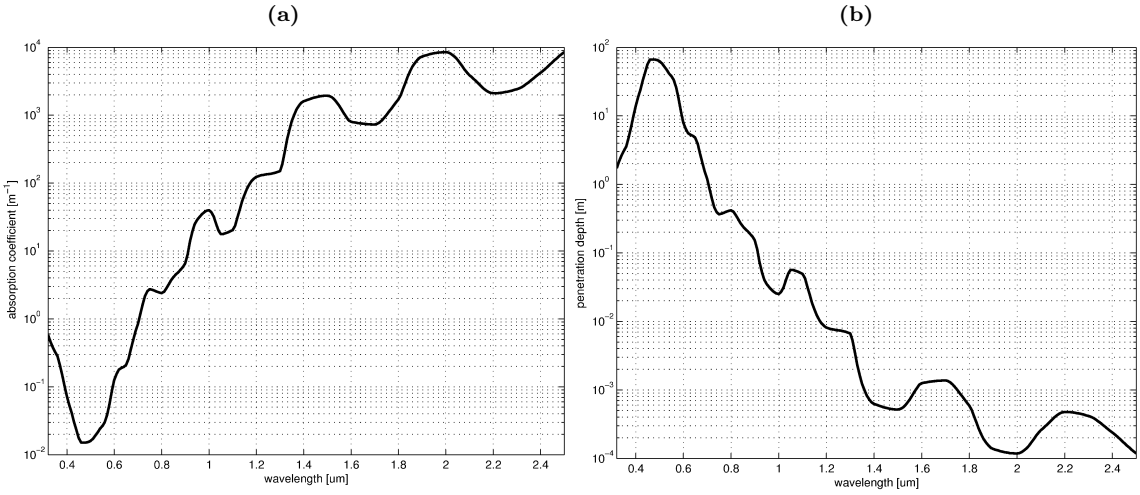

Figure 4.7: **(a)** Absorption coefficient of pure water as a function of wavelength. Values from (Zissis, 1993). **(b)** Penetration depths in pure water as a function of wavelength, computed from the absorption coefficient in (a) based on (4.24).

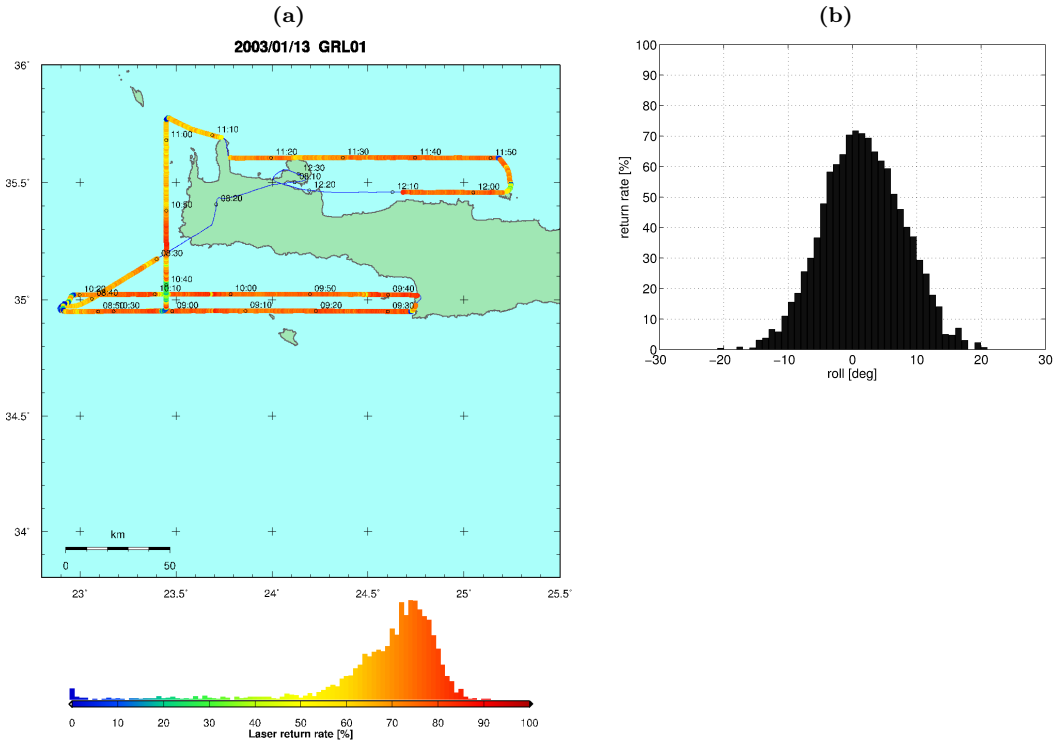

Figure 4.8: **(a)** Laser pulse return rate and its distribution from laser profiler during a survey flight. **(b)** Mean laser profiler return rate distribution as a function of off-nadir (roll) angle of the aircraft.

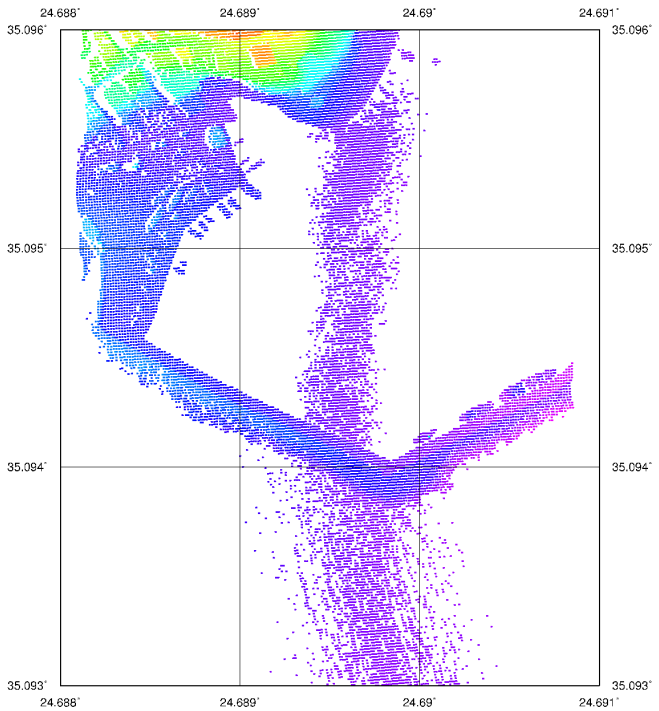

Figure 4.9: Airborne laser scan during overflight of the port of Agia Galini (Fig. 7.4a), with color-coded intensity of the return signal (blue = low intensity, red = high intensity).

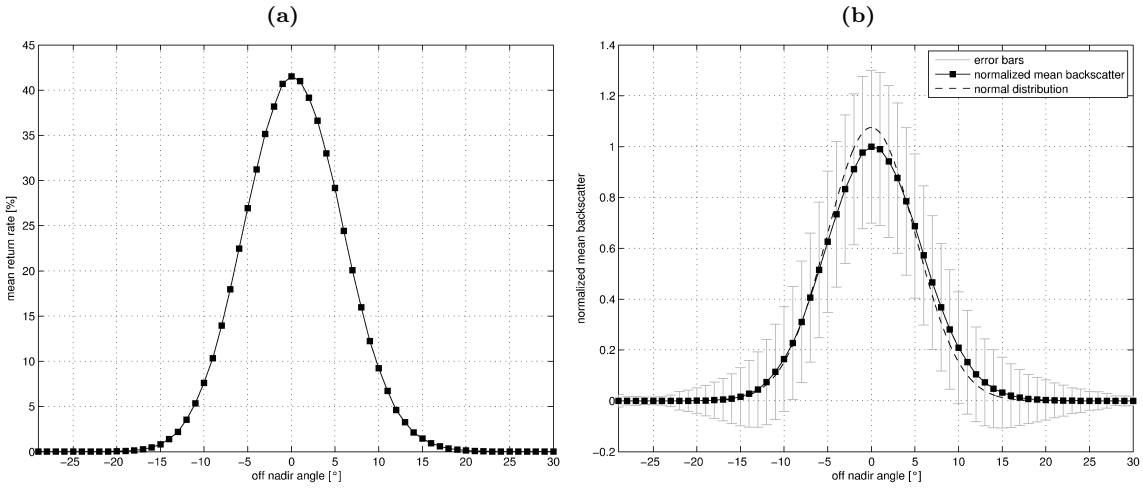

Figure 4.10: **(a)** Distribution of the return rate of the laser scanner as a function of off-nadir angle during a flight line of 150 km. **(b)** Normalized mean backscatter intensity of the scanner as a function of off-nadir angle, during the same flight line as in (a). Error bars indicate the standard deviation for each bin.

Lower return rates were obtained with the laser scanner (Section 4.2.3), with a mean return rate at nadir of 40% (Fig. 4.10a). As for the laser profiler, the return rate rapidly decreases with increasing off-nadir angles and becomes close to 0% for off-nadir angles above 15°. On water, the lateral range of the scanner is very limited as compared to land (Fig. 4.9). In Fig. 4.9, the narrowest lateral range is observed on calm water inside the port basin, where specular reflection predominates.

Beside range data, the laser scanner provides the relative intensity of the returned signal (Fig. 4.9). Normalized mean backscatter intensities were analyzed with respect to the off-nadir angle, along a straight flight line of 150 km (Fig. 4.10b). As for the return rate (Fig. 4.10a), a very smooth distribution is obtained, due to the regular distribution of observations at all off-nadir scan angles between -30° and 30°. A slight deviation of the distribution with respect to a normal distribution is observed. The distribution is centered at 0.32°. The analysis was made before boresight misalignment calibration of the laser scanner. Since the calibration of the scanner with the method described in Section 6.5.4 yielded a boresight misalignment of 0.39°, the major part of the deviation can be attributed to boresight misalignment. The remaining deviation is most likely a systematic effect produced by the sea state (direction and intesity of wind and waves) along the flight line.

5 Shipborne Ultrasound Altimetry

5.1 Introduction

Since airborne laser altimetry is very cost-intensive, a major aim of this project was the development of an alternative method for local-scale sea surface topography determination. Since the GPS-equipped buoys (Appendix C) only provide useful data when they are deployed under drifting conditions or towed at very low speed, they can only be used for punctual sea surface height observations. In order to be able to cover larger areas, a novel method of shipborne sea surface height observations was developed in the framework of this project. The method relies on one or more low-cost industrial ultrasonic distance sensors mounted on a boat, providing continuous information on the distance to the sea surface.In combination with the position and attitude information from a multi-antenna GPS system installed on the boat, this method allows for highly reliable sea surface height determination by direct georeferencing (Chapter 6). Due to its analogy to airborne laser altimetry (Chapter 4), the method is called shipborne ultrasound altimetry. The successful implementation of the new technique during several survey campaigns proved that it is a powerful method for providing offshore sea surface height observations, even under rough sea conditions, and that it provides a low-cost alternative to airborne laser altimetry.

5.2 Instrumental Setup

5.2.1 Overview

The setup of the sailing yacht for shipborne ultrasound altimetry, developed and deployed in the framework of this project, is composed of the following instruments (Fig. 5.1):

- 2 ultrasonic distance sensors, sampling rate 10 Hz (Fig. 5.2)
- 4 - 5 GPS receivers for position and attitude determination, sampling rate 1 - 2 Hz (Fig. 5.3)
- 1 inertial AHRS (Attitude and Heading Reference System), sampling rate 20 Hz (Fig. 5.4)

All instruments had to be integrated into the sensor system and synchronized with GPS time (Section 5.4).

5.2.2 Ultrasonic Distance Sensors

The two ultrasonic distance sensors used in this project are the Pepperl+Fuchs UC4000-30GM-IUR2-V15 and UC6000-30GM-IUR2-V15 (Fig. 5.2). They are industrial low-cost sensors, with a nominal detection range of 4 and 6 m, respectively. A data logger with an analog-to-digital (A/D) converter was used to record the analog signal of the sensors. Technical details of the sensors are discussed in Section 5.3. The sensors were mounted at the bow of the boat, in a way that the target water surface was not disturbed by the boat (Fig. 5.1).

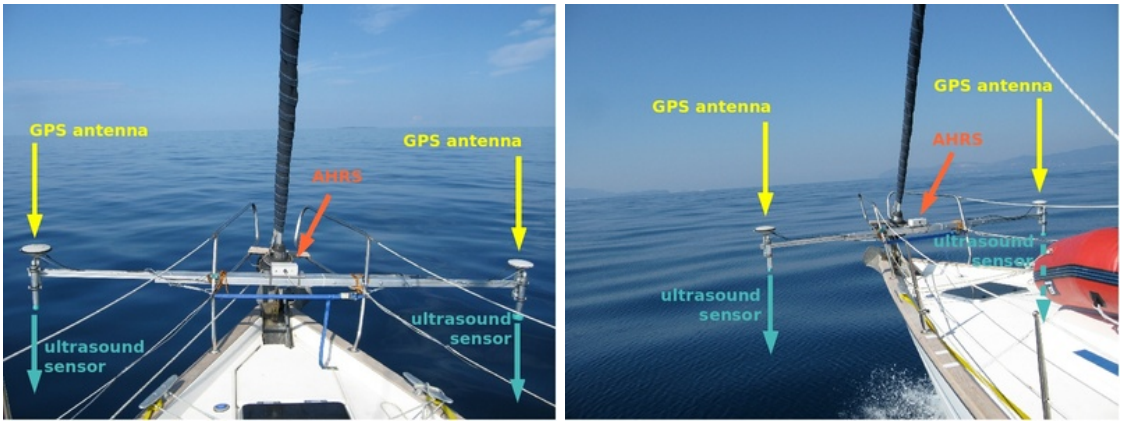

Figure 5.1: Main components of the ultrasound altimetry system mounted at the bow of a sailing yacht, including two ultrasonic distance sensors, two GPS antennas and an inertial AHRS.

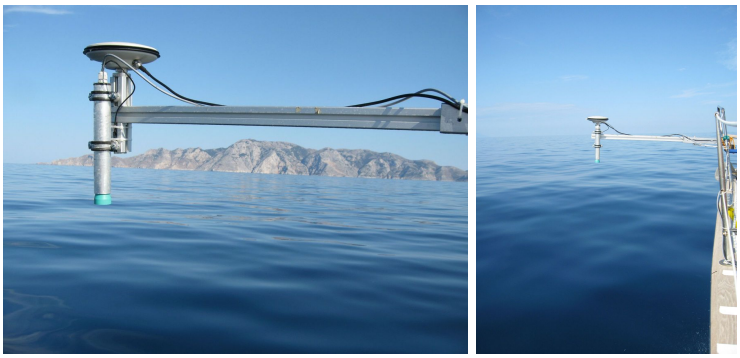

Figure 5.2: Ultrasonic distance sensor and GPS antenna.

5.2.3 GPS Antenna Configuration

The boat was equipped with an array of 4 to 5 GPS antennas (Fig. 5.3). All antennas were connected to independent dual frequency GPS receivers. The baseline lengths are 2.7 m between the portside and starboard antennas, and 12.5 m between the stern and bow antennas. This setup allowed for highly precise 3D positioning (trajectography) of the boat in combination with terrestrial GPS reference stations, as well as autonomous determination of the attitude of the boat, both needed for georeferencing the ultrasound ground point (Chapter 6).

5.2.4 Inertial Attitude and Heading Reference System

The multi-antenna GPS system used for attitude determination was augmented with an Xsens MTi inertial Attitude and Heading Reference System (AHRS) (Fig. 5.4). It is based on solid state miniature MEMS (Micro-Electro-Mechanical Systems) sensors, including 3-axis gyroscopes, 3-axis accelerometers and 3-axis magnetometers, providing 3D rate of turn, 3D acceleration and 3D magnetic field data. The data of the accelerometers and magnetometers are used to eliminate drift errors from the integration of rate of turn data. The AHRS was operated at a sampling rate of 20 Hz. With the use of the AHRS, only one GPS receiver for positioning is needed. The multi-antenna GPS array and the AHRS were operated in parallel in order to compare their benefits in shipborne applications. Details on the performance of the AHRS, based on comparisons with the results from the multi-antenna GPS system, can be found in Section 6.4.6.

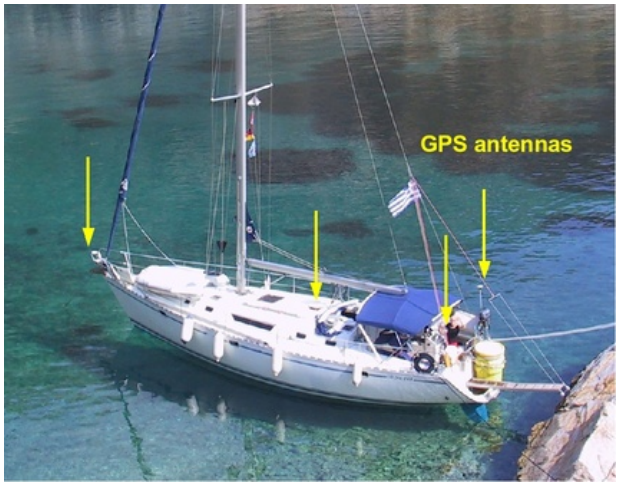

Figure 5.3: GPS antenna configuration (arrows) on the sailing yacht.

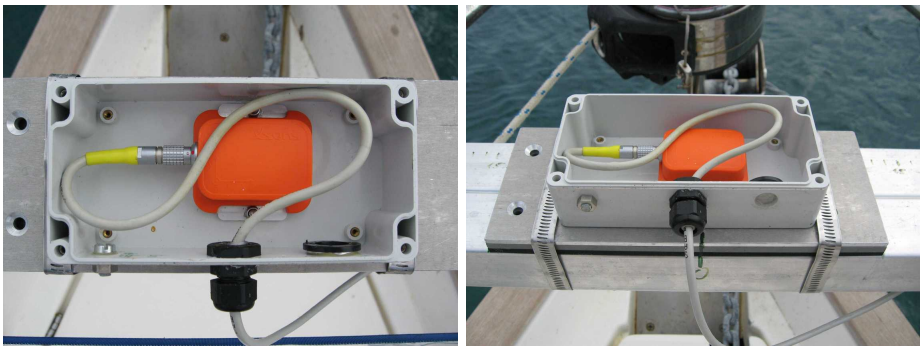

Figure 5.4: Inertial AHRS (Attitude and Heading Reference System).

5.3 Ultrasound Ranging[1]

5.3.1 Basic Principles

Analogous to pulsed laser sensors (4.1), ultrasonic sensors determine the distance r to a target by measuring the time delay t between the sending of a package of ultrasonic pulses and the reception of the returned echo reflected by the target (Fig. 5.5):

$$r = c_s \frac{t}{2} \tag{5.1}$$

where c_s is the speed of sound (344.0 m/s at 20℃, 331.6 m/s at 0℃). Hence, for a distance of 1 m to the target, the propagation time is 5.8 ms. In Fig. 5.5, the propagation time t is labeled 2τ. The ultrasonic sensors have two analog range outputs (current and voltage). They are equipped with an integrated 12-bit D/A (digital-to-analog) converter, converting the determined range in a 0 - 10 V and 4 - 20 mA signal. A resolution of 12 bits corresponds to $2^{12} = 4096$ available values. The propagation time of an ultrasonic pulse is determined with a resolution of 1 μs, given by the clock rate of the micro-controller and corresponding to a range resolution of 0.172 mm. However, this maximum range resolution is only achieved if the measuring window (distance between the

[1] This section is based on information from the manufacturer of the ultrasonic sensors (Pepperl+Fuchs, 2006).

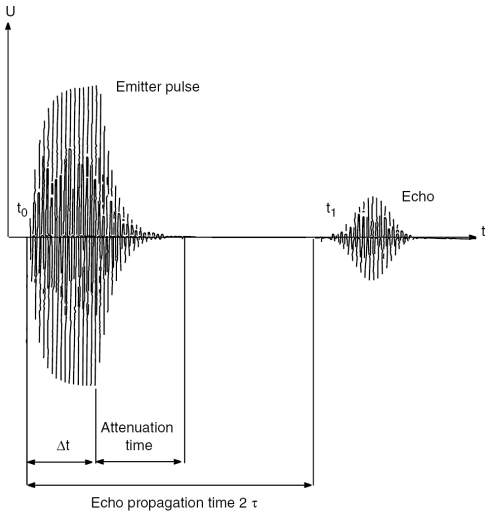

Figure 5.5: Transmitted and received signal in ultrasound ranging. From (Pepperl+Fuchs, 2006).

lower and the upper range limits) is smaller than 705 mm (= 4096 · 0.172). For a measuring window above 705 mm, the range resolution Δr is limited by the 12-bit D/A converter, according to the relation:

$$\Delta r \;=\; \frac{\text{upper limit} - \text{lower limit}}{4096} \tag{5.2}$$

The sensors used in this project have a configurable measuring window that was set between from 0.5 to 4.0 m, yielding a range resolution Δr of 0.85 mm. In order to determine the absolute accuracy of the range measured by an ultrasonic sensor, factors such as temperature, atmospheric pressure, relative humidity (Section 5.3.2), turbulences, hot spots in the air surrounding the sensor, and sensor in hot operating status must be taken into consideration. In addition, tolerances of the electronic components and differences in the response characteristic of the ultrasonic sensor due to varying signal strengths of the sound reflected by the target also have an effect. Under consideration of all these influences, an accuracy of better than 2 cm/m can generally be achieved, along with a repeatability and linearity of better than 2 mm/m (Pepperl+Fuchs, 2006).

Since the ultrasonic sensors used in this project operate with only one piezoelectric sound transducer acting alternately as transmitter and receiver, the transmitted pulse duration Δt and the attenuation time t_a of the sonic transducer result in an unusable area, called blind range r_b, in which targets cannot be detected (Fig. 5.5):

$$r_b \;<\; c_s \,\frac{\Delta t + t_a}{2} \tag{5.3}$$

The pulse duration Δt of the sensors is configurable between 0.04 and 0.55 ms. For the UC4000, $\Delta t + t_a = 1.1$ ms, corresponding to a blind range r_b of 20 cm. For the UC6000, $\Delta t + t_a = 2.0$ ms, corresponding to a blind range r_b of 35 cm.

The maximum detection range of the sensor depends on the sound reflection properties of the target. Good reflectors can be detected from up to double the nominal detection range. On the other hand, an object situated close to the sensor can produce multiple return signals, since the ultrasonic pulses may propagate several times back and forth between the target and the sensor. This can lead to erroneous distance estimation if the object is situated within the blind range. Blind range and detection range are both functions of the energy contained in the pulse. The

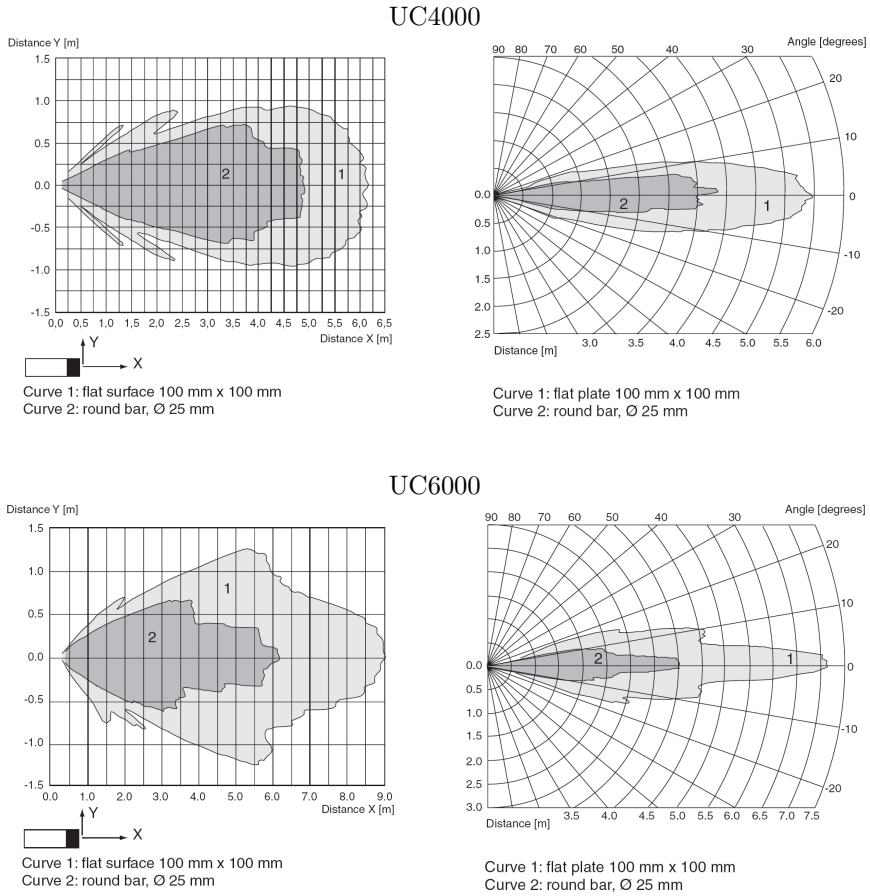

Figure 5.6: Response curves of UC4000 and UC6000 ultrasonic sensors. From (Pepperl+Fuchs, 2006).

higher the energy, the larger the detection range, but in parallel, the attenuation time and thus the blind range also increase. The spatial dimension of the sound cone emitted by the sensor is defined by the opening angle of the ultrasonic beam, which is approx. 5° for the sensors used in this project. Fig. 5.6 shows the response range for typical targets. Within these ranges, the sensor can detect the specific targets.

After the transmission of an ultrasonic pulse, the sensor waits for a time equivalent to twice the nominal detection range, since it can receive echoes from distances beyond the nominal detection range under favorable reflection conditions. This waiting phase limits the maximum sampling rate of the sensor. For the UC4000 and UC6000, the nominal detection ranges of 4 and 6 m result in waiting phases of 47 and 70 ms, corresponding to maximum sampling rates of 21 and 14 Hz, respectively. In this project, both sensors were operated in self-synchronization mode (Section 5.4), yielding a sampling interval of 0.15 s (7 Hz) for each sensor.

5.3.2 Atmospheric Influences

The sound propagation velocity and the detection range depend on the physical properties of the carrier medium. In case of a gas-air mixture, they depend on air temperature, relative humidity and barometric pressure (Fig. 5.7). The temperature greatly affects the velocity of sound, whereas air pressure and humidity are less important factors. The temperature influence on the measured range is -0.17%/°C, corresponding to a decrease of the measured range by 0.17 cm/m for a temperature

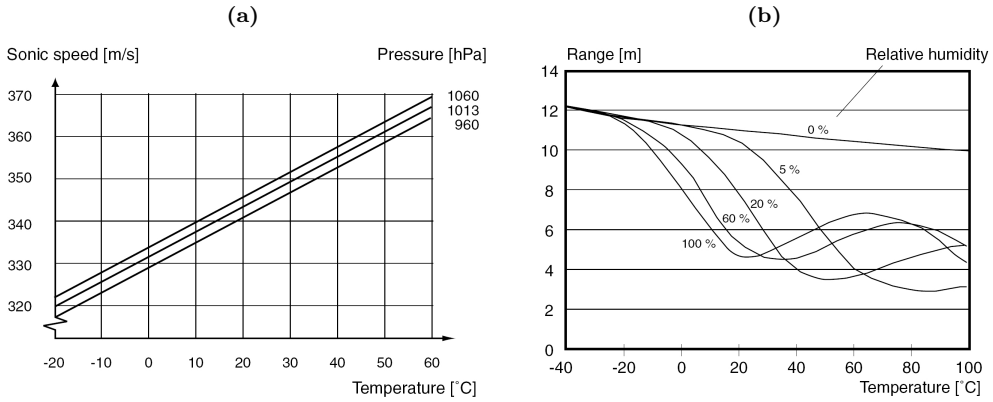

Figure 5.7: (a) Relationship between air temperature, pressure and velocity of sound. **(b)** Relationship of the maximum detection range with respect to air temperature and relative humidity, for the UC6000-30GM sensor. The nominal detection range at an ambient temperature of 20°C and a relative humidity of 50% is 6 m. Graphs from (Pepperl+Fuchs, 2006).

increase of 1°C. Due to the strong temperature dependency, the ultrasonic sensors used in this project are temperature-compensated, based on a temperature probe connected to the sensors. Fig. 5.7b shows the increased maximum detection range at low temperatures, independent of the relative humidity, as well as the reduced detection range at higher temperatures, strongly influenced by the relative humidity.

5.3.3 Ultrasonic Target Reflection

Targets detectable by ultrasonic sensors can be solid or liquid. The echo is influenced by the properties of the target surface. Even and smooth surfaces, oriented at a right angle to the sound cone, provide ideal reflection. Reliable detection is still obtained for angular deviations of 3°. Material properties like transparency, color or surface finish have no effect on detection reliability.

The roughness of the surface, together with the sensor-specific transducer wavelength, determines whether the reflection of the ultrasonic pulse is specular or diffuse (Section 4.4.2). If the wavelength is longer than the peak-to-valley height of the surface roughness, specular reflection prevails (Tab. 5.1). If it is shorter, diffuse reflection prevails. The transition from specular to diffuse reflection is continuous, and roughness depths in between the values in Tab. 5.1 will result in reflections with diffuse and specular shares. Targets with pronounced surface roughness and associated diffuse reflection will result in a reduction of the detection range. On the other hand, pronounced surface roughness allows larger deviation of the angle of incidence from normal, due to predominant diffuse reflection. As a consequence, filling level or pouring cones of coarse-grained material can e.g. be detected (at reduced sensing range) at an angular deviation of up to 45°.

The following targets are well-suited for detection:

- smooth and solid object aligned at a right angle to the axis of the sound cone
- solid object with surface roughness causing diffuse reflection, largely independent of alignment
- liquid surface, not inclined by more than 3° perpendicular to the axis of the sound cone

The following targets are poorly suited for detection:

- materials absorbing ultrasonic waves such as felt, cotton, wool, coarse textiles or plastic foam
- materials at temperatures above 100°C

Table 5.1: Ultrasound transducer frequencies and wavelengths, and associated degrees of surface roughness (peak-to-valley height) for specular and diffuse reflection. Values from (Pepperl+Fuchs, 2006).

Transducer frequency	Transducer wavelength	Surface roughness causing predominant specular reflection	Surface roughness causing predominant diffuse reflection
65 kHz	5.3 mm	$<$ 1.0 mm	$>$ 25 mm
85 kHz	4.0 mm	$<$ 0.8 mm	$>$ 20 mm
120 kHz	2.9 mm	$<$ 0.5 mm	$>$ 13 mm
175 kHz	2.0 mm	$<$ 0.4 mm	$>$ 10 mm
375 kHz	0.9 mm	$<$ 0.2 mm	$>$ 5 mm

The transducer frequencies of the sensors used in this project are 65 and 85 kHz, respectively. Since natural water surfaces like oceans are usually characterized by a peak-to-valley height above 25 mm within the ultrasound footprint of approx. 1 m diameter, the resulting reflection is predominately diffuse (Tab. 5.1), leading to reliable signal returns even for off-nadir angles above 3°.

5.4 Sensor Synchronization

5.4.1 Self-Synchronization between Ultrasonic Sensors

Mutual interference between ultrasonic sensors can occur if they are not separated by a minimum distance. The minimum distance can be relatively large, depending on the nominal detection range, the distance to the target and the site conditions. Interference can be effectively prevented by synchronizing the ultrasonic sensors. For this purpose, the sensors are equipped with a synchronization input/output interface. Synchronization pulses sent to the sensor initiate each measuring cycle and the transmission of a single ultrasonic pulse package. The two sensors used in this project were self-synchronized by interconnecting their synchronization inputs/outputs, causing the sensors to alternately transmit ultrasonic pulses.

5.4.2 Synchronization of Ultrasonic Sensors with GPS

The self-synchronization pulses described above were also used to synchronize the ultrasonic sensors with the GPS system, by simultaneously transmitting the pulses to the data logger recording the range of the sensors, as well as to a GPS receiver. Every pulse coincides with a data sample of an ultrasonic sensor. The data logger associates a time-tag to every pulse, and hence to every range observation, in his internal time system. The GPS receiver attributes a time-tag in GPS time to the same pulses, providing a precise absolute time-tag for every ultrasonic range measurement.

Due to sporadic dropouts of the hardware synchronization during the early deployment of the ultrasound altimetry system, an algorithm relying on a purely mathematical synchronization was developed. The system is based on 2D cross-correlation between the absolute height of the GPS antenna mounted close to the ultrasonic sensor and the range observed by the sensor. The antenna height is determined by GPS processing and is given in precise GPS time. The sensor range is recorded in the time frame of the data logger. The synchronization between the two time frames is defined by an offset and a scale factor. The offset accounts for the offset of the time frame of the data logger with respect to the absolute GPS time frame, whereas the scale factor accounts for a constant drift of the logger time frame. Drift variations are neglected. Since the GPS antenna and the ultrasonic sensor are rigidly mounted on the boat, the movement produced by the boat equally affects the height of the GPS antenna and the ultrasonic range (Fig. 5.8). The 2D cross-correlation, where the first dimension is the offset, and the second is the scale factor, allows to identify the offset and scale factor of the time frame for which the maximum correlation between the GPS

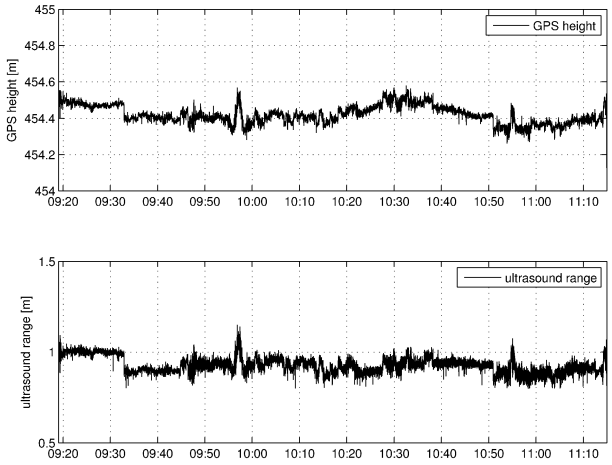

Figure 5.8: Example of mathematical synchronization under calm conditions, with height of GPS antenna (top) and ultrasonic range (bottom).

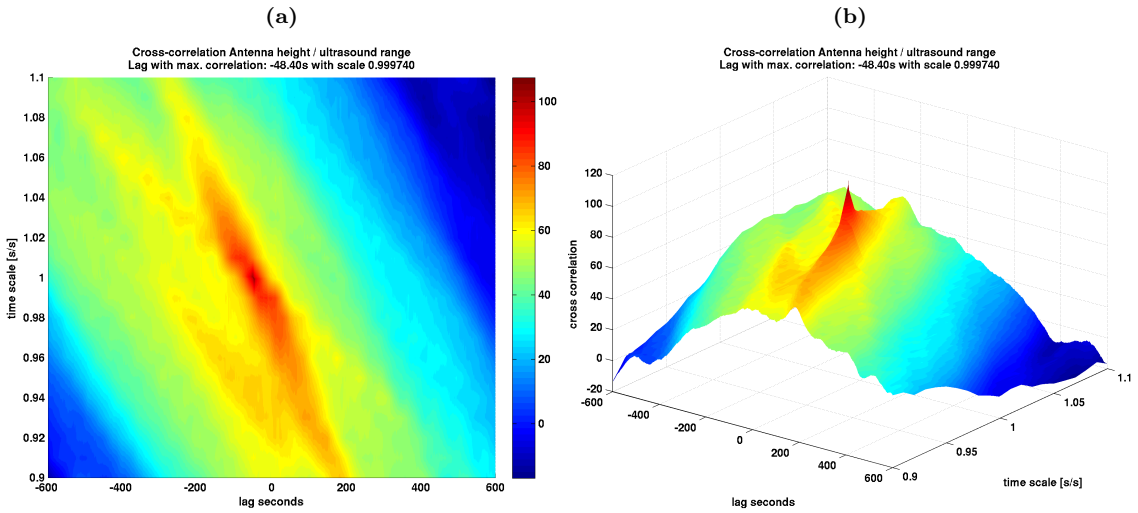

Figure 5.9: **(a)** 2D cross-correlation of the two signals in Fig. 5.8, with offset (lag) along the x-axis and scale factor along the y-axis. The (dimensionless) correlation values are color-coded. A distinct peak of maximum correlation can be identified. **(b)** 3D view of (a).

height and the ultrasound range is obtained (Fig. 5.9). The method does not suffer from the fact that the range signal is additionally affected by the undulation of waves at the target water surface. The only case where the synchronization method would not provide a solution is in the absence of vertical movement of the boat. This condition is never verified, even when the boat is floating in calm water or lying in a calm port. Theoretically, the maximum synchronization accuracy that can be achieved is governed by the largest of the two sampling intervals of the GPS and ultrasound records. However, since both signals are smooth oscillating movements, they can be interpolated to smaller sampling intervals, e.g. using cubic polynomial interpolation.

6 Direct Georeferencing

6.1 Introduction

In this chapter, an approach for direct georeferencing is shown, valid for both airborne laser altimetry (Chapter 4) and shipborne ultrasound altimetry (Chapter 5). The GPS based trajectory and attitude recovery is discussed, and comparisons with attitude solutions from inertial units are made. In addition, a calibration method for boresight misalignment in airborne laser altimetry is presented. The quality of the trajectory of the airplane or the boat determined by differential GPS, and their attitude determined by a multi-antenna GPS array or by inertial systems, are of utmost importance. These issues will be analysed in Sections 6.3 and 6.4, respectively. Another critical element is the determination of the boresight misalignment between the frame of the laser device and the body frame. This misalignment affects the georeferencing of the laser data systematically. Since they are difficult to measure directly, their determination is not trivial. In Section 6.5, the impact of boresight misalignment on computed terrain heights will be analysed and a boresight self-calibration method is presented. Considerations on the effect of atmospheric refraction in laser ranging were discussed in Section 4.3.2. Most of the elemnts in this chapter are focused on airborne laser altimetry, but unless not explicitly stated, they also apply to shipborne ultrasound altimetry. The approach of direct georeferencing described in this chapter is based on (Favey, 2001).

6.2 Basic Principle

6.2.1 Direct Georeferencing Equation

The key problem in airborne laser altimetry consists in integrating all necessary elements for georeferencing the laser beam, yielding a 3D vector between the aircraft and the ground point in an absolute coordinate system (Fig. 6.1). For each range measurement r by the laser device, the corresponding ground point is computed, involving the GPS position of the aircraft and its attitude. The observations from all devices have to be synchronized with respect to GPS time and interpolated to the corresponding measuring epoch. The observation equation for direct georeferencing in airborne laser altimetry can be written as (Favey, 2001):

$$\boldsymbol{x}^G \;=\; \boldsymbol{a}^G \;+\; \boldsymbol{R}_{G/L}\;\boldsymbol{R}_{L/B}\;\left(\;\boldsymbol{R}_{B/S}\;r\;\boldsymbol{s}^S \;+\; \boldsymbol{b}^B\;\right) \tag{6.1}$$

or in vector notation:

$$\begin{bmatrix} X \\ Y \\ Z \end{bmatrix}^G \;=\; \begin{bmatrix} X_a \\ Y_a \\ Z_a \end{bmatrix}^G \;+\; \boldsymbol{R}_{G/L}\;\boldsymbol{R}_{L/B}\;\left(\;\boldsymbol{R}_{B/S}\;r\;\begin{bmatrix} s_x \\ s_y \\ s_z \end{bmatrix}^S \;+\; \begin{bmatrix} b_x \\ b_y \\ b_z \end{bmatrix}^B\right)$$

where (Fig. 6.1):

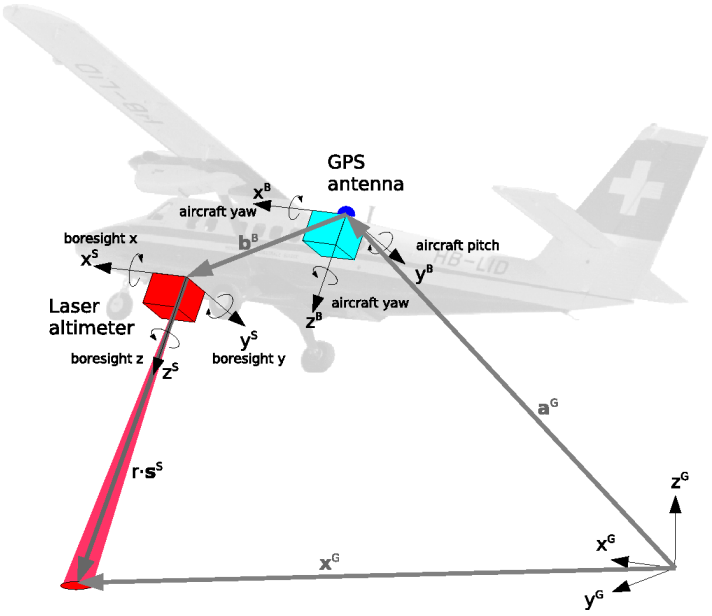

Figure 6.1: Direct georeferencing elements in airborne laser altimetry.

$\boldsymbol{x}^G$	geocentric position of laser ground point (to be determined)
$\boldsymbol{a}^G$	geocentric position of GPS antenna (determined by GPS trajectography)
$\boldsymbol{R}_{G/L}$	rotation matrix from topocentric to geocentric system, defined by the aircraft's latitude and longitude
$\boldsymbol{R}_{L/B}$	rotation matrix from body frame to topocentric system, defined by the aircraft's attitude angles roll (a_x), pitch (a_y) and yaw (a_z)
$\boldsymbol{R}_{B/S}$	rotation matrix of boresight between laser device and body frame, defined by the boresight angles β_x, β_y, β_z and the boresight misalignment angles $d\beta_x$, $d\beta_y$, β_z (to be determined by calibration)
r	slant laser range (measured by laser device)
$\boldsymbol{s}^S$	unit vector giving the laser beam direction in laser device coordinate frame
$\boldsymbol{b}^B$	offset vector between GPS antenna and laser (measured with geodetic methods)

The laser vector $\boldsymbol{s}^S$ in the laser device coordinate frame is given by:

$$\boldsymbol{s}^S = (\sin\sigma_x \cos\sigma_z,\ \sin\sigma_x \sin\sigma_z,\ \cos\sigma_x)^T \tag{6.2}$$

where σ_x is the off-nadir angle with respect to the vertical as defined in the laser frame and σ_z is the horizontal angle (azimuth) with respect to the laser frame. For a vertical profiler, $\sigma_x = \sigma_z = 0°$ and $\boldsymbol{s}^S = (0, 0, 1)^T$. For a cross-section linear scanner, σ_x is the time-varying off-nadir scan angle, σ_z = -90° and $\boldsymbol{s}^S = (0, -\sin\sigma_x, \cos\sigma_x)^T$. The signs of σ_z and $\sin\sigma_x$ depend on the definition of the direction of the scanner rotation.

The general definition of rotation matrices is given in Appendix D.1. The rotation matrix from the local level north oriented coordinate frame NED (North, East, Down) to the geocentric system (Appendix D.2) depends on the aircraft's latitude (φ) and longitude (λ), determined by GPS trajectography:

$$\boldsymbol{R}_{G/L} = \boldsymbol{R}_3(-\lambda)\ \boldsymbol{R}_2\left(\frac{\pi}{2} + \varphi\right) = \begin{bmatrix} -\sin\varphi\cos\lambda & -\sin\lambda & -\cos\varphi\sin\lambda \\ -\sin\varphi\sin\lambda & \cos\lambda & -\cos\varphi\sin\lambda \\ \cos\varphi & 0 & -\sin\varphi \end{bmatrix} \tag{6.3}$$

The rotation matrix from the body frame to the local level NED frame depends on the attitude angles roll (α_x), pitch (α_y) and yaw (α_z) of the aircraft:

$$\begin{aligned}\boldsymbol{R}_{L/B} &= \boldsymbol{R}_3(-\alpha_z)\ \boldsymbol{R}_2(-\alpha_y)\ \boldsymbol{R}_1(-\alpha_x) \\ &= \begin{bmatrix} \cos\alpha_y \cos\alpha_z & -\cos\alpha_x \sin\alpha_z + \sin\alpha_x \sin\alpha_y \cos\alpha_z & \sin\alpha_x \sin\alpha_z + \cos\alpha_x \sin\alpha_y \cos\alpha_z \\ \cos\alpha_y \sin\alpha_z & \cos\alpha_x \cos\alpha_z + \sin\alpha_x \sin\alpha_y \sin\alpha_z & -\sin\alpha_x \cos\alpha_z + \cos\alpha_x \sin\alpha_y \sin\alpha_z \\ -\sin\alpha_y & \sin\alpha_x \cos\alpha_y & \cos\alpha_x \cos\alpha_y \end{bmatrix}\end{aligned} \tag{6.4}$$

The boresight rotation is described by three rotation angles $(\beta_x, \beta_y, \beta_z)$ around the three axes of the laser device frame. Approximate values $(\beta_x^0, \beta_y^0, \beta_z^0)$ of the boresight rotation angles are known from mechanical alignment. The actual angles can slightly differ from these nominal values. This deviation is called boresight misalignment. The boresight misalignment angles $(d\beta_x, d\beta_y, d\beta_z)$ are unknown and have to be determined by calibration. The boresight rotation matrix depends on the boresight angles ($\beta = \beta^0 + d\beta$):

$$\begin{aligned}\boldsymbol{R}_{B/S} &= \boldsymbol{R}_3(-\beta_z)\ \boldsymbol{R}_2(-\beta_y)\ \boldsymbol{R}_1(-\beta_x) \\ &= \begin{bmatrix} \cos\beta_y \cos\beta_z & -\cos\beta_x \sin\beta_z + \sin\beta_x \sin\beta_y \cos\beta_z & \sin\beta_x \sin\beta_z + \cos\beta_x \sin\beta_y \cos\beta_z \\ \cos\beta_y \sin\beta_z & \cos\beta_x \cos\beta_z + \sin\beta_x \sin\beta_y \sin\beta_z & -\sin\beta_x \cos\beta_z + \cos\beta_x \sin\beta_y \sin\beta_z \\ -\sin\beta_y & \sin\beta_x \cos\beta_y & \cos\beta_x \cos\beta_y \end{bmatrix}\end{aligned} \tag{6.5}$$

In many applications, the coarse boresight angles β^0 are zero from mechanical alignment, and the rotation matrix $\boldsymbol{R}_{B/S}$ only depends on the unknown misalignment angles $d\beta$. Usually, the boresight misalignment angles are small differential angles ($< 1°$), and the rotation matrix $\boldsymbol{R}_{B/S}$ can be simplified using the properties of small angles close to 0° ($\sin d\beta \simeq d\beta$ and $\cos d\beta \simeq 1$):

$$\boldsymbol{R}_{B/S} = \begin{bmatrix} 1 & -d\beta_z & d\beta_y \\ d\beta_z & 1 & -d\beta_x \\ -d\beta_y & d\beta_x & 1 \end{bmatrix} \tag{6.6}$$

6.2.2 Vertical Component of Direct Georeferencing Equation

In boresight misalignment calibration (Section 6.5) or when estimating the impact of erroneous attitudes angles onto terrain height (Section 6.2.3), the vertical component of the laser ground point in the direct georeferencing equation (6.1) is of particular interest. Therefore, we want to first express the coordinates of the ground point in topocentric coordinates by left-multiplying (6.1) with $\boldsymbol{R}_{G/L}^{-1}$ (Appendix D.2):

$$\begin{aligned}\begin{bmatrix} N \\ E \\ D \end{bmatrix}^L &= \begin{bmatrix} N_a \\ E_a \\ D_a \end{bmatrix}^L + \boldsymbol{R}_{L/B} \left(\boldsymbol{R}_{B/S}\ r \begin{bmatrix} s_x \\ s_y \\ s_z \end{bmatrix}^S + \begin{bmatrix} b_x \\ b_y \\ b_z \end{bmatrix}^B \right) \\ &= \begin{bmatrix} N_a \\ E_a \\ D_a \end{bmatrix}^L + \begin{bmatrix} r_{11} & r_{12} & r_{13} \\ r_{21} & r_{22} & r_{23} \\ r_{31} & r_{32} & r_{33} \end{bmatrix}^{L/B} \left(\begin{bmatrix} r_{11} & r_{12} & r_{13} \\ r_{21} & r_{22} & r_{23} \\ r_{31} & r_{32} & r_{33} \end{bmatrix}^{B/S} r \begin{bmatrix} s_x \\ s_y \\ s_z \end{bmatrix}^S + \begin{bmatrix} b_x \\ b_y \\ b_z \end{bmatrix}^B \right)\end{aligned} \tag{6.7}$$

For the case of a **cross-section linear scanner**, $\boldsymbol{s}^S = (0, -\sin\sigma_x, \cos\sigma_x)^T$. Considering only the vertical down component D in (6.7) and by substituting the terms of the rotation matrices from

(6.3), (6.4) and (6.6) in (6.7), the true height difference Δh^L between the GPS antenna and the laser ground point is obtained:

$$\begin{aligned}\Delta h^L \;=\; D^L \;-\; D_a^L \;=\; &-\; \sin\alpha_y \left(r\; d\beta_z\; \sin\sigma_x \;+\; r\; d\beta_y\; \cos\sigma_x \;+\; b_x^B\right) \\ &+\; \sin\alpha_x\; \cos\alpha_y \left(-r\; \sin\sigma_x \;-\; r\; d\beta_x\; \cos\sigma_x \;+\; b_y^B\right) \\ &+\; \cos\alpha_x\; \cos\alpha_y \left(-r\; d\beta_x\; \sin\sigma_x \;+\; r\; \cos\sigma_x \;+\; b_z^B\right)\end{aligned} \tag{6.8}$$

This equation can be reformulated using the true height of the laser ground point h^L and the ellipsoidal height of the GPS antenna h_a^L in the classical ENU (East, North, Up) coordinate system:

$$\begin{aligned}h^L \;=\; h_a^L \;-\; \Delta h^L \;=\; h_a^L \;&+\; \sin\alpha_y \left(r\; d\beta_y\; \cos\sigma_x \;+\; r\; d\beta_z\; \sin\sigma_x \;+\; b_x^B\right) \\ &-\; \sin\alpha_x\; \cos\alpha_y \left(-r\; \sin\sigma_x \;-\; r\; d\beta_x\; \cos\sigma_x \;+\; b_y^B\right) \\ &-\; \cos\alpha_x\; \cos\alpha_y \left(r\; \cos\sigma_x \;-\; r\; d\beta_x\; \sin\sigma_x \;+\; b_z^B\right)\end{aligned} \tag{6.9}$$

For the case of a vertical **laser profiler**, $\boldsymbol{s}^S = (0,0,1)^T$ and (6.9) is further simplified to:

$$h^L = h_a^L - \left[\cos\alpha_x \cos\alpha_y \left(r + b_z^B\right) \;-\sin\alpha_x \cos\alpha_y \left(r\; d\beta_x - b_y^B\right) \;-\sin\alpha_y \left(r\; d\beta_y + b_x^B\right)\right] \tag{6.10}$$

In the case of a cross-section linear scanner, the vertical component does not depend on the yaw angle α_z (6.9). In the case of a laser profiler, the vertical component does not depend on the yaw angle α_z, nor on the yaw component $d\beta_z$ of the boresight misalignment (6.10).

6.2.3 Impact of Attitude Error onto Ground Point Height

Erroneous attitude angles can occur due to inaccurate attitude observations or a misalignment of the attitude measurement system. Assuming that the roll and pitch angles α_x and α_y are affected by the errors $d\alpha_x$ and $d\alpha_y$, (6.10) for a profiler becomes:

$$\begin{aligned}h^L \;=\; h_a^L &- \cos\left(\alpha_x + d\alpha_x\right) \cos\left(\alpha_y + d\alpha_y\right) \left(r + b_z^B\right) \\ &+ \sin\left(\alpha_x + d\alpha_x\right) \cos\left(\alpha_y + d\alpha_y\right) \left(r\; d\beta_x - b_y^B\right) \\ &+ \sin\left(\alpha_y + d\alpha_y\right) \left(r\; d\beta_y + b_x^B\right)\end{aligned} \tag{6.11}$$

Since attitude errors are usually small angles ($< 1°$), (6.11) can be simplified using the properties of small angles (for $d\alpha_i \to 0$, $\sin d\alpha_i \simeq d\alpha_i$, $\cos d\alpha_i \simeq 1$ and $d\alpha_i \cdot d\alpha_i \simeq 0$):

$$\begin{aligned}h^L \;=\; h_a^L &- \left(\cos\alpha_x \cos\alpha_y - d\alpha_x \sin\alpha_x \cos\alpha_y - d\alpha_y \cos\alpha_x \sin\alpha_y\right) \left(r + b_z^B\right) \\ &+ \left(\sin\alpha_x \cos\alpha_y + d\alpha_x \cos\alpha_x \cos\alpha_x - d\alpha_y \sin\alpha_x \sin\alpha_y\right) \left(r d\beta_x - b_y^B\right) \\ &+ \left(\sin\alpha_y + d\alpha_y \cos\alpha_y\right) \left(r d\beta_y + b_x^B\right)\end{aligned} \tag{6.12}$$

By subtracting (6.10) from (6.12), the effect dh of roll and pitch errors $d\alpha_x$ and $d\alpha_y$ on the ground point height is obtained (using $d\alpha_i \cdot d\beta_i \simeq 0$ and $d\alpha_i \cdot b_i^B \simeq 0$):

$$dh \;=\; r\; \left(d\alpha_x\; \sin\alpha_x\; \cos\alpha_y \;+\; d\alpha_y\; \cos\alpha_x\; \sin\alpha_y\right) \tag{6.13}$$

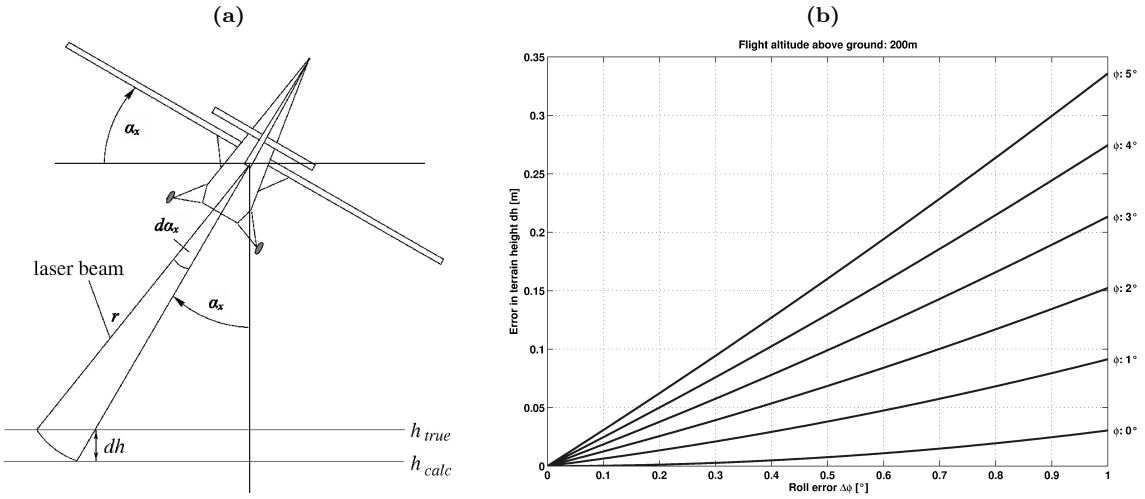

Figure 6.2: **(a)** Impact dh of roll error $d\alpha_x$ on ground point height (Graph by E. Favey). **(b)** Height error dh from (6.14) as a function of roll error $d\alpha_x$, for roll angles α_x from 0°-5° and a laser range r ($\simeq$ flight height above ground) of 200 m.

Thus, the impact dh of roll and pitch attitude errors $d\alpha_x$ and $d\alpha_y$ on ground point heights depends on the range r and on the roll and pitch angles α_x and α_y. Considering e.g. only the roll angle ($\alpha_y = 0$, $d\alpha_y = 0$), an intuitive formula for the height error dh is obtained from (6.13) (Fig. 6.2):

$$dh \;=\; r\; d\alpha_x\; \sin\alpha_x \;=\; r\; [\; \cos\alpha_x \;-\; \cos\left(\alpha_x + d\alpha_x\right)\;] \tag{6.14}$$

In airborne altimetry, for a laser range $r = 200$ m, a roll angle $\alpha_x = 3°$ and a roll error $d\alpha_x = 0.2°$, (6.14) yields a height error $dh = 4$ cm. In shipborne altimetry, the impact of erroneous roll/pitch angles on height determination is significantly reduced as compared to airborne applications, due to the smaller range between the distance sensor and the sea surface. For the same roll angle $\alpha_x = 3°$, the same roll error $d\alpha_x = 0.2°$ and a range $r = 3$ m, (6.14) yields a height error $dh < 1$ mm.

6.2.4 Required Attitude Accuracy

Using (6.13), the required attitude accuracy $d\alpha_m$ for roll or pitch angles can be computed as a function of the range r, the maximum roll/pitch angle α_m during the survey and the desired height accuracy dh_m. The largest impact on ground point heights occurs when $\alpha_x = \alpha_y = \alpha_m$ and $d\alpha_x = d\alpha_y = d\alpha_m$, yielding the following expression for the required attitude accuracy:

$$d\alpha_m \;=\; \frac{dh_m}{2\; r\; \sin\alpha_m\; \cos\alpha_m} \tag{6.15}$$

In the airborne altimetry application, the flight height r above ground (sea) is 200 m, and the roll and pitch angles α_m on a flight line are below 3°. The desired height accuracy dh_m is 4 cm, corresponding to the maximum vertical accuracy achievable by kinematic differential GPS positioning, used for the determination of the absolute altitude of the aircraft. Under the above conditions, the required accuracy $d\alpha_m$ for roll and pitch angles using (6.15) is 0.11°. In shipborne altimetry applications, the required accuracy for roll and pitch angles is lower than in airborne altimetry, due to the smaller range between the distance sensor and the sea surface. For a range $r = 3$ m, maximum roll and pitch angles $\alpha_m = 10°$ and a desired height accuracy $dh_m = 4$ cm, the required accuracy $d\alpha_m$ for the roll and pitch angles using (6.15) is 3.9°.

6.3 Kinematic GPS Positioning

6.3.1 Basic Principle

Airborne and shipborne altimetry, as well as GPS buoy observations, rely on precise kinematic positions determined by GPS. E.g. in airborne laser altimetry, the absolute position of the aircraft has to be known at any moment during a survey flight in order to georeference the laser ground point. Thus, the trajectory of the aircraft has to be tracked with continuous GPS observations aboard the aircraft. These kinematic GPS observations, together with their kinematic processing, a referred to as kinematic GPS positioning or GPS trajectography. GPS trajectography supplies $\boldsymbol{a}^G$ and $\boldsymbol{R}_{G/L}$ of the direct georeferencing equation (6.1). Precise trajectography is one of the major issues in airborne and shipborne altimetry, since positioning errors propagate one-to-one into the ground point positions and directly affect the observed sea surface heights.

High-precision kinematic GPS positioning relies on differential carrier phase observations, achieved by simultaneously operating at least one GPS receiver aboard the moving vehicle (e.g. aircraft or ship) and at least one terrestrial GPS reference station. The coordinates of the reference stations have to be known or determined with respect to the International Terrestrial Reference Frame (ITRF). The trajectory of the roving GPS antenna is computed through kinematic differential GPS carrier phase processing with respect to the reference stations. A sampling rate of at least 1 Hz is usually required on the roving receiver as well as on the reference stations. For high-precision positioning, the resolution of phase ambiguities and cycle slip detection are important issues. The quality of the GPS solutions can be degraded by various factors like tropospheric and ionospheric refraction, radio frequency interference, obstruction of satellite visibility and multi-path effects. Since in airborne and shipborne altimetry, the baselines between the reference stations and the roving receiver can exceed 100 km, the use of dual frequency receivers is mandatory to mitigate ionospheric influences.

The software primarily used in this work to process kinematic GPS data is a software package for baseline-wise differential kinematic GPS processing developed at the GGL (Cocard, 1995). Investigations were made to assess the kinematic potential of Bernese GPS Software (Beutler et al., 2007) and its capabilities to estimate tropospheric path delays in kinematic mode (Section 6.3.3).

6.3.2 Atmospheric Influences

GPS observations are affected by systematic errors due to ionospheric and tropospheric refraction. The ionosphere is a dispersive medium at microwave frequencies, thus the refractive index for GPS signals is frequency-dependent. To the first order, ionospheric refraction is inversely proportional to the square of the frequency of the electromagnetic signal. Based on this property, the effect of ionospheric refraction can be largely mitigated by the use of dual frequency receivers. Ionospheric refraction delays the GPS pseudorange code signal and advances the carrier phase. The effect has the same absolute value for code and phase observations, but with opposite signs. Two kinds of tropospheric biases can be distinguish (Beutler et al., 2007):

- Relative troposphere bias caused by errors of mismodeled tropospheric refraction at one endpoint of a baseline relative to the other endpoint, producing primarily relative height errors.
- Absolute troposphere bias caused by errors of mismodeled tropospheric refraction common to both endpoints of a baseline, producing a scale bias of the estimated baseline length.

In airborne or shipborne altimetry applications involving differential kinematic GPS data, the relative troposphere biases between the reference station and the aircraft or ship is important, due to its direct impact on the computed sea surface heights. To a first order, the station height bias

dh due to a relative troposphere error can be computed as (Beutler et al., 2007):

$$dh = \frac{dr_r}{\cos z_{max}} \tag{6.16}$$

where dr_r is the relative tropospheric zenith delay error and z_{max} is the maximum zenith angle of the observation scenario. In this order of magnitude formula, it is assumed that the satellites are uniformly distributed above the observation site. It indicates that a relative troposphere bias of 1 cm leads to an error of 3 cm in the estimated relative station height for an elevation cutoff angle of 20°. This error increases to 19 cm for an elevation cutoff angle of 3° (Beutler et al., 2007).

Due to the availability of high accuracy orbits from IGS, orbit errors need no longer be considered as an important error source (Beutler et al., 2007). The propagation delay of GPS signals due to atmospheric water vapor in the troposphere are probably the ultimate accuracy-limiting factor for geodetic applications (Beutler et al., 2007; Dodson et al., 1996). At the moment, the major error source in kinematic GPS positioning, and especially in height determination, is the insufficient modeling of the influence of tropospheric path delays. The impact of tropospheric mismodeling on differential kinematic positioning increases with the height difference between the reference station and the roving receiver on the aircraft. An example of the impact of relative troposphere biases on airborne kinematic GPS positioning is shown in Section 6.3.3.

6.3.3 Case Study: Impact of Troposphere on Airborne GPS Solutions

Aircraft trajectories were computed for the six flights of the GAVDOS airborne campaign around Crete (Section 7.1), using three reference stations (TUC1, GALI and RTHY), yielding three baselines with respect to the aircraft. Stations TUC1 and RTHY are situated at the northern coast of Crete, while station GALI is situated at the southern coast. The altitudes of stations TUC1, GALI and RTHY are 178 m, 34 m and 38 m, respectively, while the average flight height of the aircraft during surveys was 215 m. During the processing, only a priori altitude-dependent tropospheric path delay corrections where applied, based on the Saastamoinen tropospheric refraction model together with standard atmosphere values, without any in situ meteorological information. Height differences were computed between the baseline-wise trajectories of the moving antenna aboard the aircraft, obtained using the three reference stations. The height differences range between -0.40 and 0.25 m (Fig. 6.3 to Fig 6.7). The differences depend on both the used reference station and the flight day. Two different behaviours can be distinguished. On the first three days of the campaign (09/01/2003 to 11/01/2003), the aircraft heights obtained with GALI and TUC1 show mean differences of up to -0.26 m and standard deviations of up to 0.20 m (Fig. 6.3a to Fig 6.5a, Tab. 6.1). The aircraft heights obtained with RTHY and TUC1 show mean differences around 0.05 m and standard deviations of up to 0.12 m (Fig. 6.3b to Fig 6.5b, Tab. 6.1). Especially for the differences RTHY-TUC1 on flights GRL03 and GRL05, the distributions of height differences show several peaks, indicating inconsistent ambiguity resolutions on several flight sections. On 12/01/2003, flight operations had to be canceled due to bad weather conditions. As can be seen from the ECMWF atmospheric pressure grids (Appendix F), the first four days are characterized by a large atmospheric depression over the Mediterranean basin, accompanied by strong pressure gradients around Crete and the entire region. These gradients are obviously producing inhomogeneous tropospheric path delays between the reference stations and the moving receiver, strongly deviating from the a priori tropospheric corrections. On the last two days of the campaign (13/01/2003 and 14/01/2003), the differences between GALI and TUC1 and between RTHY and TUC1 are in good agreement, with small mean offsets between -0.04 and 0.03 m and near normal distributions with standard deviations below 0.04 m (Fig. 6.6 and Fig 6.7, Tab. 6.1). These two days are characterized by a high pressure regime and small pressure gradients (Appendix F), indicating a more homogeneous troposphere that is better approximated by the a priori tropospheric corrections.

Table 6.1: Mean aircraft height differences dh and their standard deviation (Std) between trajectory determined with reference stations GALI and TUC1 and with RTHY and TUC1.

Date	Flight	GALI - TUC1 mean dh ± Std [m]	RTHY - TUC1 mean dh ± Std [m]
09/01/2003	GRL02	-0.26 ± 0.05	0.05 ± 0.04
10/01/2003	GRL03	-0.16 ± 0.20	0.03 ± 0.11
11/01/2003	GRL05	-0.21 ± 0.06	0.03 ± 0.12
13/01/2003	GRL01	-0.02 ± 0.04	0.03 ± 0.03
14/01/2003	GRL04	-0.04 ± 0.04	0.00 ± 0.04

The height differences of the aircraft determined with different reference stations correspond in a good approximation to the height differences directly obtained by kinematic processing of the static baselines between these reference stations, since influences on the airborne data are largely canceled out in the difference. Hence, height differences of the aircraft between solutions with different reference stations primarily reflect mismodeled effects between the reference stations. In order to further asses the origin of these height differences, the tropospheric zenith path delays (ZPD) estimated at the reference stations during the static network processing with Bernese GPS software were analysed. The impacts of these ZPD on the baselines between the reference stations are influenced by elevations and azimuths of the considered satellite constellation. The impacts were computed based on (Geiger, 1987), by considering the satellite constellation used in the airborne GPS processing. These impacts correspond to the theoretical influences of the troposphere on the differences of aircraft positions computed with respect to the different reference stations (Fig. 6.8a and Fig. 6.8b, black line). A correlation is observed with respect to the position differences of the aircraft obtained from GPS processing (Fig. 6.8a and Fig. 6.8b, gray line), at least on several sections. On 10/01/2003 (Fig. 6.8a), where inhomogeneous troposheric effects were assumed, the theoretical impact of the estimated ZPD is higher than on 10/01/2003 (Fig. 6.8b), where more homogeneous troposheric effects were assumed. This underlines the fact that the inconsistent GPS solutions on the first three days must be linked to unmodeled tropospheric effects. Jumps on the theoretical impacts (black line) are produced by abrupt changes in the satellite constellation (rise or fall of a satellite). The observed height differences are not always following these jumps, since the GPS solution is influenced and stabilized over longer time periods by the phase ambiguities of constantly tracked satellites. This aspect also explains part of the deviations between the observed differences and the theoretical impacts.

Based on the conclusions stated above, investigations were made to assess the kinematic potential of Bernese GPS Software Version 5 (Beutler et al., 2007) and its capabilities of estimating tropospheric path delays in kinematic mode. The Bernese GPS Software is a very powerful state-of-the-art GPS processing software, widely approved by the geodetic community for static processing of permanent GPS networks. The original source code had to be adapted to the estimation of path delays in kinematic mode. Kinematic positionning solutions of a quality similar to the classic solution with path delays predicted from an a priori model were obtained under homogeneous atmospheric conditions. Under extreme tropospheric conditions, differences between the two solutions could easily reach 0.5 m. The analysis of resulting sea surface height differences at crosspoints (Section 7.4.2) showed that with the estimation of tropospheric parameters, it was possible to locally improve the solution, but the overall agreement was always degraded. The analysis also showed that under such conditions, the Bernese solution including the estimation of tropospheric path delays was extremely sensitive to the parameter settings, like e.g. the interval of the piecewise linear tropospheric parameters and their relative constraints, but also a priori weights of observations and parameters. Small changes of the parameters could induce height differences of 1 m. The instability of the solution leads to the conclusion that the algorithms used to model the troposphere are not sophisticated enough to provide a realistic representation of extreme inhomogeneous atmospheric conditions (e.g. atmospheric inversion) in kinematic mode.

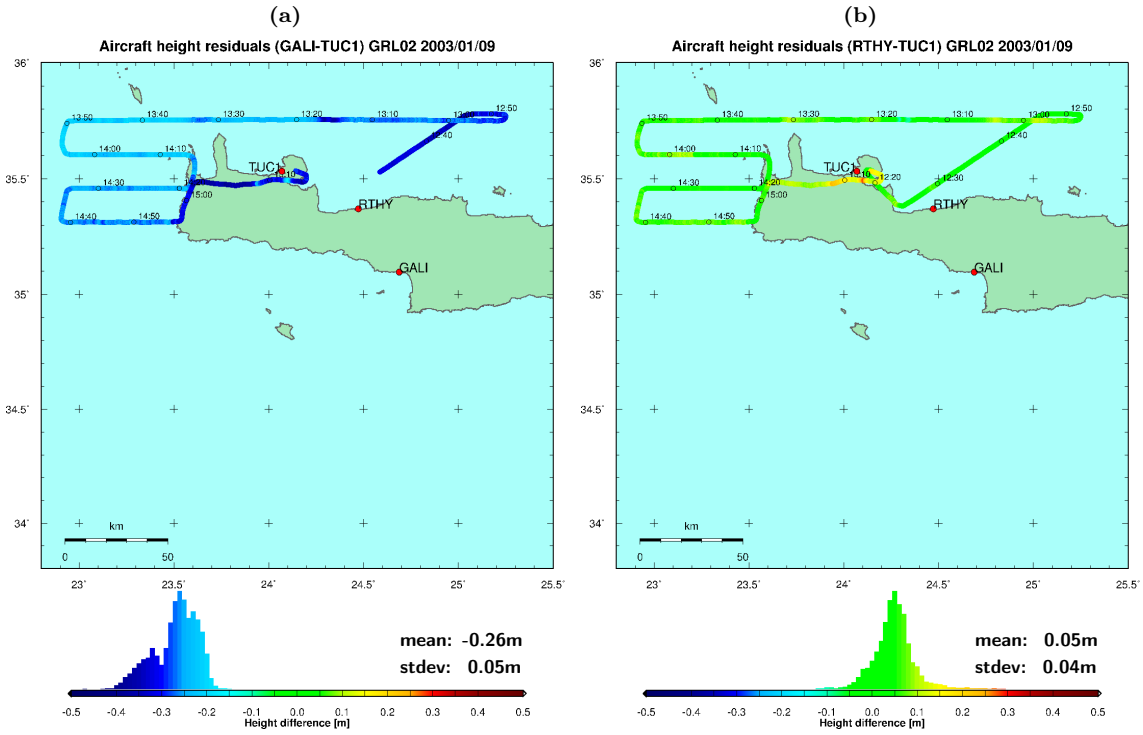

Figure 6.3: Aircraft height differences on 09/01/2003 (flight GRL02) between trajectory determined with reference stations **(a)** GALI and TUC1 and **(b)** RTHY and TUC1.

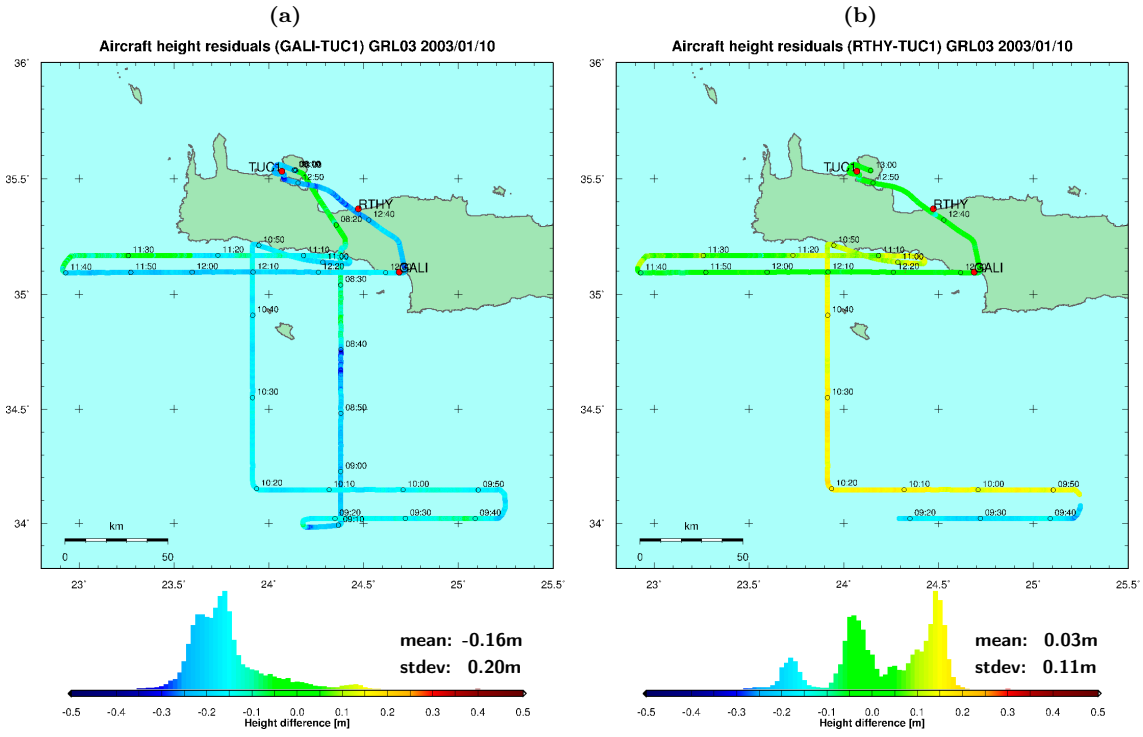

Figure 6.4: Aircraft height differences on 10/01/2003 (flight GRL03) between trajectory determined with reference stations **(a)** GALI and TUC1 and **(b)** RTHY and TUC1.

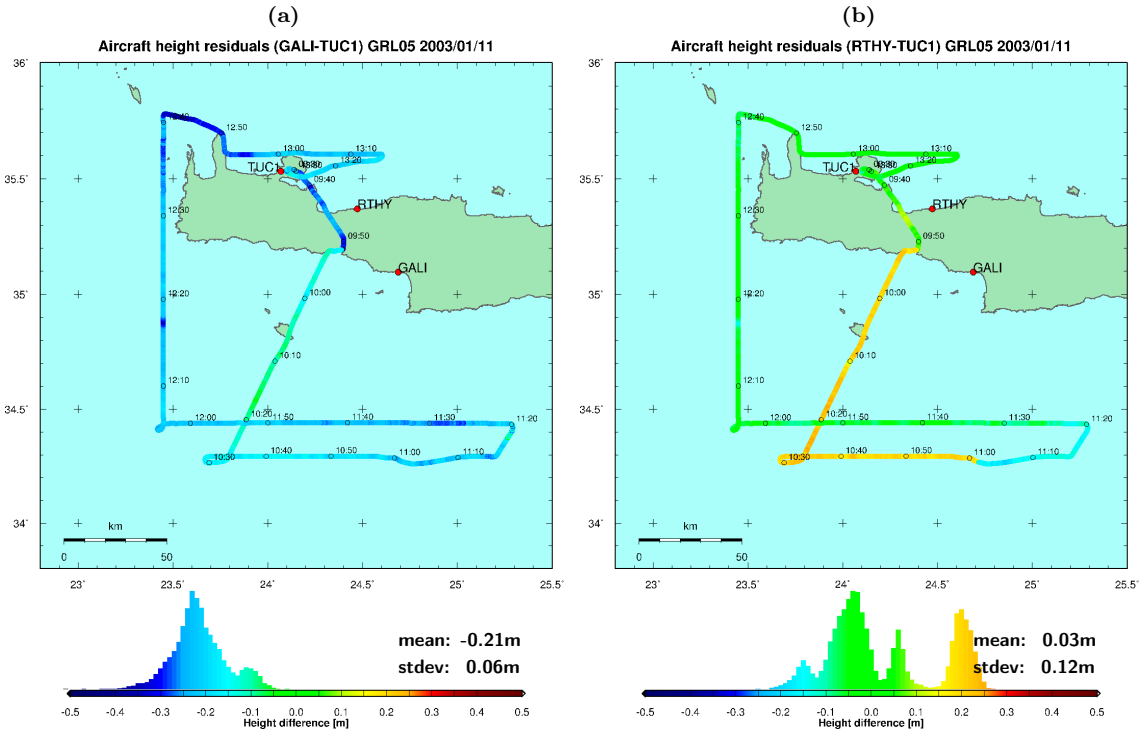

Figure 6.5: Aircraft height differences on 11/01/2003 (flight GRL05) between trajectory determined with reference stations **(a)** GALI and TUC1 and **(b)** RTHY and TUC1.

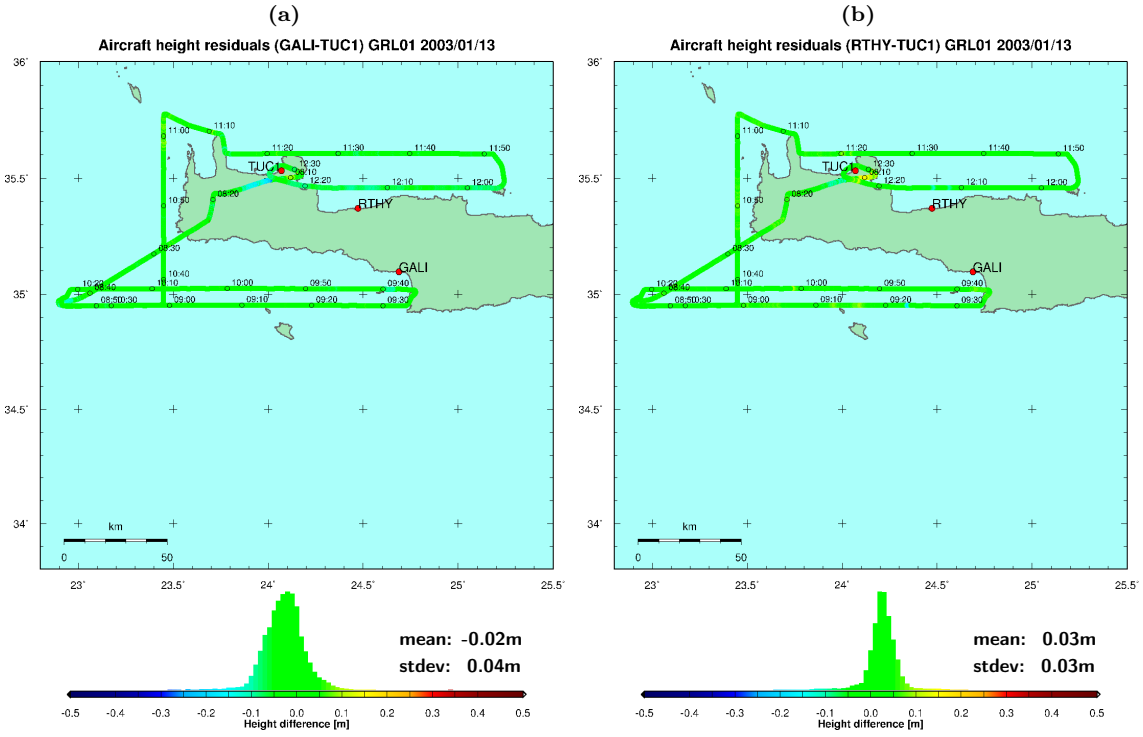

Figure 6.6: Aircraft height differences on 13/01/2003 (flight GRL01) between trajectory determined with reference stations **(a)** GALI and TUC1 and **(b)** RTHY and TUC1.

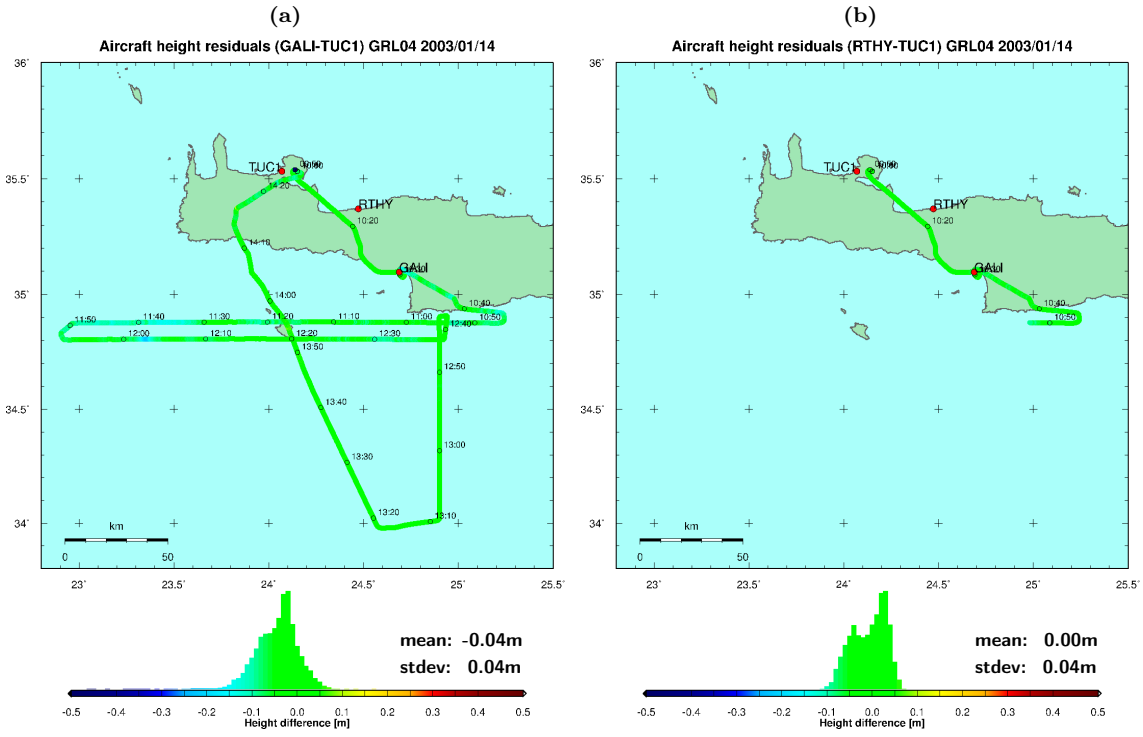

Figure 6.7: Aircraft height differences on 14/01/2003 (flight GRL04) between trajectory determined with reference stations **(a)** GALI and TUC1 and **(b)** RTHY and TUC1.

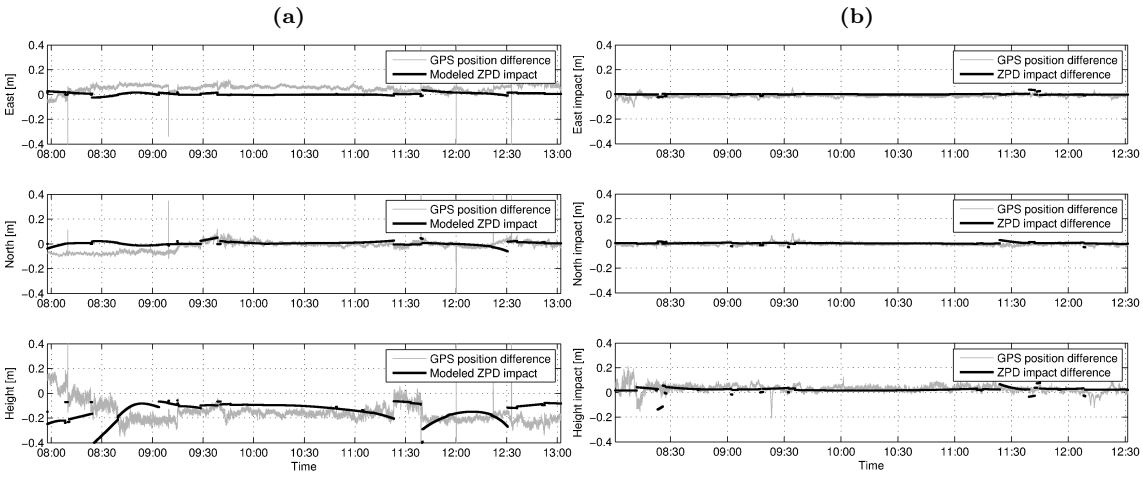

Figure 6.8: **(a)** Aircraft position differences on 10/01/2003 (flight GRL03) between trajectory determined with reference stations GALI and TUC1 (corresponding to Fig. 6.4a), and modeled theoretical impact of tropospheric zenith path delays estimated at the reference stations. **(b)** Same as (a), for 13/01/2003 (flight GRL01) with reference stations RTHY and TUC1 (corresponding to Fig. 6.6b)

6.4 Multi-Antenna GPS Attitude Determination

6.4.1 Basic Principle

The attitude of an aircraft or any other vehicle or platform is given by its roll, pitch and yaw angles, which constitute the rotation matrix $\boldsymbol{R}_{L/B}$ of (6.1) and (6.4). Whereas the classic technique to acquire the attitude of a platform relies on inertial measuring units (IMU), another approach for attitude determination is based on a multiple-antenna GPS array. Since three points on a platform completely determine its orientation, the relative positions of at least three points on the platform need to be continuously monitored in order to derive its attitude. This is achieved by equipping the platform with at least three GPS antennas, adequately mounted on the platform's topside, so that they form non-collinear baseline vectors between each other. The approach of attitude determination by multi-antenna GPS described in this section is based on (Favey, 2001).

The moving vectors of the antenna array are first rotated from the geocentric GPS reference frame to a topocentric, north oriented frame, using the latitudes and longitudes of the moving reference antenna (6.3). As the antennas are rigidly mounted on the aircraft, their coordinates are also known in the body frame by terrestrial calibration measurements. Thus, the core problem of attitude determination using a multi-antenna array can be formulated as follows (Favey, 2001): Given two or more non-collinear vectors in the topocentric coordinate frame L and in the body frame B, find the rotation matrix $\boldsymbol{R}_{L/B}$ (6.4) that transforms the vectors from the body frame into the topocentric frame (Fig. 6.9).

Acquiring attitude information from GPS or IMU shows properties individual to each method (Favey, 2001). As the GPS attitude solution is computed on a per epoch basis, independently from subsequent epochs (except the link through GPS carrier phase ambiguities), the major advantage of the GPS attitude is that it is exempt from random walk (drift) effects. Regarding the IMU attitude, epochs are correlated and can suffer from drift effects, that have to be corrected by e.g. coupling a GPS receiver to the IMU. The major advantage of IMU is its higher sampling rate. Comparisons between GPS and IMU attitudes are shown in Section 6.4.5 and Section 6.4.6.

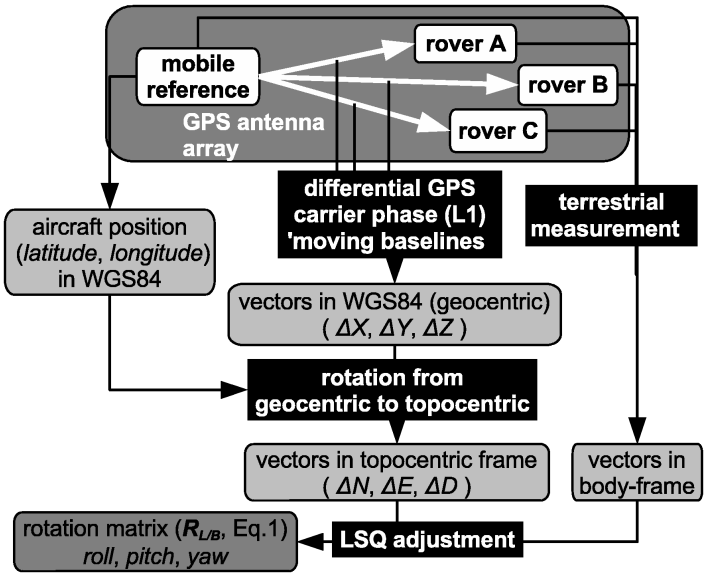

Figure 6.9: Attitude determination with multi-antenna GPS array.

6.4.2 Processing of Moving GPS Baselines

The relative positions of the GPS antennas used to compute the vectors for attitude determination are obtained by so-called moving baseline processing (Fig. 6.9). Like in conventional differential kinematic GPS processing, moving baseline processing is based on differential GPS carrier phase processing, with the only difference that both receivers forming a baseline are moving. During processing, one receivers is defined as reference. The coordinates of its antenna are fixed to an approximate kinematic position (e.g. stande-alone code solution), since only the relative vector is of interest. The reference receiver is used to compute the relative positions of the other antennas by differential GPS carrier phase processing. Since the lengths of the baseline is usually below 10 m, relative atmospheric path delay errors between the reference and remote receivers are negligible and ambiguity resolution usually causes no major problems, unless interferences or lack of satellite visibility are encountered. Since the lengths of the vector is theoretically constant and known by terrestrial measurements, it may be introduced in the GPS baseline processing as additional information. Especially in highly dynamic applications, the obtained GPS vectors must be corrected for differential clock biases (Appendix E) before the attitude computation (Section 6.4.3). The approach of moving baseline processing used in this project is based on (Favey, 2001).

6.4.3 Algorithm for Multi-Antenna GPS Attitude Determination

Considering the vector $\boldsymbol{k}_i^L$ between two GPS antennas in the topocentric frame L, obtained from moving baseline processing (Section 6.4.2), and the corresponding vector $\boldsymbol{k}_i^B$ determined by terrestrial calibration measurements in the body frame B, the basic equation for attitude determination can be written as (Favey, 2001):

$$\boldsymbol{k}_i^L \;=\; \boldsymbol{R}_{L/B}\;\boldsymbol{k}_i^B \tag{6.17}$$

where $\boldsymbol{R}_{L/B}$ is the rotation matrix from the body frame B to the topocentric frame L. The attitude angles roll (α_x), pitch (α_y) and yaw (α_z) are derived directly from the elements r_{ij} of the rotation matrix $\boldsymbol{R}_{L/B}$ (6.4):

$$\alpha_x \;=\; \arctan\left(r_{32}/r_{33}\right), \quad \alpha_y \;=\; \arcsin\left(r_{31}\right), \quad \alpha_z \;=\; \arctan\left(r_{21}/r_{11}\right) \tag{6.18}$$

An approximate attitude solution can be computed using two vectors (three GPS antennas). The approximate solution for the rotation matrix in (6.17) is obtained by:

$$\boldsymbol{R}_{L/B} \;\approx\; \boldsymbol{L}\boldsymbol{B}^T \;=\; \boldsymbol{R}_0 \tag{6.19}$$

where $\boldsymbol{R}_0$ is the approximate rotation matrix, and $\boldsymbol{L}$ and $\boldsymbol{B}$ are rotation matrices given by:

$$\boldsymbol{L} \;=\; \left(\boldsymbol{i}_1^L,\; \boldsymbol{i}_2^L,\; \boldsymbol{i}_3^L\right), \quad \boldsymbol{B} \;=\; \left(\boldsymbol{i}_1^B,\; \boldsymbol{i}_2^B,\; \boldsymbol{i}_3^B\right) \tag{6.20}$$

with

$$\boldsymbol{i}_1^L = \frac{\boldsymbol{k}_1^L}{\left\|\boldsymbol{k}_1^L\right\|}, \quad \boldsymbol{i}_2^L = \boldsymbol{i}_3^L \times \boldsymbol{i}_1^L, \quad \boldsymbol{i}_3^L = \frac{\boldsymbol{k}_1^L \times \boldsymbol{k}_2^L}{\left\|\boldsymbol{k}_1^L \times \boldsymbol{k}_2^L\right\|} \tag{6.21}$$

$$\boldsymbol{i}_1^B = \frac{\boldsymbol{k}_1^B}{\left\|\boldsymbol{k}_1^B\right\|}, \quad \boldsymbol{i}_2^B = \boldsymbol{i}_3^B \times \boldsymbol{i}_1^B, \quad \boldsymbol{i}_3^B = \frac{\boldsymbol{k}_1^B \times \boldsymbol{k}_2^B}{\left\|\boldsymbol{k}_1^B \times \boldsymbol{k}_2^B\right\|} \tag{6.22}$$

If more than two vectors (more than three antennas) are available, an optimal solution can be estimated by least-squares (LSQ) adjustment. Based on (6.17), an observation equation can be written for each vector $\boldsymbol{k}_i$ and each epoch (Favey, 2001):

$$\boldsymbol{k}_i^L \; - \; \boldsymbol{v}_i \; = \; \boldsymbol{R}_{L/B} \; \boldsymbol{k}_i^B \tag{6.23}$$

which is of the general form $\boldsymbol{l} - \boldsymbol{v} = F(\boldsymbol{x})$. In (6.23), the vectors $\boldsymbol{k}_i^L$ in the topocentric frame, derived from GPS moving baseline processing, are considered as the observations l, with residuals $\boldsymbol{v}$. The unknown parameters $\boldsymbol{x}$ are the attitude angles forming the rotation matrix $\boldsymbol{R}_{L/B}$ (6.4). The vectors $\boldsymbol{k}_i^B$ in the body frame, determined by terrestrial calibration measurements, are considered as error-free. Linearization of (6.23) near the approximate values yields:

$$\boldsymbol{k}_i^L \; - \; \boldsymbol{v}_i \; = \; \boldsymbol{R}_0 \; \boldsymbol{k}_i^B \; + \; \boldsymbol{A}_i \; \delta\boldsymbol{x} \tag{6.24}$$

which is of the general form:

$$\boldsymbol{l} \; - \; \boldsymbol{v} \; = \; F(\boldsymbol{x}_0) \; + \; \left| \frac{\partial F(\boldsymbol{x})}{\partial \boldsymbol{x}} \right|_{\boldsymbol{x}_0} (\boldsymbol{x} - \boldsymbol{x}_0) \; = \; F(\boldsymbol{x}_0) \; + \; \boldsymbol{A} \; \delta\boldsymbol{x} \tag{6.25}$$

where $\boldsymbol{x}_0$ are the approximate attitude angles from (6.19), $\delta\boldsymbol{x} = (\boldsymbol{x} - \boldsymbol{x}_0)$ are the increments of the parameters, $\boldsymbol{R}_0 = \boldsymbol{R}_{L/B}(\boldsymbol{x}_0)$ is the approximate rotation matrix calculated from two vectors (6.19) and $\boldsymbol{A}_i$ is the design matrix of the LSQ adjustment, with:

$$\boldsymbol{A}_i \; = \; \left| \frac{\partial F_i}{\partial \boldsymbol{x}} \right|_{\boldsymbol{x}_0} = \; \left| \frac{\partial (\boldsymbol{R}_{L/B} \; \boldsymbol{k}_i^B)}{\partial \boldsymbol{x}} \right|_{\boldsymbol{x}_0} \approx \; \left| \frac{\partial \boldsymbol{R}_0 \; \boldsymbol{k}_i^B \; + \; \boldsymbol{R}_0 \; \boldsymbol{K}_i^B \; \delta\boldsymbol{x}}{\partial \boldsymbol{x}} \right|_{\boldsymbol{x}_0} = \; \boldsymbol{R}_0 \; \boldsymbol{K}_i^B \tag{6.26}$$

In (6.26), only the rotation matrix $\boldsymbol{R}_{L/B}$ is a function of $\boldsymbol{x}$. Thus, the expression to be differentiated in (6.26) was linearized using:

$$\boldsymbol{R}_{L/B} \; \boldsymbol{k}_i^B = \; \boldsymbol{R}(\boldsymbol{x}_0 + \delta\boldsymbol{x}) \; \boldsymbol{k}_i^B \; = \; \boldsymbol{R}_0 \; \boldsymbol{R}(\delta\boldsymbol{x}) \; \boldsymbol{k}_i^B \approx \; \boldsymbol{R}_0 \; (\boldsymbol{I} + \boldsymbol{\Omega}) \; \boldsymbol{k}_i^B \; = \; \boldsymbol{R}_0 \; \boldsymbol{k}_i^B + \boldsymbol{R}_0 \; \boldsymbol{K}_i^B \; \delta\boldsymbol{x} \tag{6.27}$$

with

$$\boldsymbol{\Omega} \; \boldsymbol{k}_i^B \; = \; \begin{pmatrix} 0 & \delta x_3 & -\delta x_2 \\ -\delta x_3 & 0 & \delta x_1 \\ \delta x_2 & -\delta x_1 & 0 \end{pmatrix} \begin{pmatrix} k_{i,1}^B \\ k_{i,2}^B \\ k_{i,3}^B \end{pmatrix} \; = \; \begin{pmatrix} 0 & -k_{i,3}^B & k_{i,2}^B \\ k_{i,3}^B & 0 & -k_{i,1}^B \\ -k_{i,2}^B & k_{i,1}^B & 0 \end{pmatrix} \begin{pmatrix} \delta x_1 \\ \delta x_2 \\ \delta x_3 \end{pmatrix} \; = \; \boldsymbol{K}_i^B \; \delta\boldsymbol{x} \tag{6.28}$$

where $\boldsymbol{K}_i^B$ is a skew symmetric matrix containing the elements of $\boldsymbol{k}_i^B$. The solution of the LSQ adjustment for one epoch is finally given by (Favey, 2001):

$$\delta\boldsymbol{x} \; = \; \left(\sum_i \; \boldsymbol{A}_i^T \; \boldsymbol{P}_i \; \boldsymbol{A}_i \right)^{-1} \cdot \sum_i \; \boldsymbol{A}_i^T \; \boldsymbol{P}_i \; \boldsymbol{v}_{0,i} \tag{6.29}$$

where $\boldsymbol{P}_i$ is the weight matrix and $\boldsymbol{v}_{0,i}$ are the approximate residuals obtained by:

$$\boldsymbol{v}_{0,i} \; = \; \boldsymbol{l}_i \; - \; F_i\,(\boldsymbol{x}_0) \; = \; \boldsymbol{k}_i^L \; - \; \boldsymbol{R}_0 \; \boldsymbol{k}_i^B \tag{6.30}$$

Since the observation equation (6.23) is nonlinear, the LSQ adjustment needs to be iterated a few times with $\boldsymbol{R}_0$ improved as $\boldsymbol{R}_{L/B}(\boldsymbol{x}_0 + \delta\boldsymbol{x})$ (Favey, 2001).

6.4.4 Accuracy of Multi-Antenna GPS Attitude Determination

Since the attitude of a platform determined with a multi-antenna GPS array is computed using GPS baseline vectors, its accuracy σ_a depends on the differential GPS positioning error σ_r, the baseline length l and the antenna vector geometry (Fig. 6.10):

$$\sigma_a = \frac{\sigma_r}{l} \quad [\text{rad}] \tag{6.31}$$

The geometrical configuration is optimal in the sense of minimizing attitude errors when the antennas are forming orthogonal vectors, which is not always possible to realize on an aircraft or a boat. Another strategy to reduce the attitude error σ_a consists in increasing the baseline lengths l. For example, in order to reach an attitude accuracy σ_a of 0.01° with a vector accuracy σ_r of 1 cm, a baseline length l of 57 m is required.

The attitude accuracy cannot be measured directly, but it can be quantified by different methods (Tab. 6.2). First, the accuracy can be assessed using (6.31). In the airborne application, two antennas were mounted on the wing engines (Fig. 4.1), in order to reach the best compromise between wing flexure effects and baseline length. Maximizing baseline lengths by mounting the antennas on the wing tips would reduce the accuracy, since the wing flexure at the tips can exceed 10 cm. The distance between the engine antennas, relevant for the roll angle, was 5.5 m, whereas the baseline length between the front and tail antennas, relevant for the pitch and yaw angles, was 10.0 m. The RMS of the difference between the baseline lengths obtained by GPS and the terrestrially calibrated lengths is in the order of 0.9 cm, yielding a theoretical attitude accuracy of 0.08° for the roll and 0.05° for the pitch and yaw (Tab. 6.2), based on (6.31). The average attitude standard deviations estimated by the LSQ adjustment during attitude determination are in the same order of magnitude. Finally, the standard deviation of the differences between attitudes determined with GPS and INS are in the order of 0.11° for the roll and pitch, and 0.06° for the yaw. The differences between GPS and INS attitudes are analysed in more detail in Section 6.4.5. It can be concluded that the obtained attitude accuracies are in the order of 0.10° and that they meet the required accuracy value of 0.11° established in Section 6.2.4.

Similar to the airborne case, the attitude accuracy of the shipborne antenna setup was quantified by different methods (Tab. 6.2). The baseline length between the portside and starboard antennas, relevant for the roll angle, was 2.7 m, whereas the baseline length between the bow and stern antennas, relevant for the pitch and yaw angle, was 12.5 m (Fig. 5.3). The RMS of the difference between the baseline lengths determined by GPS and the terrestrially calibrated lengths is 0.9 cm,

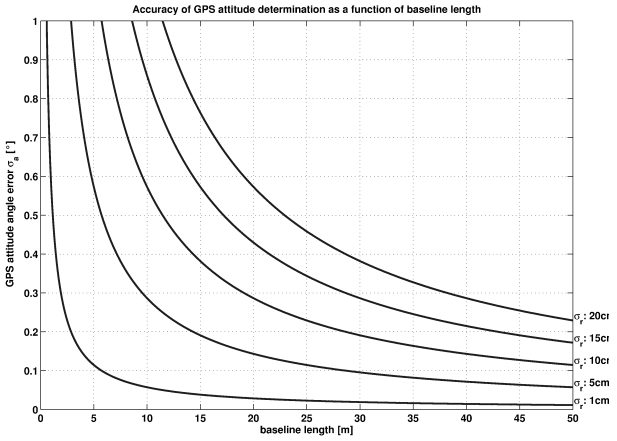

Figure 6.10: Error σ_a of attitude determined by multi-antenna GPS array, according to (6.31), as a function of baseline length l, for differential GPS positioning errors σ_r from 1 to 20 cm.

Table 6.2: Estimated accuracy of attitude from multi-antenna GPS array, for the airborne and shipborne setups. The airborne data correspond to averages over all flights of the GAVDOS campaign (Fig. 7.1). The shipborne data correspond to averages over 18 survey tracks of the 2007 campaign (Fig. 8.1).

	Roll		Pitch		Yaw	
	airborne	shipborne	airborne	shipborne	airborne	shipborne
Relevant baseline length [m]	5.5	2.7	10.0	12.5	10.0	12.5
Baseline RMS [m][1]	0.008	0.009	0.009	0.009	0.009	0.009
Theor. attitude Std [°][2]	0.08	0.19	0.05	0.04	0.05	0.04
GPS LSQ Std [°][3]	0.14	0.31	0.05	0.08	0.06	0.08
GPS-INS Std [°][4]	0.11	0.32	0.11	0.22	0.08	0.38

[1] Average RMS of differences between baseline lengths determined by GPS and by terrestrial calibration
[2] Average attitude standard deviation (Std) from (6.31) using baseline RMS and relevant baseline length
[3] Average attitude standard deviation (Std) estimated during vector LSQ adjustment
[4] Average standard deviation (Std) of differences between GPS and INS attitude

yielding a theoretical attitude accuracy of 0.19° for the roll and 0.04° for the pitch and yaw, based on (6.31). The obtained attitude accuracies from LSQ adjustment are about twice the theoretical values (Tab. 6.2). This is most likely due to inaccurate because hard to measure bodyframe coordinates on the boat. Nevertheless, it can be concluded that the obtained attitude accuracies are far below the required value of 3.9° established in Section 6.2.4. The differences between GPS and INS attitudes are discussed in Section 6.4.6.

6.4.5 Case Study: Airborne Multi-Antenna GPS vs. Tactical-Grade INS

Two independent systems for attitude determination were operated aboard the aircraft: a multi-antenna GPS array (Section 4.2.4, Fig. 4.1) and a Honeywell H-764G tactical-grade inertial navigation system (INS), coupled with GPS (Section 4.2.5, Fig. 4.2a). The simultaneous operation of the two systems allows to directly compare their performance (Fig. 6.11). Significant offsets between the GPS and INS attiude solutions are observed, persisting throughout the campaign (Tab. 6.3). The mean offsets are 0.50°, -0.91° and -0.42° on the roll, pitch and yaw, respectively. These offsets are similar to those observed by (Favey, 2001) using the same GPS antenna array on the same aircraft, but a different inertial system. The offsets reveal a misalignment between the body frames defined by the GPS antennas and the INS. The coordinates of the GPS antennas with respect to the aircraft body frame were determined using a terrestrial tachymeter setup (Favey, 2001). For this purpose, the aircraft was jacked up and leveled out in the hangar. Precise antenna coordinates in the aircraft body frame were obtained, with a standard deviation below 1 mm. If the offsets in Tab. 6.3 were produced by wrong coordinates of the GPS antennas in the aircraft body frame, the offset of 0.50° on the roll would correspond to a vertical error of 4.8 cm on the 5.5 m baseline between the wing antennas, and the offset of -0.91° on the pitch would correspond to a vertical error of 15.9 cm on the 10.0 m baseline between the front and tail antennas. Since such large errors on the terrestrial observations can be excluded, the offsets must be produced by a misalignment between the INS and the aircraft body frames. Since the INS unit and the laser profiler were mounted on the same rigid platform (Fig. 4.2a), it can be assumed that the body frame defined by the INS is more consistent with the frame of the laser device than the body frame defined by the GPS antenna array. This assumption was confirmed during the boresight misalignment calibration, where smaller misalignments are obtained between the laser frame and INS body frame (Tab. 6.6 and Tab. 6.7). Apart from the offsets, a good agreement is observed between the attitude solutions provided by the two independent systems, with mean standard deviations of 0.11° on the roll and pitch, and 0.08° on the yaw (Tab. 6.3). The standard deviations are of the same order of magnitude as the expected accuracy of the multi-antenna GPS attitude determination (Tab. 6.2). Furthermore, no noticeable drift effect on the INS attitudes is detected.

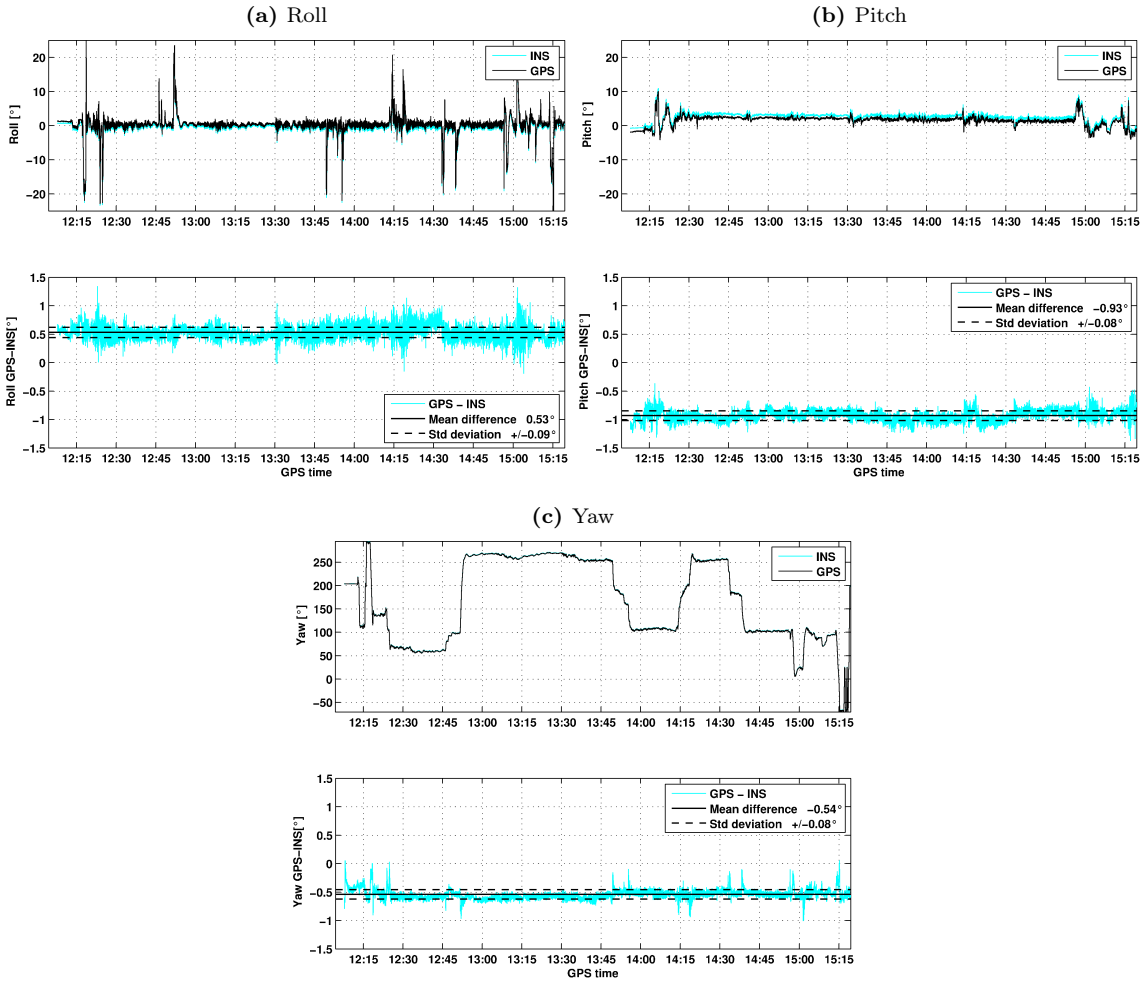

Figure 6.11: Attitude angles from the Honeywell H-764G tactical-grade INS and the multi-antenna GPS array, and their differences, during survey flight GRL02.

Table 6.3: Mean differences and standard deviations (Std) between airborne attitude angles from multi-antenna GPS array and Honeywell H764G tactical-grade INS.

Date	Flight	Roll GPS-INS Mean ± Std [°]	Pitch GPS-INS Mean ± Std [°]	Yaw GPS-INS Mean ± Std [°]
09/01/2003	GRL06	0.50 ± 0.09	-0.88 ± 0.12	-0.50 ± 0.07
09/01/2003	GRL02	0.53 ± 0.09	-0.93 ± 0.08	-0.54 ± 0.08
10/01/2003	GRL03	0.53 ± 0.12	-0.92 ± 0.13	-0.32 ± 0.07
11/01/2003	GRL05	0.50 ± 0.12	-0.92 ± 0.11	-0.35 ± 0.09
13/01/2003	GRL01	0.45 ± 0.15	-0.89 ± 0.10	-0.34 ± 0.07
14/01/2003	GRL04	0.38 ± 0.25*	-0.90 ± 0.09	-0.49 ± 0.10
	Mean	**0.50 ± 0.11**	**-0.91 ± 0.11**	**-0.42 ± 0.08**

* GPS attitude computed without left wing antenna due to receiver failure, yielding poor roll angle determination. This roll information was excluded from mean computation.

6.4.6 Case Study: Shipborne Multi-Antenna GPS vs. MEMS-Based AHRS

Two independent systems for attitude determination were operated aboard the boat during the 2007 campaign: a multi-antenna GPS array (Section 5.2.3, Fig. 5.3) and an Xsens MTi miniature MEMS-based AHRS (Attitude and Heading Reference System) (Section 5.2.4, Fig. 5.4). The simultaneous operation of the two independent systems allowed to directly compare their performance under the given conditions (Tab. 6.4 and Fig. 6.13). The differences between the attitudes determined by the two systems revealed no noticeable drift effects on the AHRS, demonstrating the efficiency of the stabilization of the gyro data with the magnetometer and accelerometer data in the Xsens sensor fusion algorithm. Due to the good agreement between the multi-antenna GPS system and the Honeywell H-764G tactical-grade INS in the airborne application (Section 6.4.5), the GPS derived attitude can be considered as reference solution for the AHRS.

Significant offsets between the GPS and AHRS attitude solutions were observed, persisting throughout the campaign (Tab. 6.4). The mean offsets are -2.67° and -4.83° on the roll and pitch. These offsets are produced by the approximate mechanical alignement of the AHRS with respect to the boat axes and the horizontal plane. They are in accordance with roll an pitch misalignments approximately measured with a clinometer with respect to the horizontal plane. Apart from the offsets, a good agreement between the attitude solutions provided by the two independent systems was observed, with mean standard deviations of 0.32° on the roll and 0.22° on the pitch (Tab. 6.4). The standard deviation on the roll is significantly larger than the one on the pitch, and it is very similar to the standard deviation of 0.31° of the roll estimation with the multi-antenna GPS system (Tab. 6.2). As opposed to the multi-antenna GPS system, the AHRS produces the same accuracy for the roll and pitch. Hence, the roll agreement between the GPS system and the AHRS is limited by the weak roll determination of the GPS system, due to the short distance between the starboard and portside antennas. On the other hand, the standard deviation of 0.22° on the pitch differences is significantly larger than the standard deviation of 0.08° of the pitch estimation with the multi-antenna GPS system (Tab. 6.2). Considering the strong pitch estimation by the GPS system, due to the long distance between the bow and stern antennas, the pitch agreement between the GPS system and the AHRS is limited by the accuracy of the AHRS.

Since the yaw (heading) determination of the AHRS mainly relies on 3D magnetometer data, it suffers from disturbances of the Earth magnetic field. In shipborne applications, the disturbances are mainly produced by the magnetic field caused by the structure and machinery of the ship. The deviation or heading error $\Delta\omega$ of a magnetic compass can be modeled by (NGA, 2004):

$$\Delta\omega = A + B\sin\omega + C\cos\omega + D\sin 2\omega + E\cos 2\omega \tag{6.32}$$

where ω is the heading angle. Coefficient A accounts for a permanent offset, while B and C account for effects produced by the hard-iron parts of the ship's structure. Hard iron behaves like a permanent magnet and retains its polarity as the ship rotates (Kayton and Fried, 1997), causing a magnetic disturbance with a period of 360°. Electrical equipment, motors and wiring aboard the ship produce fixed magnetic fields that rotate with the ship and hence have the same effect as hard iron (Kayton and Fried, 1997). However, the magnetic field depends on the power-on status of the electrical equipment. Coefficients D and E account for effects produced by the soft-iron parts of the ship's structure, made of highly permeable magnetic material. Soft iron is magnetized by the Earth by induction. As the ship rotates, soft iron remains polarized so that its north-facing poles always face the north pole (Kayton and Fried, 1997), causing a magnetic disturbance with a period of 180°.

Depending on the calibration method, 4 types of AHRS yaw angles are given in Tab. 6.4:

1. Uncalibrated AHRS yaw. The yaw deviation of the AHRS depends on the yaw angle itself, yielding variable mean offsets with respect to the GPS yaw, irregular distributions of the differences (Fig. 6.13c) and consequently a high mean standard deviation of 1.62°.

Table 6.4: Mean differences and standard deviations (Std) between shipborne attitude angles from multi-antenna GPS array and Xsens MTi miniature AHRS.

Date		Roll GPS-AHRS Mean ± Std [°]	Pitch GPS-AHRS Mean ± Std [°]	Yaw GPS-AHRS * Mean ± Std [°]	Yaw GPS-AHRS * Mean ± Std [°]
08/09/2007	moving	-2.61 ± 0.28	-4.97 ± 0.20	6.16 ± 1.02[1]	4.61 ± 0.46[2]
08/09/2007	static	-2.60 ± 0.37	-4.85 ± 0.16	1.86 ± 0.33[1]	4.73 ± 0.33[2]
08/09/2007	static	-2.69 ± 0.32	-4.81 ± 0.16	1.92 ± 0.32[1]	4.78 ± 0.33[2]
09/09/2007	moving	-2.58 ± 0.49	-4.89 ± 0.27	4.63 ± 2.29[1]	4.44 ± 0.47[2]
09/09/2007	static	-2.68 ± 0.21	-4.81 ± 0.14	3.85 ± 2.02[1]	4.79 ± 0.42[2]
09/09/2007	moving	-2.57 ± 0.32	-4.86 ± 0.21	4.30 ± 2.57[1]	4.69 ± 0.42[2]
10/09/2007	static	-2.72 ± 0.23	-4.79 ± 0.14	5.50 ± 2.05[1]	4.79 ± 0.30[2]
10/09/2007	moving	-2.65 ± 0.24	-4.88 ± 0.19	4.74 ± 2.34[1]	4.47 ± 0.39[2]
10/09/2007	static	-2.61 ± 0.22	-4.87 ± 0.12	3.80 ± 1.35[1]	4.82 ± 0.24[2]
11/09/2007	moving	-2.70 ± 0.32	-4.88 ± 0.23	3.75 ± 1.86[1]	4.62 ± 0.41[2]
	Mean			**4.05 ± 1.62**[1]	**4.67 ± 0.38**[2]
15/09/2007	moving	-2.74 ± 0.38	-4.63 ± 0.23	4.83 ± 0.85[3]	5.53 ± 0.64[4]
16/09/2007	moving	-2.64 ± 0.48	-4.95 ± 0.32	4.87 ± 1.27[3]	4.63 ± 0.97[4]
17/09/2007	moving	-2.63 ± 0.31	-4.80 ± 0.18	6.12 ± 0.51[3]	5.53 ± 0.52[4]
18/09/2007	moving	-2.65 ± 0.35	-4.80 ± 0.22	5.37 ± 0.76[3]	4.80 ± 0.67[4]
19/09/2007	moving	-2.90 ± 0.33	-4.80 ± 0.54	4.91 ± 0.88[3]	5.51 ± 0.60[4]
20/09/2007	static	-2.72 ± 0.30	-4.74 ± 0.18	4.98 ± 0.44[3]	5.38 ± 0.41[4]
	Mean	**-2.67 ± 0.32**	**-4.83 ± 0.22**	**5.18 ± 0.79**[3]	**5.23 ± 0.64**[4]

[1] Uncalibrated AHRS yaw anlge.
[2] AHRS yaw anlge calibrated with GPS reference yaw based on (6.32) (Fig. 6.12).
[3] AHRS yaw anlge calibrated by instrumental magnetometer calibration.
[4] AHRS yaw anlge calibrated by instrumental magnetometer calibration and GPS reference yaw.
[*] Yaw offsets include magnetic declination, since yaw angles from GPS and AHRS are referenced to the geographic and the magnetic North, respectively. For the given location and time, a magnetic declination of 3.5° has to be subtracted from the mean values.

2. AHRS yaw calibrated in post-processing with the yaw from GPS, based on (6.32). Using the yaw determined by the multi-antenna GPS system as reference, the heading deviation $\Delta\omega$ between the GPS and AHRS solution can be computed as a function of the yaw angle ω (Fig. 6.12). A heading deviation curve defined by the five coefficients of (6.32) can be estimated using a least-squares adjustment. The calibrated AHRS yaw yields a more constant offset with respect to the yaw from GPS and a normal distribution of the differences (Fig. 6.13d). The calibration allowed to reduce the mean standard deviation to 0.38°.

3. AHRS yaw determined with magnetometers previously calibrated using the Xsens Magnetic Field Mapper software. The calibration is obtained by performing a complete heading rotation of the ship with the sensor mounted in its final position. Since this calibration does not rely on a reference yaw, this case corresponds to the yaw accuracy that can be obtained with the Xsens MTi in stand-alone operation. The mean standard deviation of 0.79° with respect to the GPS solution is less good than the results of type 2. However, a clear improvement with respect to the uncalibrated heading (type 1) is obtained.

4. AHRS yaw determined with calibrated magnetometers (type 3), followed by a post-processing yaw calibration (type 2). The post-processing calibration allowed to reduce the mean standard deviation to 0.64°.

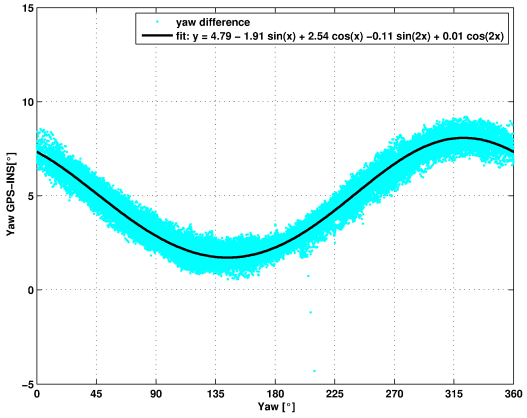

coefficient	value [°]	Std [°]
A	4.786	0.0013
B	-1.908	0.0018
C	2.544	0.0019
D	-0.113	0.0017
E	0.007	0.0018

Figure 6.12: Difference between yaw (heading) from shipborne multi-antenna GPS array and Xsens MTi AHRS (labeled INS) as a function of yaw angle, over a time period of 10 hours. A heading deviation curve of the AHRS was estimated by a least-squares adjustment based on (6.32). The magnetic deviation coefficients and their standard deviation (Std) are shown on the right.

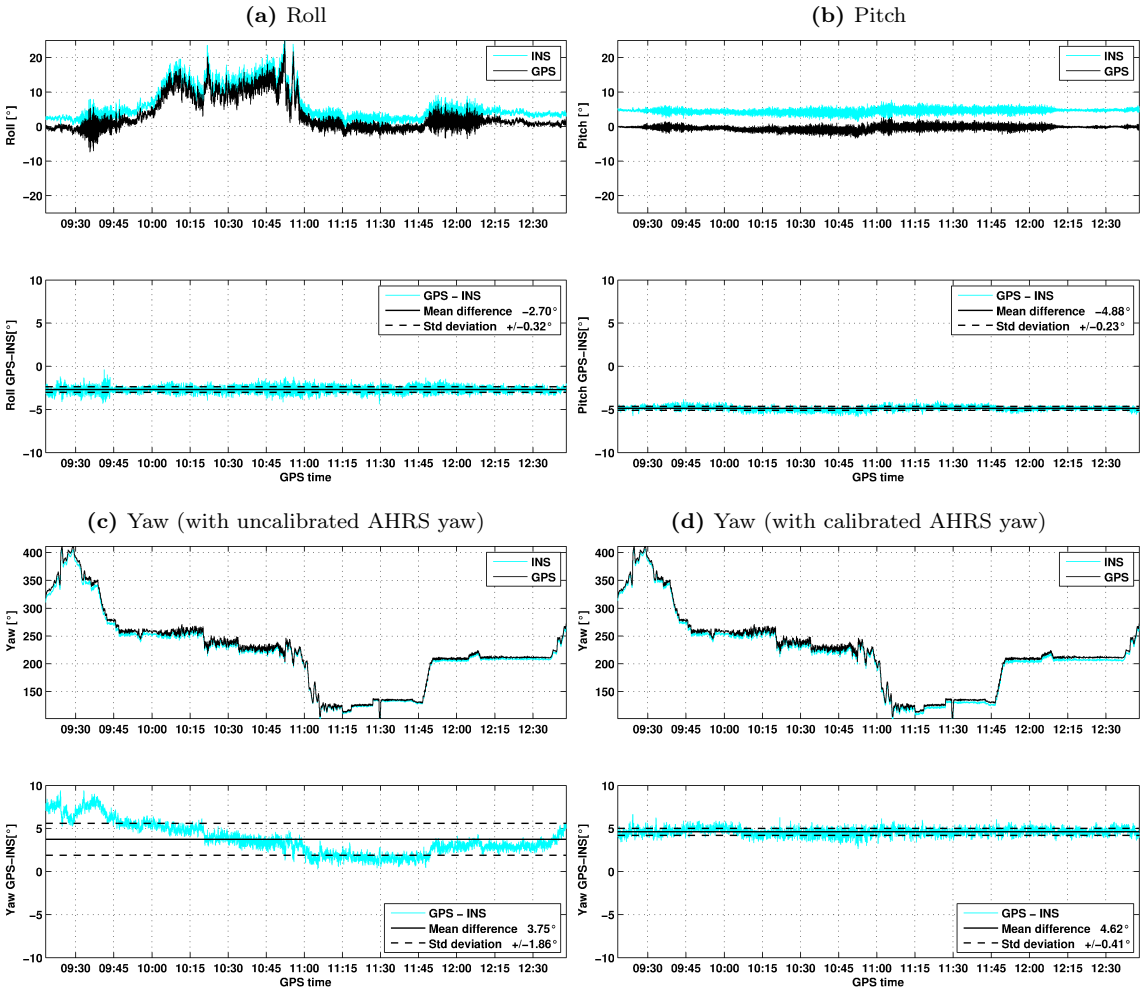

Figure 6.13: Attitude angles from the Xsens MTi miniature AHRS (labeled INS) and the multi-antenna GPS array, and their differences, during a survey track on 11/09/2007.

6.5 Boresight Misalignment Calibration in Airborne Altimetry

6.5.1 Introduction

Critical elements in the direct georeferencing equation (6.1) for airborne laser altimetry are the inner orientation parameters (Favey, 2001), and especially the boresight misalignment between the body frame B and the laser frame S. Boresight misalignment can affect the georeferencing of the laser data systematically, yet it is not trivial to determine. Boresight misalignment is usually assumed to remain constant during the whole flight, tough it may be subject to vibrations and aircraft deformations to a small degree. The aim of boresight misalignment calibration is the estimation of the boresight misalignment angles $(d\beta_x, d\beta_y, d\beta_z)$, forming the boresight misalignment rotation matrix $\boldsymbol{R}_{B/S}$ of (6.1).

6.5.2 Impact of Boresight Misalignment on Ground Point Height

In order to estimate the boresight misalignment angles, their effect on the ground point position, and especially on its vertical component, have to be modeled. (6.9) gives the true height h^L of the laser ground point for the case of a **cross-section linear scanner**. If boresight misalignment is not considered, e.g. in a preliminary data processing before calibration, the approximate height h_0^L of the laser ground point becomes, based on (6.9):

$$h_0^L \;=\; h_a^L \;-\; \left[\cos\alpha_x \cos\alpha_y \left(r\cos\sigma_x + b_z^B\right) \;-\; \sin\alpha_x \cos\alpha_y \left(r\sin\sigma_x - b_y^B\right) \;-\; b_x^B \sin\alpha_y\right] \quad (6.33)$$

Thus, the effect dh_β of boresight misalignment on the height is given by the difference between the true height h^L from (6.9) and the approximate height h_0^L (without considering boresight misalignment) from (6.33):

$$dh_\beta \;=\; r\;\left[\left(\cos\alpha_x \sin\sigma_x + \sin\alpha_x \cos\sigma_x\right) d\beta_x \cos\alpha_y \;+\; \sin\alpha_y \left(d\beta_y \cos\sigma_x + d\beta_z \sin\sigma_x\right)\right] \quad (6.34)$$

For the special case of a **laser profiler**, $\boldsymbol{s}^S = (0,0,1)^T$, and (6.33) and (6.34) can be simplified using $\sin\sigma_x = 0$ and $\cos\sigma_x = 1$:

$$h_0^L \;=\; h_a^L \;-\; \left[\cos\alpha_x \cos\alpha_y \left(r + b_z^B\right) \;+\; b_y^B \sin\alpha_x \cos\alpha_x \;-\; b_x^B \sin\alpha_y\right] \quad (6.35)$$

$$dh_\beta \;=\; h^L \;-\; h_0^L \;=\; r\;\left(d\beta_x\;\sin\alpha_x\;\cos\alpha_y \;+\; d\beta_y\;\sin\alpha_y\right) \quad (6.36)$$

6.5.3 Impact of Simplification for Small Boresight Misalignment Angles

In (6.34) and (6.36), simplifications for small boresight misalignment angles (6.6) were applied. Without these simplifications, the true height h^L of the laser ground point for the case of a **laser profiler** becomes, based on (6.7):

$$\begin{aligned} h^L \;=\; h_a^L \;&-\; \cos\alpha_x\;\cos\alpha_y\;\left(r\;\cos d\beta_x\;\cos d\beta_y \;+\; b_z^B\right) \\ &+\; \sin\alpha_x\;\cos\alpha_y\;\left(r\;\sin d\beta_x\;\cos d\beta_y \;-\; b_y^B\right) \\ &+\; \sin\alpha_y\;\left(r\;\sin d\beta_y \;+\; b_x^B\right) \end{aligned} \quad (6.37)$$

Table 6.5: Impact [cm] of boresight misalignment simplification on ground point height from (6.40), for roll = pitch = 0° and $d\beta_x = d\beta_y$

boresight	flight height above ground				
angles	100 m	200 m	300 m	500 m	1000 m
0.10°	0.0	0.1	0.1	0.2	0.3
0.25°	0.2	0.4	0.6	1.0	1.9
0.50°	0.8	1.5	2.3	3.8	7.6
0.75°	1.7	3.4	5.1	8.6	17.1
1.00°	3.0	6.1	9.1	15.2	30.5

The non-simplified impact dh_β of boresight misalignment on the height is given by the difference between (6.37) and (6.35):

$$dh_\beta \;=\; r\;(\sin\alpha_x \cos\alpha_y \sin d\beta_x \cos d\beta_y \;+\; \sin\alpha_y \sin\beta_y \;-\; \cos\alpha_x \cos\alpha_y \cos d\beta_x \cos d\beta_y) \quad (6.38)$$

The impact $dh_{\beta,s}$ of the simplification of the boresight misalignment on the height of the laser ground point is given by the difference between (6.37) and (6.10):

$$\begin{aligned} dh_{\beta,s} \;=\; & r\;\cos\alpha_x\;\cos\alpha_y\;(1\;-\;\cos d\beta_x\;\cos d\beta_y) \\ & +r\;\sin\alpha_x\;\cos\alpha_y\;(\sin d\beta_x\;\cos d\beta_y\;-\;d\beta_x) \\ & +r\;\sin\alpha_y\;(\sin d\beta_y\;+\;d\beta_y) \end{aligned} \quad (6.39)$$

Hence, the impact of the boresight simplification on the height is proportional to the laser range r. Assuming the simple case where the roll and pitch angles are perfectly zero on a flight line ($\alpha_x = \alpha_y = 0$), (6.39) becomes:

$$dh_{\beta,s} \;=\; r\;(1\;-\;\cos d\beta_x\;\cos d\beta_y) \quad (6.40)$$

The impact for different flight heights above ground ($\simeq$ laser range r) and boresight misalignment angles are given in Tab. 6.5, for $\alpha_x = \alpha_y = 0$ (6.40). Note that this case represents the minimum impact of boresight misalignment, and that in case of roll and pitch angle deviating from zero, or in case of a laser scanner, the impact would drastically increase. Tab. 6.5 shows that for high flight heights and relatively large boresight misalignment angles, the simplification of the boresight rotation matrix is not recommended in high-accuracy applications. In this case, (6.37) rather than (6.10) should be used to compute ground point heights.

6.5.4 Self-Calibration Based on Piecewise Polynomial Fit of Water Surfaces

Although several well-developed boresight calibration approaches for airborne camera systems exist, e.g. (Škaloud and Schaer, 2003), the correct recovery of airborne laser scanner misalignments still remains elusive (Škaloud and Lichti, 2006). In airborne laser scanning, the usual approach to estimate boresight misalignment angles relies directly on the laser distance measurements, using a least squares adjustment. These self-calibration techniques are based on the assumption that laser ground points from different shots close to each other have the same height when the scanned area is rather continuous and planar (Škaloud and Lichti, 2006). In this case, the data from one scan subset should have the same characteristics as the data from an adjacent scan subset covering the same area. Differences are then functionally modeled to be an error induced by the boresight

angles. The method described above is based on the assumption that the target surface remains the same between two subsequent scans of the same target. This assumption does not hold for natural water surfaces, where the topography of the surface permanently changes with time, e.g. due to waves. Thus, the same surface height can never be observed twice at the same position. This means that in self-calibration techniques based on water surfaces, an adapted model for surface characteristics has to be applied.

In the following, a method for boresight misalignment calibration relying on water surfaces is described. It is based on former investigations at the GGL (Peter, 1994; Geiger et al., 1994) and is applicable for both airborne laser profilers and scanners. The method directly relies on ellipsoidal water surface heights provided by airborne laser altimetry. The boresight misalignment calibration model is based on the following general observation equation:

$$h_0^L \;=\; h^L \;-\; dh_\beta \;=\; F(x) \tag{6.41}$$

The observations are the approximate ground point heights h_0^L without considering boresight misalignment, h^L is the true but unknown surface height and dh_β is the effect of boresight misalignment on the ground point height. Due to geoid undulations, ellipsoidal water surfaces cannot be satisfactorily modeled by a single horizontal or inclined plane over large distances. Hence, the true water surface of height h^L in (6.41) is modeled by piecewise planar surfaces:

$$h^L \;=\; a_i\; x \;+\; b_i\; y \;+\; c_i \tag{6.42}$$

where (x, y) are the horizontal coordinates of the laser ground point. a_i, b_i and c_i are the planar coefficients of the piecewise interval i, leading to one set of polynomial parameters for every chosen interval of typically 5 - 10 km flight distance. Additionally, the piecewise polynomials are constrained from one interval to the next with a continuity condition at the common point $(x_{1,i}, y_{1,i})$:

$$h_{1,i}^L \;=\; a_{i-1}\; x_{1,i} \;+\; b_{i-1}\; y_{1,i} \;+\; c_{i-1} \;=\; a_i\; x_{1,i} \;+\; b_i\; y_{1,i} \;+\; c_i \tag{6.43}$$

If the aircraft is flying on a more or less straight line during an interval i, the planar fit is weakly determined because an infinite number of planes can be defined by a single line. To avoid this problem, the coordinates (x, y) are defined in a local coordinate system, the origin $(x_{1,i}, y_{1,i})$ being the first ground point of the interval, and the x-axis defined in flight direction. Using this coordinate system, the parameter b_i can be constrained to zero on a straight flight line, leading to a linear fit of the sea surface in flight direction. If the interval comprises a turn between two flight lines, a planar polynomial is used. In the case of a laser profiler, the latter intervals contain the most significant information on boresight misalignment, especially for the roll angle, due to the banking of the aircraft. Hence, a special algorithm was applied to obtain an ideal interval distribution with intervals centered around turns.

A least-squares (LSQ) adjustment of (6.41) attributes the difference between the approximate ground point heights and the true height modeled by the surface polynomials (i.e. the deviations from the piecewise planar surfaces) to the effect of the boresight misalignment angles ($d\beta_x$, $d\beta_y$, $d\beta_z$). For **cross-section linear laser scanners**, (6.33), (6.42) and (6.34) are inserted in (6.41), yielding the following observation equation:

$$\begin{aligned} &h_a^L - \left[\cos\alpha_x \cos\alpha_y \left(r\cos\sigma_x + b_z^B\right) - \sin\alpha_x \cos\alpha_y \left(r\sin\sigma_x - b_y^B\right) - b_x^B \sin\alpha_y\right] \\ &= \\ &a_i x + b_i y + c_i - r\left[\left(\cos\alpha_x \sin\sigma_x + \sin\alpha_x \cos\sigma_x\right) d\beta_x \cos\alpha_y + \sin\alpha_y \left(d\beta_y \cos\sigma_x + d\beta_z \sin\sigma_x\right)\right] \end{aligned} \tag{6.44}$$

It is seen from (6.44) that the surface height does not depend on the yaw angle a_z. The unknown parameters for an interval i are the three boresight calibration angles ($d\beta_x$, $d\beta_y$, $d\beta_z$) (the same for every interval i), plus three surface polynomial coefficients (a_i, b_i, c_i). Thus, the total number of unknowns is $3+3n_i$, where n_i is the number of polynomial intervals. Compared to the large number of laser observations at a sampling rate of 1 kHz, redundancy is guaranteed even in case of short polynomial intervals. The observation equation (6.44) is linear with respect to the unknown parameters.

For boresight misalignment calibration of airborne **laser profilers**, (6.35), (6.42) and (6.36) are inserted in (6.41), yielding the following observation equation:

$$\begin{aligned} h_a^L \;-\; \left(r + b_z^B\right)\, \cos\alpha_x\, \cos\alpha_y \;+\; b_x^B\, \sin\alpha_y \;-\; b_y^B\, \sin\alpha_x\, \cos\alpha_y \\ = \\ a_i x \;+\; b_i y \;+\; c_i \;-\; r\, d\beta_x\, \sin\alpha_x\, \cos\alpha_y \;-\; r\, d\beta_y\, \sin\alpha_y \end{aligned} \tag{6.45}$$

It is seen from (6.45) that the surface height depends neither on the yaw angle α_z, nor on the yaw boresight misalignment angle $d\beta_z$, which is meaningless for a laser profiler. Thus, the number of unknowns is decreased by one as compared to the scanner model. In order to enhance the estimation, the aircraft may fly at different levels and do banking turns.

Note that if the scan angle $\sigma_x = 0$, (6.44) and (6.45) for the scanner and profiler are identical. The models (6.44) and (6.45) do not allow to distinguish between boresight misalignment and systematic errors on the attitude angles, caused by a misalignment between the attitude measurement system and the body frame. The introduction of constant unknown roll and pitch offsets as additional parameters in the calibration models revealed very high negative correlations of more than 99.99% with the boresight misalignment parameters, due to the small size of the lever arm vector $\boldsymbol{b}^B$ (6.1) as compared to the laser range r.

The boresight misalignment calibration method for airborne laser altimetry described above is a truly self-calibrating technique in the sense that it exclusively relies on the sea surface height observations themselves. There is no need for overflying special calibration surfaces. Additionally, the method relies directly on subsequent observations within the same flight line, with no need for overflying the same area more than once. Furthermore, the calibration algorithm is completely independent of any a priori information about the relief of the measured water surface, like e.g. geoid heights. The calibration method allowed to estimate boresight misalignment angles with an accuracy better than 0.1° (Section 6.5.5), corresponding to the expected order of magnitude of boresight misalignment variations during flight operations, as well as to the estimated attitude accuracy (Section 6.4.4). Due to the small ranges of less than 3 m in shipborne ultrasound altimetry, and the large size of the ultrasound footprint, there was no need for boresight misalignment calibration in shipborne ultrasound altimetry.

6.5.5 Case Study: Airborne Laser Profiler Calibration

The attitude of the aircraft was determined using two independent systems: a multi-antenna GPS array and a Honeywell H764G tactical-grade INS coupled with GPS (Section 6.4.5). The laser profiler data was georeferenced twice using each attitude solution. The two ground point solutions were entered separately into the boresight calibration algorithm described in Section 6.5.4, yielding two sets of boresight misalignment angles (Tab. 6.6 and Tab. 6.7). The roll and pitch misalignment angles obtained from the same attiude solution agree better than 0.1° between the 6 flights, except for two outliers on the pitch angle on flights GRL03 and GRL05 for both the GPS and INS solutions. The outliers are due to a complete lack of significant pitch maneuvers on these specific flights. In general, the pitch misalignment estimation suffers from larger standard deviations due

Table 6.6: Boresight misalignment angles estimated from calibration (6.45) using attitudes from the multi-antenna GPS system. The * are marking outliers.

Date	Flight	droll [°]	Std [°]	dpitch [°]	Std [°]
09/01/2003	GRL06	-0.71	±0.006	0.53	±0.010
09/01/2003	GRL02	-0.73	±0.007	0.61	±0.018
10/01/2003	GRL03	-0.77	±0.007	0.42*	±0.018
11/01/2003	GRL05	-0.76	±0.009	0.68*	±0.022
13/01/2003	GRL01	-0.70	±0.008	0.57	±0.017
14/01/2003	GRL04	-0.65	±0.006	0.53	±0.009
	Mean	**-0.72**	**±0.007**	**0.56**	**±0.016**
	Std	**±0.045**		**±0.087**	

Table 6.7: Boresight misalignment angles estimated from calibration (6.45) using INS attitudes. The * are marking outliers.

Date	Flight	droll [°]	Std [°]	dpitch [°]	Std [°]
09/01/2003	GRL06	-0.21	±0.006	-0.28	±0.010
09/01/2003	GRL02	-0.20	±0.007	-0.23	±0.018
10/01/2003	GRL03	-0.25	±0.007	-0.37*	±0.018
11/01/2003	GRL05	-0.25	±0.009	-0.12*	±0.022
13/01/2003	GRL01	-0.20	±0.007	-0.25	±0.016
14/01/2003	GRL04	-0.23	±0.005	-0.32	±0.008
	Mean	**-0.22**	**±0.007**	**-0.26**	**±0.015**
	Std	**±0.021**		**±0.086**	

Table 6.8: Differences between boresight misalignment angles estimated using attitudes from the multi-antenna GPS system (Tab. 6.6) and INS (Tab. 6.7).

Date	Flight	droll GPS-INS [°]	dpitch GPS-INS [°]
09/01/2003	GRL06	-0.50	0.81
09/01/2003	GRL02	-0.53	0.85
10/01/2003	GRL03	-0.53	0.79
11/01/2003	GRL05	-0.51	0.79
13/01/2003	GRL01	-0.50	0.82
14/01/2003	GRL04	-0.42	0.86
	Mean	**-0.50**	**0.82**
Mean from Tab. 6.3		**0.50**	**-0.91**

to less significant pitch maneuvers as compared to roll maneuvers (turns) during the survey flights. The estimated standard deviations of the GPS and INS solutions are similar. This shows that the slightly higher accuracy and the higher sampling rate of the INS does not result in a significant advantage in boresight calibration and that the efficiency of the calibration is primarily governed by the characteristics of the aircraft maneuvers during a survey flight. The differences between the boresight angles of the GPS and INS solution are listed in Tab. 6.8. Theoretically, these differences should correspond to the mean attitude differences obtained by the two systems (Tab. 6.3). For the roll angle, both differences are identical, while for the pitch angle, a deviation of 0.09° is observed. Obviously, the attitude differences are of opposite sign than the boresight differences.

An example of boresight misalignment calibration of the laser profiler using attitudes from the multi-antenna GPS system on survey flight GRL01 is shown in Fig. 6.15. Fig. 6.14 shows the attitude of the aircraft during the flight. It is seen that during strong roll maneuvers, the laser altimeter receives no return from the sea surface, whereas the pitch movements on survey flights

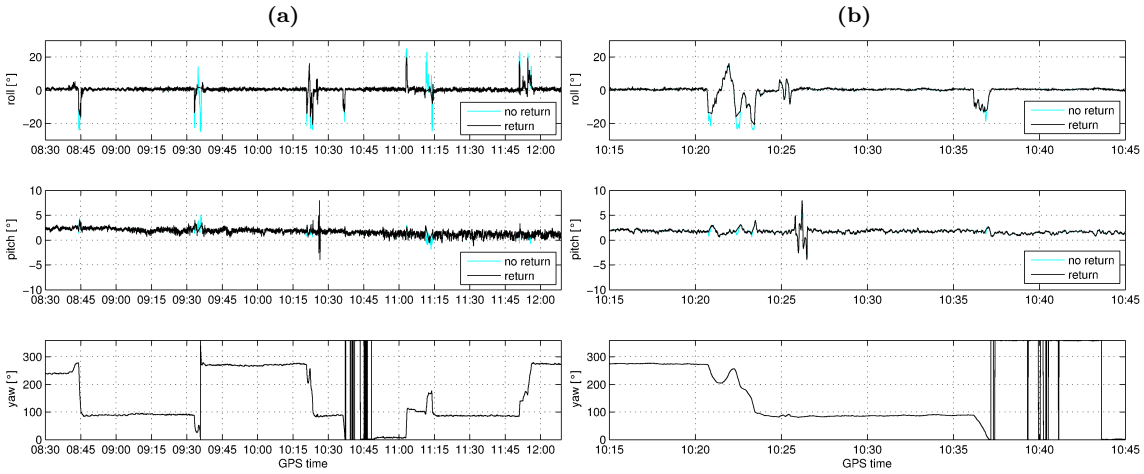

Figure 6.14: **(a)** Attitude of the aircraft during flight GRL01 from multi-antenna GPS. Light line on roll and pitch: attitudes where no returns of the laser profiler were obtained. **(b)** Zoom into part of (a), with special roll and pitch maneuvers without heading change (constant yaw) around 10:26.

are not strong enough to produce significant lacks of laser returns. Fig. 6.15a and Fig. 6.15b show the original sea surface height observations without considering boresight misalignment (6.35), as well as the adjusted sea surface height observations from LSQ adjustment. The adjusted sea surface heights are given by the difference between the original sea surface height observations and their residuals from LSQ adjustment. They reveal the effect of boresight misalignment during turns, characterized by oversized variations of the sea surface heights (Fig. 6.15a and Fig. 6.15b, top). The residuals contain the part of the sea surface height that is not modeled by (6.45). This part is mainly formed by ocean waves, as well as residual system noise. The residuals are normally distributed around zero (Fig. 6.15a and Fig. 6.15b, bottom), underlining the conformity of the model. The good performance of the model is demonstrated by its capability of separating the waves, considered as residuals, from the effects of boresight misalignment, both contained in the original sea surface height observations.

The effect of the boresight misalignment correction on ground point height can reach 1 m during turns, due to large roll angles of 20° (Fig. 6.15c and Fig. 6.15d, bottom). A common approach to avoid strong boresight misalignment effects on laser profilers consists in considering only data along straight flight lines and neglecting data during turns or other roll and pitch maneuvers. On flight GRL01, the decrease of the pitch angle from 2.5° at the beginning of the flight to 1° towards the end of the flight (Fig. 6.14a) results in a vertical boresight effect decreasing from 5 cm to 2.5 cm (Fig. 6.15c, bottom). This underlines the benefit of boresight calibration even when only straight flight lines are considered. Even on straight lines, aircrafts usually fly with more or less constant pitch angles (different from 0), or they may fly at constant roll angles due to strong side winds. This can cause systematic ground point errors of several cm if boresight misalignment is not considered.

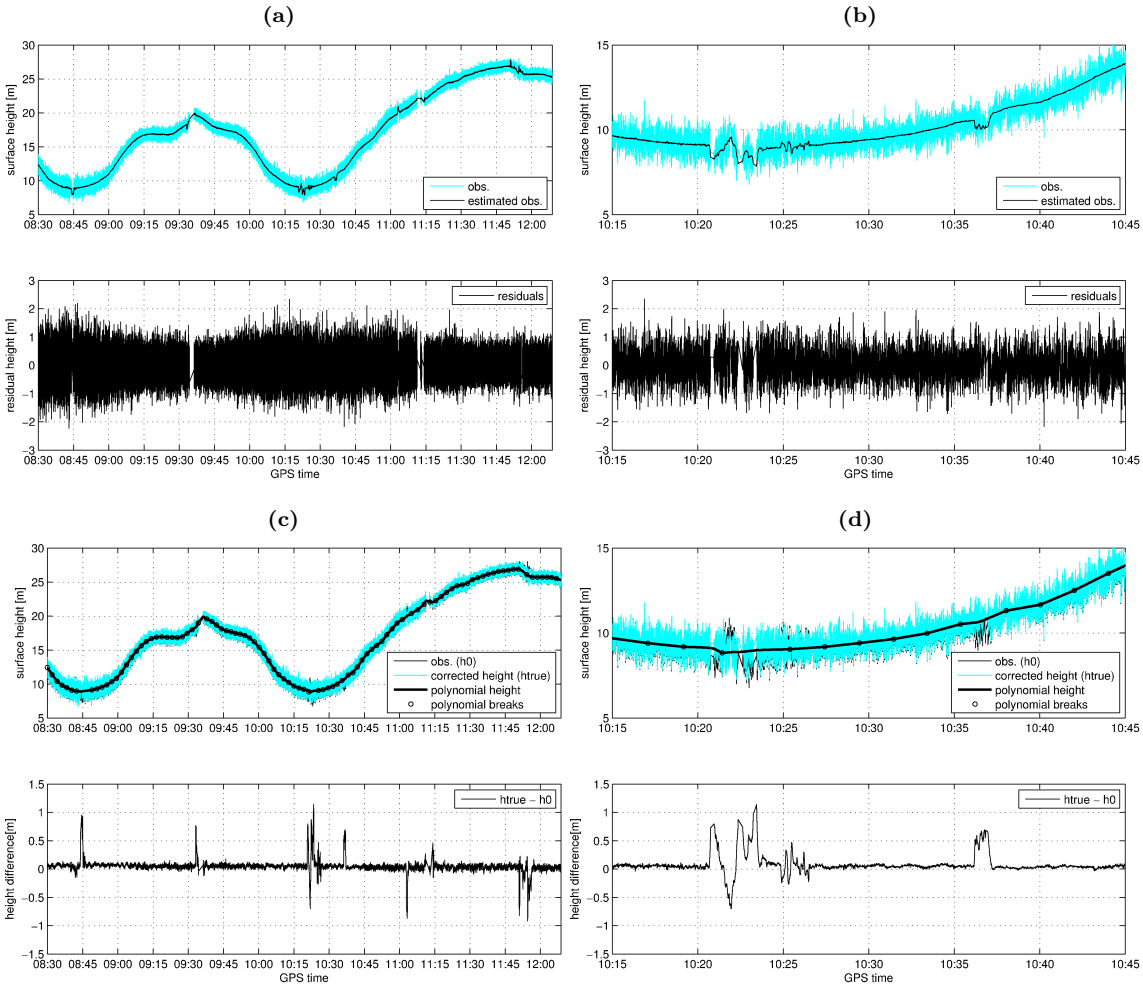

Figure 6.15: **(a)** Boresight misalignment calibration of the laser profiler (6.45) during flight GRL01 using the attitude solution from multi-antenna GPS. Top: Original sea surface height observations without considering boresight misalignment (light line) and adjusted sea surface height observations from LSQ adjustment (black line). Bottom: Residuals on sea surface height observations from LSQ adjustment. **(c)** Same boresight misalignment calibration as in (a). Top: Sea surface heights corrected for boresight misalignment (light line), original sea surface height observations without boresight misalignment correction (black line in the background) and sea surface heights modeled with piecewise polynomials (black line with circles indicating polynomial breaks). Bottom: Difference between sea surface heights corrected for boresight misalignment and original sea surface heights without boresight misalignment correction, corresponding to the estimated effect of boresight misalignment on on ground point heights. **(b)** and **(d)** Zoom into part of (a) and (c) with special roll and pitch maneuvers without heading change (constant yaw) around 10:26.

7 Sea Surface Heights by Airborne Laser Altimetry around Western Crete

7.1 GAVDOS Airborne Laser Altimetry Campaign

The GAVDOS project, supported by the European Union, formed an integral part of an international effort to establish European absolute sea level monitoring facilities and calibration sites for radar altimetry satellites (Pavlis et al., 2004). The isle of Gavdos, situated south of Crete (Greece), was selected to host the facilities due to its offshore location under a crossover of two ground tracks of the radar altimetry missions TOPEX/Poseidon and Jason-1. The GAVDOS project was an international cooperation between the following institutions:

- Technical University of Crete (TUC), Geodesy and Geomatics Engineering, Greece
- Joint Center for Earth Systems Technology (JCET), University of Maryland, Baltimore County, USA
- Aristotle University of Thessaloniki (AUTH), Department of Geodesy and Surveying, Greece
- Institute of Marine Biology of Crete (IMBC), Department of Oceanography, Heraklion, Greece (now Hellenic Center for Marine Research, HCMR)
- Austrian Space Research Institute, Department of Satellite Geodesy, Austria
- National Survey and Cadastre of Denmark (KMS), Geodynamics Department, Denmark
- Observatoire de la Cote d'Azur (OCA), France
- Centre d'Etudes et de Recherches en Géodynamique et Astrométrie (CERGA), CNRS, France
- Hellenic Navy Hydrographic Service (HNHS), Athens, Greece
- University of Bergen, Institute of Solid Earth Physics, Norway
- ETH Zurich, Geodesy and Geodynamics Lab (GGL), Switzerland

During the GAVDOS project (2001 - 2004), coordinated survey campaigns were carried out in the area around Gavdos and Crete, with the primary aim to calibrate Jason-1 observations. The project included data collected from tide-gauges, airborne laser altimetry, airborne gravimetry, GPS buoys, hydrodynamic leveling, satellite laser ranging (SLR), DORIS radio positioning, altimeter transponder observations and continuous GPS stations. In order to reference the radar altimeter observations at the calibration facility and to study the regional sea current circulation, detailed regional models of the geoid and sea surface topography are required. This task was achieved by carrying out a regional flight campaign for airborne gravimetry and laser altimetry. A high-resolution geoid has been derived from the gravimetric data (Tziavos et al., 2004).

The airborne campaign took place during 7 consecutive days, from 09/01/2003 to 15/01/2003, with a total of 35 survey flight hours. An area of approximately 200 by 200 km was covered with two different flight levels around Gavdos and the western part of Crete, in the vicinity of the Hellenic Trench. The higher flight level, with 8 flight lines at 11500 ft (3500 m) altitude, was reserved

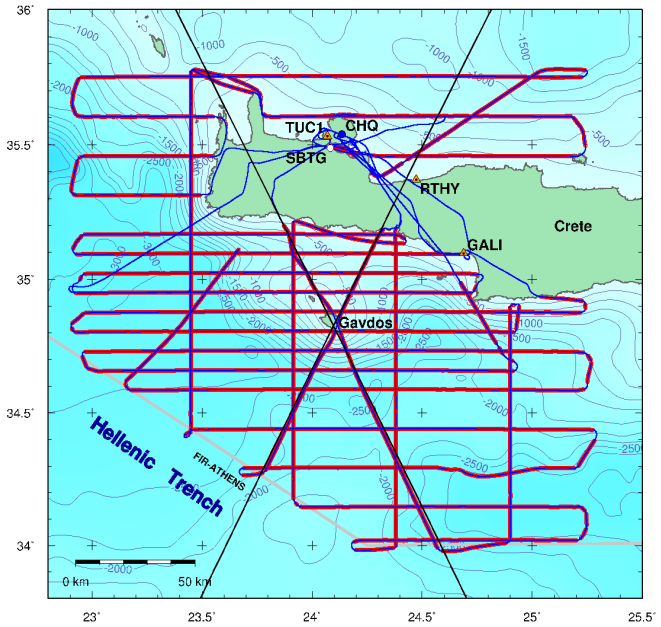

Figure 7.1: Low altitude (700 ft) flight lines of the GAVDOS combined airborne gravimetry and laser altimetry campaign around Crete, with aircraft trajectories (thin blue line) and laser data (thick red line). Black diagonal lines: Jason-1 radar altimeter ground tracks. Orange triangles: GPS reference stations (TUC1, GALI, RTHY). White circle: Souda Bay tide-gauge (SBTG). Blue circle: Chania Airport (CHQ). Gray line: boundary of FIR-Athens. Background: bathymetry in [m].

for gravimetric surveying. The lower flight level, with 24 lines at 700 ft (215 m) altitude flown during 6 consecutive days was a combined gravimetric and laser altimetry survey (Fig. 7.1). Three GPS reference stations (TUC1, GALI, RTHY) were operated on the island of Crete during flight operations. Data from the permanent tide-gauge station in Souda Bay (SBTG), operated by the Hellenic Navy Hydrographic Service, was available. All flights were flown out of Chania Airport (CHQ) and remained within the Athens Flight Information Region (FIR-Athens). The campaign was carried out in close cooperation with the National Survey and Cadastre of Denmark (KMS) and the Institute of Solid Earth Physics of the University of Bergen. The survey vessel Pytheas of the Hellenic Navy Hydrographic Service (HNHS) took part in the campaign. There has been a close collaboration with the Hellenic Military Geographic Service, Civil and Military Aviation Control Authorities and Chania Airport.

7.2 Instantaneous Sea Surface Height Profiles

7.2.1 Sea Surface Height Profiles

Sea surface height profiles (Fig. 7.2 and Fig. 7.3) were computed with respect to the WGS84 ellipsoid, based on airborne laser range data, aircraft trajectories and attitudes, using the direct georeferencing method described in Chapter 6. The original sea surface height results with a sampling rate of 1 kHz were low-pass filtered using a 1D spline filter with a cut-off wavelength of 10 km (Fig. 7.2 and Fig. 7.3). The spline filter algorithm is robust against outliers and is capable of handling the large amount of data yielded by the 1 kHz laser observations. In addition, as opposed to filter algorithms in the frequency domain based on Fourier transforms, the spline filter is insensitive to data gaps as occurring throughout the laser datasets. Further information on spline filters can be found in (Goto et al., 2005; Hernla, 2000; Numada et al., 2007; Törnig and Spellucci, 2000).

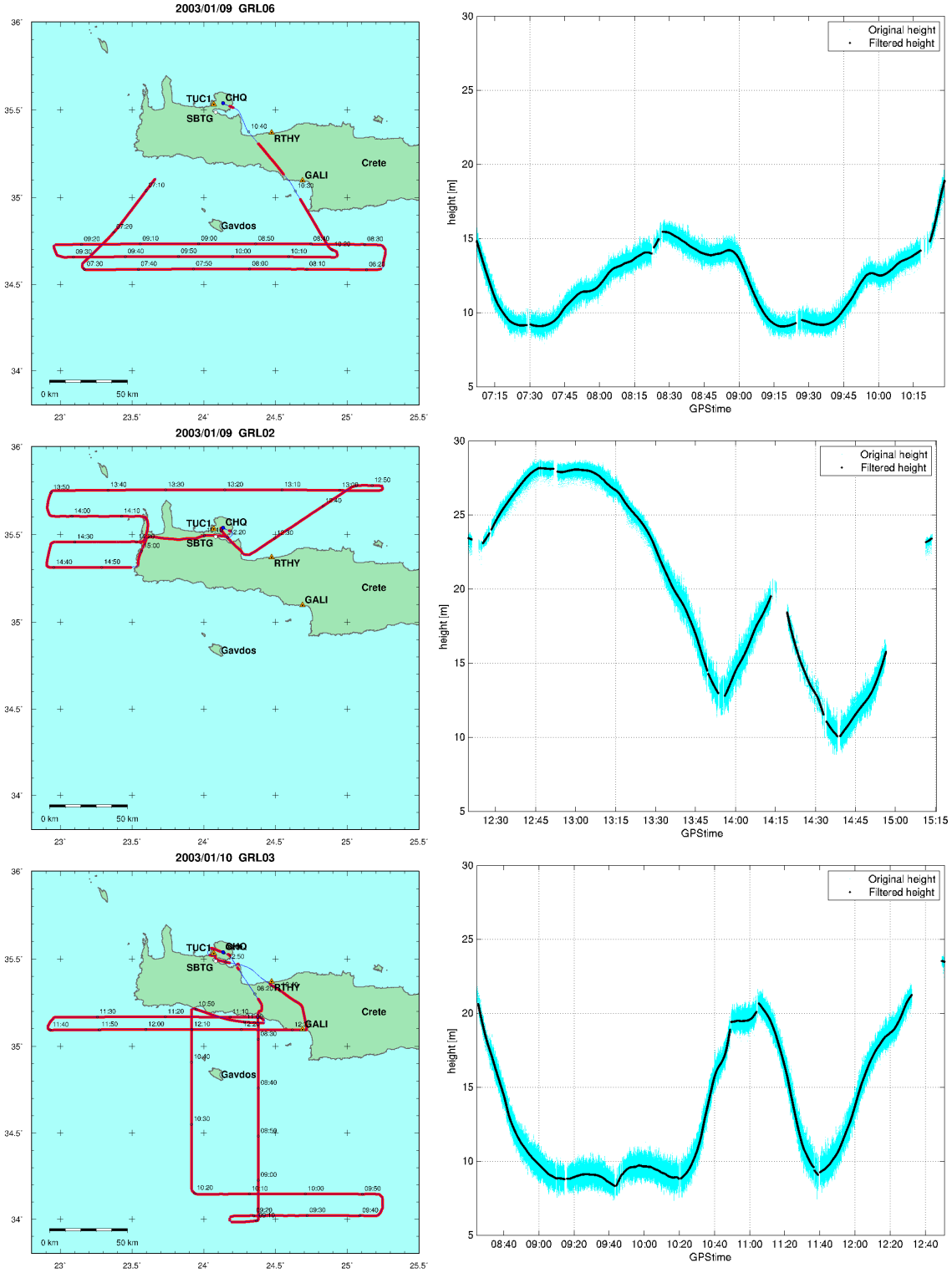

Figure 7.2: Left: Tracks of flights GRL06, GRL02 and GRL03, with aircraft trajectory (thin line) and laser data (thick line). Right: Corresponding time series of instantaneous sea surface height profiles (with respect to the WGS84 reference ellipsoid) from airborne laser altimetry, with original sampling rate of 1 kHz (light line) and heights smoothed using a low-pass spline filter with a cut-off wavelength of 10 km (black line). Time indications on the left-hand graphs correspond to the time axis of the right-hand graphs.

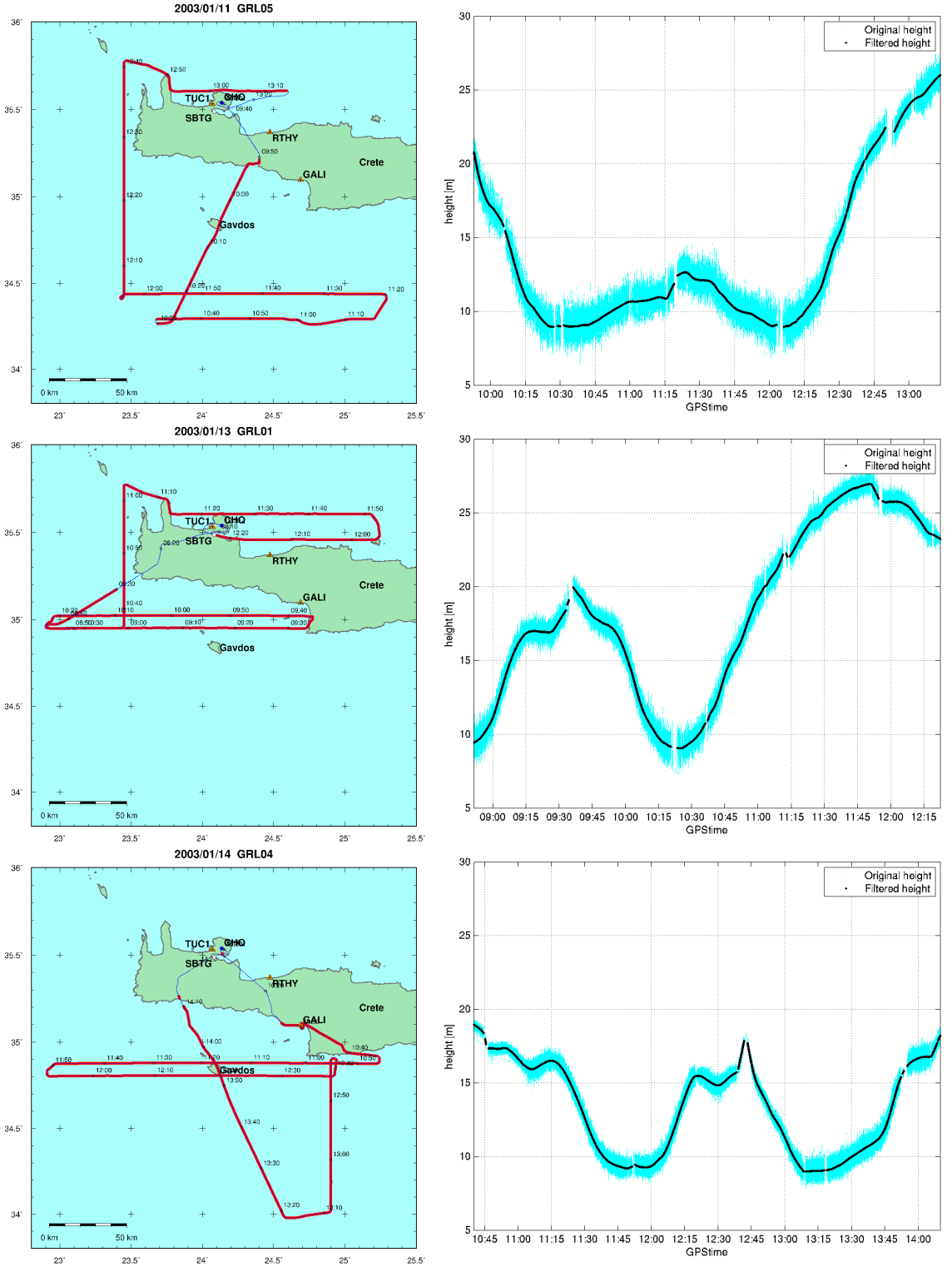

Figure 7.3: Left: Tracks of flights GRL05, GRL01 and GRL05, with aircraft trajectory (thin line) and laser data (thick line). Right: Corresponding time series of instantaneous sea surface height profiles (with respect to the WGS84 reference ellipsoid) from airborne laser altimetry, with original sampling rate of 1 kHz (light line) and heights smoothed using a low-pass spline filter with a cut-off wavelength of 10 km (black line). Time indications on the left-hand graphs correspond to the time axis of the right-hand graphs.

7.2.2 Calibration of Airborne Laser Altimetry Data with GPS Buoys

GPS-equipped buoys were deployed simultaneously with the airborne surveys, providing ground-truth sea surface heights for the verification and calibration of the airborne laser altimetry system. Two lightweight buoys (Appendix C.2) were used at a sampling rate of 1 Hz. The GPS data of the buoys was processed by double-differenced carrier phase, using the reference stations TUC1 and GALI (Fig. 7.1). Several overflights of the buoys were performed. Two verifications of airborne laser altimetry results with GPS buoy observations during flight GRL04 are presented in this section.

A first calibration was performed in the port of Agia Galini (GALI in Fig. 7.1, Fig. 7.4). The buoy data reveals the presence of a wave with a period close to 10 minutes and an amplitude of about 2 cm inside the port (Fig 7.4d). The laser data also indicates the presence of a wave, since the filtered height is not constant inside the port (Fig 7.4c). Due to this wave, in conjunction with the horizontal offset of 87 m between the laser profile and the buoy, the comparison between the two

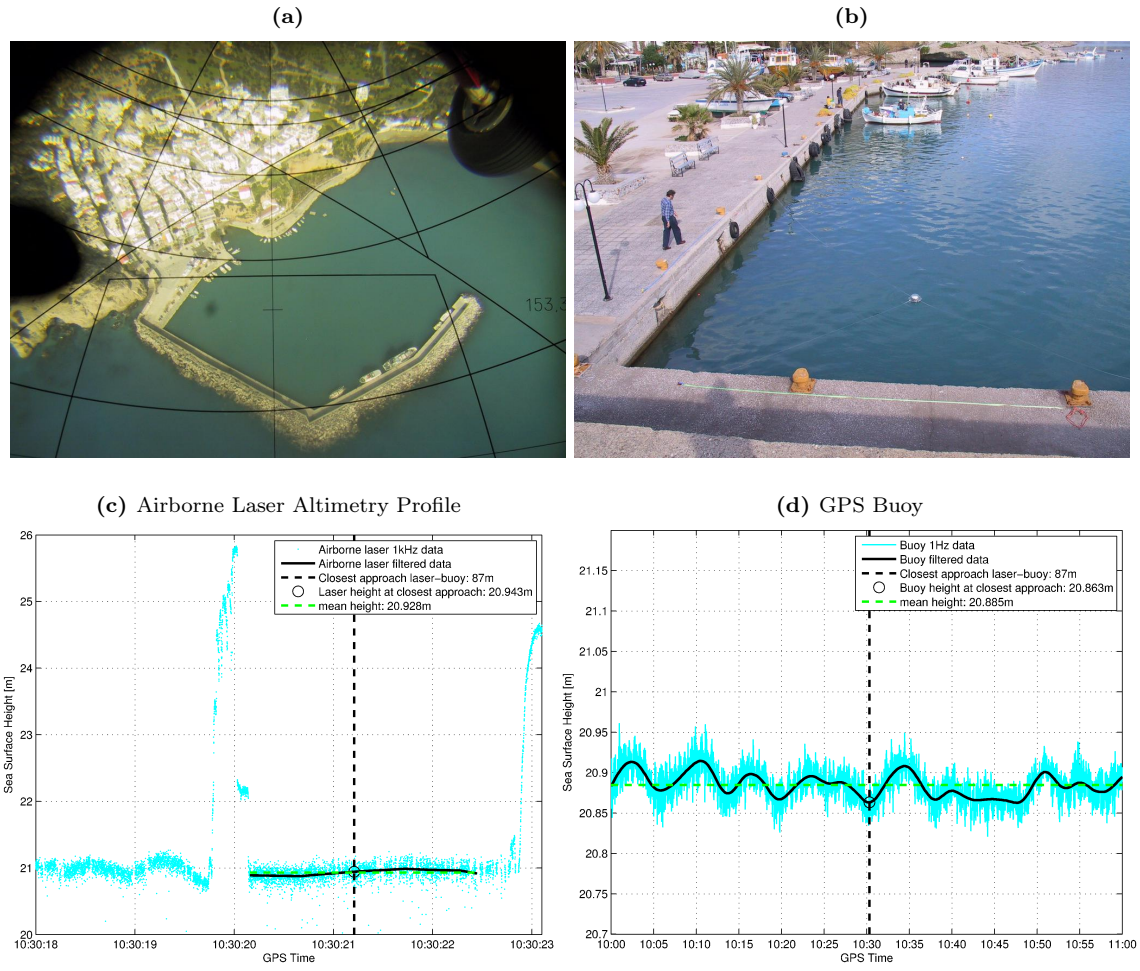

Figure 7.4: **(a)** Overflight of the port of Agia Galini as seen from the aircraft. **(b)** GPS buoy deployed in the port of Agia Galini during overflight. **(c)** Height profile from airborne laser altimetry during overflight of the port of Agia Galini. Light dots: original data (sampling rate 1 kHz). From left to right, the laser data shows the sea surface outside the port, the wave-breaker, the sidewalk, the sea surface inside the port and the pear. The cross-section of the port is 150 m. **(d)** Sea surface height from GPS buoy in the port of Agia Galini during 1 hour centered around the overflight.

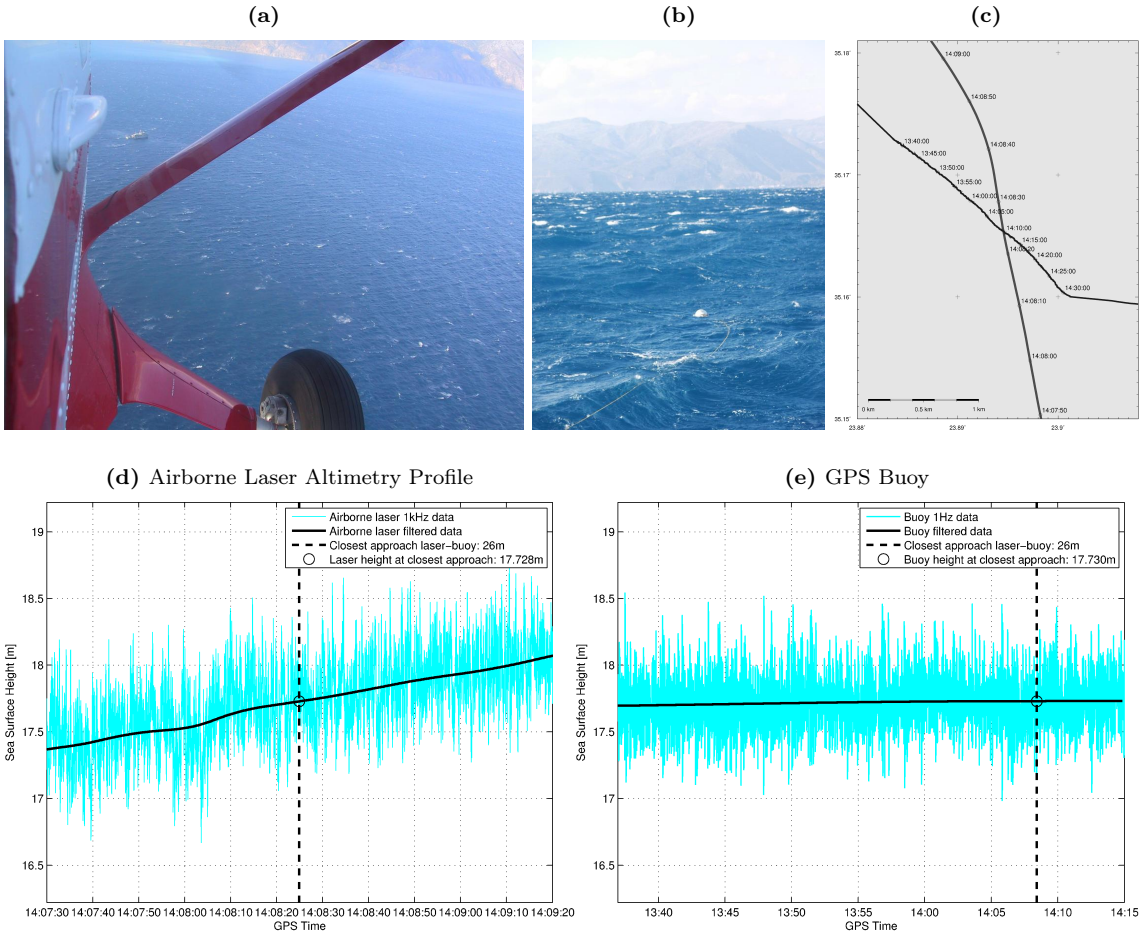

Figure 7.5: **(a)** Overflight of the survey vessel Pyhteas as seen from the aircraft. **(b)** GPS buoy deployed during overflight, under rough sea conditions. **(c)** Situation of the overflight with airborne laser altimetry profile (gray line) and GPS buoy trajectory (black line), with time indications corresponding to (d) and (e). **(d)** Sea surface height profile from airborne laser altimetry during offshore buoy overflight. The laser data cover 120 s corresponding to a distance of 5 km. **(e)** Sea surface height from GPS buoy during overflight, covering 40 minutes and corresponding to a drifted distance of 1.5 km.

datasets at the closest approach is meaningless. Therefore, the mean buoy height observed during 1 hour and the mean laser height over the entire cross-section of the port basin were considered in the comparison. A height difference of 4.3 cm is observed, which lies within the expected accuracies, regarding the noisy laser data inside the port.

In order to obtain an offshore calibration, a GPS buoy was deployed in the open sea south of Crete, at 35.17°N and 23.90°E. The buoy was deployed under drifting conditions by the survey vessel Pytheas of the Hellenic Navy Hydrographic Service, during an overflight of the survey aircraft (Fig. 7.5). The horizontal distance between the buoy and the laser profile during the overflight (closest approach) was 26 m. Both datasets were smoothed using a spline filter with the same cut-off wavelength of 2 km. A good agreement was obtained between the two independent observations, with a height difference of only 0.2 cm (Fig 7.5d and Fig 7.5e). In addition, similar wave amplitudes were observed by both systems. The good agreement between the ground-truth GPS buoy observations and airborne laser altimetry enabled the validation of the laser altimetry system and the direct georeferencing algorithm, without any further calibration.

7.2.3 Significant Wave Heights

Due to the high sampling rate of the airborne laser altimetry data, the residuals between the original and filtered data correspond to the ocean wave undulations, neglecting system noise. Based on these wave undulations, significant wave heights $\bar{H}_{1/3}$ (Section 3.2) were computed from the airborne laser altimetry data (Fig. 7.6). For each significant wave height sample, an overlapping data interval of 10 km was considered. During the airborne campaign, the sea surface was characterized by a wide variety of sea states, with significant wave heights ranging from 0.3 to 2.8 m. Significant wave heights from a dedicated profile are compared to significant wave heights from Jason-1 GDR data in Section 9.2.

7.3 Sea Surface Height Corrections

7.3.1 Ocean Wave Correction

The oscillation effects of ocean waves are eliminated by the low-pass filtering (Section 7.2.1). Further details on ocean waves are given in Section 3.2.

7.3.2 Ocean Tide Correction

The amplitudes of the major ocean tide constituents M2 and S2 are below 2 cm in the survey area around Crete (Fig. 3.3). Hence, only very small tidal effects are to be expected. Tidal corrections along the airborne laser altimetry tracks were computed with the global tide models FES2004 (Fig. 7.7a) and GOT00.2[1] (Fig. 7.7b), as well as with the POL (Proudman Oceanographic Laboratory) model for the Mediterranean Sea (Fig. 7.7c). Further details on these ocean tide models can be found in Section 3.3.2. All three models predict ocean tides below 2.5 cm. However, the predictions are highly contradictory, since the differences between the models reach up to 3 cm (Fig. 7.7d). Considering the small size of the tidal amplitudes and of the differences between the models, the choice of the tide model is not crucial for the accuracy of the corrected sea surface heights. Nevertheless, in order to select the most appropriate model for the considered survey area, a validation of the tidal corrections obtained from the three models was performed, based on tide-gauge observations and on a crosspoints analysis. The validation of FES2004 and POL with local tide-gauge data showed that the POL predictions agree better with the tide-gauge observations (Section 7.3.4). Since the tidal amplitudes and the differences between the predictions of the three models are in the same order of magnitude as the expected accuracy of the sea surface height observations from airborne laser altimetry, it was not possible to discredit one model in favor of another based on the crosspoints analysis (Section 7.4.2). Similar validations were performed for the shipborne data in the North Aegean Sea (Section 8.3.4 and Section 8.4.1). Due to the fact that tidal amplitudes are higher in that survey area, the POL model was identified to agree best with the in situ observations. This model was therefore used to correct the shipborne sea surface height data in the North Aegean Sea. For consistency reasons, the POL model was also used to correct the airborne sea surface height data around western Crete.

7.3.3 Correction for Atmospheric Pressure and Wind Forcing

Corrections for the effect of atmospheric pressure and wind forcing on sea surface heights were computed from the MOG2D correction grids (Section 3.4.2 and Appendix G). Corrections along the airborne laser altimetry tracks were obtained by spatiotemporal interpolation of the MOG2D

[1] Tide corrections from GOT00.2 model were provided by E.C. Pavlis from JCET.

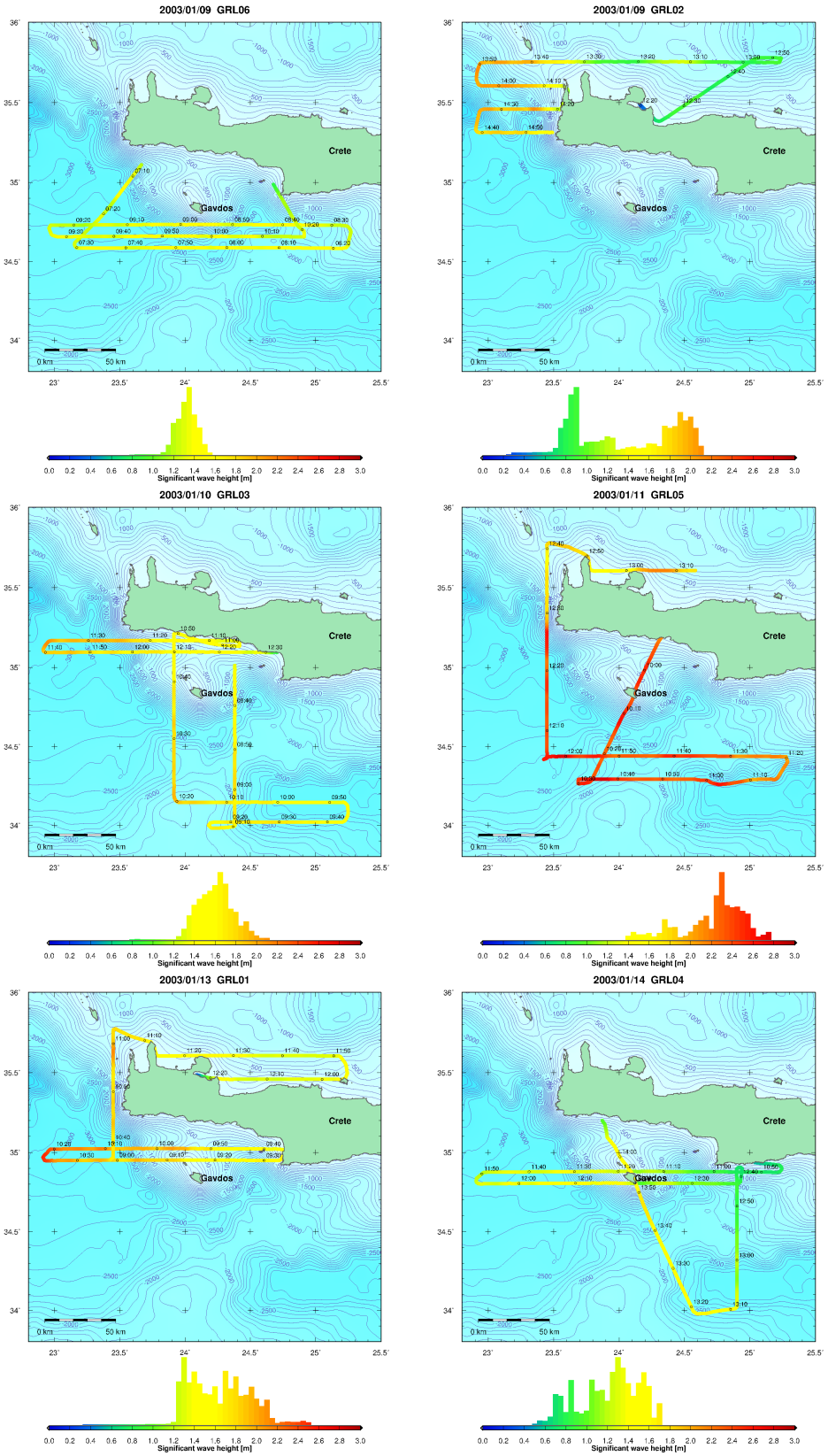

Figure 7.6: Significant wave heights estimated from airborne laser altimetry (background: bathymetry).

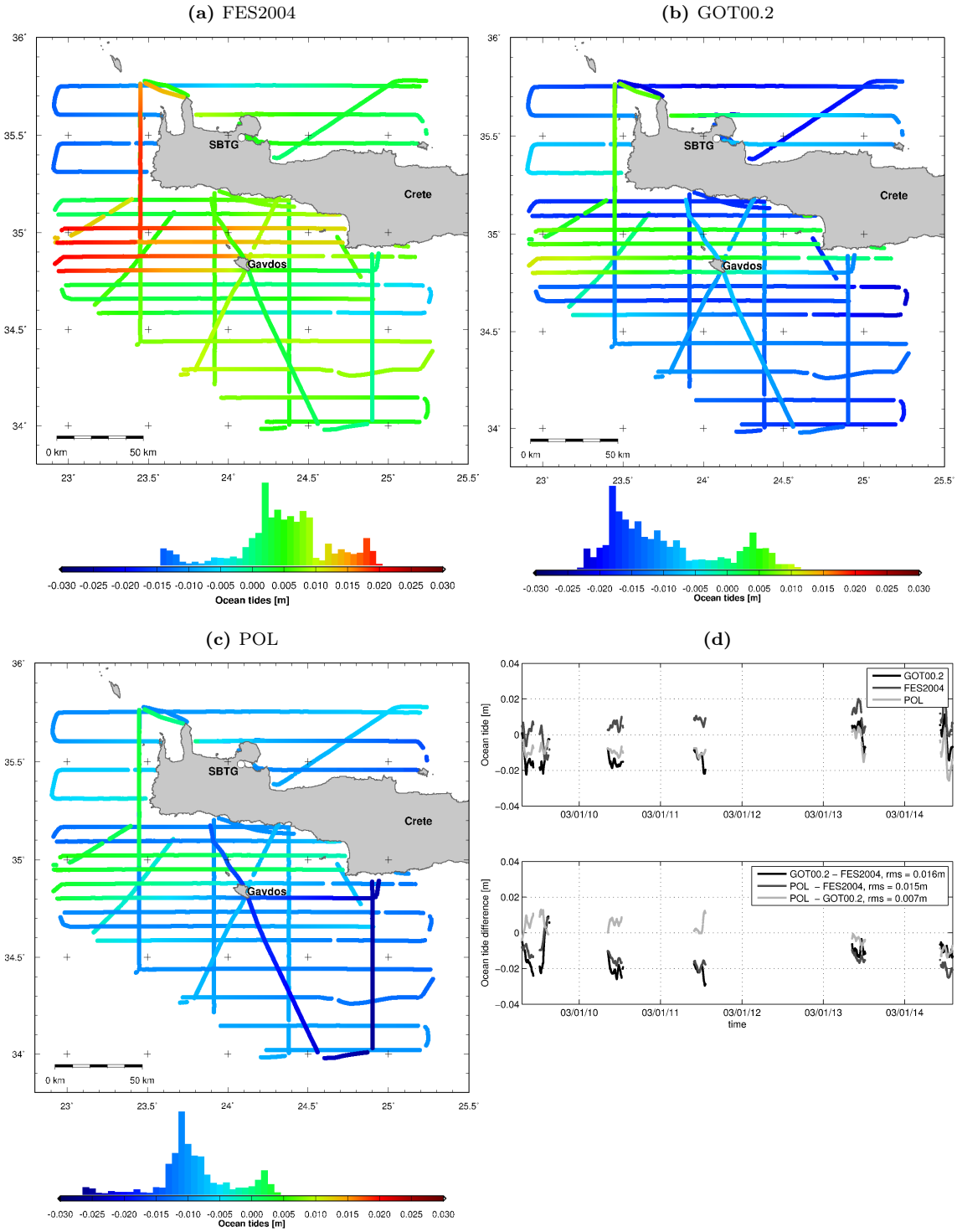

Figure 7.7: Ocean tide predictions along airborne laser altimetry tracks from the models **(a)** FES2004, **(b)** GOT00.2 and **(c)** POL (Proudman Oceanographic Laboratory). **(d)** Top: time series of ocean tides along airborne laser altimetry tracks from FES2004 corresponding to (a), GOT00.2 corresponding to (b) and POL corresponding to (c). **(d)** Bottom: differences between the models.

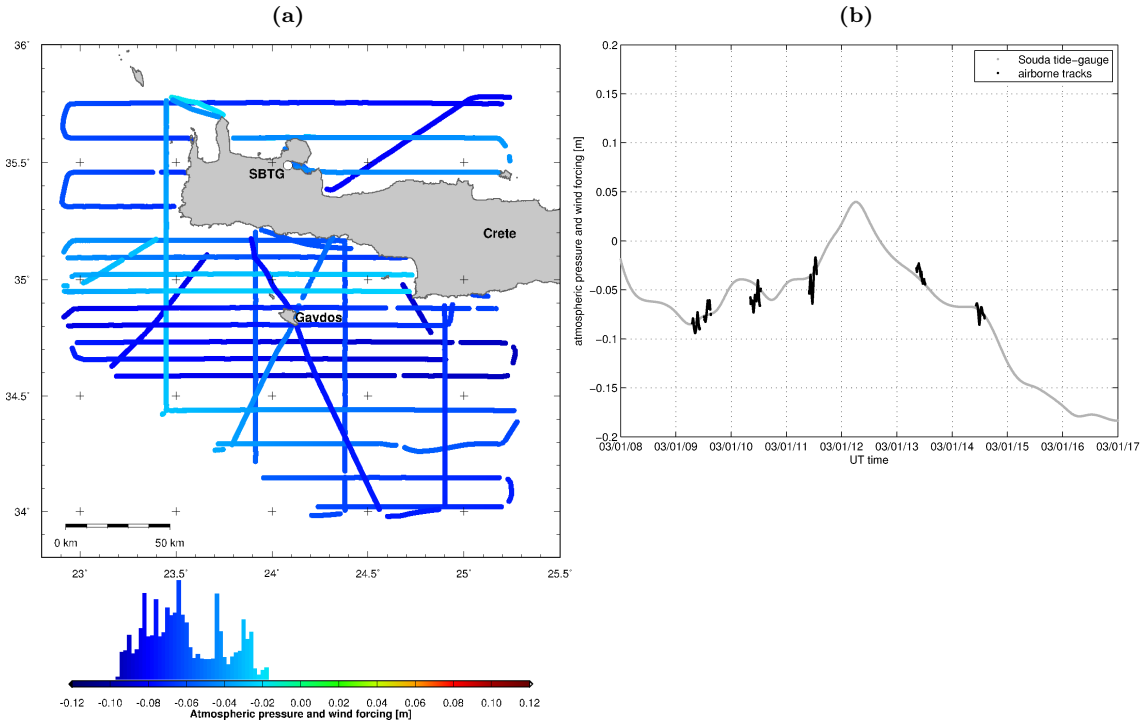

Figure 7.8: **(a)** Effect of atmospheric pressure and wind forcing on sea surface height along airborne laser altimetry tracks, based on MOG2D correction grids. **(b)** Time series of the effect of atmospheric pressure and wind forcing along flight tracks (black line, corresponding to (a)) and at Souda Bay tide-gauge station (gray line, SBTG).

grids (Fig. 7.8). At the tide-gauge station in Souda Bay (SBTG), the atmospheric effect varies between -18 cm and 4 cm during the 9 consecutive days of the survey campaign (Fig. 7.8b, light line). The maximum positive effect occurrs during the morning of 12/01/2003, coinciding with the passage an atmospheric depression (Appendix F). The atmospheric effect along the flight tracks ranges from -10 cm to -2 cm, and variations of up to 5 cm are encountered during the same flight (Fig. 7.8a and Fig. 7.8b dark line). For the area and period of the considered dataset, the effect of atmospheric pressure and wind forcing (Fig. 7.8) is larger than the ocean tide effect (Fig. 7.7).

7.3.4 Validation of Tidal and Atmospheric Corrections with Tide-Gauge

A validation of the FES2004 and POL tidal corrections, as well as the MOG2D atmospheric corrections, was carried out using observations from Souda Bay tide-gauge station (SBTG, Fig. 7.1), operated by the Hellenic Navy Hydrographic Service. The sea surface heights recorded by tide-gauges are affected by astronomic ocean tides and the forcing of atmospheric pressure and wind. In order to compare tide-gauge data to the predictions obtained from tide models, the effects of atmospheric forcing have to be removed from the tide-gauge data. Tide data of 9 consecutive days of the airborne campaign were analyzed (Fig. 7.9). In a first step, the atmospheric effect from MOG2D correction grids were removed from the tide-gauge observations (Fig. 7.9a). In a second step, a remaining low frequency trend (period $>$ 48 h) was removed from the observations. This trend mainly represents the remaining local effect of atmospheric forcing, not resolved by MOG2D. Differences between the corrected tide-gauge observations and predications of FES2004 show a standard deviation of 2.0 cm and maximum values of 5 cm (Fig. 7.9b). Differences with respect to the POL model have a smaller standard deviation of 1.3 cm and maximum values of

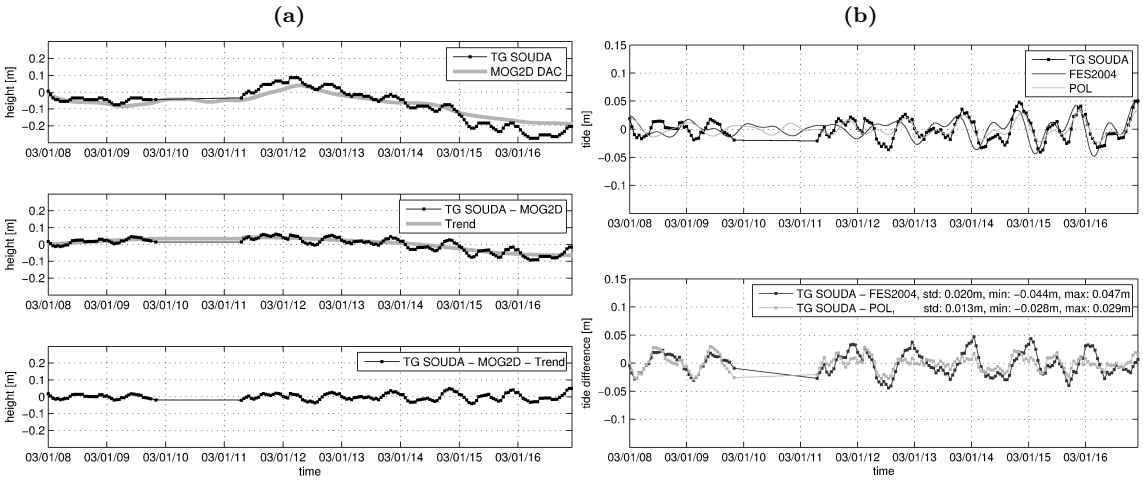

Figure 7.9: **(a)** Top: Sea level observations from Souda Bay tide-gauge, Crete (with data gap on 10/01/2003), during 9 consecutive days of the airborne campaign, and dynamic atmospheric corrections (DAC) from MOG2D. Center: Tide-gauge data corrected with MOG2D DAC and remaining trend. Bottom: Tide-gauge data corrected with MOG2D DAC and with remaining trend removed. **(b)** Top: Sea level observations from Souda Bay tide-gauge station, corrected with MOG2D DAC and with remaining trend removed (corresponding to (a) bottom), as well as tidal predictions from FES2004 and POL models. Bottom: Difference between tide-gauge data and FES2004 and POL predictions.

3 cm. The differences with respect to both tide models still contain periodic signals, meaning that the models do not entirely match the observed tide. The discrepancies between the tide-gauge observations and the models are most likely due to local coastal effects, not resolved by the tidal and atmospheric forcing models. It can be assumed that the models perform better offshore, in the absence of strong and hardly predictable coastal effects.

7.3.5 Sea Level Anomaly Correction

Sea level anomalies (SLA) were computed for the survey area around Crete during the airborne campaign, based on SSALTO/DUACS products (Section 2.4). For the considered area and period (1 week), the SLA range from -2,cm to 18 cm (Fig. 7.10). The average sea surface height in the area is higher than the reference height, with a positive mean SLA of 10.9 cm and 4.5 cm for 08/01/2003 and 15/01/2003, respectively. Hence, during only one week, an important decrease of the mean SLA by 6.3 cm and local SLA variations of up to 12 cm is observed in the survey area (Fig. 7.10c). The SLA show that even after removing the effects of waves, tides and atmospheric forcing, the sea surface topography cannot be considered as constant during the 6 days of the airborne campaign. Thus, an additional sea surface height correction was computed along the flight tracks, based on spatiotemporal interpolation of the SSALTO/DUACS SLA (Fig. 7.10d). The resulting SLA corrections take significant values between -1 cm and 15 cm. These corrections, however, should only be applied when the resulting sea surface heights are meant to represent the mean sea surface MSS, as defined in (2.2) and (2.28). They must not be applied when the resulting sea surface heights are meant to represent corrected sea surface heights SSH, including the variable part of the dynamic topography, as defined in (2.1) and (2.27).

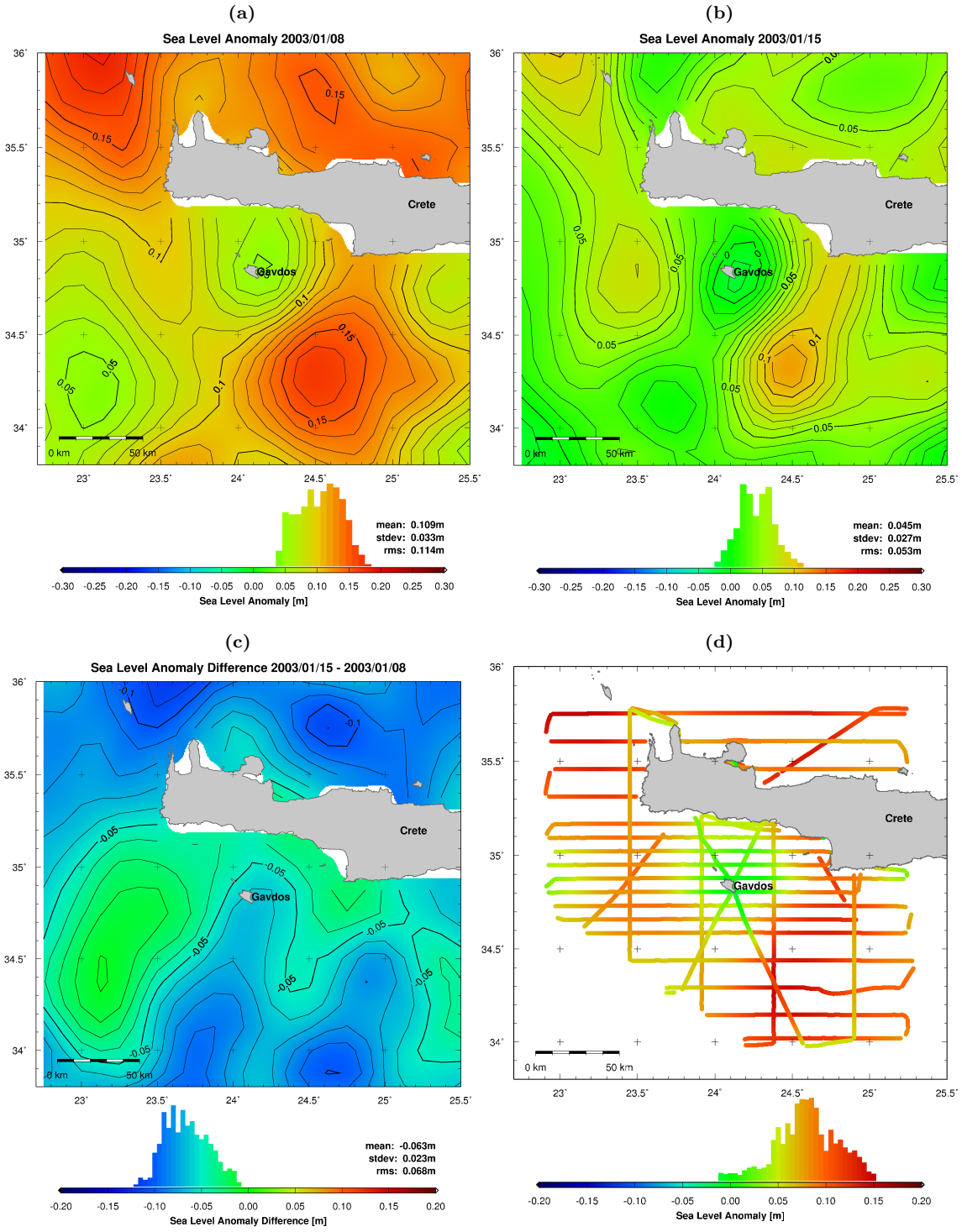

Figure 7.10: Weekly sea level anomaly (SLA) from SSALTO/DUACS merged multi-mission altimetric data around Crete, on 08/01/2003 **(a)** and 15/01/2003 **(b)**. Contour interval: 0.01 m. **(c)** Sea level anomaly difference between the two consecutive weekly datasets in (a) and (b). Contour interval: 0.01 m. **(d)** Sea level anomaly along airborne laser altimetry tracks, based on SSALTO/DUACS sea level anomalies in (a) and (b).

7.4 Repeatability Analysis

7.4.1 Analysis of Repeated Tracks

A good indicator for the repeatability of the airborne laser altimetry system are height differences on repeated tracks. Repeated tracks provide information on the repeatability and on the behavior of the height difference along a whole track, rather than only at punctual crossovers. Three repeated tracks were flown (Fig. 7.11). Cross-track distances between the repeated tracks remained mostly below 100 m. Statistics on the height differences using different combinations of tidal and atmospheric sea surface height corrections are shown in Tab. 7.1. Good agreements are obtained between the repeated tracks, with the majority of the height differences remaining below 10 cm. Strong winds and heavy turbulences were encountered on flight GRL05, which degraded the quality of the resulting sea surface heights on this flight. The tidal and atmospheric corrections do not allow to substantially improve the height differences on the repeated tracks (Fig. 7.11), since the

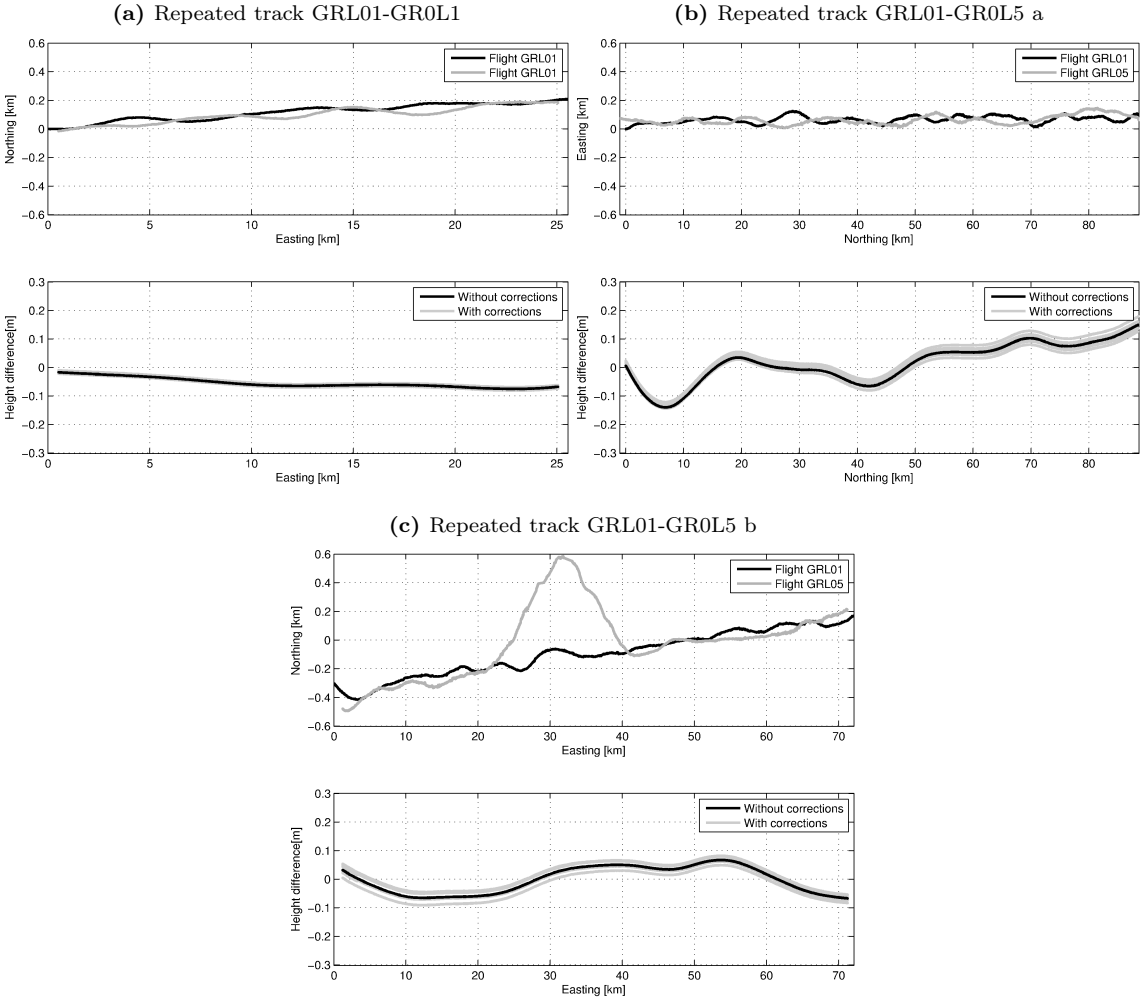

Figure 7.11: Repeated tracks on flights GRL01 and GRL05. Top of (a), (b), (c): cross-track coordinate as a function of along-track horizontal coordinate. Bottom of (a), (b), (c): height difference between repeated tracks without sea surface height corrections (black line) and with different combinations of sea surface heigtht corrections (gray lines), corresponding to Tab. 7.1.

Table 7.1: Height differences on repeated tracks for solutions with different combinations of tidal and atmospheric sea surface height corrections.

	Tidal/Atmospheric sea surface height correction							
Tidal	-	FES2004	GOT00.2	POL	-	FES2004	GOT00.2	POL
Atmospheric	-	-	-	-	MOG2D	MOG2D	MOG2D	MOG2D
Repeated track GRL01-GR0L1 (Fig. 7.11a)								
Mean [m]	-0.054	-0.048	-0.053	-0.055	-0.059	-0.052	-0.058	-0.060
StD [m]	0.017	0.017	0.018	0.018	0.017	0.017	0.018	0.018
RMS [m]	0.057	0.051	0.056	0.058	0.061	0.055	0.060	0.062
|Max| [m]	0.075	0.069	0.075	0.077	0.080	0.074	0.079	0.081
Repeated track GRL01-GR0L5 1 (Fig. 7.11b)								
Mean [m]	0.015	0.026	0.037	0.028	-0.000	0.011	0.022	0.013
StD [m]	0.069	0.069	0.072	0.069	0.063	0.063	0.066	0.063
RMS [m]	0.070	0.074	0.081	0.074	0.063	0.064	0.070	0.064
|Max| [m]	0.150	0.161	0.179	0.163	0.144	0.137	0.155	0.139
Repeated track GRL01-GR0L5 2 (Fig. 7.11c)								
Mean [m]	-0.003	-0.003	-0.024	-0.005	0.013	0.013	-0.008	0.011
StD [m]	0.047	0.048	0.049	0.048	0.046	0.047	0.047	0.047
RMS [m]	0.047	0.048	0.054	0.049	0.048	0.049	0.048	0.048
|Max| [m]	0.068	0.070	0.091	0.072	0.080	0.082	0.074	0.080

order of magnitude of the height differences is higher than the estimated corrections. This confirms the conclusion of Section 7.4.2, where no significant improvement at the crosspoints is obtained using the different combinations of tidal and atmospheric corrections.

7.4.2 Crosspoints Analysis

The airborne laser altimetry profiles yield 100 crosspoints, where the sea surface height was observed twice at the same position (Fig. 7.13). Height differences at crosspoints are a good indicator for the repeatability and the accuracy of the airborne laser altimetry system. An analysis of these height differences computed with different combinations of tidal and atmospheric sea surface height corrections, as well as sea level anomaly (SLA) corrections, was carried out (Tab. 7.2 and Fig. 7.12). The various combinations yield no significant difference, with the RMS of the height differences varying less than 0.6 cm. Furthermore, no improvement at the crosspoints is observed using the different combinations of tidal and atmospheric corrections. This is a consequence of the fact that the orders of magnitude of the tidal and atmospheric effects are small compared to the accuracy of the airborne laser altimetry method. The beneficial impact on sea surface height differences at crosspoints of the same corrections applied to the shipborne data in the North Aegean Sea is shown in Section 8.4.1.

After the application of tidal, atmospheric and SLA corrections, the final RMS of the height differences at the 100 crosspoints is in the order of 8.5 cm (Tab. 7.2). The RMS at the 18 inner-flight crosspoints is about 6.5 cm, whereas the RMS at the remaining 82 inter-flight crosspoints is 9.0 cm. For the solution using POL tidal corrections, MOG2D atmospheric corrections and SLA corrections, the height difference remains below 10 cm at 76% of the crosspoints, below 15 cm at 89% and below 20 cm at 99% of the crosspoints (Fig. 7.12). The maximum observed height difference is 21.6 cm. A final outlier rejection was carried out during the surface generation and data gridding (Section 7.5). An outlier removal further improves the height differences at crosspoints and eliminates most of the differences above 15 cm. At this stage, however, the objective of the crosspoint analysis was not to give the best possible result by eliminating all outliers, but to give a realistic impression of the accuracy and repeatability of the airborne laser altimetry method, prior to a thorough outlier removal.

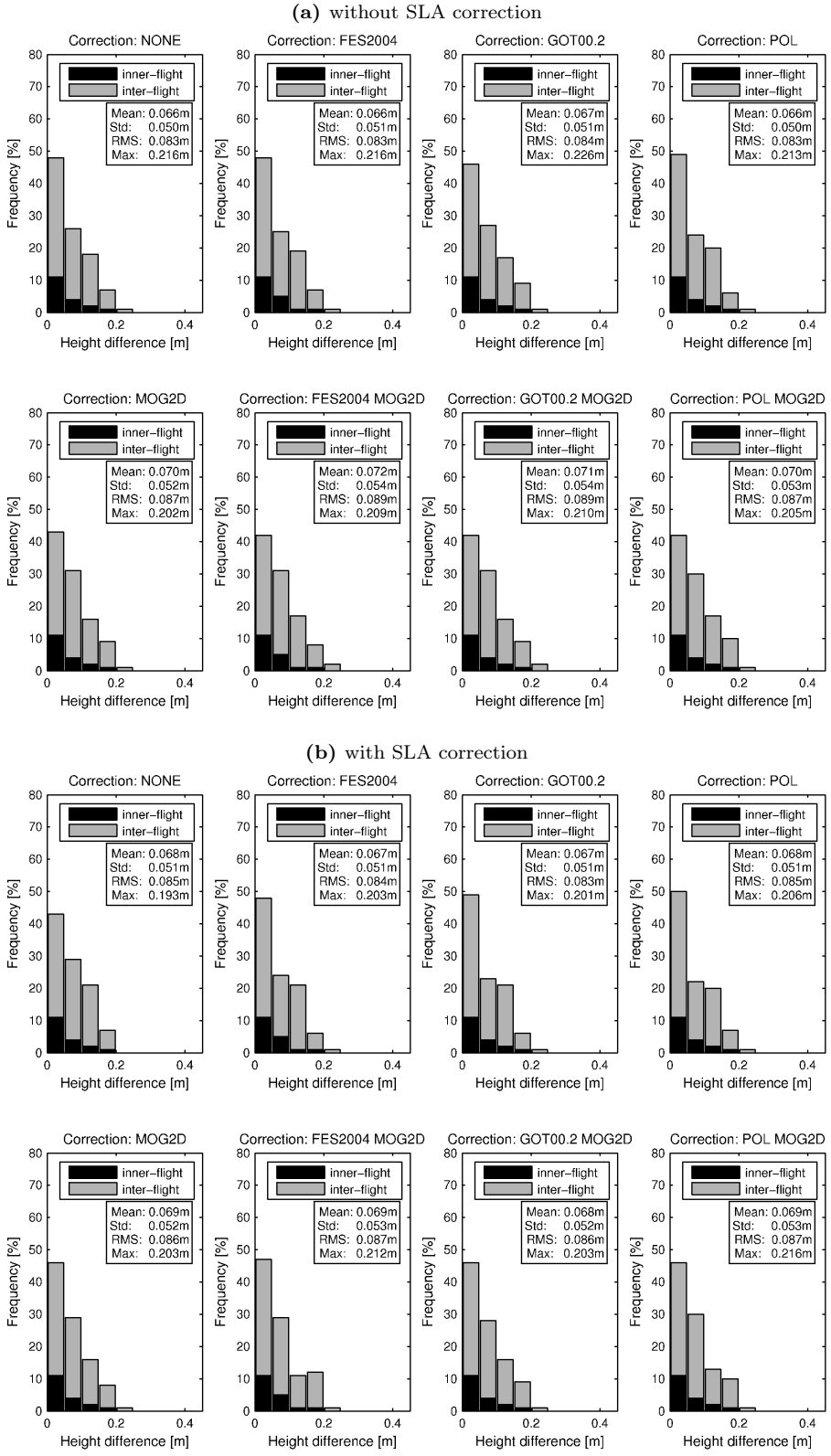

Figure 7.12: Distributions of height differences at crosspoints using different combinations of tidal and atmospheric corrections (corresponding to Tab. 7.2), without **(a)** and with **(b)** sea level anomaly (SLA) correction. Black: inner-flight crosspoints. Gray: inter-flight crosspoints.

Table 7.2: RMS [m] of height differences at crosspoints for solutions with different combinations of tidal and atmospheric sea surface height corrections, without sea level anomaly (SLA) correction, with SLA correction and with combined SLA correction and LSQ adjustment.

	Tidal/Atmospheric sea surface height correction							
Tidal	-	FES2004	GOT00.2	POL	-	FES2004	GOT00.2	POL
Atmospheric	-	-	-	-	MOG2D	MOG2D	MOG2D	MOG2D
All 100 crosspoints								
RMS [m]	0.083	0.083	0.084	0.083	0.087	0.089	0.089	0.087
RMS [m] (SLA)	0.085	0.084	0.083	0.085	0.086	0.087	0.086	0.087
RMS [m] (SLA+LSQ)	-	-	-	-	-	-	-	0.045
Inner-flight 18 crosspoints								
RMS [m]	0.068	0.066	0.066	0.066	0.067	0.066	0.066	0.065
RMS [m] (SLA)	0.067	0.066	0.066	0.066	0.067	0.066	0.065	0.065
RMS [m] (SLA+LSQ)	-	-	-	-	-	-	-	0.050
Inter-flight 82 crosspoints								
RMS [m]	0.086	0.087	0.087	0.086	0.091	0.094	0.093	0.092
RMS [m] (SLA)	0.088	0.087	0.087	0.088	0.090	0.091	0.089	0.091
RMS [m] (SLA+LSQ)	-	-	-	-	-	-	-	0.044

7.4.3 LSQ Adjustment Based on Crosspoints

After the application of all corrections, a relatively large amount (24%) of height differences at crosspoints remains above 10 cm (Section 7.4.2). These misfits are causing problems during surface generation (Section 7.5). Hence, as a final correction, an LSQ adjustment of the profiles was carried out, estimating a linear correction for every flight line that reduces the height differences at crosspoints in a least-squares sense. The LSQ adjustment benefits from the grid-like configuration of the densely spaced flight tracks. Corrections of up to 15.7 cm are obtained by the LSQ adjustment, providing a significant improvement of the height differences at crosspoints (Tab. 7.2 and Fig. 7.13b). Using POL tidal corrections, MOG2D atmospheric corrections and SLA corrections in combination with the LSQ adjustment, the RMS of the height differences is reduced to 4.5 cm, corresponding to an improvement of 50%. After the LSQ adjustment, height differences remain below 5 cm at 77% of the 100 crosspoints and below 10 cm at 98% of the crosspoints. The maximum observed height difference was reduced from 21.6 to 14.9 cm. The beneficial impact of the LSQ adjustment for the surface generation procedure is shown in Section 7.5.

7.5 Time-Independent Sea Surface Topography

By subtracting the time-dependent corrections (Section 7.3) from the low-pass filtered instantaneous sea surface heights (Section 7.2.1, Fig. 7.2 and Fig. 7.3), time-independent sea surface height profiles are obtained (Fig. 7.14). The sea surface heights are computed with respect to the WGS84 reference ellipsoid. Based on the analysis of sea surface height corrections in Section 7.4.2, the observed sea surface heights were corrected using POL tidal corrections, MOG2D atmospheric corrections and SLA corrections from SSALTO/DUACS. Furthermore, the sea surface heights were corrected using an LSQ adjustment of the profiles in order to reduce the height differences at crosspoints (Section 7.4.3).

The resulting punctual time-independent sea surface heights were interpolated onto a regular grid using a bicubic spline interpolation with continuous curvature and adjustable tension. In a second step, the obtained gridded sea surface heights were low-pass filtered using a 2D FFT filter with a cut-off wavelength of 10 km. The cut-off wavelength of the FFT filter was optimally chosen in order to keep the residuals small, without obtaining an unrealistically rough surface. The gridded

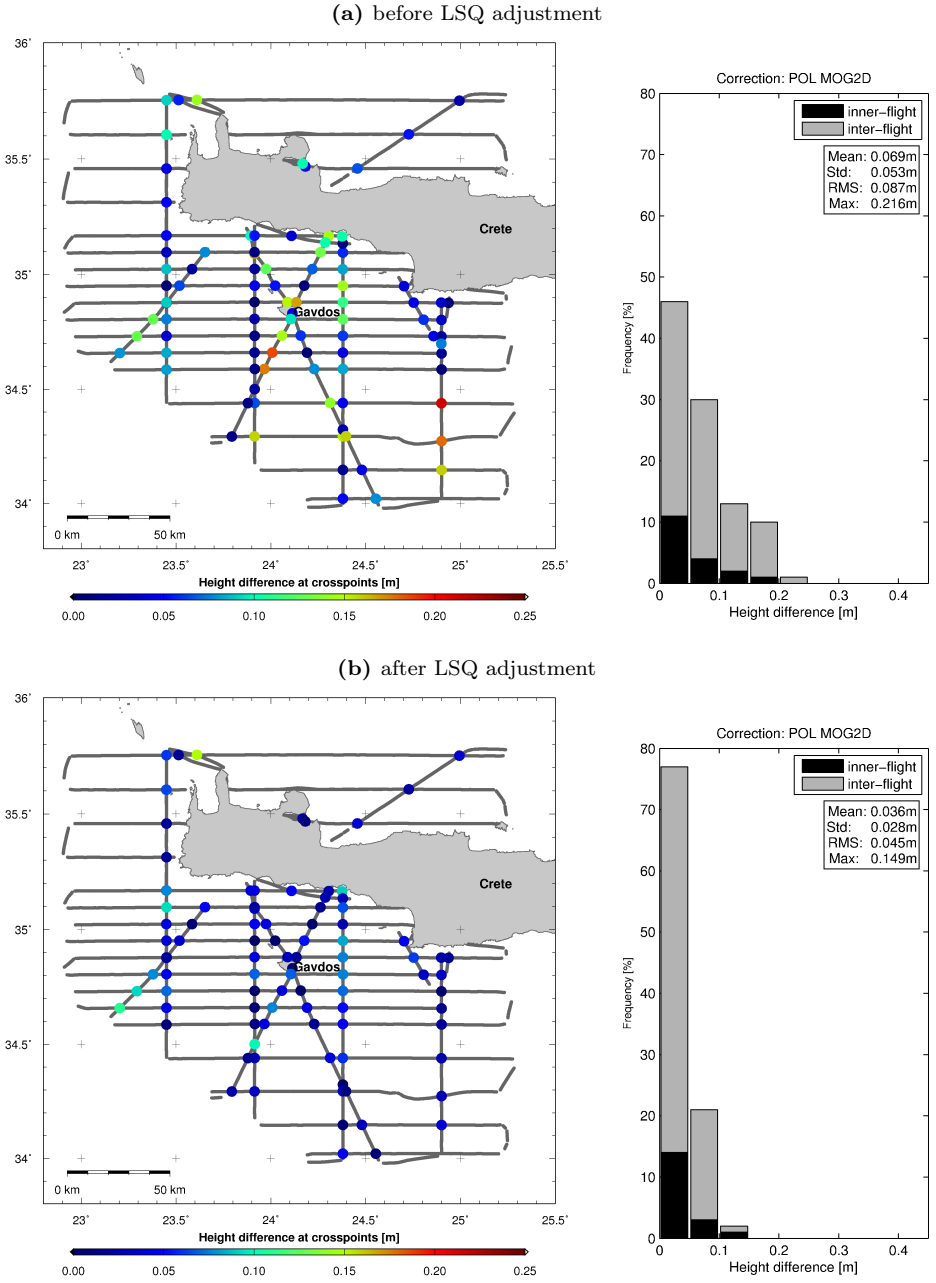

Figure 7.13: **(a)** Crosspoints of sea surface height profiles with height differences and their distribution, using POL tidal corrections, MOG2D atmospheric corrections and SSALTO/DUACS sea level anomaly corrections. **(b)** Same as (a), but with LSQ adjustment of flight lines based on crosspoints.

data are forming a surface representing the time-independent sea surface topography (Fig. 7.15).

A final indication for the accuracy of the sea surface heights is given by the residuals between the time-independent sea surface height profiles (Fig. 7.14) and the gridded sea surface topography (Fig. 7.15). Without the LSQ adjustment (Section 7.4.3), the along-track residuals have a standard deviation of 4.1 cm and large local values of up to 28.5 cm (Fig. 7.16a). After the LSQ adjustment, the residuals are significantly improved (Fig. 7.17a). The standard deviation is reduced to 3.1 cm, but large residuals of up to 26.6 cm locally remain. In order to avoid unrealistic strong gradients

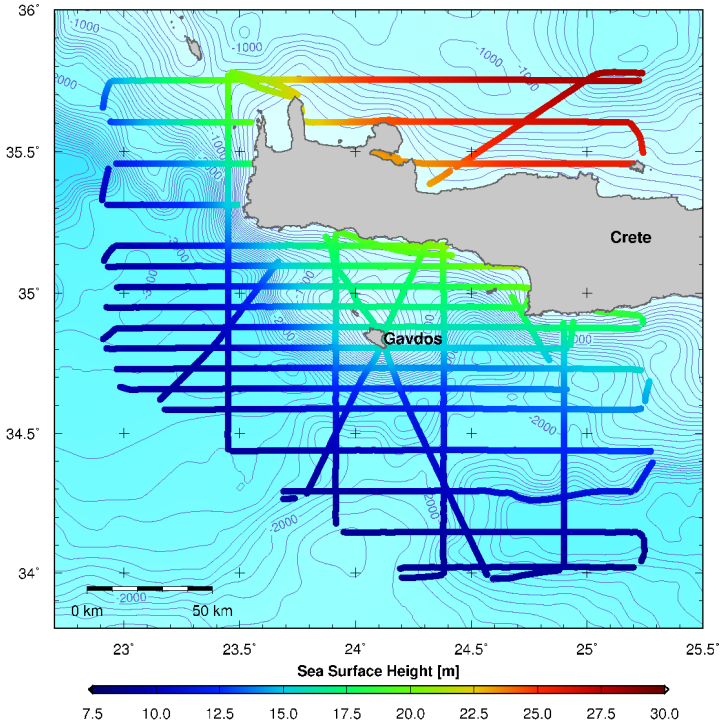

Figure 7.14: Time-independent sea surface height profiles (with respect to the WGS84 ellipsoid) from airborne laser altimetry around Crete. The sea surface height profiles were low-pass filtered using a 1D spline filter with a cut-off wavelength of 10 km. Background: bathymetry in [m] (contour interval 100 m).

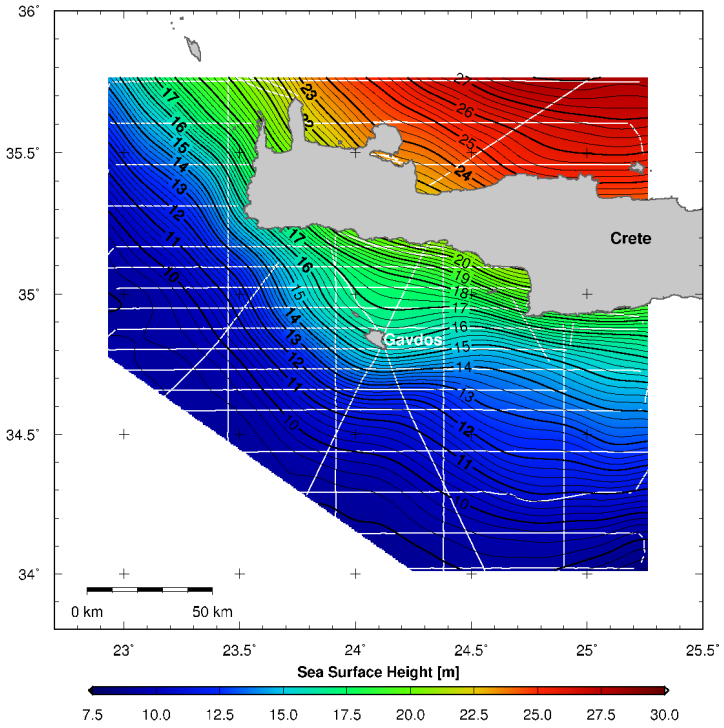

Figure 7.15: Sea surface topography (with respect to WGS84) obtained from airborne altimetry profiles around Crete (Fig. 7.14) by bicubic spline interpolation. The topography was low-pass filtered using a 2D FFT filter with a cut-off wavelength of 10 km. White lines: flight tracks. Contour interval: 0.25 m.

(a) without LSQ adjustment, without outlier removal

(b) without LSQ adjustment, with outlier removal

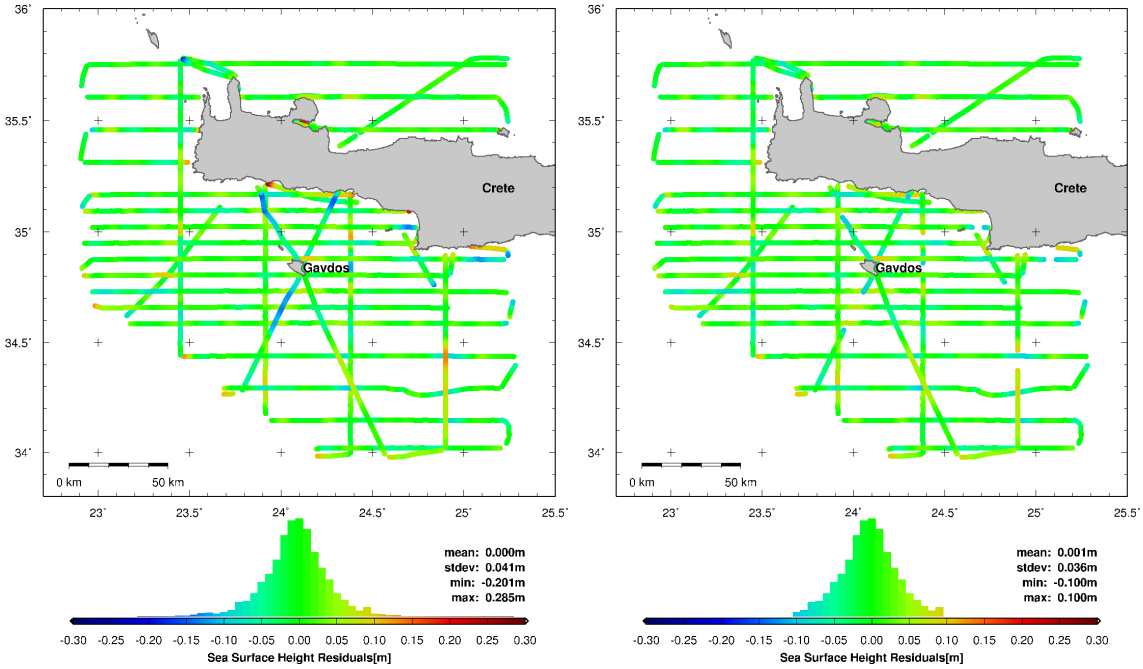

Figure 7.16: Residuals between along-track sea surface heights (Fig. 7.14) and gridded sea surface topography (Fig. 7.15), without correction from LSQ adjustment based on crosspoints, before **(a)** and after **(b)** outlier removal.

(a) with LSQ adjustment, without outlier removal

(b) with LSQ adjustment, with outlier removal

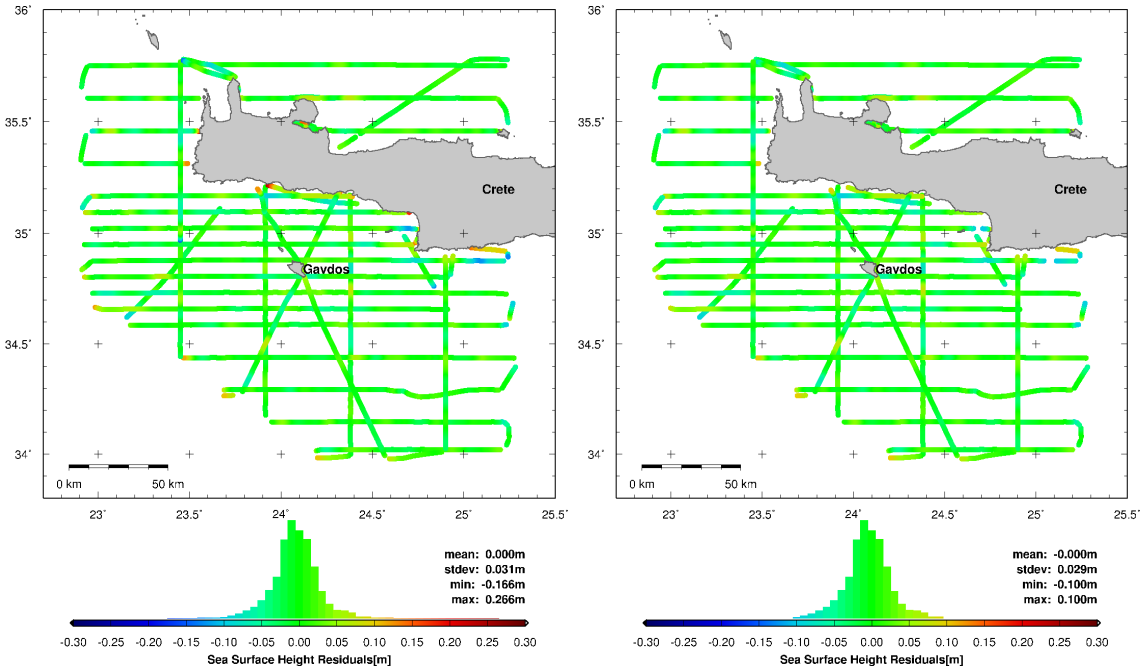

Figure 7.17: Residuals between along-track sea surface heights (Fig. 7.14) and gridded sea surface topography (Fig. 7.15), with correction from LSQ adjustment based on crosspoints, before **(a)** and after **(b)** outlier removal.

in the gridded sea surface topography, it is advisable to eliminate along-track data with large residuals prior to the surface generation. Using the LSQ adjustment, less observations had to be removed (Fig. 7.16b and Fig. 7.17b). After the removal of the outliers, the final residuals are all below 10 cm, with a standard deviation of only 2.9 cm (Fig. 7.17b).

The sea surface height results reveal very strong gradients, with heights decreasing from 28 m above the reference ellipsoid in the north-eastern part of the survey area down to 8 m towards the Hellenic Trench in the southern part, along a distance of only 200 km (Fig. 7.15). Further analysis and interpretation of the observed sea surface heigths are treated in Chapter 10.

8 Sea Surface Heights by Shipborne Ultrasound Altimetry in the North Aegean Sea

8.1 Shipborne Ultrasound Altimetry Campaigns

The survey area is situated in the North Aegean Sea and covers part of the North Aegean Trough (NAT), which is a tectonic graben-like feature characterized by a zone of deep water reaching 1500 m and trending from north-east to south-west in the North Aegean Sea (Fig. 8.1). The North Aegean Trough is considered to form the western continuation of the seismically active North Anatolian Fault Zone (McNeill et al., 2004). For calibration and validation purposes of radar altimeter missions, the survey area was chosen in the vicinity of Jason-1 ground tracks, including the crossover of Jason-1 ascending track 33 and descending track 94.

Five successful campaigns for shipborne sea surface height surveys were carried out in the North Aegean Sea from 2004 to 2008, totaling more than 2000 nautical miles of ship tracks (Fig. 8.1). The campaigns were carried out in Sept. 2004, June 2005, Sept. 2006, Sept. 2007 and July 2008. The boat was equipped with a multi-antenna GPS array of 4 - 5 GPS receivers, 1 - 2 ultrasonic distance sensors and an inertial Attitude and Heading Reference System (Section 5.2). Dedicated GPS buoy observations were performed on Jason-1 ground tracks and at other key spots, including deployments with simultaneous Jason-1 crossover. Five GPS reference stations, situated on the islands of Alonissos (ALON), Agios Efstratios (EFST), Limnos (LIMS) and Skiros (NSKS), as well as in Neohori (NEOH), were operated at a sampling rate of 1 Hz during the shipborne campaign. In June 2005 and Sept. 2007, the permanent tide-gauge stations PELAS and PELAN were installed in the survey area and operated since then.

8.2 Instantaneous Sea Surface Height Profiles

Sea surface profiles (Fig. 8.2 and Fig. 8.3) were computed with respect to the WGS84 reference ellipsoid, based on shipborne ultrasound range data, ship trajectories and attitudes, using the direct georeferencing method described in Chapter 6. During the shipborne campaigns, sea surface height data was collected while the ship was at rest and moving with varying velocity. This made inadequate the use of the spline filter algorithm, developed and applied for sea surface height observations by airborne laser altimetry (Section 7.2.1). Hence, a robust windowed median filter algorithm, allowing to switch between window sizes in the time and distance domain, was developed. The shipborne sea surface height results, with sampling rates of 1 Hz and 10 Hz, were low-pass filtered using the median filter with a moving-window size of 30 minutes or 500 m, depending on whether the ship was at rest or moving. The used windowed median filter algorithm is robust against outliers and is capable of processing the enormous amount of data points yielded by the 10 Hz ultrasound observations. In addition, as opposed to filter algorithms in the frequency domain based on Fourier transforms, the windowed median filter is indifferent to data gaps as observed throughout the ultrasound datasets.

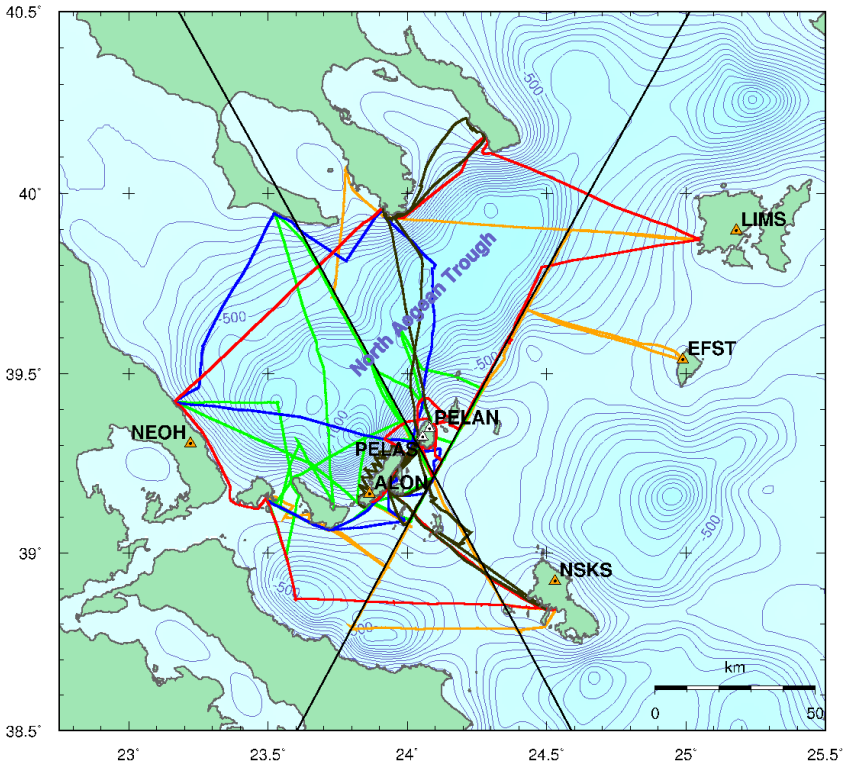

Figure 8.1: Shipborne sea surface height campaigns in the North Aegean Sea. Boat tracks from the campaigns in 2004 (orange line), 2005 (green line), 2006 (blue line), 2007 (red line) and 2008 (brown line). Black diagonal lines: Jason-1 tracks 33 (ascending) and 94 (descending). Orange triangles: GPS reference stations (ALON, EFST, LIMS, NSKS, NEOH). White triangles: tide-gauge stations (PELAS, PELAN). Background: bathymetry in [m] with contour interval 50 m.

8.3 Sea Surface Height Corrections

8.3.1 Ocean Wave Correction

The oscillation effects of ocean waves are eliminated by the low-pass filtering (Section 8.2). Further details on ocean waves are given in Section 3.2.

8.3.2 Ocean Tide Correction

In the North Aegean Sea, the amplitudes of the major ocean tide constituents M2 and S2 are in the order of 15 cm and 10 cm, respectively (Fig. 3.3). The tidal effects to be expected in the North Aegean Sea are thus stronger than in the survey area around Crete. Tidal corrections along the shipborne altimetry tracks were computed with the global tide model FES2004 (Fig. 8.4a) and the POL (Proudman Oceanographic Laboratory) model for Mediterranean (Fig. 8.4b). Further details on these ocean tide models can be found in Section 3.3.2. Both models predict ocean tide amplitudes in the order of 15 - 20 cm. However, the predictions are contradictory, since the differences between the models reach up to 20 cm (Fig. 8.4c). Considering the size of the tidal amplitudes and of the differences between the models, the choice of the tide model is crucial for the accuracy of the corrected sea surface heights.

In order to select the most appropriate model for the considered survey area, a validation of the

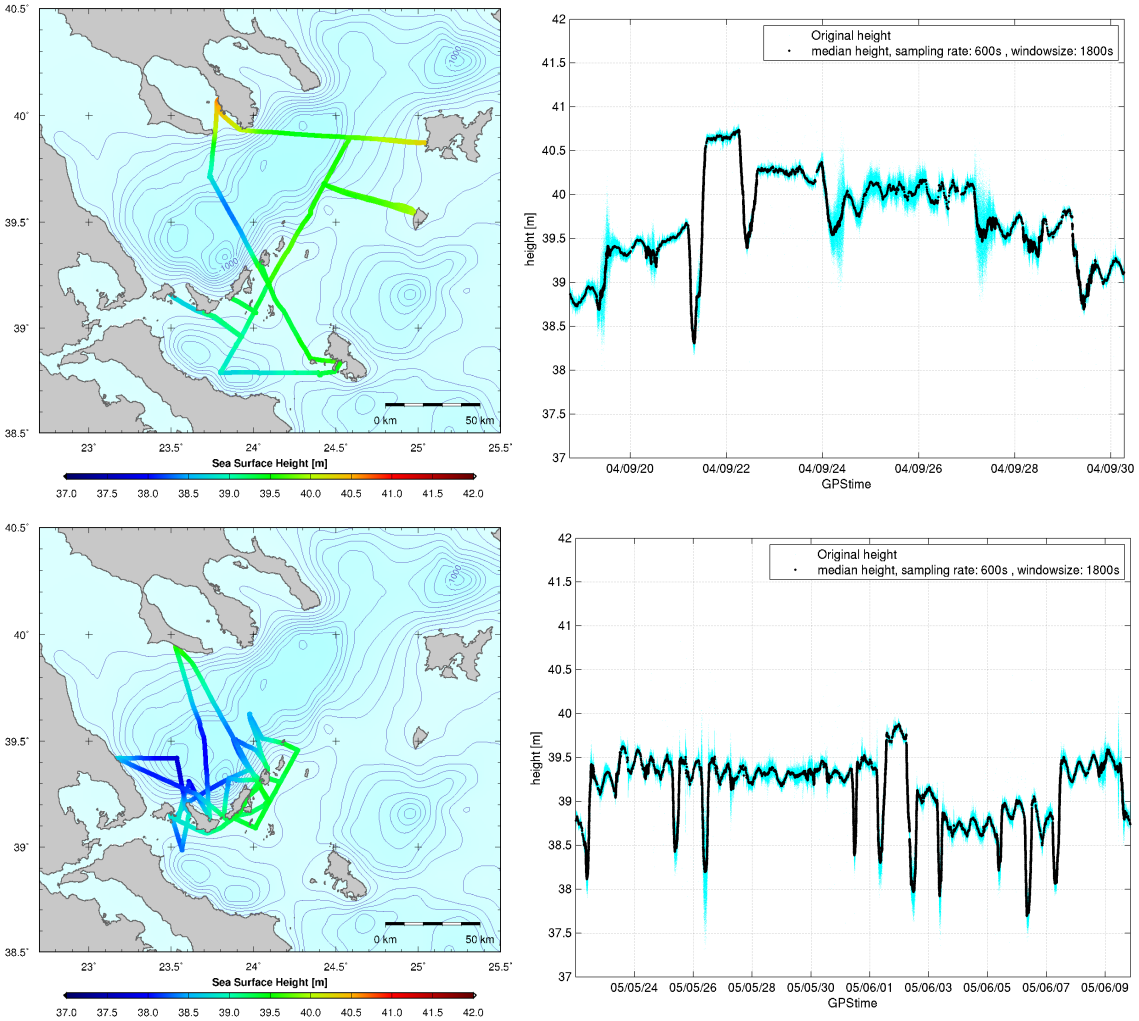

Figure 8.2: Left: Sea surface height profiles from shipborne altimetry campaigns in 2004 (top) and 2005 (bottom). Right: Corresponding time series of instantaneous sea surface heights (with respect to the WGS84 reference ellipsoid) with original sampling rate of 10 Hz (light line) and filtered heights (black line).

tidal corrections obtained from the two models was performed, based on tide-gauge observations (Section 8.3.4) and on a crosspoints analysis (Section 8.4.1). The POL model was identified to agree better with the in situ observations and was therefore chosen to correct the shipborne sea surface height data in the North Aegean Sea.

8.3.3 Correction for Atmospheric Pressure and Wind Forcing

Corrections for the effect of atmospheric pressure and wind forcing on sea surface heights were computed from the MOG2D correction grids (Section 3.4.2 and Appendix G). Corrections along the shipborne altimetry tracks were obtained by spatiotemporal interpolation of the MOG2D grids (Fig. 8.5). The atmospheric effect along the ship tracks ranges from -16 cm to 12 cm during the survey campaigns. Extreme variations of the atmospheric effect of up to 10 cm/day are encountered. For the area and period of the considered dataset, the effect of atmospheric pressure and wind forcing reaches values similar to the amplitudes of ocean tides (Fig. 8.4).

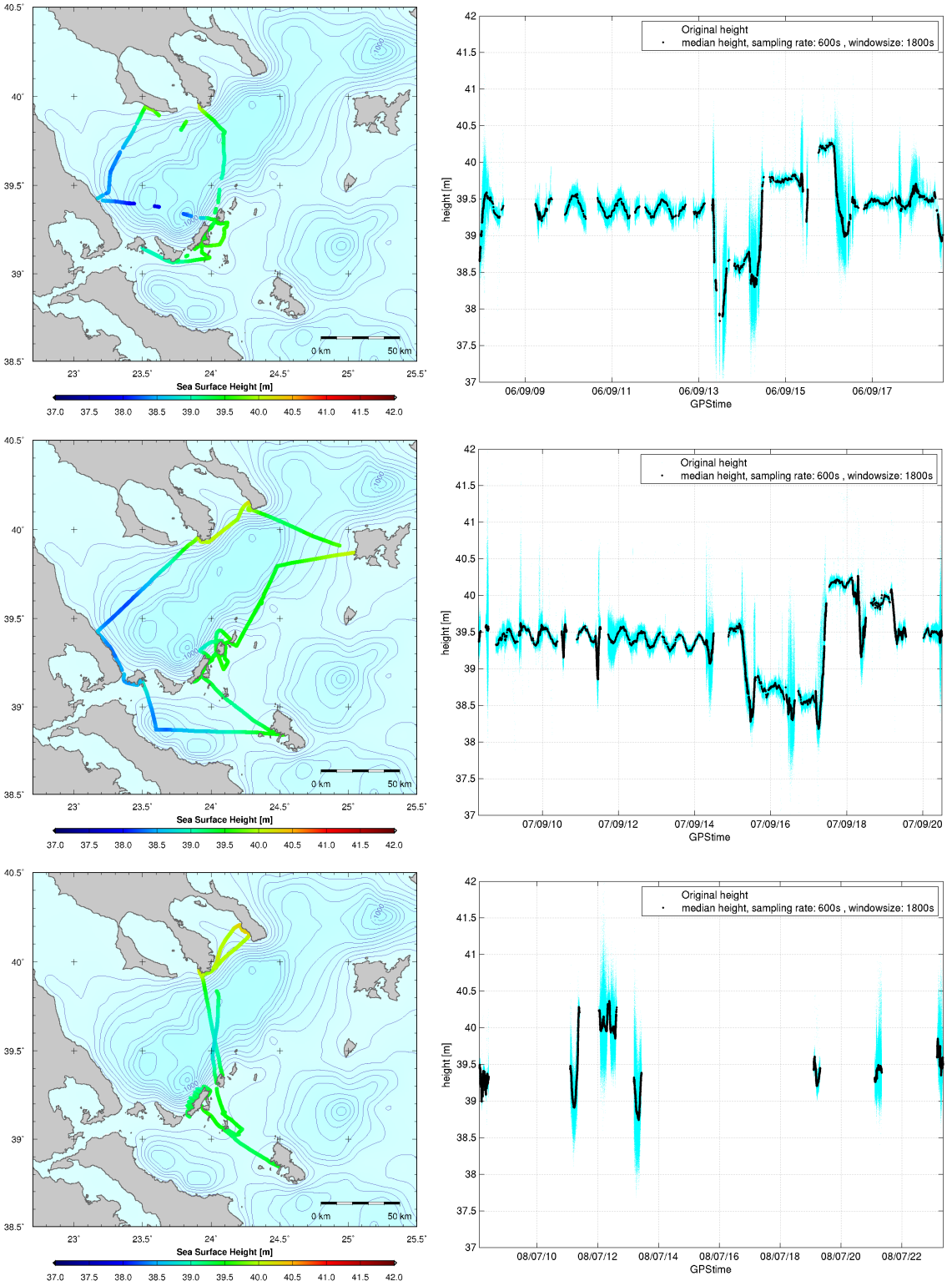

Figure 8.3: Left: Sea surface height profiles from shipborne altimetry campaigns in 2006 (top), 2007 (center) and 2008 (bottom). Right: Corresponding time series of instantaneous sea surface heights (with respect to the WGS84 reference ellipsoid) with original sampling rate of 10 Hz (light line) and filtered heights (black line).

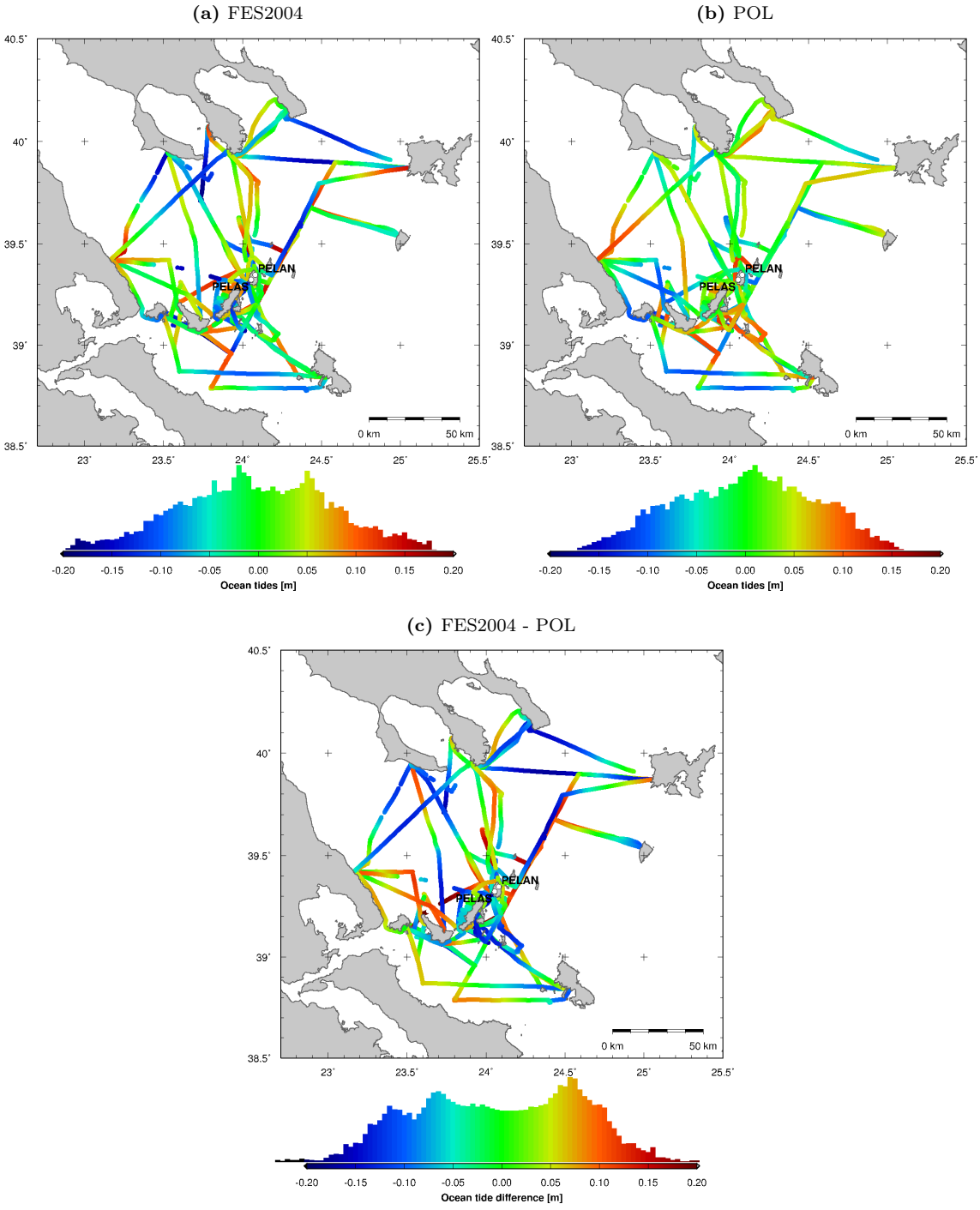

Figure 8.4: Ocean tide predictions along shipborne tracks from the models **(a)** FES2004 and **(b)** POL (Proudman Oceanographic Laboratory). **(c)** Differences between the tides from FES2004 and POL.

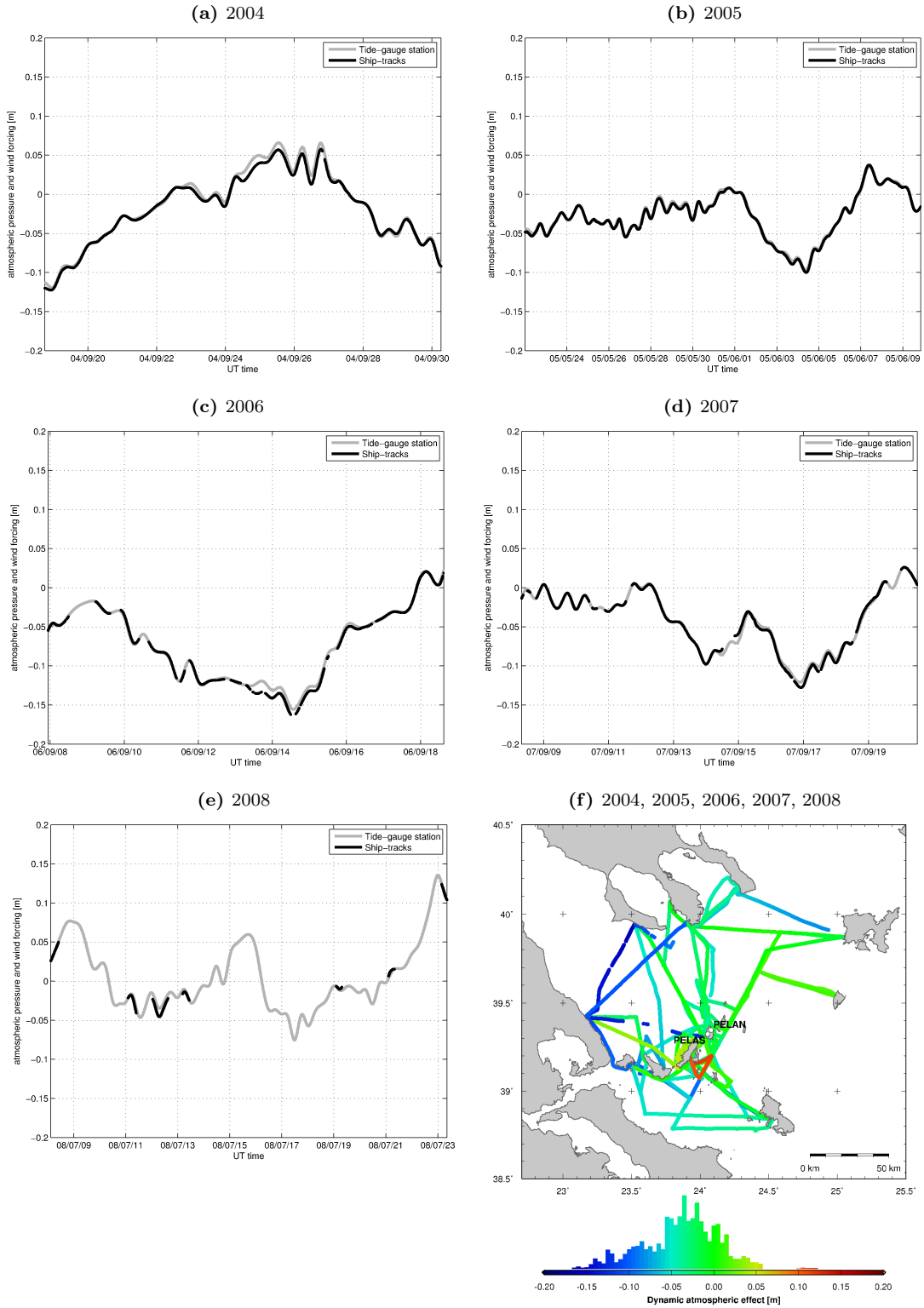

Figure 8.5: Effect of atmospheric pressure and wind forcing on sea surface height during shipborne surveys in 2004 **(a)**, 2005 **(b)**, 2006 **(c)**, 2007 **(d)** and 2008 **(e)**, based on MOG2D correction grids. Black line: time series along ship tracks. Gray line: time series at PELAN tide-gauge station. **(f)** Effect along ship tracks during all campaigns, corresponding to the time series of (a) to (e).

8.3.4 Validation of Tidal and Atmospheric Corrections with Tide-Gauge

A validation of the FES2004 and POL tidal corrections, as well as the MOG2D atmospheric corrections, was carried out using local tide-gauge data. The considered tide observations are from the PELAN tide-gauge station, installed in the framework of this project (Fig. 8.1 and Fig. 8.6). The sea surface heights recorded by tide-gauges are affected by astronomic ocean tides and the forcing of atmospheric pressure and wind. In order to compare tide-gauge data to the predictions obtained from tide models, the effects of atmospheric forcing have to be removed from the tide-gauge data. Tide data covering 9 consecutive months were analyzed. In a first step, the atmospheric effect from MOG2D correction grids were removed from the tide-gauge observations (Fig. 8.7). In a second step, a remaining low frequency trend (period $>$ 48 h) was removed from the observations. This trend, ranging between -18.5 cm and 14.3 cm, mainly represents the remaining local effect of atmospheric forcing, not resolved by MOG2D.

Differences between the corrected tide-gauge observations and predictions from FES2004 show a large standard deviation of 8.6 cm and large maximum values of 25 cm (Fig. 8.8a). The FES2004 predictions do not match the observed tidal signal: e.g. the spring and neap tides do not coincide in time (Fig. 8.8b). Predictions from the POL model show a good agreement with the observed tidal signal (Fig. 8.8c and Fig. 8.8d). Differences have a standard deviation of 2.5 cm and maximum values of 8 cm. Hence, despite the fact that only 4 tidal constituents (M2, S2, K1, O1) are included in the POL model (against 14 constituents for FES2004), the POL predictions are in better agreement with local tide-gauge data than FES2004. The discrepancies between the tide-gauge observations and the POL model are most likely due to local coastal effects, not resolved by the tidal and atmospheric forcing models. It can be assumed that the model performs better offshore, in the absence of strong and hardly predictable coastal effects.

To further analyze the tidal signal observed in the survey area of the North Aegean Sea, amplitudes and phase lags of the 9 major tidal constituents (M2, S2, K2, N2, 2N2, K1, O1, P1, Q1) were estimated by harmonic analysis (3.4) of the corrected tide-gauge data at PELAN. The amplitudes and phase lags obtained by harmonic analysis are in good agreement with the POL model (Tab. 8.1). The amplitudes agree better than 0.4 cm and the phase lags better than 9°. On the other hand, a poor agreement with the amplitudes and phase lags of FES2004 is obtained. The maximum amplitude difference is 2.9 cm and the maximum phase lag difference is 107°. The poor agreement is most likely a consequence of a lack of Aegean tide-gauge data in the assimilation of FES2004. This assumption was confirmed by analysing tidal predictions from FES2004 and POL in the Western Mediterranean, where local tide-gauge data are assimilated in FES2004. In this area, a good agreement between the two models is observed. Using the amplitudes and phase lags

Figure 8.6: Left: Pressure tide-gauge station PELAN, with GPS antenna for the determination of absolute position and height. Right: view of the pressure gauge inside the tube.

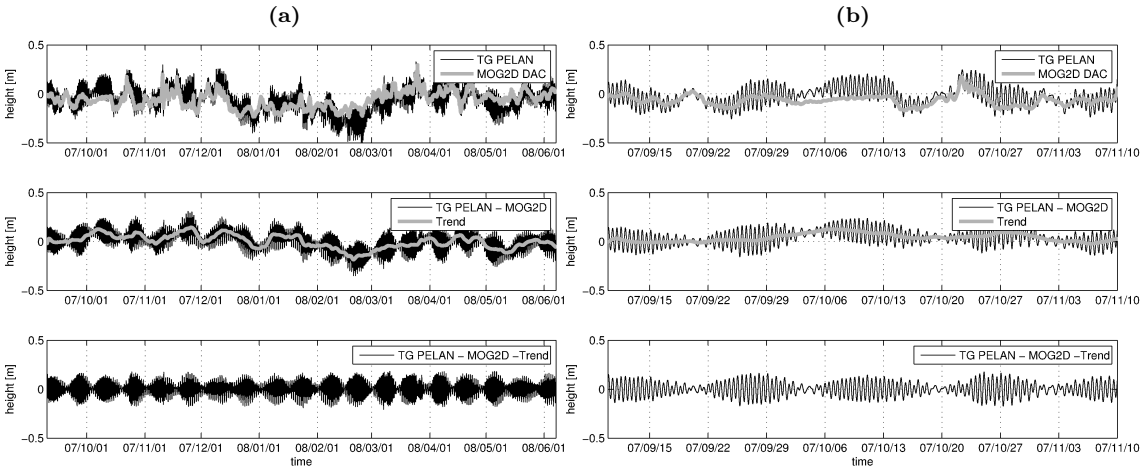

Figure 8.7: **(a)** Top: Sea level observations from PELAN tide-gauge in the North Aegean Sea, from Sept. 2007 to June 2008 (9 months), and dynamic atmospheric corrections (DAC) from MOG2D. Center: Tide-gauge data corrected with MOG2D DAC and remaining trend. Bottom: Tide-gauge data corrected with MOG2D DAC and with remaining trend removed. **(b)** Zoom into first 2 months of (a).

Table 8.1: Amplitudes and phase lags of the major harmonic constituents of the astronomical ocean tide at the PELAN tide-gauge site in the North Aegean Sea, estimated by harmonic analysis of local tide-gauge data (TG) and extracted from FES2004 and POL grids.

	Period	Amplitude [m]			Phase lag [°]		
Wave	[days]	TG	FES2004	POL	TG	FES2004	POL
M2	0.51753	0.075	0.078	0.079	59	-25	68
S2	0.50000	0.052	0.035	0.054	80	103	82
K2	0.49863	0.020	0.014	-	52	88	-
N2	0.52743	0.015	0.044	-	55	-17	-
2N2	0.53772	0.002	0.006	-	85	74	-
K1	0.99727	0.029	0.017	0.029	-18	-69	-17
O1	1.07581	0.014	0.035	0.015	-47	-58	-40
P1	1.00275	0.009	0.007	-	-15	-70	-
Q1	1.11951	0.002	0.006	-	-71	36	-

obtained by harmonic analysis of the tide-gauge data (Tab. 8.1), local tides can be predicted using (3.4). Residuals between the corrected tide-gauge data and the predictions from the harmonic analysis have a small standard deviation of 1.3 cm and maximum values of 8 cm (Fig. 8.8e and Fig. 8.8f), showing the good approximation of the observed tides by the harmonic model of the 9 tidal constituents M2, S2, K2, N2, 2N2, K1, O1, P1, Q1.

8.3.5 Sea Level Anomaly Correction

Sea level anomalies (SLA) were computed for the survey campaigns in the North Aegean Sea, based on SSALTO/DUACS products (Section 2.4). During the 5 campaigns, the SLA vary between -6 cm and 13 cm (Fig. 8.9). Within the same campaign of 2 - 3 weeks, SLA variations of 5 - 10 cm are encountered, and systematic SLA differences are observed between the campaigns. The campaigns of 2004, 2006 and 2007, carried out in September, show positive SLA of 5 - 13 cm, whereas the campaigns of 2005 and 2008, carried out in May/June and July, show negative SLA of -5 to 0 cm. The SLA show that even after removing the effects of waves, tides and atmospheric forcing, the

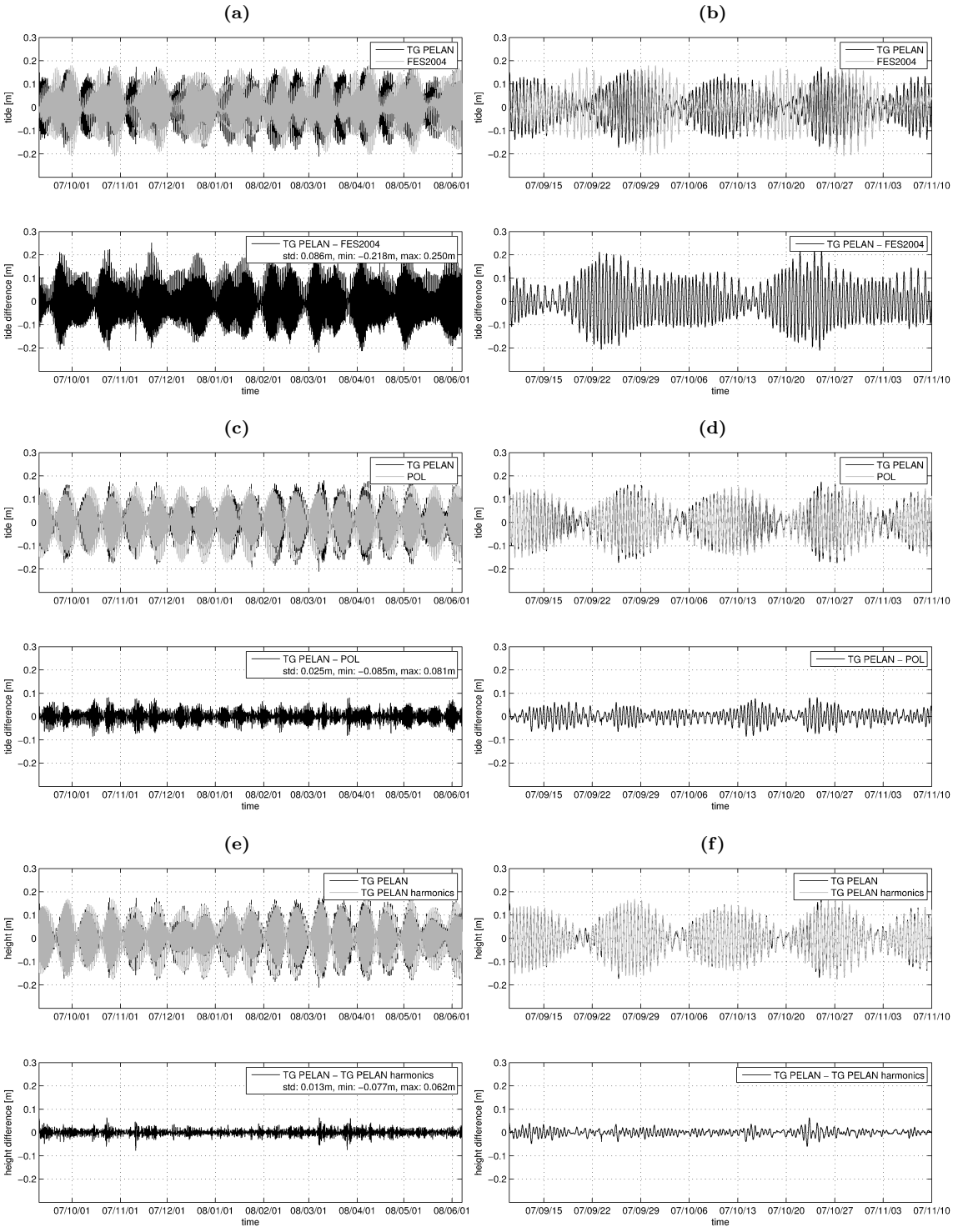

Figure 8.8: **(a)** Top: Tidal predictions from FES2004 against corrected observations from PELAN tide-gauge in the North Aegean Sea, from Sept. 2007 to June 2008 (9 months), corresponding to Fig. 8.7, bottom. Bottom: Difference between tide-gauge data and FES2004 predictions. **(c)** Same as (a), but for FES2004 predictions replaced with POL predictions. **(e)** Same as (a), but for FES2004 predictions replaced with predictions based on the harmonic analysis of the PELAN tide-gauge data (Tab. 8.1). **(b)**, **(d)** and **(f)** Zoom into first 2 months of (a), (d) and (e).

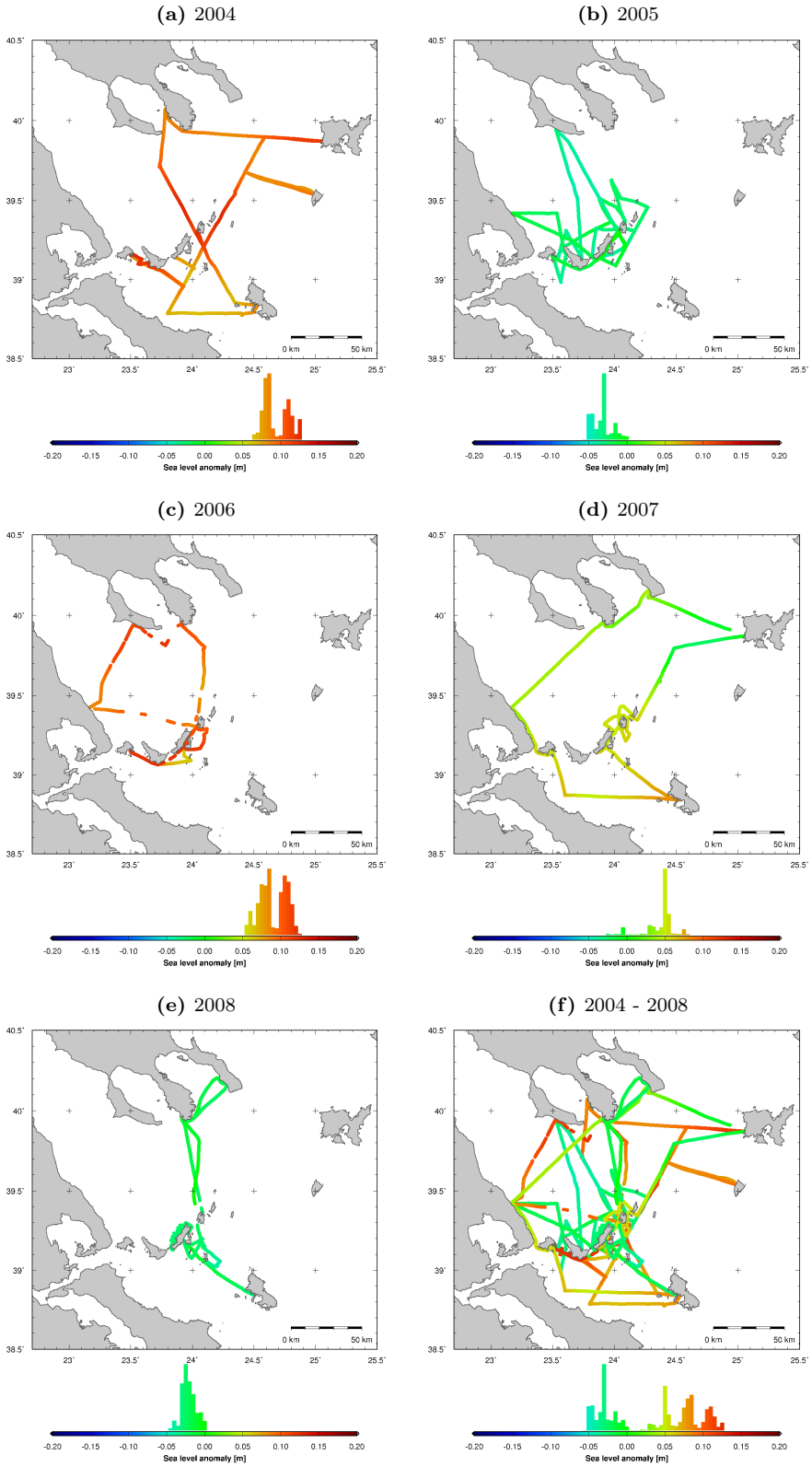

Figure 8.9: Sea level anomalies along ship tracks, based on SSALTO/DUACS sea level anomalies, during shipborne surveys in 2004 **(a)**, 2005 **(b)**, 2006 **(c)**, 2007 **(d)**, 2008 **(e)** and from 2004 to 2008 **(f)**.

sea surface topography cannot be considered as constant from one campaign to the next, and even not during the same campaign. The significant improvement of height differences at crosspoints of the shipborne profiles after application of the SLA corrections is shown in Section 8.4.1. These corrections should therefore be applied when the resulting heights are meant to represent the mean sea surface MSS, as defined in (2.2) and (2.28). On the other hand, they must not be applied when the resulting heights are meant to represent corrected sea surface heights SSH, including the variable part of the dynamic topography, as defined in (2.1) and (2.27).

8.4 Repeatability Analysis

8.4.1 Crosspoints Analysis

The shipborne profiles yield 1999 crosspoints, where the sea surface height was observed twice at the same position (Fig.8.11). Height differences at crosspoints are a good indicator for the repeatability and the accuracy of the shipborne altimetry system. An analysis of these height differences computed with different combinations of tidal and atmospheric sea surface height corrections, as well as sea level anomaly (SLA) corrections, was carried out (Tab. 8.2 and Fig. 8.10). Significant differences are observed between the various combinations of corrections. The analysis shows that the POL (Proudman Oceanographic Laboratory) tidal corrections reduce the RMS on the height differences at crosspoints by 4.8 cm and the maximum absolute difference by 8.0 cm. Applying tidal corrections directly from local tide-gauge data produces a slightly worse agreement with the shipborne data (not shown), due to the fact that the tide-gauge data is affected by local coastal effects. The FES2004 tidal corrections have no improving effects on the height differences. The MOG2D atmospheric corrections reduce the RMS on the height differences by 2.0 cm and the maximum absolute difference by 7.7 cm. Finally, the SLA corrections reduce the RMS on the height differences by 3.8 cm and the maximum absolute difference by 8.6 cm. The beneficial effect of the SLA corrections is further shown by analyzing height differences at crosspoints separately for each campaign. Offsets at crosspoints between the campaigns were estimated (Tab. 8.3). Without SLA corrections, systematic offsets of up to 13.5 cm are observed when at crosspoints between one campaign and the other four campaigns. These offsets are reduced to below 2 cm by applying SLA corrections.

The crosspoint analysis leads to the conclusion that the best result is obtained using POL tidal corrections in combination with MOG2D atmospheric corrections and SSALTO/DUACS SLA corrections (Fig. 8.10). Using this set of corrections, the final RMS of height differences at the 1999 crosspoints is 7.9 cm (Tab. 8.2 and Fig. 8.11a). The RMS at the 824 inner-campaign crosspoints is 6.8 cm, whereas the RMS at the remaining 1175 inter-campaign crosspoints is 8.6 cm. The height difference remains below 10 cm at 80% of the crosspoints, below 15 cm at 94% and below 20 cm at 99% of the crosspoints. The maximum observed height difference is 28.7 cm. A final outlier rejection was only carried out during the surface generation and data gridding (Section 8.5). The outlier removal would further improve the height differences at crosspoints and eliminate most of the differences above 15 cm. At this stage, however, the objective of the crosspoint analysis was not to give the best possible results by eliminating all outliers, but to give a realistic impression of the accuracy and repeatability of the shipborne altimetry method, prior to a thorough outlier removal.

8.4.2 LSQ Adjustment Based on Crosspoints

After the application of the best combination of corrections, namely POL tidal corrections in combination with the MOG2D atmospheric corrections and the SSALTO/DUACS SLA corrections, a relatively large amount (20%) of height differences at crosspoints remains above 10 cm (Sec-

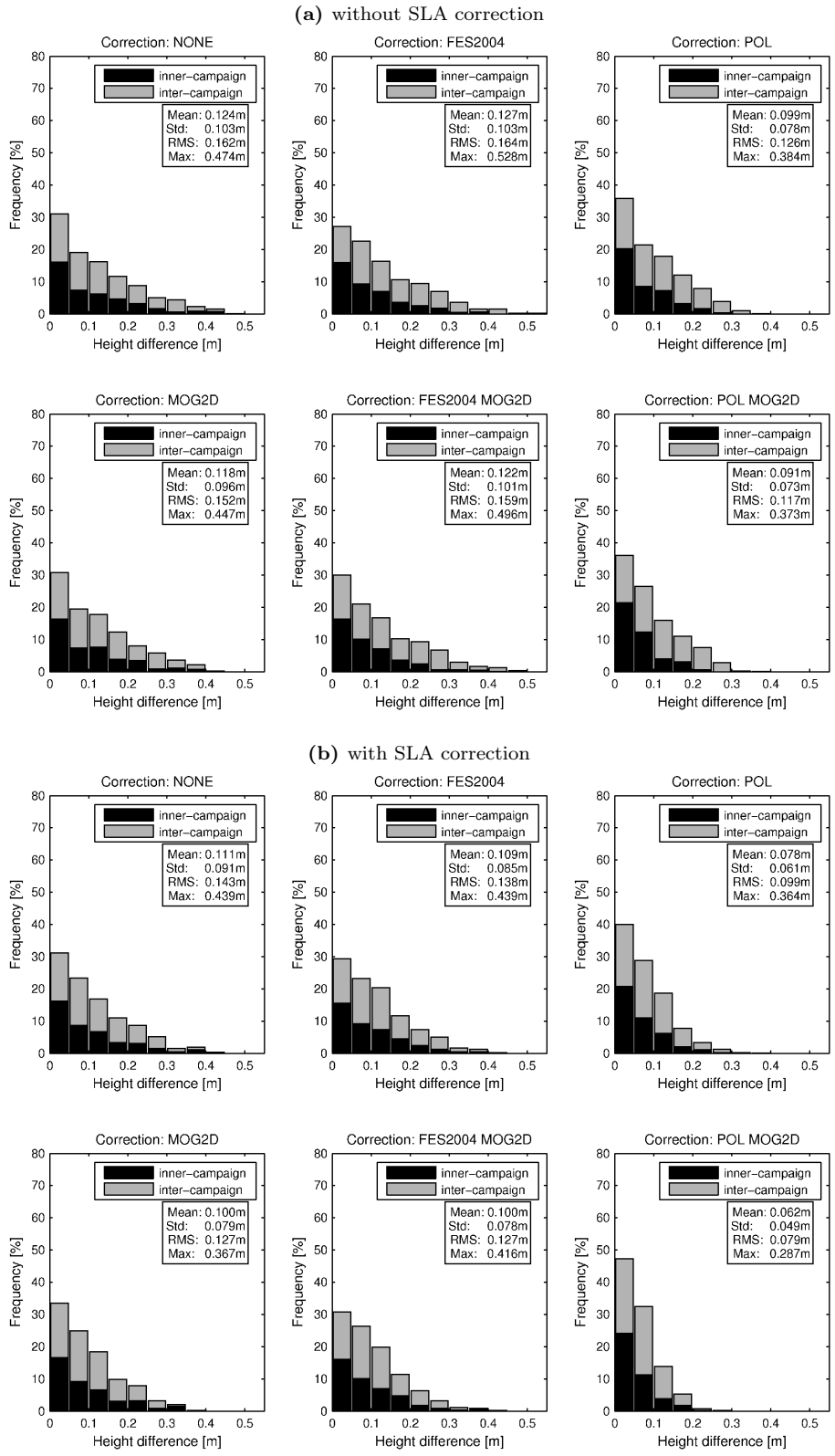

Figure 8.10: Distributions of height differences at crosspoints using different combinations of tidal and atmospheric corrections (corresponding to Tab. 8.2), without **(a)** and with **(b)** sea level anomaly (SLA) correction. Black: inner-campaign crosspoints. Gray: inter-campaign crosspoints.

Table 8.2: RMS [m] of height differences at crosspoints for solutions with different combinations of tidal and atmospheric sea surface height corrections, without sea level anomaly (SLA) correction, with SLA correction and with combined SLA correction and LSQ adjustment.

	Tidal/Atmospheric sea surface height correction					
Tidal	-	FES2004	POL	-	FES2004	POL
Atmospheric	-	-	-	MOG2D	MOG2D	MOG2D
All 1999 crosspoints						
RMS [m]	0.162	0.164	0.126	0.152	0.159	0.117
RMS [m] (SLA)	0.143	0.138	0.099	0.127	0.127	0.079
RMS [m] (SLA+LSQ)	-	-	-	-	-	0.055
Inner-campaign 824 crosspoints						
RMS [m]	0.144	0.129	0.095	0.131	0.119	0.078
RMS [m] (SLA)	0.137	0.124	0.084	0.125	0.116	0.068
RMS [m] (SLA+LSQ)	-	-	-	-	-	0.042
Inter-campaign 1175 crosspoints						
RMS [m]	0.173	0.185	0.144	0.165	0.181	0.137
RMS [m] (SLA)	0.147	0.147	0.108	0.129	0.134	0.086
RMS [m] (SLA+LSQ)	-	-	-	-	-	0.062

Table 8.3: Offsets (dh) and their standard deviations (std) between height differences at crosspoints from different campaigns. The offset of the 2004 campaign was set to 0.

	without SLA correction		with SLA correction	
Campaign	dh [m]	±std [m]	dh [m]	±std [m]
2004	0.000	±0.000	0.000	±0.000
2005	0.135	±0.005	0.002	±0.004
2006	0.027	±0.006	0.006	±0.005
2007	0.036	±0.006	-0.019	±0.006
2008	0.100	±0.007	-0.020	±0.007

tion 8.4.1). These misfits are causing problems during surface generation (Section 8.5). Hence, as a final correction, an LSQ adjustment of the profiles was carried out, estimating a linear correction for every ship track that reduces the height differences at the crosspoints in a least-squares sense. The irregular distribution of the ship tracks yields an inhomogeneous distribution of crosspoints along the tracks, which makes the LSQ adjustment less efficient than in the case of the airborne data (Section 7.4.3). Corrections of up to 15.4 cm are obtained by the LSQ adjustment, providing a significant improvement of the height differences (Tab. 8.2 and Fig. 8.11b). Using POL tidal corrections, MOG2D atmospheric corrections and SLA corrections in combination with the LSQ adjustment, the RMS of the height differences is reduced to 5.5 cm, corresponding to an improvement of 30%. After the LSQ adjustment, height differences remain below 5 cm at 67% of the 1999 crosspoints and below 10 cm at 94% of the crosspoints. The maximum observed height difference was reduced from 28.7 to 23.1 cm. The beneficial impact of the LSQ adjustment for the surface generation procedure is shown in Section 8.5.

8.5 Time-Independent Sea Surface Topography

By subtracting the time-dependent corrections (Section 8.3) from the low-pass filtered instantaneous sea surface heights (Section 8.2, Fig. 8.2 and Fig. 8.3), time-independent sea surface height profiles are obtained (Fig. 8.12).The sea surface heights are computed with respect to the WGS84 reference ellipsoid. Based on the analysis of sea surface height corrections in Section 8.4.1, the observed sea surface heights were corrected using POL tidal corrections, MOG2D atmospheric cor-

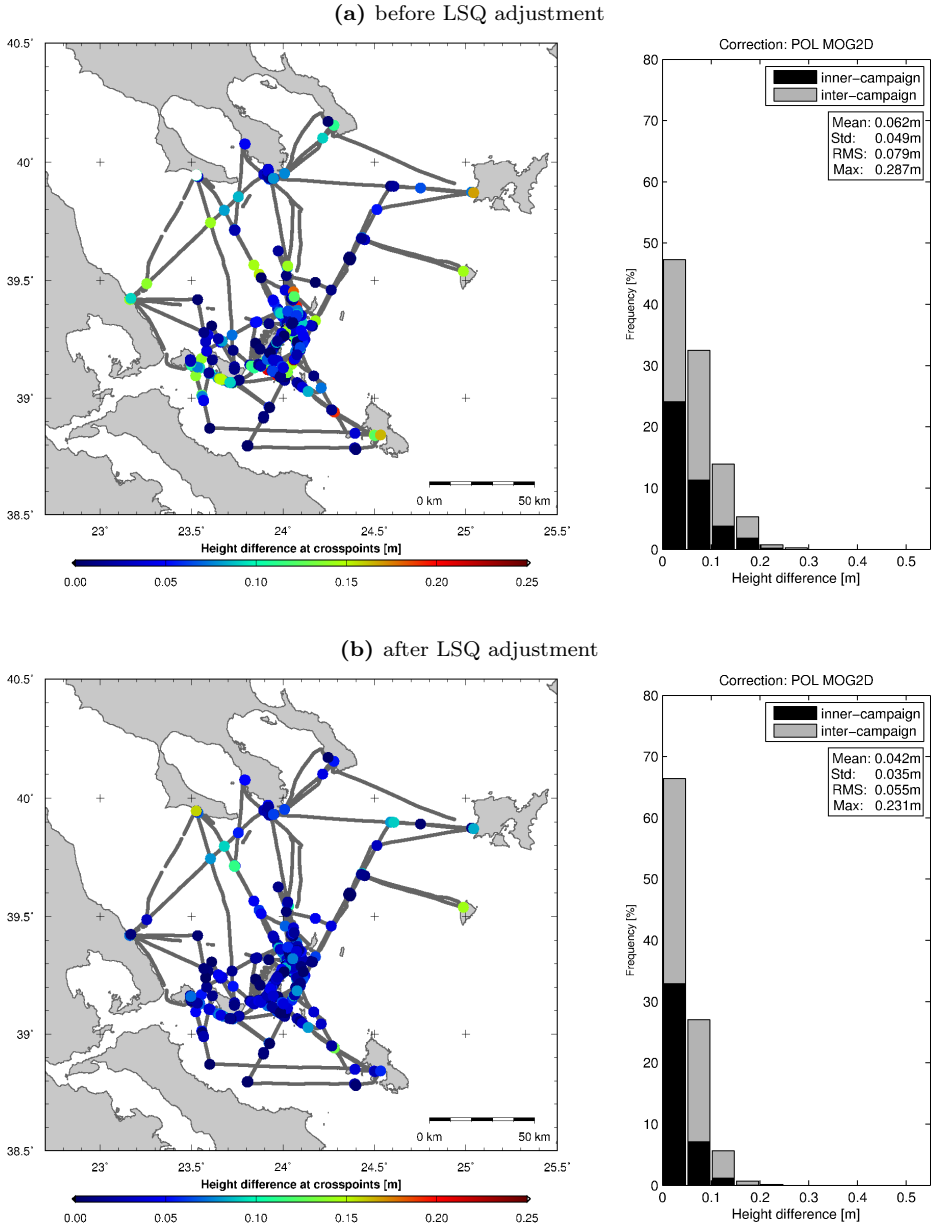

Figure 8.11: **(a)** Crosspoints of sea surface height profiles with height differences and their distribution, using POL tidal corrections, MOG2D atmospheric corrections and SSALTO/DUACS sea level anomaly corrections. **(b)** Same as (a), but with LSQ adjustment of ship tracks based on crosspoints.

rections and SLA corrections from SSALTO/DUACS. Furthermore, the sea surface heights were corrected using an LSQ adjustment of the profiles in order to reduce the height differences at crosspoints (Section 8.4.2).

The resulting punctual time-independent sea surface heights were interpolated onto a regular grid using a bicubic spline interpolation with continuous curvature and adjustable tension. In a second step, the obtained gridded sea surface heights were low-pass filtered using a 2D FFT filter with a cut-off wavelength of 10 km. The cut-off wavelength of the FFT filter was optimally chosen in order to keep the residuals small, without obtaining an unrealistically rough surface. The gridded data are forming a surface representing the time-independent sea surface topography (Fig. 8.13).

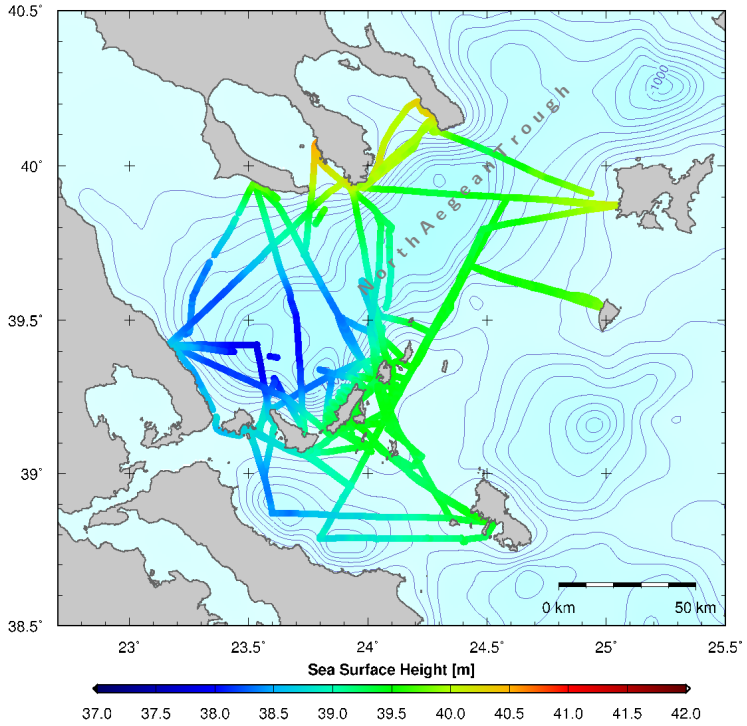

Figure 8.12: Time-independent sea surface height profiles (with respect to WGS84 ellipsoid) from shipborne altimetry in the North Aegean Sea. The sea surface height profiles were low-pass filtered using a windowed median filter. Background: bathymetry in [m] (contour interval 100 m).

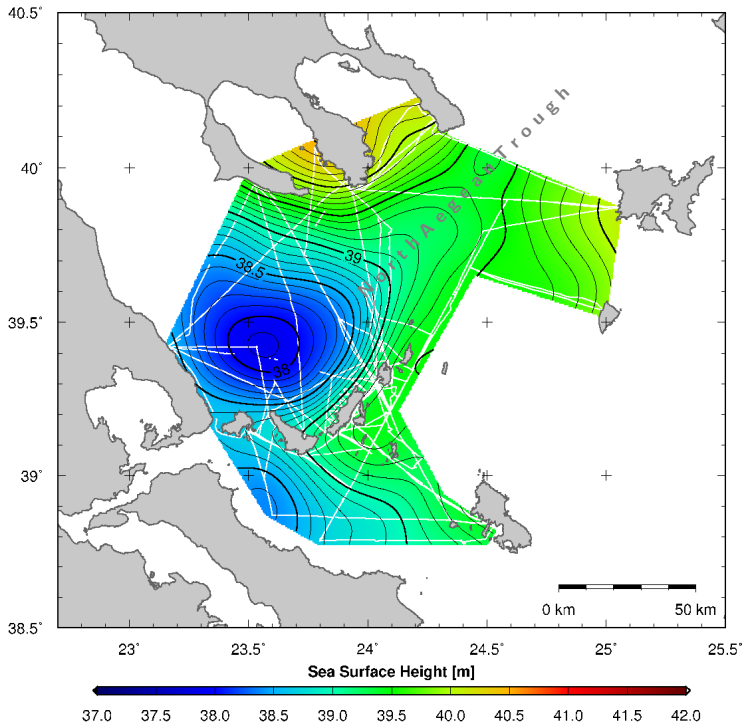

Figure 8.13: Sea surface topography (with respect to WGS84) obtained from shipborne altimetry profiles in the North Aegean Sea (Fig. 8.12) by bicubic spline interpolation. The topography was low-pass filtered using 2D FFT filter with a cut-off wavelength of 10 km. White lines: ship tracks. Contour interval: 0.1 m.

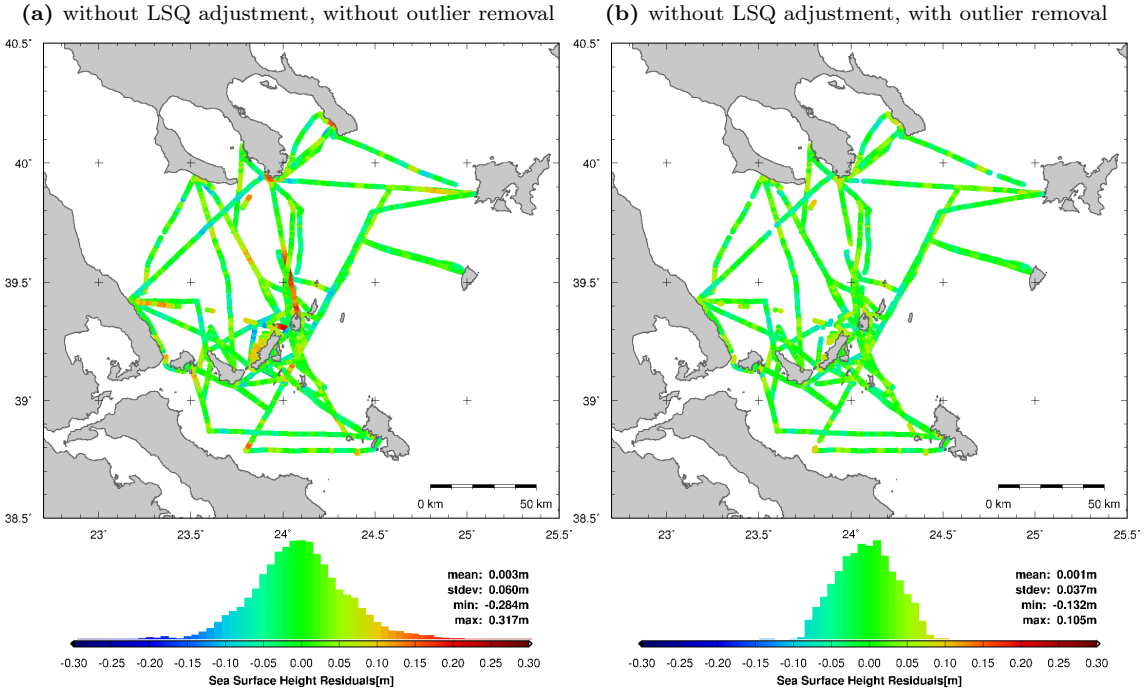

Figure 8.14: Residuals between along-track sea surface heights (Fig. 8.12) and gridded sea surface topography (Fig. 8.13), without correction from LSQ adjustment based on crosspoints, before **(a)** and after **(b)** outlier-removal.

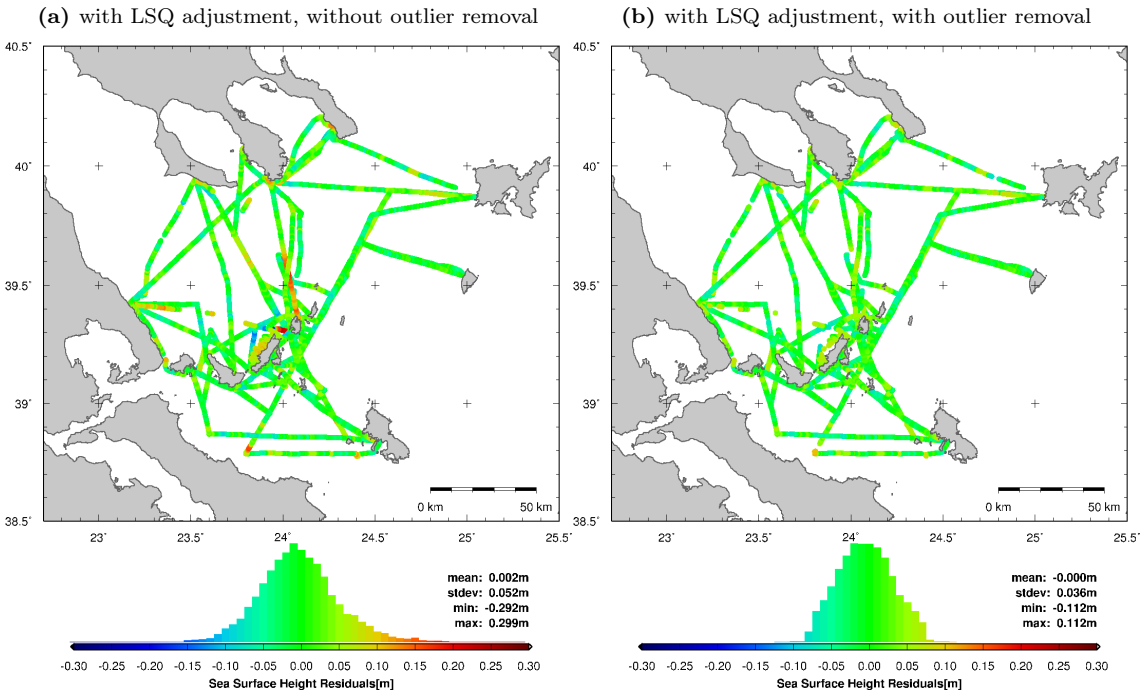

Figure 8.15: Residuals between along-track sea surface heights (Fig. 8.12) and gridded sea surface topography (Fig. 8.13), with correction from LSQ adjustment based on crosspoints, before **(a)** and after **(b)** outlier-removal.

A final indication for the accuracy of the sea surface heights is given by the residuals between the time-independent sea surface height profiles (Fig. 8.12) and the gridded sea surface topography (Fig. 8.13). Without the LSQ adjustment (Section 8.4.2), the along-track residuals have a standard deviation of 6.0 cm and large local values of up to 32 cm (Fig. 8.14a). After the LSQ adjustment, the residuals are significantly improved (Fig. 8.15a). The standard deviation is reduced to 5.2 cm, but large residuals of up to 30 cm locally remain. In order to avoid unrealistic strong gradients in the gridded sea surface topography, it is advisable to eliminate along-track data with large residuals prior to the surface generation. Using the LSQ adjustment, less observations had to be removed (Fig. 8.14b and Fig. 8.15b). After the removal of the outliers, the final residuals are all below 12 cm, with a standard deviation of only 3.6 cm (Fig. 8.15b).

The sea surface height results in the North Aegean Sea reveal a distinct depression of the sea surface in the western part of the survey area, associated with the bathymetric low of the south-western end of North Aegean Trough (Fig. 8.13). The depression reaches a minimum of 37.9 m above the WGS84 ellipsoid, while the height in the surrounding area is more than 39.5 m and reaches even 40.5 m towards the north of the survey area. Further analysis and interpretation of the observed sea surface heights are treated in Chapter 11.

9 Validation of Satellite Radar Altimetry Data

9.1 Introduction

The basic means to monitor the sea surface on a global scale is satellite radar altimetry. Technological developments have transformed satellite radar altimetry from a technique by which major geoid features with order 10 m amplitudes could be resolved to one where resolution of dynamic ocean signals as small as a few cm is possible (Chelton, 1988). Details on satellite radar altimetry can be found in (Chelton, 1988; Chelton et al., 2001; Picot et al., 2003; OSTM, 2008).

An important aspect when analyzing satellite radar altimetry data in region with steep geoid gradients is the slope-induced height error. Radar altimeters measure the two-way travel time to the closest point on the Earth's surface within the antenna beam (Fig. 9.1). The footprint diameter of the Jason-1 and TOPEX/Poseidon altimeters is e.g. around 10 km. Hence, steep geoid gradients can have minor effects on the observed sea surface heights, since the point at the sea surface closest to the radar altimeter, to which the range is measured, can differ from the sub-satellite nadir point. For a planar surface of constant slope α, the slope-induced height error Δh with respect to nadir is given by (Zwally and Brenner, 2001) (Fig. 9.1):

$$\Delta h \;=\; h \;-\; r \;=\; h\,(1 \;-\; \cos\alpha) \tag{9.1}$$

where h is the true altitude of the satellite above ground and r is the range measured by the radar altimeter. The altitude h is the target parameter actually sought by radar altimetry, in order to subtract it from the satellite altitude with respect to the reference ellipsoid. The horizontal displacement Δx of the measured point P with respect to the sub-satellite nadir point S is given by (Zwally and Brenner, 2001) (Fig. 9.1):

$$\Delta x \;=\; h\;\cos\alpha\;\sin\alpha \tag{9.2}$$

Without prior detailed knowledge of the topography of the surface observed by radar altimetry, the location from which the radar reflection originates cannot be determined. One difficulty in correcting for slope-induced errors is the variation of the slope within the beam-limited footprint, both along and across the satellite ground track, which makes the selection of an appropriate slope α difficult (Zwally and Brenner, 2001). Due to these difficulties and the negligible impact of slope-induced errors in most cases, it is common practice not to correct satellite radar altimetry data for slope-induced errors. In this case, the altitude h is approximated by the observed range r.

In the survey area around Crete, extreme geoid gradients of up to 0.22 m/km (45 arcsec) are observed (Fig. 10.1c), corresponding to a slope α of 0.013°. Using the equatorial reference altitude of 1336 km for Jason-1 as approximate altitude h above ground in (9.1), a slope-induced height error Δh of 3.2 cm is obtained. The associated horizontal displacement Δx is 294 m (9.2). Hence, under the extreme geoid gradients encountered in the survey area, the maximum slope-induced height error of satellite radar altimetry observations can reach noticeable values, but it still remains within the expected accuracy level of airborne, shipborne and spaceborne altimetry.

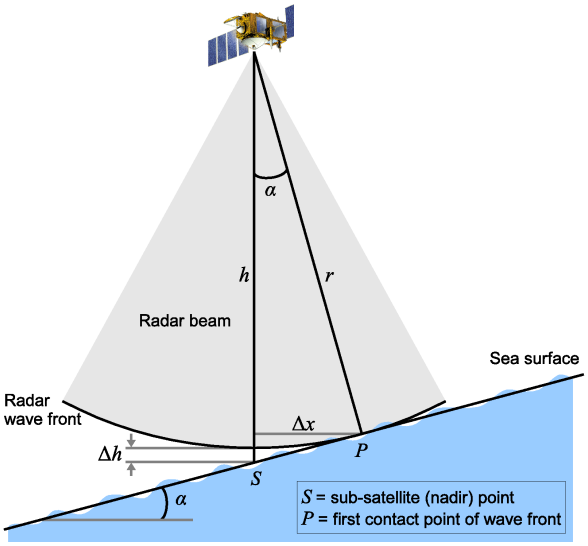

Figure 9.1: Slope-induced height error Δh in satellite radar altimetry for an inclined planar surface, illustrating (9.1) and (9.2).

9.2 Validation of Jason-1 Data with Airborne Laser Altimetry

Two flights were conducted along the two Jason-1 ground tracks traversing the survey area (Fig. 7.1). A coinciding track of over 100 km of flight GRL05 on 11/01/2003 is of special interest, since airborne laser altimetry observations were performed during a Jason-1 crossover, providing quasi-simultaneous observations of the same sea surface (Fig. 9.2 and Fig. 9.2). Jason-1 passed over the isle of Gavdos at 10:09 UT and needed 30 s to cross the area of interest, while the aircraft covered the same profile in 30 minutes, from 9:55 to 10:25 UT. Thus, the time offset between Jason-1 and airborne observations is less than 15 minutes along the track, and variations of the sea surface height over this short time period can be neglected. Hence, in the comparison between the two datasets, there is no need to apply corrections for time-dependent sea surface height variations like tides and atmospheric forcing. The airborne laser altimetry observations allow to make direct comparisons with the sea surface heights provided by Jason-1. However, since the sea surface heights from airborne laser altimetry are mostly free of solid Earth tides due to differential GPS processing (Section 3.3.3), solid Earth tide corrections have to be applied to the Jason-1 data for the comparison. Prior to the comparison, the sea surface heights from Jason-1 were transformed to the WGS84 reference ellipsoid, yielding a mean vertical shift of -0.705 m at the considered latitude. In addition, cross-track gradient corrections were applied to the airborne data in order to account for the horizontal offset between the radar altimeter ground points and the airborne profile.

The observed differences between sea surface heights from Jason-1 and airborne laser altimetry reveal variations between -0.10 and 0.20 m along the dedicated profile of more than 100 km (Fig. 9.2b). These variations are too large to be explained by slope-induced errors (Section 9.1). However, the overall agreement is good, with a mean difference of only 0.04 m and a standard deviation of 0.08 m. The distinct negative difference reaching -0.65 m at the northern end of the airborne profile (Fig. 9.2a) is due to a lack of Jason-1 data approaching the coast, where sea surface heights from Jason-1 are interpolated from the next data points north of Crete. This underlines the need for satellite-independent methods like airborne laser altimetry to cover coastal regions. Additional comparisons were made between significant wave heights derived from airborne laser altimetry (Fig. 7.6) and from Jason-1 GDR data (Picot et al., 2003) along the dedicated profile (Fig. 9.2c). A good agreement of better than 20 cm is obtained using Jason-1 Ku-band data. Differences with the noisier C-band are larger.

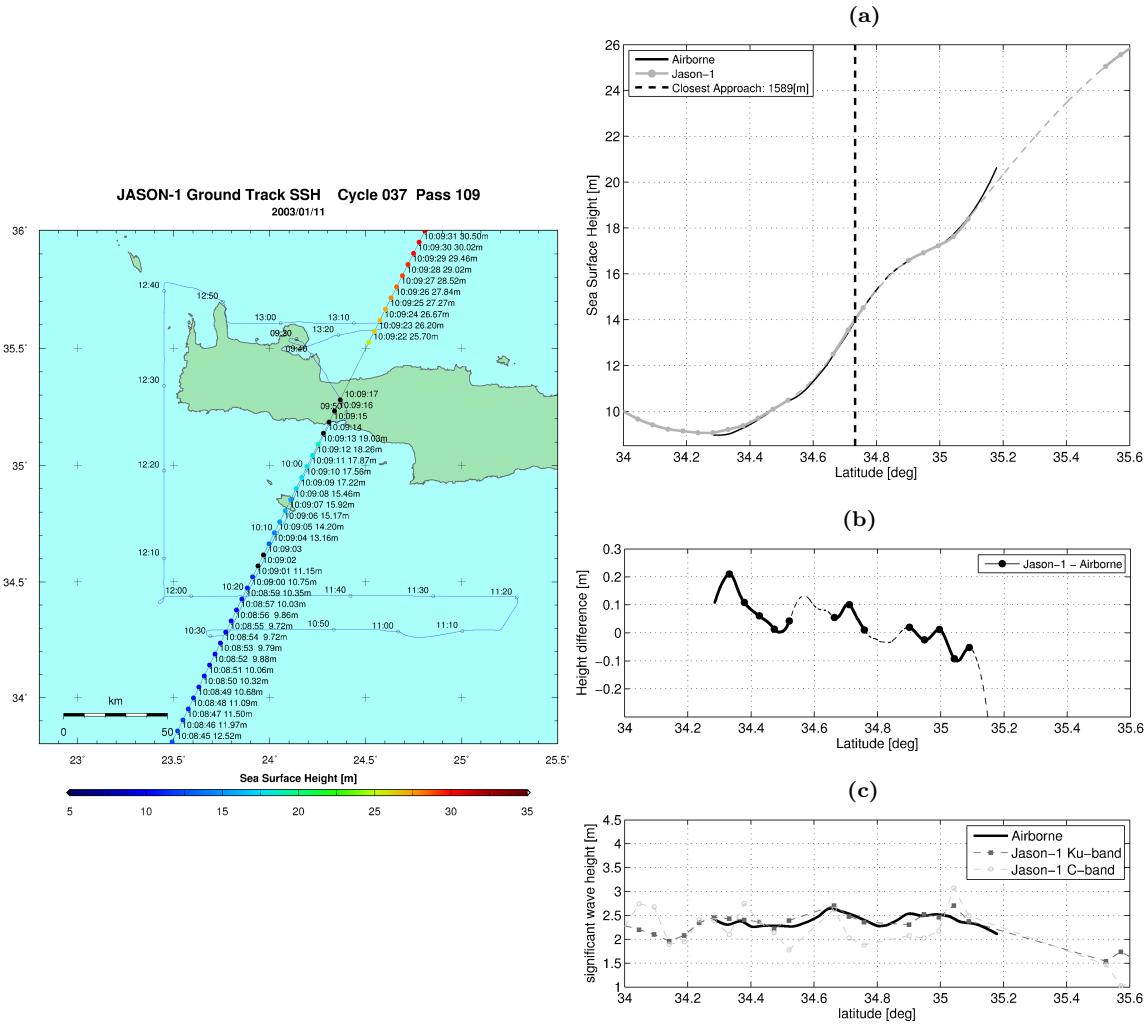

Figure 9.2: Left: Ascending Jason-1 track 109 with 1 Hz sea surface height samples (dots with time and height labels, black dots indicate erroneous data). Airborne laser altimetry flight (blue line with time labels) at the same day, covering Jason-1 track with direct crossover. **(a)** Comparison between sea surface height profile from Jason-1 (dots marking 1 Hz samples and dashed line marking lack of data) and airborne laser altimetry. **(b)** Height differences between Jason-1 and airborne laser altimetry data (dashed line marks lacks of Jason-1 data). **(c)** Significant wave heights from airborne altimetry and Jason-1 GDR data.

9.3 Validation of Mean Sea Surface from Radar Altimetry

9.3.1 Validation with Airborne Laser Altimetry around Western Crete

Comparisons were made between the sea surface topography derived from airborne laser altimetry (Fig. 7.15) and mean sea surfaces (MSS) from multi-mission radar altimetry, namely CLS01 (Fig. 9.3a) and DNSC08 (Fig. 9.3b). Both MSS were previously transformed to the WGS84 reference ellipsoid. Note that the sea surface topography from airborne laser altimetry includes SSALTO/DUACS sea level anomaly corrections (Sections 2.4 and 7.3.5). Theoretically, the CLS01 and DNSC08 resolve wavelengths down to 10 - 20 km (Section 2.3). The residuals between the sea surface topography from airborne laser altimetry and the MSS from CLS01 have a standard deviation of 8.6 cm (Fig. 9.4a and Tab. 9.1). A mean offset of 15.7 cm was previously removed. This implies that there is a bias of 5.7 cm in the survey area, additionally to the global bias of

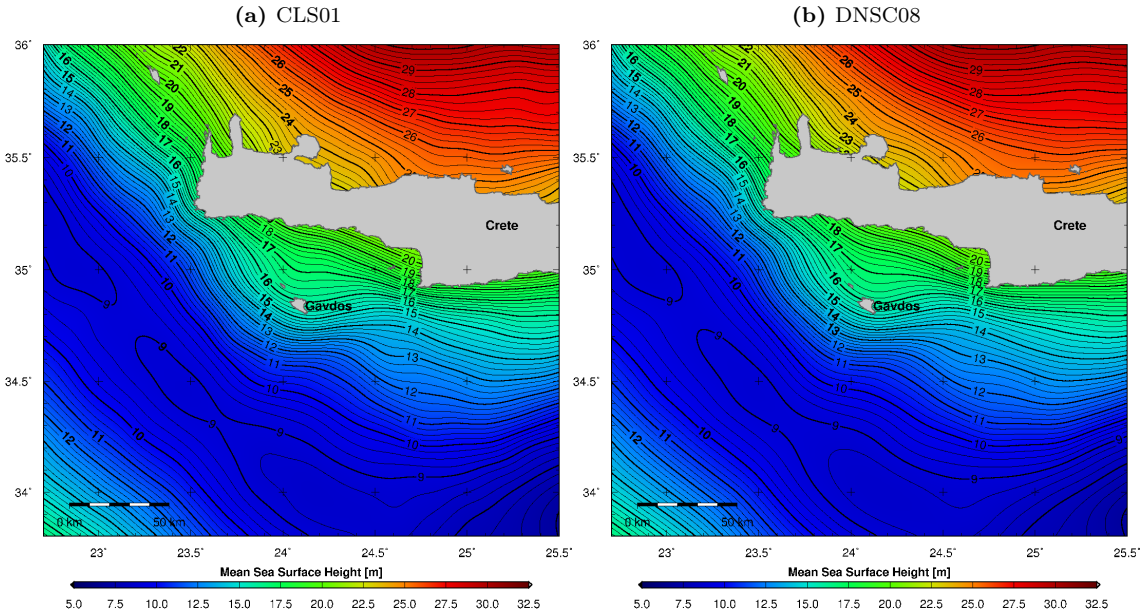

Figure 9.3: Mean sea surface heigths above the WGS84 reference ellipsoid from **(a)** CLS01 and **(b)** DNSC08. Contour intervals: 0.25 m.

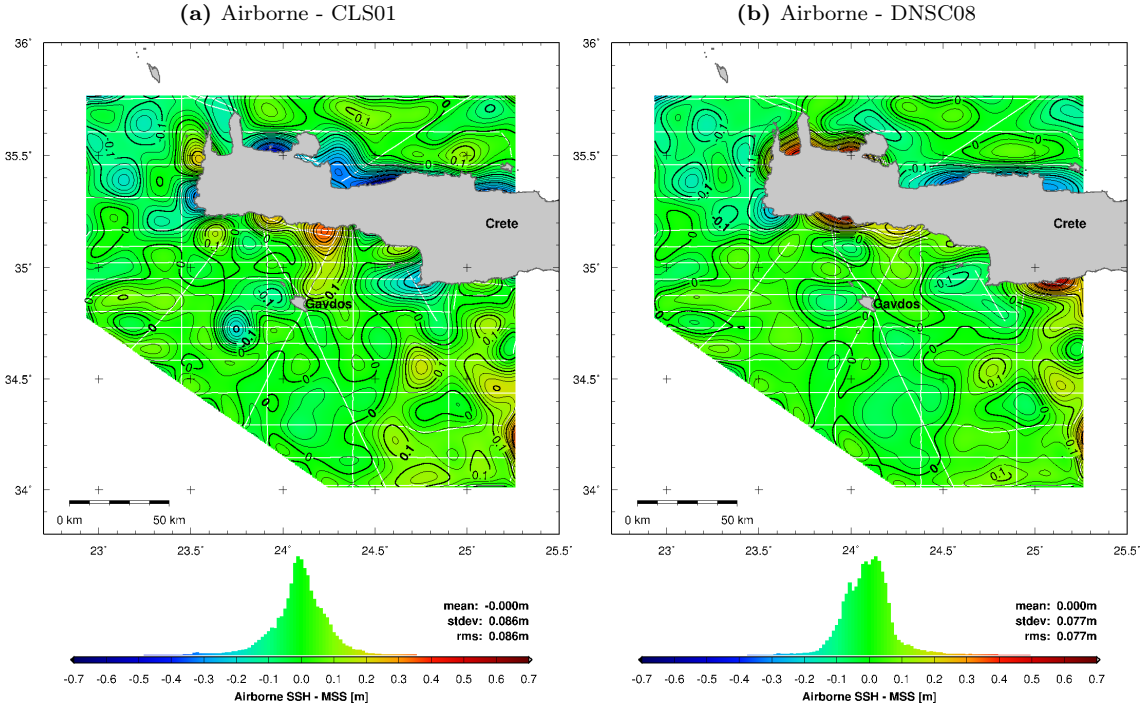

Figure 9.4: Residuals between sea surface topography from airborne laser altimetry (Fig. 7.15) and mean sea surface (MSS) from **(a)** CLS01 (Fig. 9.3a) and **(b)** DNSC08 (Fig. 9.3b). Mean offsets of respectively 15.7 cm and 17.7 cm were previously removed. White lines: airborne tracks. Contour intervals: 0.025 m.

Table 9.1: Mean offset and standard deviation (std) of residuals of local sea surface topographies (SST) from airborne laser altimetry around Crete and shipborne ultrasound altimetry in the North Aegean Sea with respect to mean sea surfaces CLS01 and DNSC08 from multi-mission radar altimetry.

		SST - CLS01	SST - DNSC08
Survey area	Method	Mean ± std [cm]	Mean ± std [cm]
Crete	Airborne	15.7 ± 8.6	17.7 ± 7.7
North Aegean	Shipborne	10.5 ± 6.6	10.7 ± 5.8

10 cm between SSALTO/DUACS reference heights and CLS01. The overall agreement between the two datasets is very good. However, high residuals of up to 50 cm are observed in a belt of 20 km around the coast of Crete, where the strongest geoid gradients of the entire survey area occur, reaching 0.22 m/km (Fig. 10.1c). In these coastal areas, CLS01 sea surface heights are interpolated due to a lack of satellite radar altimetry data. Since the coastline was not systematically covered by airborne laser altimetry as well, uncertainties also remain in the airborne sea surface topography regarding these areas. Similar residuals are observed between the airborne sea surface topography and the MSS from DNSC08 (Fig. 9.4b and Tab. 9.1). As compared to CLS01, the standard deviation improved to 7.7 cm. A similar offset of 17.7 cm was previously removed. As for CLS01, the highest absolute residuals of up to 50 cm are observed in a belt of 20 km around the coast of Crete. Besides the validation of the MSS products, the good agreement with the MSS from CLS01 and DNSC08 also allows to assess the good accuracy and resolution of the sea surface topography determined by airborne laser altimetry.

9.3.2 Validation with Shipborne Altimetry in the North Aegean Sea

Comparisons were made between the sea surface topography derived from shipborne altimetry (Fig. 8.13) and mean sea surfaces (MSS) from multi-mission radar altimetry, namely CLS01 (Fig. 9.5a) and DNSC08 (Fig. 9.5b). Both MSS were previously transformed to the WGS84 reference ellipsoid. Note that the sea surface topography from shipborne altimetry includes SSALTO/DUACS sea level anomaly corrections (Sections 2.4 and 8.3.5). Theoretically, the CLS01 and DNSC08 resolve wavelengths down to 10 - 20 km (Section 2.3). The residuals between the sea surface topography from shipborne altimetry and the MSS from CLS01 have a standard deviation of 6.9 cm (Fig. 9.6a and Tab. 9.1). A mean offset of 10.5 cm was previously removed. This bias corresponds to the global bias of 10 cm between SSALTO/DUACS reference heights and CLS01, meaning that there is no additional bias between the two sea surface solutions in the survey area. The overall agreement between the two datasets is very good. They both similarly resolve the sea surface depression at the south-western end of the North Aegean Trough. An interesting feature is the positive difference of up to 20 cm near the island of Alonnisos. North of the island, pronounced gradients of the sea surface of up to 10 cm/km were observed by dedicated shipborne surveys in this area (Fig. 11.1c). The MSS from radar altimetry do not fully resolve this local steep gradient. Similar residuals are observed between the shipborne sea surface topography and the MSS from DNSC08 (Fig. 9.6b and Tab. 9.1). As compared to CLS01, the standard deviation improved to 5.8 cm. A similar offset of 10.7 cm was previously removed. The highest absolute residuals of up to 22 cm are observed in the north-eastern part of the survey area, probably linked to extrapolation of the shipborne data (Fig. 9.6b). Besides the validation of the MSS products, the good agreement with the MSS from CLS01 and DNSC08 allows to assess the good accuracy and resolution of the sea surface topography determined by shipborne ultrasound altimetry. In terms of standard deviation, the agreement of both CLS01 and DNSC08 with the shipborne altimetry data in the North Aegean Sea is slightly better than with the airborne altimetry data around Crete (Tab. 9.1). This is not a consequence of a better accuracy of the shipborne altimetry data, but rather related to the extreme sea surface height gradients encountered around Crete.

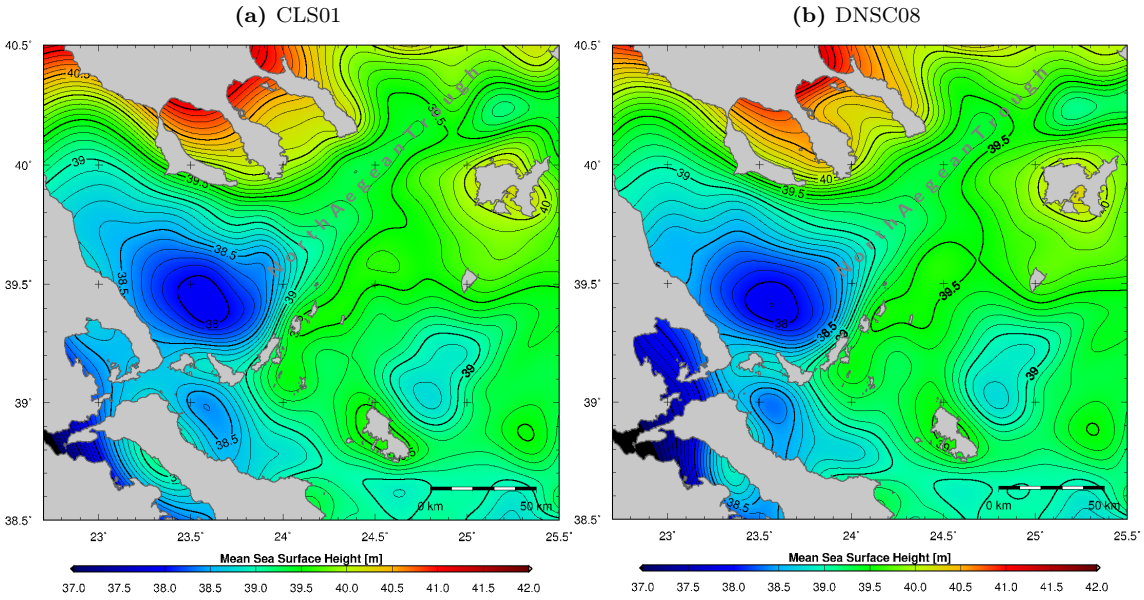

Figure 9.5: Mean sea surface heigths above the WGS84 reference ellipsoid from **(a)** CLS01 and **(b)** DNSC08. Contour intervals: 0.1 m.

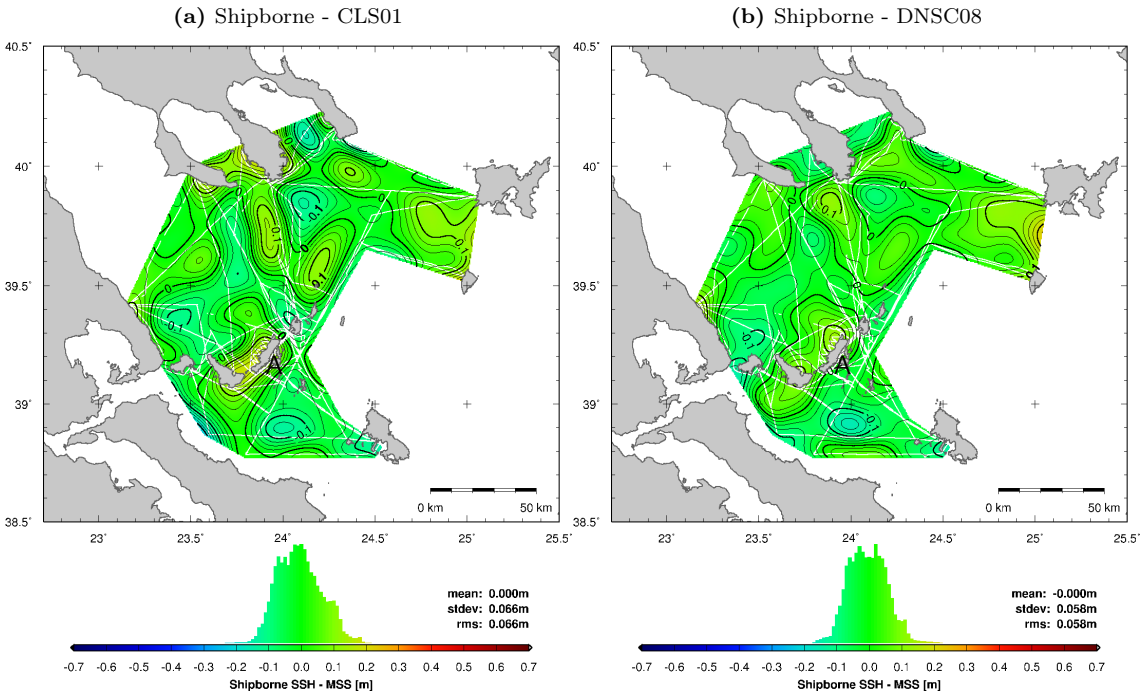

Figure 9.6: Residuals between sea surface topography from shipborne altimetry (Fig. 8.13) and mean sea surface (MSS) from **(a)** CLS01 (Fig. 9.5a) and **(b)** DNSC08 (Fig. 9.5b). Mean offsets of respectively 10.5 cm and 10.7 cm were previously removed. White lines: ship tracks. A = Alonnisos. Contour intervals: 0.025 m.

10 Geoscientific Exploitation of Airborne Altimetry Data around Western Crete

10.1 Marine Geoid, Gravity Anomalies and Deflections of the Vertical from Sea Surface Heights

Assuming the mean dynamic topography (MDT) as known, marine geoid heights can be derived from observed sea surface heights by subtracting the MDT (2.2). The MDT used in this study is the RioMed mean dynamic topography of the Mediterranean Sea (Section 2.5.3, Fig. 2.5a). The maximum effect of the MDT in the survey area reaches -15 cm south of Crete (Fig. 2.6a). By subtracting the RioMed MDT (Fig. 2.6a) from the sea surface heights obtained by airborne laser altimetry (Fig. 7.15), altimetric geoid heights are obtained (Fig. 10.1a). The geoid heights are given with respect to the WGS84 ellipsoid. The obtained geoid heights are characterized by a pronounced overall gradient, with heights decreasing from 28 m in the north-eastern part of the survey area to 8 m in the southern part, along a distance of only 200 km. This gradient indicates the strong effect on gravity caused by the bathymetry and geodynamic system of the Hellenic Trench. An interesting feature is the weakened gradient around the isle of Gavdos, where the geoid height is increased by about 2 m as compared to the overall downward trend towards the Hellenic Trench. Further details on the geodynamic processes associated with the Hellenic Trench subduction zone are given in Section 1.2.

Gravity anomalies (Fig. 10.1b) were computed from the altimetric geoid heights (Fig. 10.1a), based on Laplace's equation (2.19) and the curvature of the geoid (2.20), using the GMT (Generic Mapping Tools) software (Wessel and Smith, 1998, 2005). As compared to geoid heights, gravity anomalies are less affected by the long-wavelength part of the gravitational potential and are therefore better suited for the analysis of local gravity anomalies. E.g. a pronounced positive local gravity anomaly around the isle of Gavdos, reaching 120 mGal, is depicted (Fig. 10.1b).

Variations of the geoid were further quantified by computing horizontal gradients (Fig. 10.1c) and deflections of the vertical (2.14) (Fig. 10.1d) from the geoid heights. Maximum gradients of up to 0.22 m/km are encountered along the southern and western coast of Crete, corresponding to a deflection of the vertical of 45 arcsec. Another local maximum of similar magnitude is observed south of the isle of Gavdos. A significant correlation is observed between the Hellenc Trench and the variations of the gravity anomalies and geoid gradients (Fig. 10.1b and Fig. 10.1c). Further interpretation of the obtained geoid heights and gravity anomalies is carried out in the framework of the reduction of mass effects in Section 10.5.

10.2 Local Altimetric Geoid vs. Existing Models

To validate the marine geoid heights (Fig. 10.1a) obtained by airborne laser altimetry (Section 10.1), they were compared to geoid heights from several gravity models. The analyzed global gravity models are EGM96 (Fig. 10.2a), EGM2008 (Fig. 10.2b), EIGEN-5S (Fig. 10.2c) and EIGEN-5C (Fig. 10.2d). All geoid heights were computed with respect to the WGS84 ellipsoid. Further details on the gravity models are given in Section 2.2.3. The different resolutions of the geoid models are

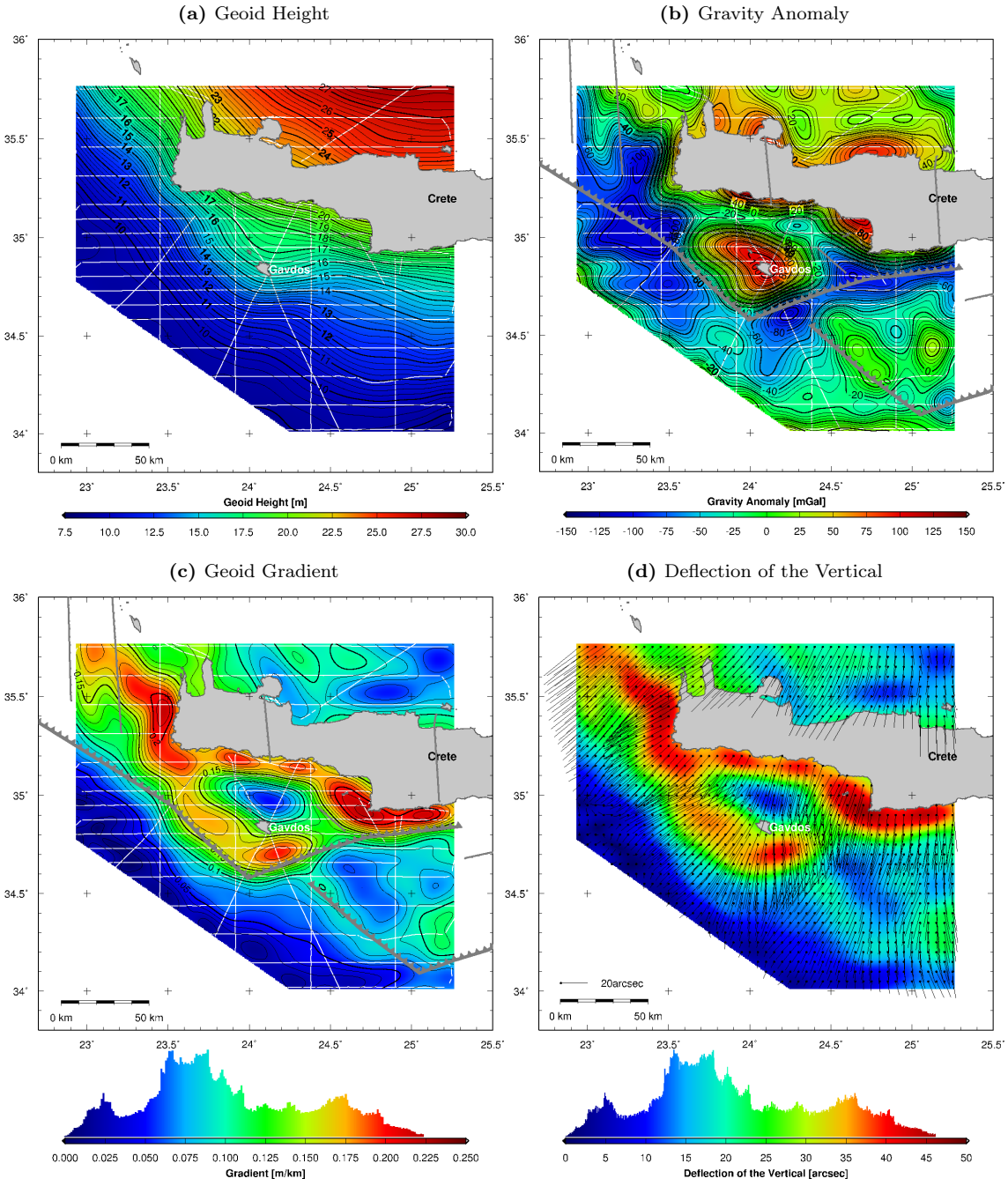

Figure 10.1: **(a)** Altimetric geoid heights with respect to the WGS84 reference ellipsoid, obtained by subtracting the RioMed mean dynamic topography (Fig. 2.6a) from sea surface heights determined by airborne laser altimetry (Fig. 7.15). Contour interval: 0.25 m. White lines: airborne tracks. **(b)** Gravity anomalies derived from geoid heights in (a). Contour interval: 5 mGal. Gray lines: fault system of the Hellenic Arc. **(c)** Horizontal gradients of the geoid heights in (a). Contour interval: 0.01 m/km. **(d)** Deflections of the vertical from geoid heights in (a).

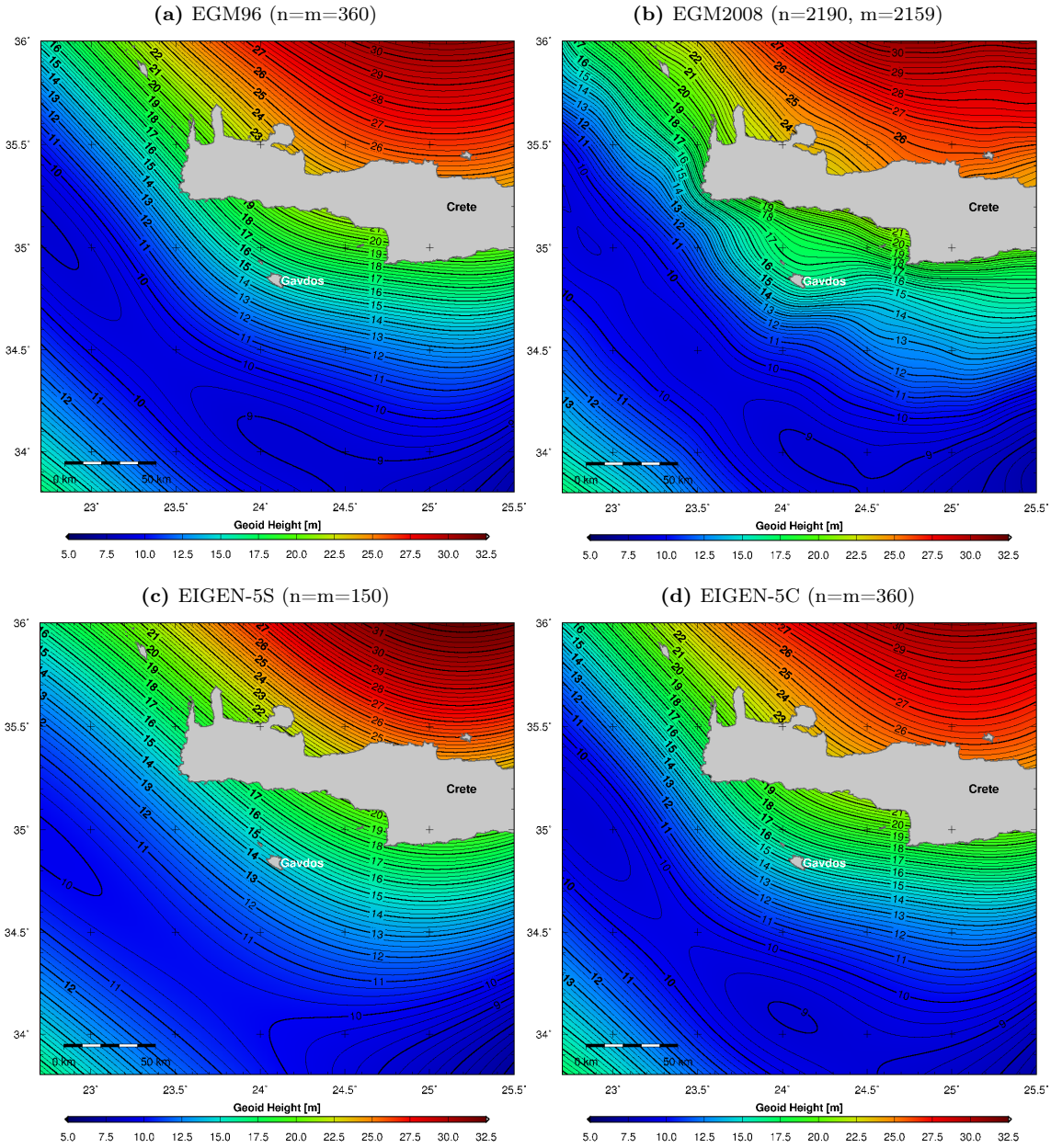

Figure 10.2: Geoid heights to degree n and order m with respect to the WGS84 reference ellipsoid, from **(a)** EGM96, **(b)** EGM2008, **(c)** EIGEN-5S and **(d)** EIGEN-5C. Contour intervals: 0.25 m.

seen (Fig. 10.2), e.g. by their capability of resolving the feature around the isle of Gavdos.

The residuals between the altimetric geoid (Fig. 10.1a) and the geoid models (Fig. 10.2) are shown in Fig. 10.3. Mean offsets and standard deviations are summarized in Tab. 10.1. In the ideal case of error-free sea surface heights, dynamic topography and geoid models, these residuals should be zero according to (2.27). The residuals with respect to EIGEN-5S have large values of more than 1.5 m, large gradients and a high standard deviation of 0.81 m (Fig. 10.3c). The poor agreement is due to the low resolution (approx. 130 km) of the EIGEN-5S. The two combined geoid solutions EGM96 and EIGEN-5C have a theoretical resolution of 55 km. They produce very similar results in the survey area (Fig. 10.3a and Fig. 10.3d). The mean differences between the altimetric geoid

Table 10.1: Mean offsets and standard deviations (STD) between the altimetric geoid from airborne laser altimetry and geoid models.

Geoid Model	(degree,order)	mean offset [m]	STD [m]
EIGEN-5S	(150,150)	-0.23	0.81
EIGEN-5C	(360,360)	-0.18	0.40
EGM96	(360,360)	-0.20	0.40
EGM2008	(360,360)	-0.23	0.37
EGM2008	(2190,2159)	-0.14	0.11
AUTH2008	-	-0.24	0.15

and EGM96 and EIGEN-5C are -0.20 m and -0.18 m, respectively, both with a standard deviation of 0.40 m. As for EIGEN-5S, both models do not resolve the local positive anomaly around the isle of Gavdos, with residuals reaching 1 m. Similarly, the local negative anomaly north-east of Gavdos is not resolved by both models, with residuals reaching -1.2 m. The best agreement is obtained with EGM2008, with a mean difference of -0.14 m and a standard deviation of 0.11 m (Fig. 10.3b). The good agreement is due to the high resolution of EGM2008. Its expansion to degree 2190 and order 2159 corresponds to a resolution of approx. 10 km.

The improved input data in terms of resolution and accuracy of the recent EIGEN-5C, as compared to EGM96, does not yield a significant improvement of the spatial resolution of EIGEN-5C (Fig. 10.3a and Fig. 10.3d). The limiting factor in terms of spatial resolution of the geoid models is their mathematical expansion of the spherical harmonics. This is confirmed by computing an EGM2008 solution with a spherical harmonics expansion limited to degree and order 360 (Fig. 10.4a). The residuals with respect to the altimetric geoid have a standard deviation of 0.37 m (Fig. 10.5a), similar to those of EGM96 (Fig. 10.3a) and EIGEN-5C (Fig. 10.3d). The extension of the expansion of EGM2008, from degree and order 360 to degree 2190 and order 2159, yields an improvement of 0.26 m of the standard deviation with respect to the altimetric geoid, corresponding to an improvement of 69%. Additional residuals were computed between the altimetric geoid and the local gravimetric geoid model AUTH2008 (Fig. 10.4b) (Section 2.2.3). The residuals have a standard deviation of 0.15 m (Fig. 10.5b), similar to the one obtained with respect to EGM2008.

The mean offsets (Tab. 10.1) are different from the ones obtained with respect to the shipborne altimetric geoid in the North Aegean Sea (Tab. 11.1), indicating discrepancies in the long wavelength geoid undulations between the two areas under investigation. Since the absolute geoid height is not of major interest, the offsets are not critical and were therefore not further investigated.

10.3 Mean Dynamic Topography Estimation

Among the geoid models used in Section 10.2, the satellite-only solution EIGEN-5S and the local gravimetric geoid model AUTH2008 are the only geoid solutions that are independent of altimetric sea surface height data. Hence, they would be the only appropriate models to determine the mean dynamic topography (MDT) using the direct method after (2.28) (Section 2.5). The pronounced residuals between the airborne data and EIGEN-5S (Fig. 10.3c) are obviously making the EIGEN-5S unusable for realistic MDT determination at wavelengths below 130 km. The same remark holds for EGM96 and EIGEN-5C (Fig. 10.3a and Fig. 10.3d). Even if these models were independent of altimetric data, they would not be appropriate to determine the MDT at wavelengths below 55 km. Hypothetic MDT were computed from the residual fields of the sea surface heights from airborne laser altimetry (Fig. 7.15) with respect to EGM2008 (Fig. 10.6a) and AUTH2008 (Fig. 10.6b) geoid heights. Geostrophic circulation fields were derived from the hypothetic MDT based on (2.30). Compared to the RioMed mean geostrophic circulation (Fig. 2.6a), the obtained circulations are unrealistic and spoiled by noisy eddies. The main anti-clockwise circulation around Crete is not

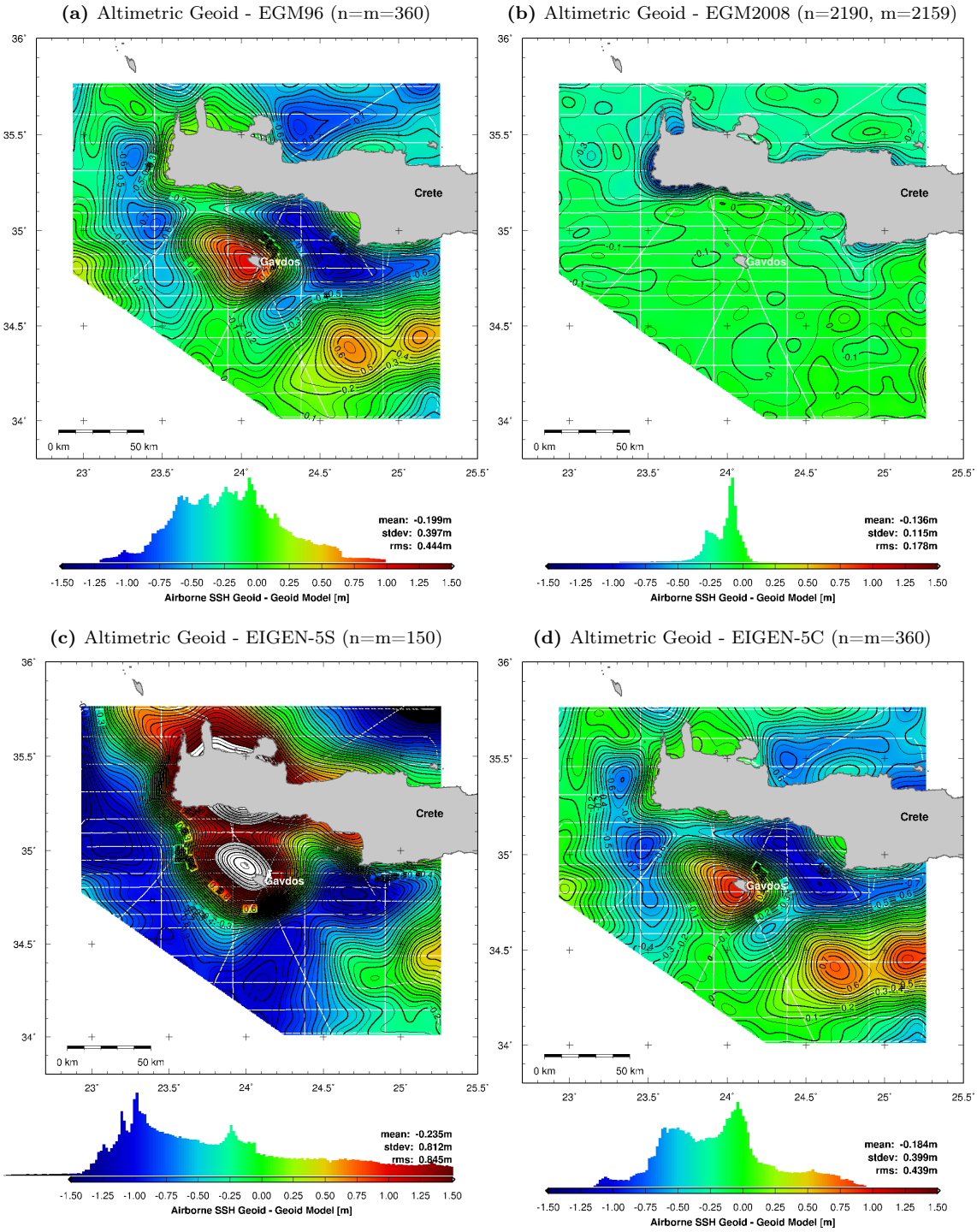

Figure 10.3: Difference between airborne altimetric geoid (Fig. 10.1a) and geoid heights to degree n and order m from **(a)** EGM96, **(b)** EGM2008, **(c)** EIGEN-5S and **(d)** EIGEN-5C. White lines: airborne laser ground tracks. In (c), black and white surface colors indicate differences below -1.5 m and above 1.5 m. Contour intervals: 0.05 m.

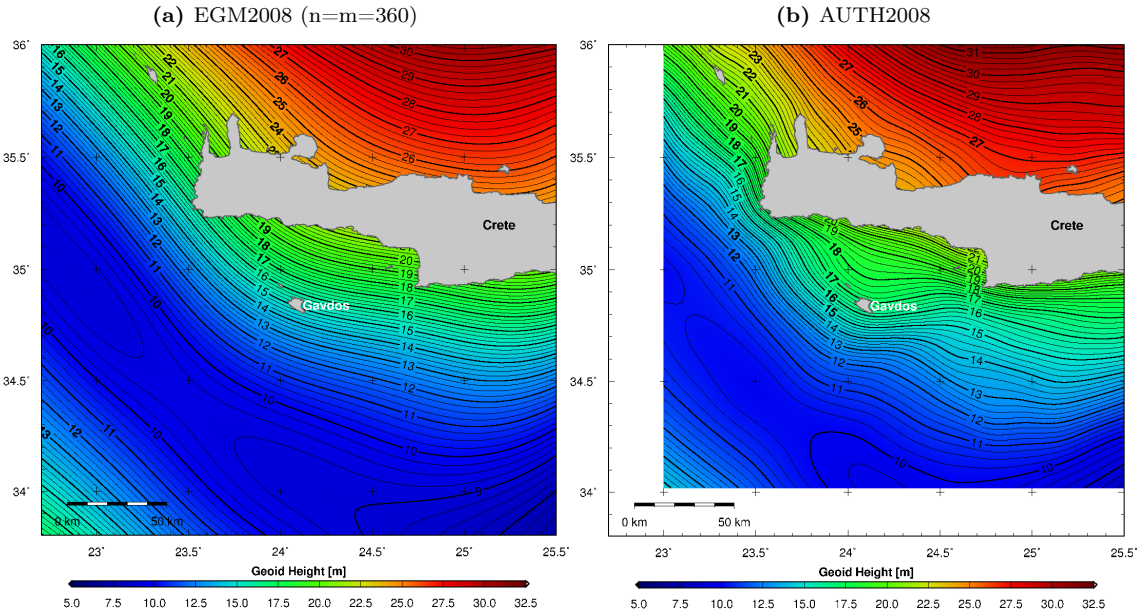

Figure 10.4: Geoid heights with respect to the WGS84 reference ellipsoid, from **(a)** EGM2008 with expansion limited to degree and order 360 and from **(b)** the gravimetric model AUTH2008. Contour intervals: 0.25 m.

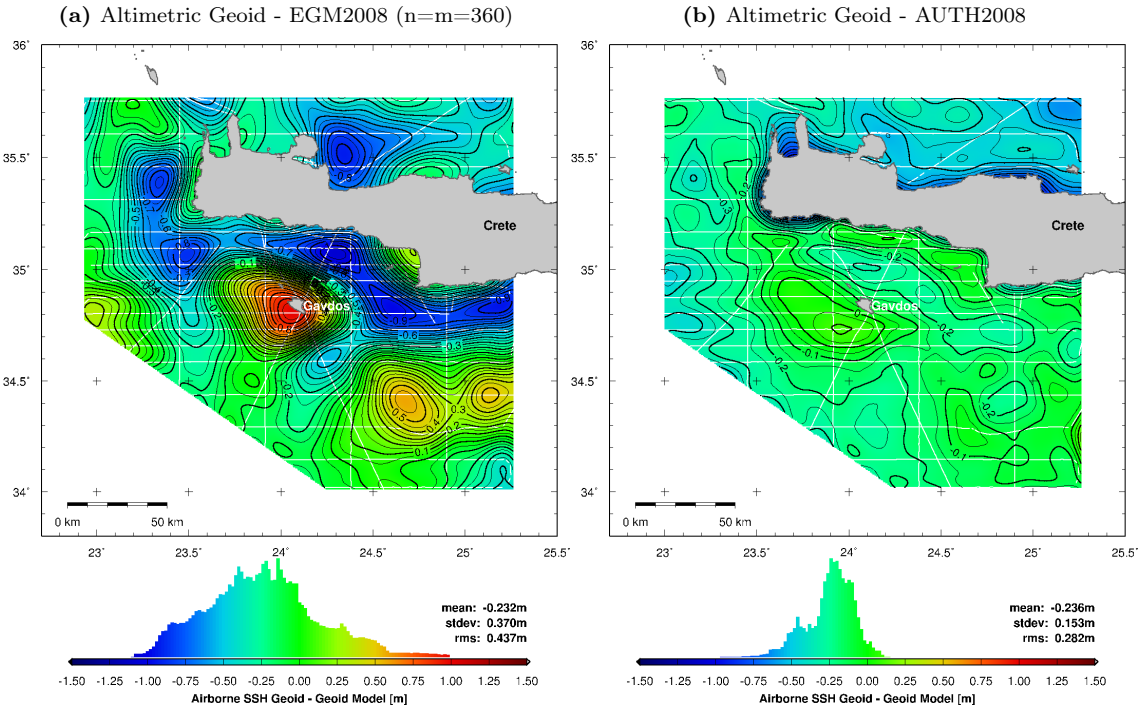

Figure 10.5: Difference between airborne altimetric geoid (Fig. 10.1a) and geoid heights from **(a)** EGM2008 to degree and order 360 and **(b)** AUTH2008. White lines: airborne laser ground tracks. Contour intervals: 0.05 m.

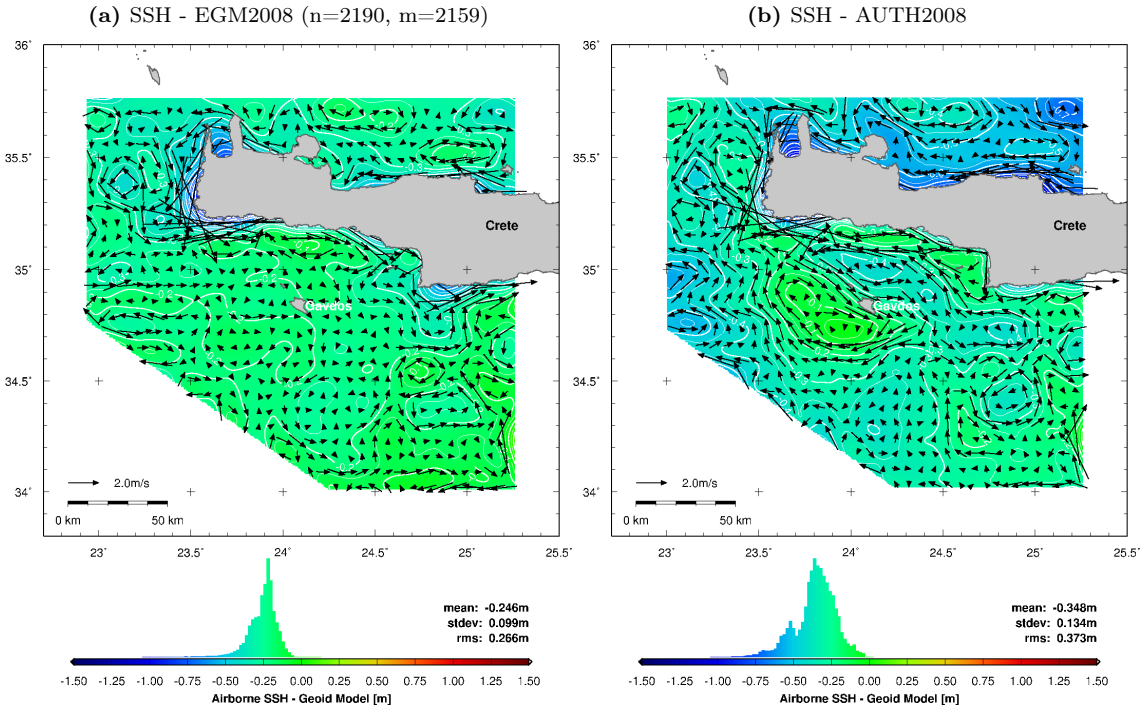

Figure 10.6: Hypothetic mean dynamic topography (background) and ocean circulation (arrows) from differences between sea surface heights from airborne laser altimetry (Fig. 7.15) and geoid heights from **(a)** EGM2008 and **(b)** AUTH2008.

resolved. By applying low-pass filters to both datasets, it was possible to eliminate the noisy eddies, but no significant circulation remained. Hence, it was not possible to derive a realistic circulation pattern based on the sea surface height observations and the used geoid models. The major reason lies in the fact that the presumed MDT, as e.g. given by RioMed (Fig. 2.6a), varies only within a range of 10 cm over the entire survey area. Furthermore, the gradients of the MDT associated with the circulation are below 1 cm/10 km. Hence, the MDT signal in the survey area in the same order of magnitude as the accuracy of the airborne sea surface heights and the used geoid models. It can be concluded that the sea surface height observations by airborne laser altimetry and the considered geoid models are not accurate enough to resolve such small dynamic effects. In addition, EGM2008 is not independent of altimetric sea surface height data.

10.4 Modeled Mass Effects on Geoid Heights and Gravity

10.4.1 Introduction

The effects of mass anomalies on geoid heights were computed for the survey area around western Crete, based on (2.22) and on cuboid masses (2.24). The grid spacing of the computation points and the mass elements was 30' × 30', corresponding to approx. 900 m. The distances between the mass elements and the computation points were computed using geocentric coordinates, in order to avoid effects of Earth's curvature. A maximum radius of influence of 275 km was considered for the masses effects. The area of influence extends from 19°E to 29°E and from 31°N to 39°N (Fig. 10.7a). The mass densities in Tab. 2.1 were used. Geoid heights are highly influenced by large-scale mass anomalies (Section 2.2.2). As compared to geoid heights, gravity anomalies are less affected by the

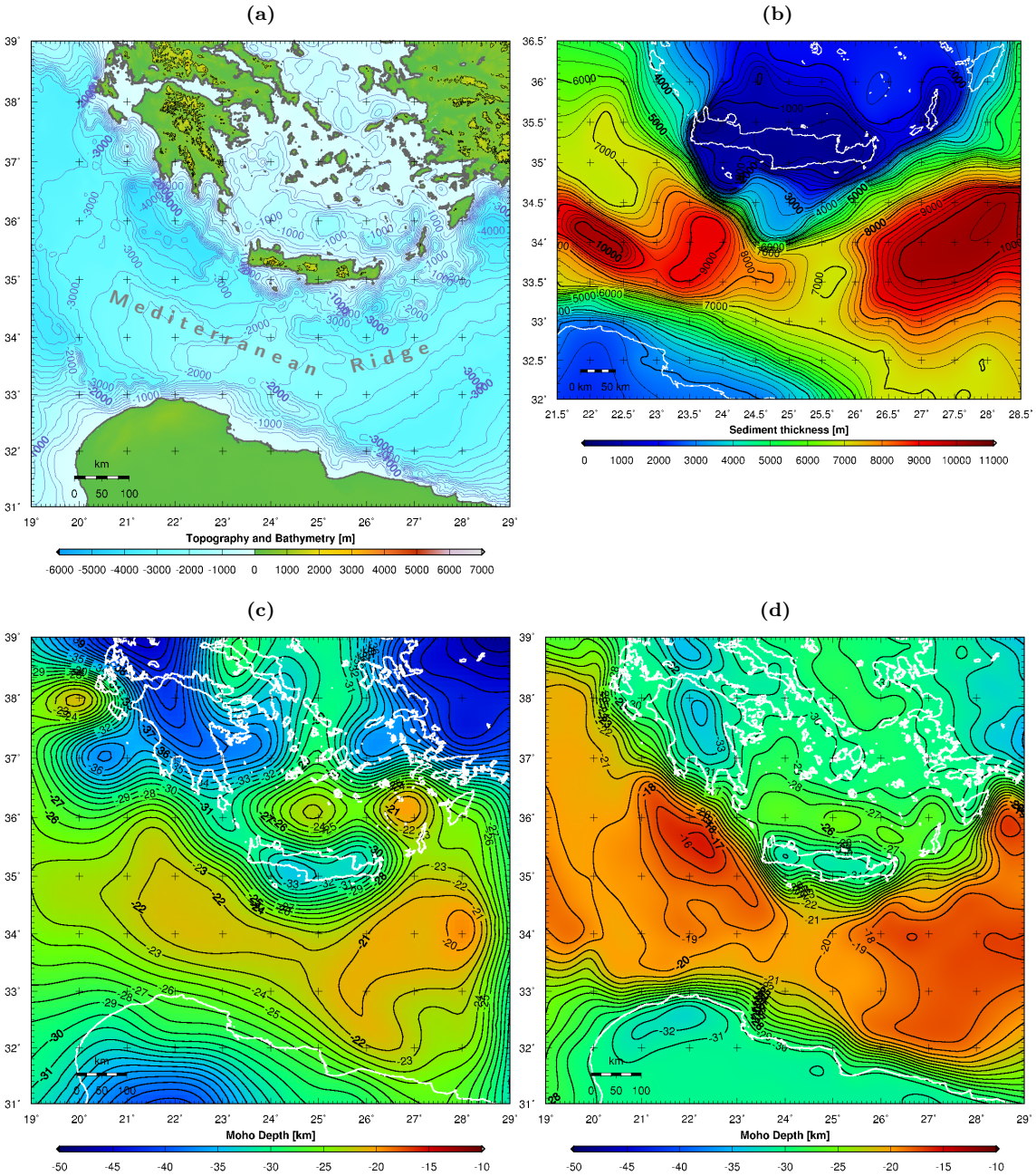

Figure 10.7: **(a)** Topography/bathymetry of the area of influence considered in the modeling of mass effects (contour interval topo: 1000 m, bathy: 250 m). **(b)** Light sediment thickness from (Makris and Yegorova, 2006) (contour interval: 250 m). **(c)** Moho depth from ESC (Grad et al., 2009) (contour interval: 1 km). **(d)** Moho depth from isostatic compensation (reference depth: 30 km, contour interval: 1 km).

long-wavelength part of the gravitational potential and are therefore better suited for the analysis of local gravity anomalies. Hence, the effects of mass anomalies on gravity were computed, based on (2.23) and (2.25), in order to obtain additional information on the local gravity field, although the major investigations were carried out on geoid heights. The gravity anomalies were computed at sea level, yielding e.g. exclusively negative effects of the topography on gravity anomalies. The mass effects are used in the Section 10.5 to reduce the geoid heights and gravity anomalies derived

from airborne laser altimetry. The theoretical background of the computation of mass effects on geoid heights and gravity anomalies is given in Section 2.2.2.

10.4.2 Mass Effect of Topography and Bathymetry

The topography and bathymetry were taken from the SRTM30 (Shuttle Radar Topography Mission) digital terrain model, published by the United States Geological Survey (USGS). It has a resolution of 30' × 30', corresponding to approx. 900 m. The topography and bathymetry of the area of influence are characterized by deep water zones reaching -4000 m (Fig. 10.7a). Hence, the topography and bathymetry (including water masses) are producing pronounced negative effects on geoid heights, ranging between -12 m north and -50 m west of Crete (Fig. 10.8a). Associated gravity anomalies are shown in Fig. 10.8b. Within the effect of topography and bathymetry, the water masses have strong positive effects on geoid heights, reaching 32 m west of Crete, related to the deep bathymetry in that area (Fig. 10.9a). Associated gravity anomalies are shown in Fig. 10.9b.

10.4.3 Mass Effect of Sediments

The survey area is characterized by large layers of light sedimentary deposits along the Mediterranean Ridge, between Crete and the African coast (Fig. 10.7b). The sediments locally reach very large thicknesses of more than 10 km. The information on sediment thickness used in the modeling is based on (Makris and Yegorova, 2006). The mass deficiency associated with the sediments has a pronounced negative effect on geoid heights, between -6 m north and -25 m south of Crete (Fig. 10.10a). Associated gravity anomalies are shown in Fig. 10.10b.

10.4.4 Mass Effect of Moho Depths

For the computation of the effect of crust-mantle boundary (Moho) anomalies, Moho depths from the digital Moho depth map published by the ESC (European Seismological Commission) Working Group (Grad et al., 2009) were used. The ESC Moho map covers the European plate from 40°W to 70°E and from 28°N to 86°N, with a resolution of 0.1° × 0.1°. It was compiled from more than 250 datasets of individual seismic profiles, 3D models obtained by body and surface waves, receiver function results and maps of seismic and gravity data compilations. The Moho in the survey area is characterized by a strong uplift to a depth of -21 km south of Crete, along the Mediterranean Ridge (Fig. 10.7c). The mass excess caused by this uplift has a pronounced positive effect of up to 25 m on geoid heights, whereas the effect is only 0 - 5 m north of Crete (Fig. 10.11a). Associated gravity anomalies are shown in Fig. 10.11b.

10.4.5 Mass Effect of Isostatic Moho Depths

As an alternative to the ESC Moho, Moho depths were computed based on the isostatic compensation theory using the Airy-Heiskanen isostasy model (Heiskanen and Moritz, 1967; Hofmann-Wellenhof and Moritz, 2006) and considering the masses of topography, bathymetry, water and sediments. A reference depth of -30 km was used. The obtained Moho depths were smoothed to obtain a more realistic regional compensation. A more rigorous method to obtain regional compensation would rely on flexure theory of a thin elastic plate floating on a fluid mantle. Since the model of isostatic compensation only reflects a theoretical correlation between the masses above the crust-mantle boundary (Moho) and the compensating depth of the boundary, it may sound more appropriate to use a Moho model predicted by real observations, like the ESC Moho (Section 10.4.4). In the present study, however, better reduction results were obtained with the isostatic Moho (Section 10.5).

The isostatic compensation has a dominant uplift effect on the Moho in the survey area (Fig. 10.7d), due to the large mass deficiency caused by the deep water and thick sediments along the Mediterranean Ridge. The isostatic Moho rises up to a depth of -16 km west of Crete. Considering the fact that the water has a depth of 3 km west of Crete, and the sediment thickness is 7 km, the crust thickness is only 6 km in this area. The mass excess caused by the uplift of the isostatic Moho has a pronounced positive effect on geoid heights, ranging between 11 m north and 41 m west and south-east of Crete (Fig. 10.12a). Associated gravity anomalies are shown in Fig. 10.12b.

10.4.6 Combined Mass Effects

The combination of the effects of topography and bathymetry (Fig. 10.8a) with the effects of sediments (Fig. 10.10a) yield pronounced negative effects on geoid heights (Fig. 10.13a). They range between -18 m north and -72 m west and south-east of Crete. Associated gravity anomalies are shown in Fig. 10.13b.

The combination of the negative effects of topography, bathymetry and sediments (Fig. 10.13a) with the positive effects of the ESC Moho (Fig. 10.11a) yield an overall negative effect on geoid heights, ranging between -17 m north and -55 m west of Crete (Fig. 10.14a). The modeled geoid heights present pronounced gradients along the southern coast of Crete and towards the North-West. Along the north-eastern coast of Crete, the structure of the modeled geoid is rather flat. Associated gravity anomalies are shown in Fig. 10.14b.

The combination of the negative effects of topography, bathymetry and sediments (Fig. 10.13a) with the positive effects of the isostatic Moho (Fig. 10.12a) yield an overall negative effect on geoid heights, ranging between -7 m north and -30 m west and south-east of Crete (Fig. 10.15a). The modeled geoid heights present pronounced gradients along the southern coast of Crete and towards the North-West. Along the northern coast of Crete, the structure of the modeled geoid is rather flat. Associated gravity anomalies are shown in Fig. 10.15b.

By visually comparing the modeled geoid (Fig. 10.14a and Fig. 10.15a) to the observed geoid (Fig. 10.1a) and to EGM2008 (Fig. 10.2b), an overall good agreement is observed, except for the flat structure of the modeled geoid north of Crete.

10.4.7 Cuboids vs. Point Mass Modeling

The mass effects (Fig. 10.8 to Fig. 10.15) were computed based on cuboid masses using (2.24) and (2.25). Since the computation involving cuboid masses can be very CPU-intensive depending on the size and resolution of the data grids, a simplified method to compute mass effects on geoid heights and on gravity based on (2.22) and (2.23) consists in concentrating the mass of each cuboid at its center of mass. To assess the impact of this approximation, the effects on geoid heights computed by cuboid masses (Fig. 10.8a to Fig. 10.15a) were recomputed based on the center of mass (point mass) method. Differences between the cuboid and point mass methods are increased by the presence of elongated cuboids close to the computation point, typically produced by high mountains, deep sea, large sediment layers and large Moho depth variations.

Small differences between the two methods are obtained for the sediments effects, while larger differences are obtained for the effect of topography and bathymetry and the effect of the Moho (Tab. 10.2). The differences of the effect of topography and bathymetry on the geoid are below 17 cm (Fig. 10.16a). The differences of Moho effects on the geoid reach 25 cm (Fig. 10.16b) and have a larger variation than the differences on the topography and bathymetry effect. The larger differences on the Moho effect are caused by the elongated shape of the Moho cuboids that can reach heights of more than 10 km. The differences on the final solution combining topography, bathymetry, sediments and Moho depths range between -25 cm and 10 cm, with an RMS of 9.6 cm. Hence, if an accuracy better than 10 cm is sought, the application of the cuboid model is mandatory.

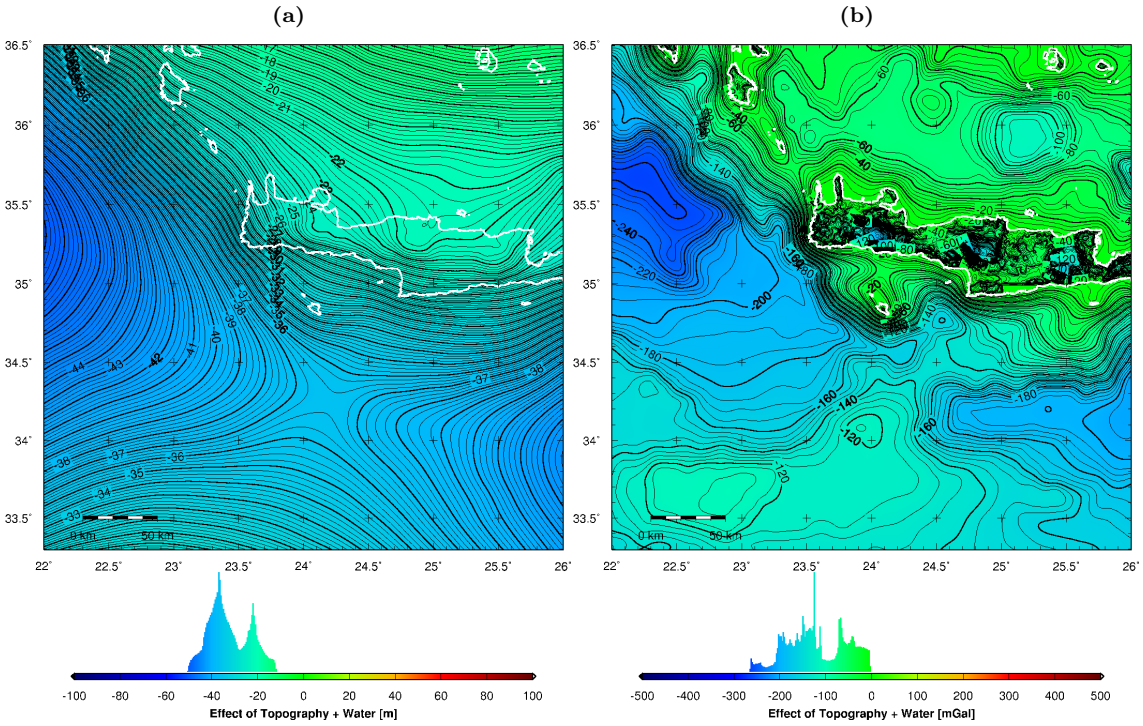

Figure 10.8: Effects of topography and bathymetry (including water masses) on **(a)** geoid heights (contour interval: 0.25 m) and **(b)** gravity (contour interval: 5 mGal).

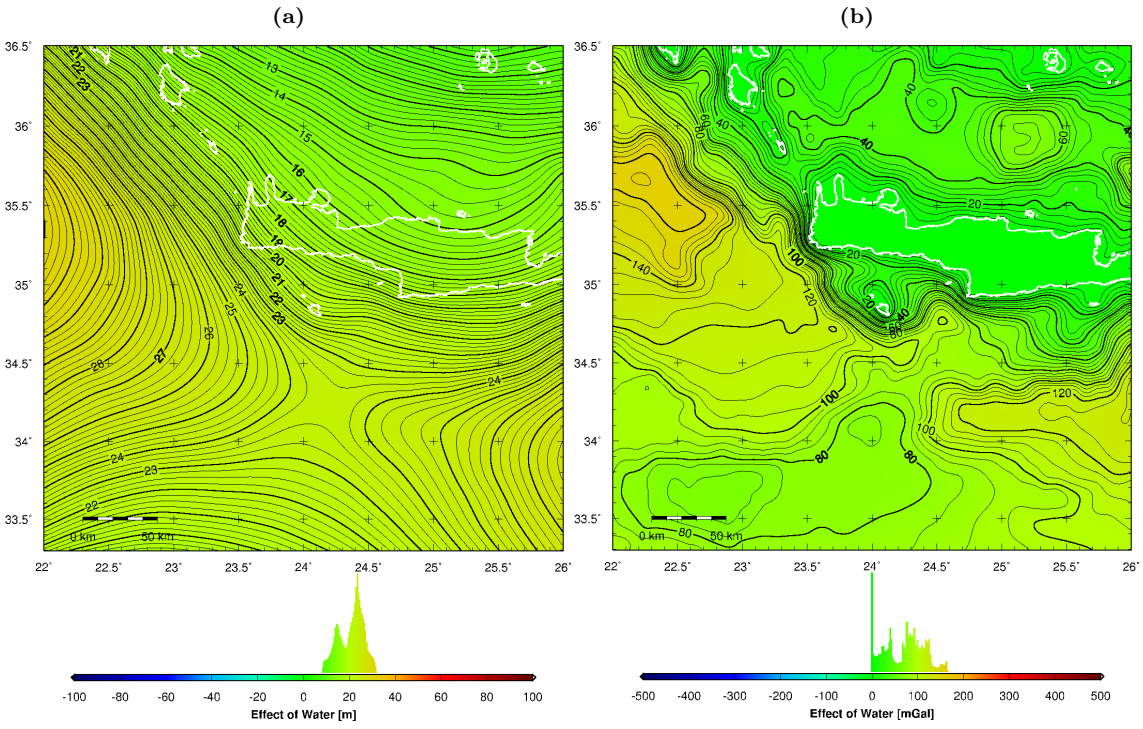

Figure 10.9: Effect of water masses on **(a)** geoid heights (contour interval: 0.25 m) and **(b)** gravity (contour interval: 5 mGal).

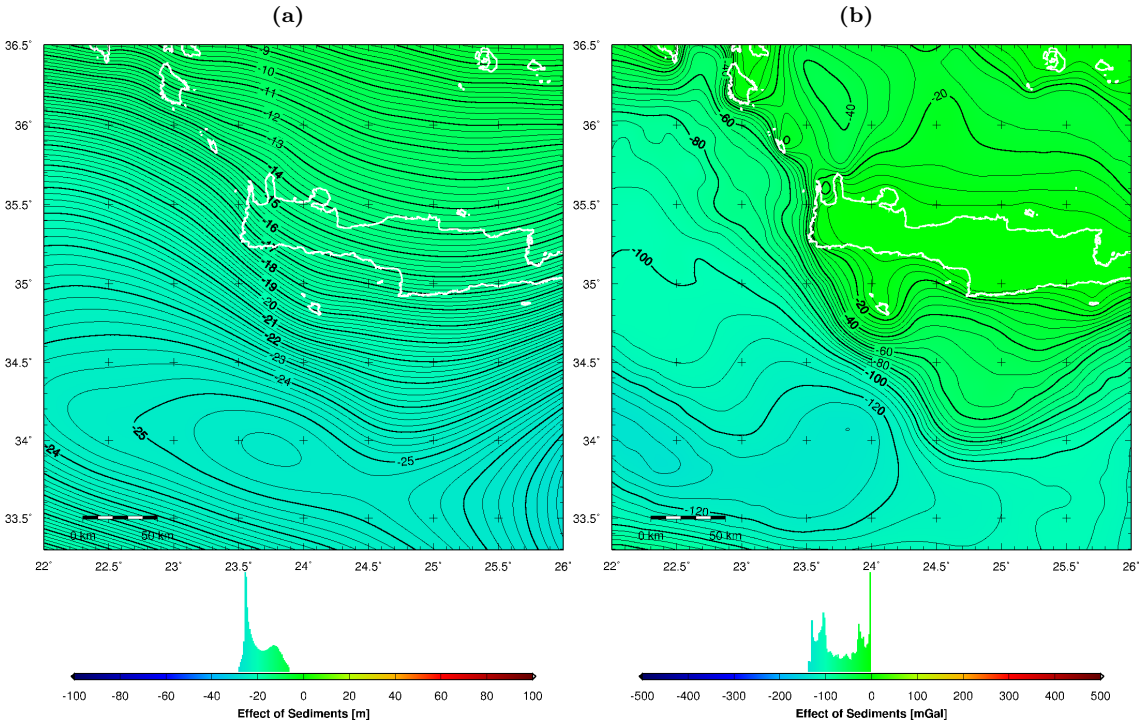

Figure 10.10: Effect of mass deficiency caused by sediments on **(a)** geoid heights (contour interval: 0.25 m) and **(b)** gravity (contour interval: 5 mGal).

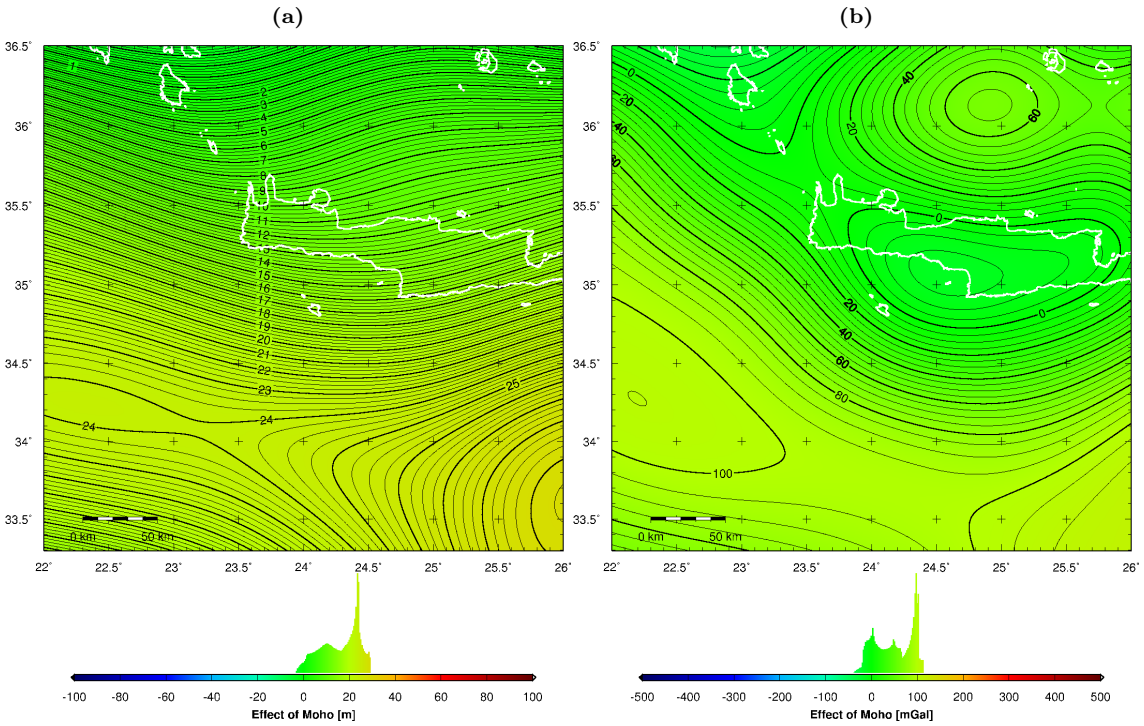

Figure 10.11: Effect of mass anomalies caused by Moho depths from ESC map (Fig. 10.7c) on **(a)** geoid heights (contour interval: 0.25 m) and **(b)** gravity (contour interval: 5 mGal).

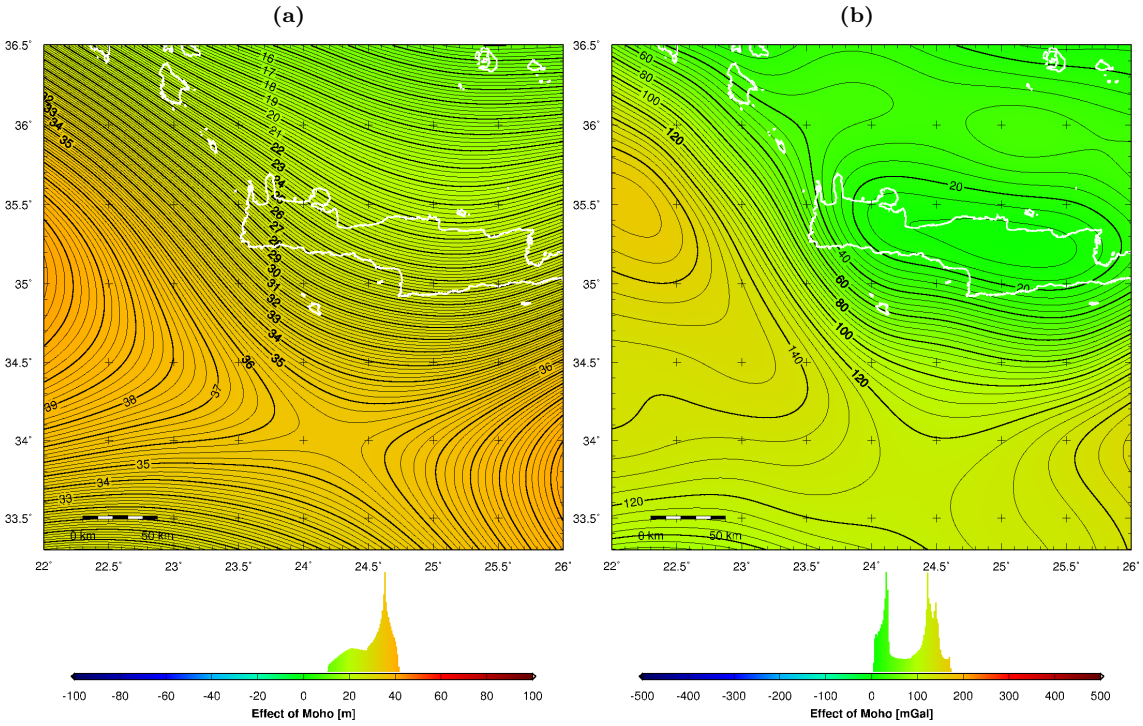

Figure 10.12: Effect of mass anomalies caused by Moho depths from isostatic compensation (Fig. 10.7d) on **(a)** geoid heights (contour interval: 0.25 m) and **(b)** gravity (contour interval: 5 mGal).

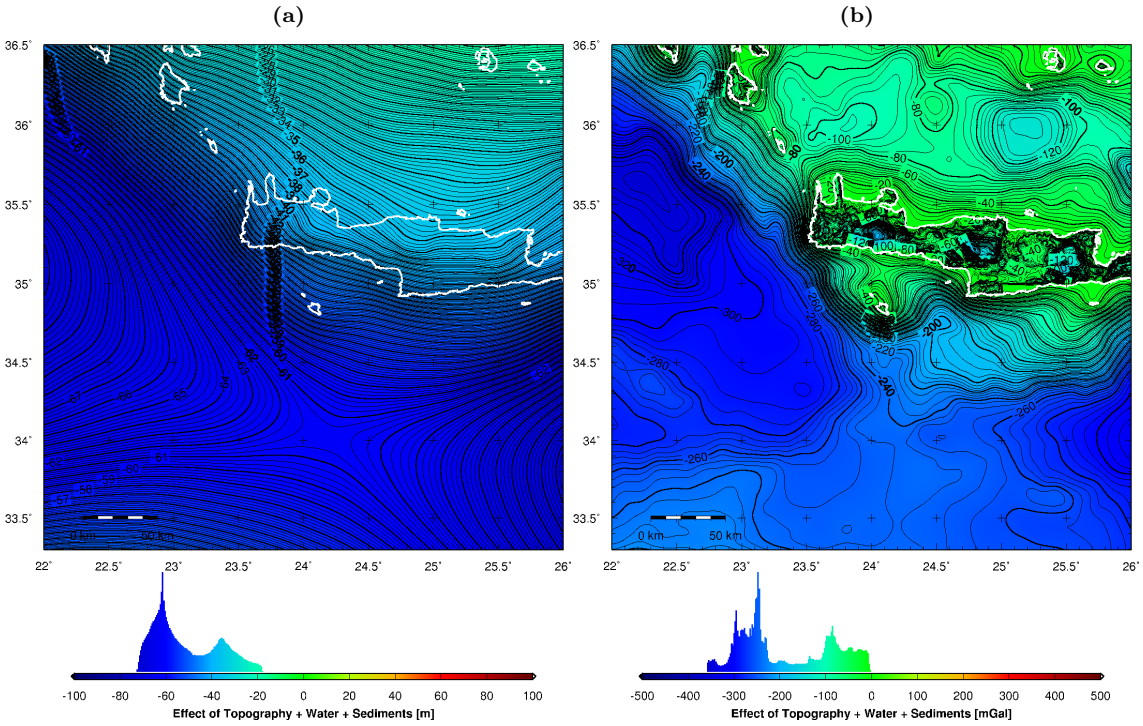

Figure 10.13: Sum of effects of topography, bathymetry (Fig. 10.8) and sediments (Fig. 10.10) on **(a)** geoid heights (contour interval: 0.25 m) and **(b)** gravity (contour interval: 5 mGal).

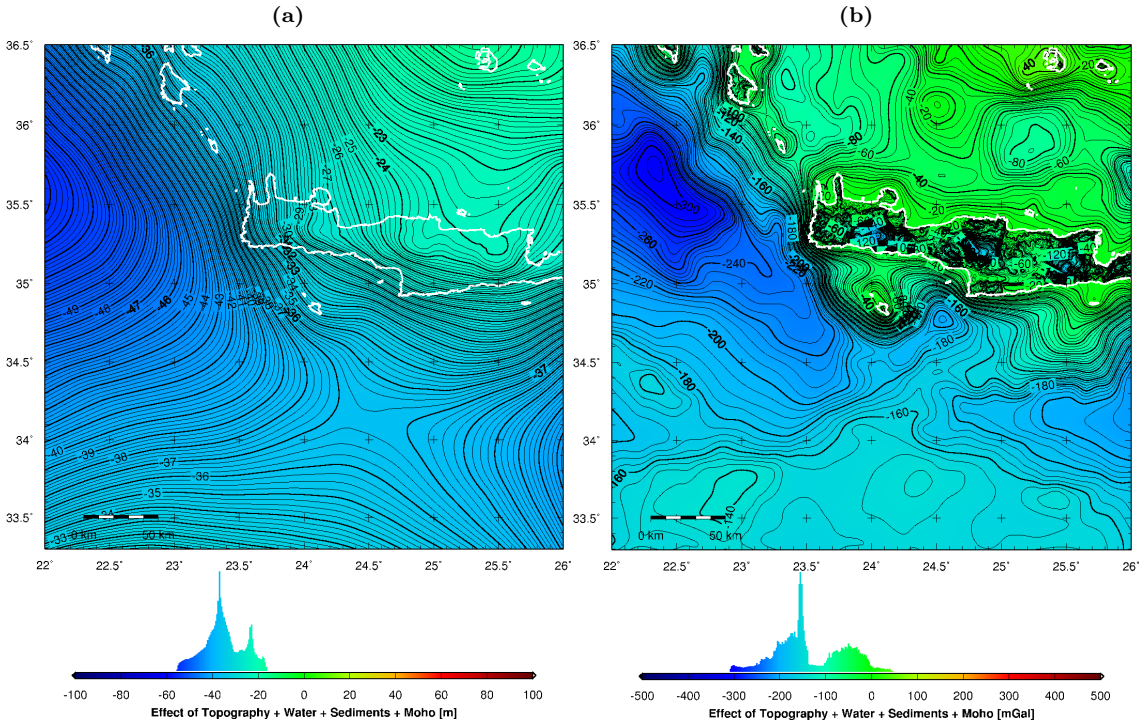

Figure 10.14: Sum of effects of topography, bathymetry, sediments (Fig. 10.13) and ESC Moho depths (Fig. 10.11) on **(a)** geoid heights (contour interval: 0.25 m) and **(b)** gravity (contour interval: 5 mGal).

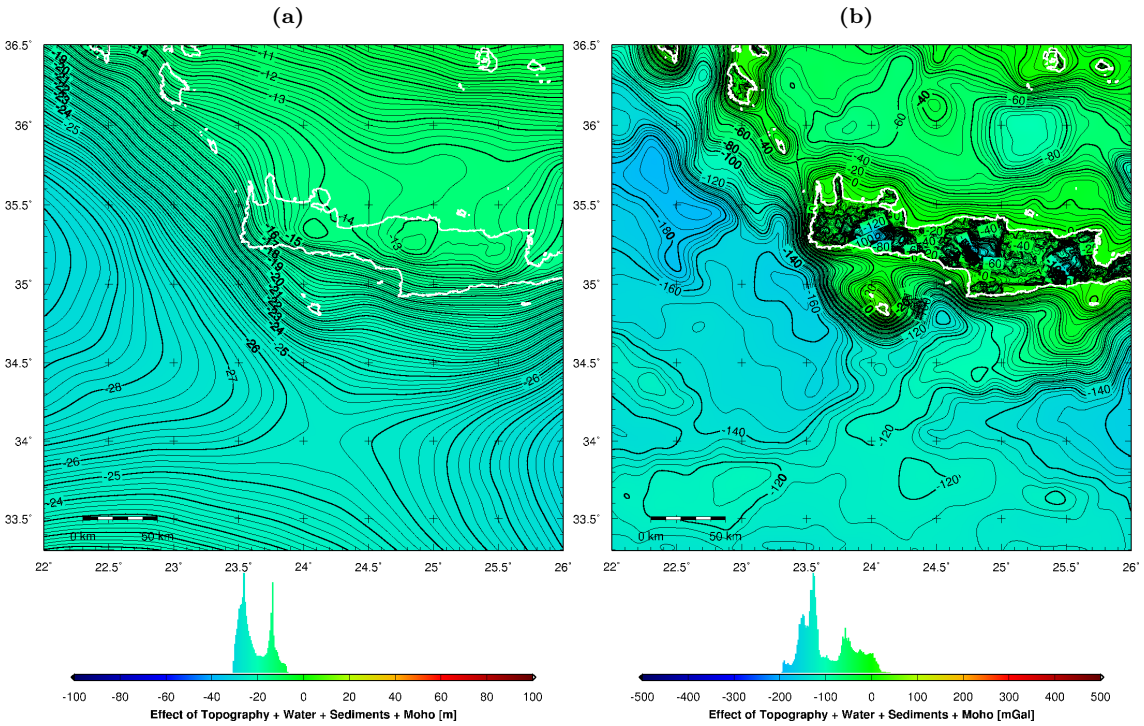

Figure 10.15: Sum of effects of topography, bathymetry, sediments (Fig. 10.13) and isostatic Moho depths (Fig. 10.12) on **(a)** geoid heights (contour interval: 0.25 m) and **(b)** gravity (contour interval: 5 mGal).

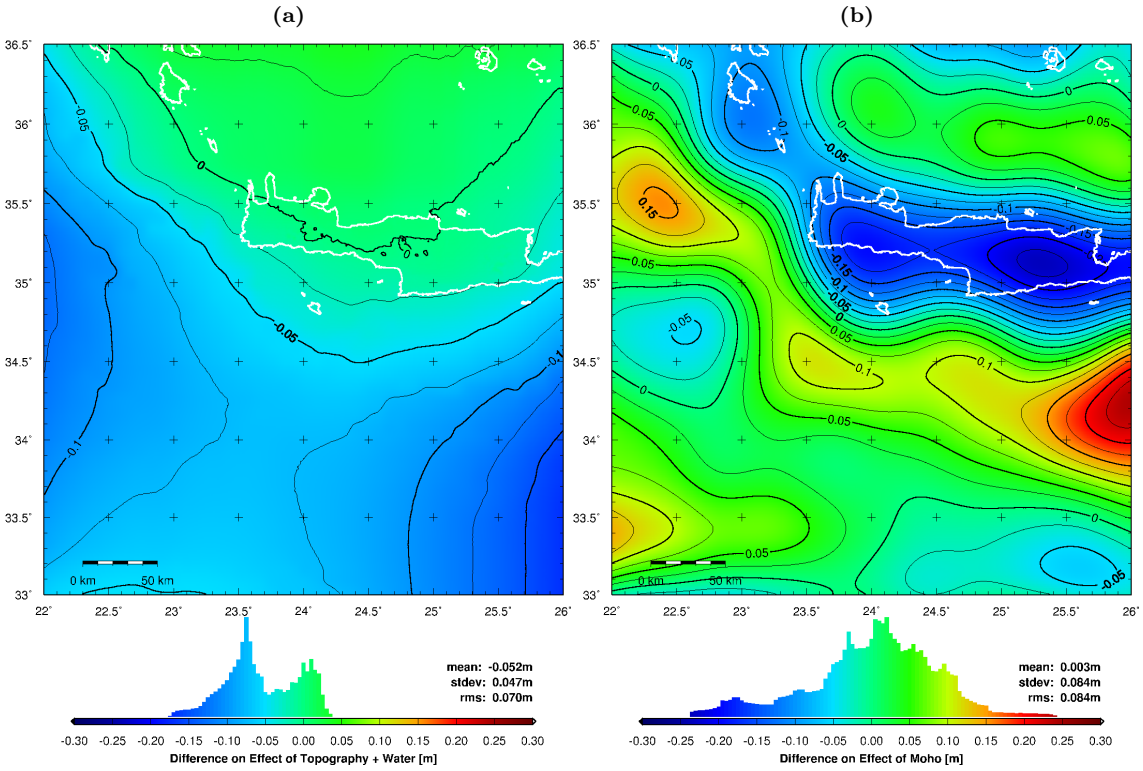

Figure 10.16: Differences on geoid heights between mass effects computed by cuboid masses and point masses from **(a)** topography/bathymetry and **(b)** Moho depths. Contour intervals: 0.025 m.

Table 10.2: Differences (mean offset, standard deviation (STD) and RMS) on geoid heights between mass effects computed by cuboid masses and point masses.

Effect	mean [cm]	STD [cm]	RMS [cm]
Topo/Bathy	-5.2	4.7	7.0
Sediments	-0.1	2.3	2.3
Moho	0.3	8.4	8.4
Topo/Bathy, Sediments, Moho	-5.0	8.1	9.6

In the present case, regarding the sizes of the residual geoid heights after the reduction of mass effects (Section 10.5, Fig. 10.17a to Fig. 10.20a), the approximation of the point mass model has no significant effect on the size and spatial structure of the residuals. Uncertainties of the topography, sediments and Moho, as well as of the exact mass distribution inside the different layers, induce larger errors than the point mass approximation. The same conclusions were drawn from a similar investigation in the survey area of the North Aegean Sea (Section 11.4.7).

10.5 Mass Reduction of Local Altimetric Geoid

10.5.1 Introduction

The mass effects computed in Section 10.4 were used to reduce the marine geoid heights obtained by airborne laser altimetry (Fig. 10.1a). While geoid undulations are mainly affected by large-scale mass anomalies, gravity anomalies are better suited to describe the short-wavelength part of the gravity field, affected by local mass anomalies. Hence, marine gravity anomalies derived from airborne altimetry (Fig. 10.1b) were also mass-reduced in order to obtain additional information on the local gravity field, although the major investigations were carried out on geoid heights. With the mass reduction, the mass effects are removed from the geoid heights or gravity anomalies. The residual geoid heights or gravity anomalies represent the effects caused by unmodeled masses. Hence, the mass reduction allows to detect anomalous mass distributions.

10.5.2 Topography-Bathymetry Cogeoid

In a first step, marine geoid heights from airborne laser altimetry (Fig. 10.1a) were reduced for the mass effects of topography and bathymetry (including water masses) (Fig. 10.8a). The mass-reduced geoid heights (Fig. 10.17a) correspond to the topography-bathymetry cogeoid. Associated mass-reduced gravity anomalies are shown in Fig. 10.17b. After the removal of a mean offset, the mass-reduced geoid heights range between -2.5 m and 4.0 m. The positive geoid anomaly around the isle of Gavdos (Fig. 10.1a) is removed by the reduction, meaning that this local feature is caused by the effects of the topographic masses of Gavdos and its surrounding bathymetry. Pronounced residual gradients in different directions remain in the entire survey area, indicating that besides the mass effects of topography and bathymetry, the structure of the geoid is influenced by additional effects. However, the major part of the geoid slope of 20 m across the survey area (Fig. 10.1a) was reduced to 6.5 m by removing the effects of topography and bathymetry.

10.5.3 Topography-Bathymetry-Sediments Cogeoid

In a second step, marine geoid heights from airborne laser altimetry (Fig. 10.1a) were reduced for the mass effects of topography, bathymetry and sediments (Fig. 10.13a). The mass-reduced geoid heights (Fig. 10.18a) correspond to the topography-bathymetry-sediments cogeoid. Associated mass-reduced gravity anomalies are shown in Fig. 10.18b. After the removal of a mean offset, the mass-reduced geoid heights range between -7 m in the north-east and 8 m in the south-west, with pronounced gradients in south-west direction south of Crete. Assuming the ideal case where the mass effects of topography, bathymetry and sediments were perfectly modeled and entirely removed by the reduction, and where no other mass anomalies except those produced by the Moho are present, the mass-reduced geoid heights (Fig. 10.18a) and gravity anomalies (Fig. 10.18b) would correspond to the mass effects produced by the real Moho. Under these assumptions, the pronounced mass-reduced geoid gradients south of Crete are an indicator for a significant Moho uplift along the Mediterranean Ridge towards the south of the survey area. This is confirmed by the pronounced positive mass-reduced gravity anomalies towards the south-west of the survey area, reaching up to 300 mGal (Fig. 10.18b). However, the residuals at the borders of the survey area need to be considered with reservation due to possible boundary effects. The predicted Moho uplift along the Mediterranean Ridge is in accordance with the uplifts of the ESC Moho (Fig. 10.7c) and the isostatic Moho (Fig. 10.7d). The nearly flat structure of the cogeoid north of Crete (Fig. 10.18a) indicates that the modeled geoid is almost parallel to the observed geoid. This means that the remaining mass effects of the Moho on geoid heights have to be more or less constant in this area. This is, however, in disagreement with the modeled mass effects of the ESC Moho (Fig. 10.11a) and the isostatic Moho (Fig. 10.12a).

10.5.4 Topography-Bathymetry-Sediments-Moho Cogeoid

In a third step, marine geoid heights from airborne laser altimetry (Fig. 10.1a) were reduced for the mass effects of topography, bathymetry, sediments and ESC Moho (Fig. 10.14a). The mass-reduced geoid heights (Fig. 10.19a) correspond to the topography-bathymetry-sediments-Moho cogeoid. Associated mass-reduced gravity anomalies are shown in Fig. 10.19b. After the removal of a mean offset, the mass-reduced geoid heights range between -4.5 m and 7.5 m, with pronounced gradients in west direction across a major part of the survey area. These gradients are produced by a large positive mass anomaly with respect to the modeled masses, situated beyond the western boundary of the survey area. The origin of this anomaly can be anomalously dense crustal material, an overestimation of the thickness of the sediment layer or an anomalously high Moho discontinuity with respect to the ESC Moho. The last hypothesis could be confirmed by comparing the ESC Moho (Fig. 10.7c) with the isostatic Moho (Fig. 10.7d). The strong local uplift of the isostatic Moho west of Crete, produced by the deep water zone of 4000 m, is less pronounced in the ESC Moho. Although the Moho associated with the subduction zone north of Crete is better modeled by the ESC Moho than by the isostatic Moho, the overall pronounced residual geoid gradients in west direction prevent a stringent interpretation of the topography-bathymetry-sediments-Moho cogeoid in the area north of Crete.

10.5.5 Topography-Bathymetry-Sediments-Isostasy Cogeoid

In a final step, marine geoid heights from airborne laser altimetry (Fig. 10.1a) were reduced for the mass effects of topography, bathymetry, sediments and isostatic Moho (Fig. 10.15a). The mass-reduced geoid heights (Fig. 10.20a) correspond to the topography-bathymetry-sediments-isostasy cogeoid. Associated mass-reduced gravity anomalies are shown in Fig. 10.20b. After the removal of a mean offset, the mass-reduced geoid heights range between -1.5 m and 5 m. The gradients south of Crete, observed in the topography-bathymetry-sediments cogeoid (Fig. 10.18a), have disappeared, indicating that they can be explaiend by the mass effects of the isostatic Moho. South of Crete, the predominant geoid gradients towards the Mediterranean Ridge, reaching impressive 0.22 m/km and characterizing the geoid of the entire region (Fig. 10.1a), were completely eliminated by the mass-reduction. The mass effects are mainly caused by the deep bathymetry down to -4000 m and the thick sedimentary deposits of up to 10 km. The variations of the mass-reduced geoid heights were reduced to 1.7 m south of Crete.

North of Crete, a pronounced geoid gradient of 0.1 m/km in north direction appears after the reduction (Fig. 10.20a), indicating a significant positive mass anomaly north of Crete. Since the gradient is not weakening towards the northern border of the survey area and since the mass-reduced gravity anomalies (Fig. 10.20b) are not indicating a local mass excess inside the survey area, the positive mass anomaly must be situated beyond the northern border of the survey area. The origin of this mass anomaly can be anomalously dense crustal material or an anomalously high Moho with respect to the isostatic Moho. Both hypotheses are in accordance with density models based on seismic soundings in the area of the Hellenic subduction zone and the Hellenic Trench, characterized by the collision between the African and European lithospheric plates (Snopek et al., 2007; Makris and Yegorova, 2006; Casten and Snopek, 2006). These density models indicate an upwelling of the European mantle north of Crete, related to the subduction of the African oceanic lithosphere beneath the Eurasian (Aegean) continental lithosphere and causing a significant positive mass anomaly. It is obvious that the complexity of the Moho discontinuity and mass anomalies associated with the subduction zone cannot be adequately modeled by isostatic compensation. As a consequence, the major geoid anomaly in the area is the elevation of the geoid north of Crete, rather than the depression south of Crete along the Mediterranean Ridge, since the latter can be explained by the mass effects of the topography, batymetry, sediments and isostasy. In order to localize the mass anomaly north of Crete, an extension of the survey area towards the North would be necessary.

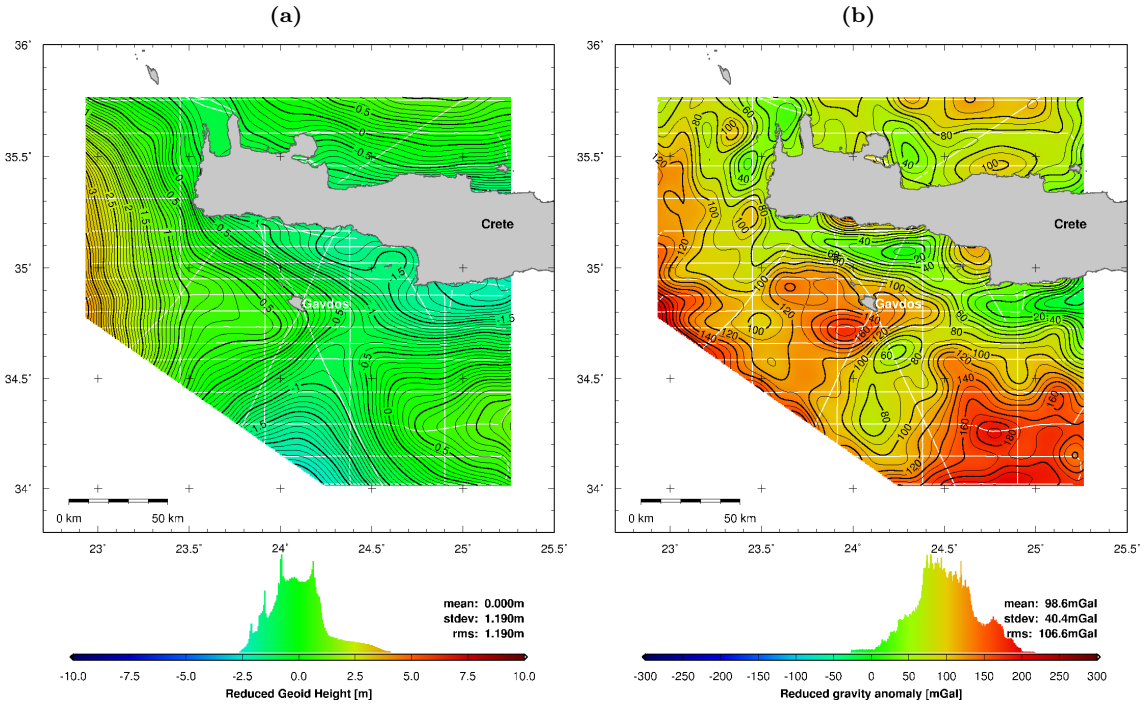

Figure 10.17: **(a)** Geoid heights from airborne laser altimetry (Fig. 10.1a) reduced for the mass effects of topography and bathymetry (Fig. 10.8a), with mean offset removed. **(b)** Associated gravity anomalies from reduction of Fig. 10.1b with Fig. 10.8b. Contour intervals: 0.1 m and 10 mGal.

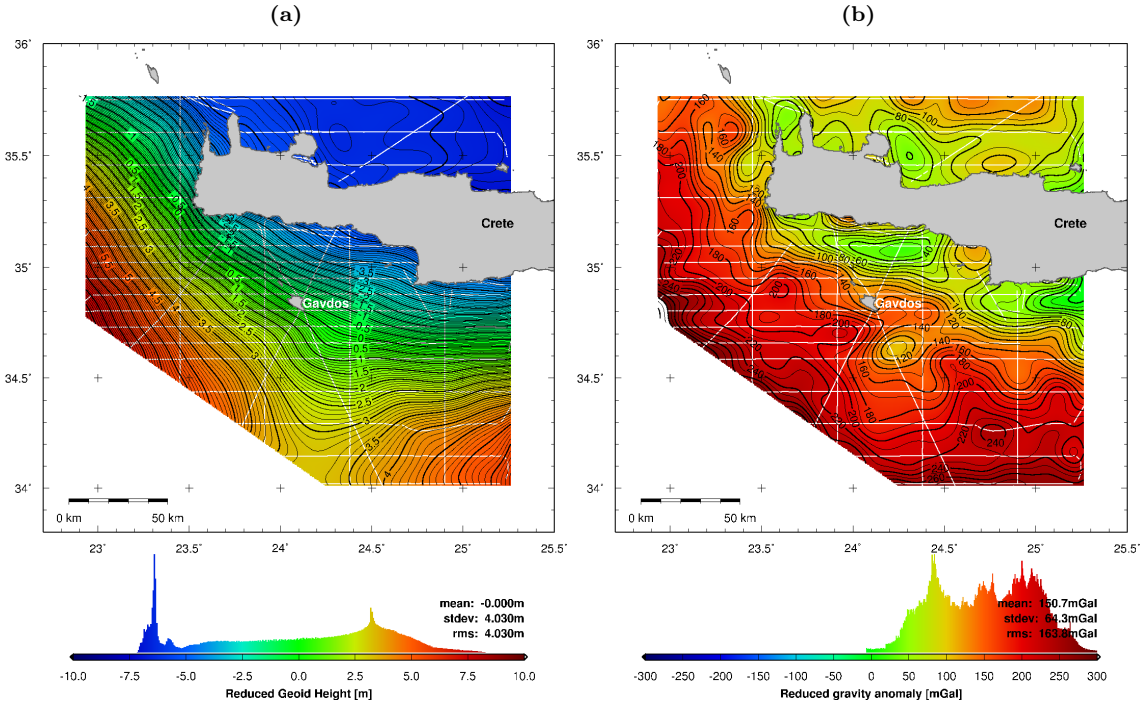

Figure 10.18: **(a)** Geoid heights from airborne laser altimetry (Fig. 10.1a) reduced for the mass effects of topography, bathymetry and sediments (Fig. 10.13a), with mean offset removed. **(b)** Associated gravity anomalies from reduction of Fig. 10.1b with Fig. 10.13b. Contour intervals: 0.1 m and 10 mGal.

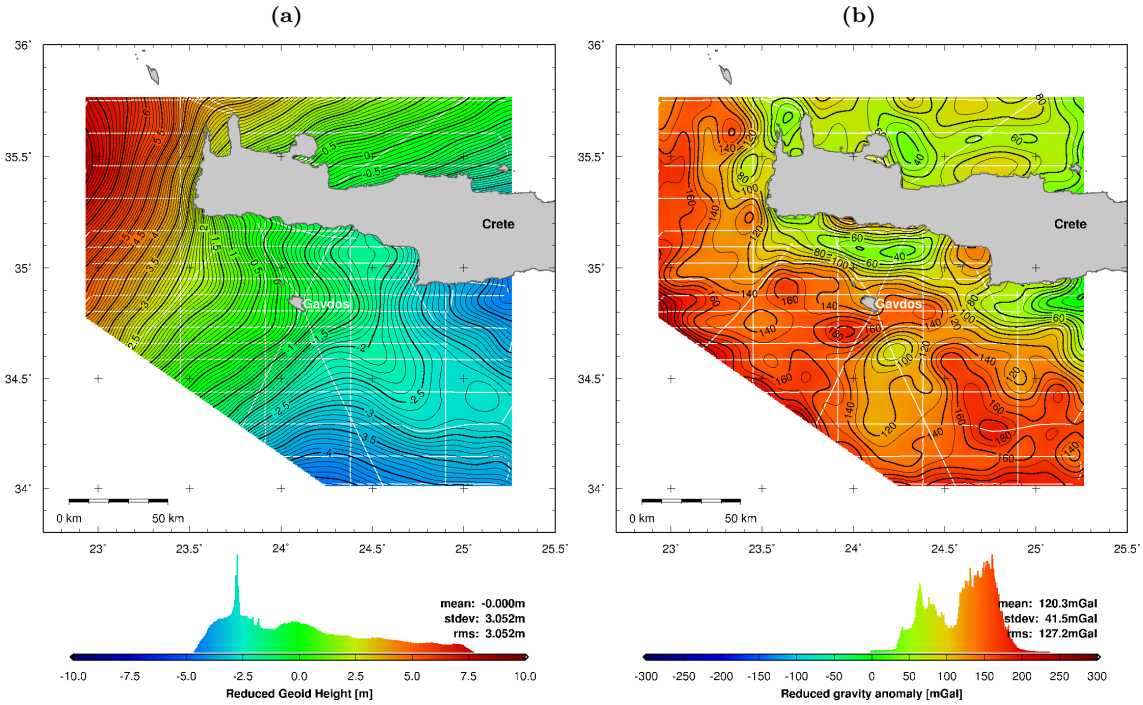

Figure 10.19: **(a)** Geoid heights from airborne laser altimetry (Fig. 10.1a) reduced for the mass effects of topography, bathymetry, sediments and ESC Moho (Fig. 10.14a), with mean offset removed. **(b)** Associated gravity anomalies from reduction of Fig. 10.1b with Fig. 10.14b. Contour intervals: 0.1 m and 10 mGal.

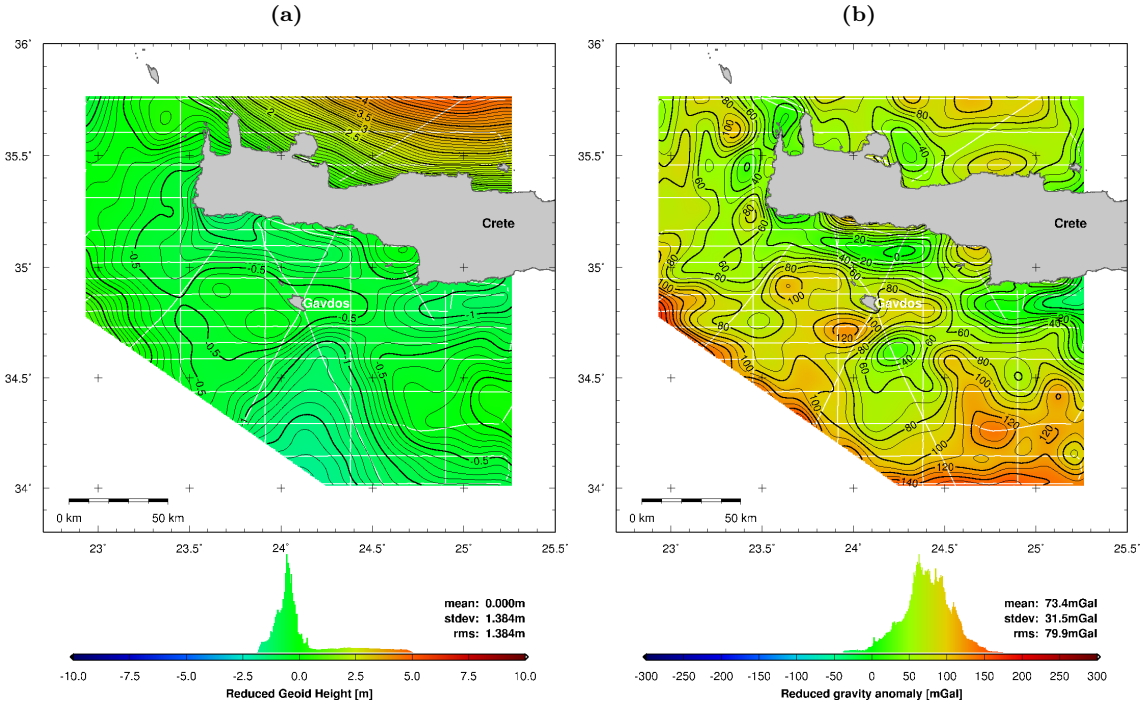

Figure 10.20: **(a)** Geoid heights from airborne altimetry (Fig. 10.1a) reduced for the mass effects of topography, bathymetry, sediments and isostatic Moho (Fig. 10.15a), with mean offset removed. **(b)** Associated gravity anomalies from reduction of Fig. 10.1b with Fig. 10.15b. Contour intervals: 0.1 m and 10 mGal.

11 Geoscientific Exploitation of Shipborne Altimetry Data in the North Aegean Sea

11.1 Marine Geoid, Gravity Anomalies and Deflections of the Vertical from Sea Surface Heights

Assuming the mean dynamic topography (MDT) as known, marine geoid heights can be derived from observed sea surface heights by subtracting the MDT (2.2). The MDT used in this study is the RioMed mean dynamic topography of the Mediterranean Sea (Section 2.5.3, Fig. 2.5a). The effects of the MDT in the survey area are small, with values between 0 and 5 cm only (Fig. 2.6b). By subtracting the RioMed MDT (Fig. 2.6b) from the sea surface heights obtained by shipborne altimetry (Fig. 8.13), altimetric geoid heights with respect to the WGS84 ellipsoid are obtained (Fig. 11.1a). The obtained geoid heights reveal that the bathymetric low of the North Aegean Trough is associated with a distinct depression of the geoid at the south-western end of the North Aegean Trough. The depression reaches a minimum of 37.9 m, while the geoid height in the surrounding area is more than 39.5 m and reaches 40.5 m towards the north of the survey area. Further details on the geodynamic processes associated with the North Aegean Trough are given in Section 1.2.

Gravity anomalies (Fig. 11.1b) were computed from the marine geoid heights (Fig. 11.1a), based on Laplace's equation (2.19) and the curvature of the geoid (2.20), using the GMT (Generic Mapping Tools) software (Wessel and Smith, 1998, 2005). As compared to geoid heights, gravity anomalies are less affected by the long-wavelength part of the gravitational potential and are therefore better suited for the analysis of local gravity anomalies. Gravity anomalies in the survey area range from -60 mGal at the geoid depression at the south-western end of the North Aegean Trough to 60 mGal in the North (Fig. 11.1b).

Variations of the geoid were further quantified by computing horizontal gradients (Fig. 11.1c) and deflections of the vertical (2.14) (Fig. 11.1d) from the geoid heights. Maximum geoid gradients of up to 0.1 m/km are observed north of the island of Alonnisos, corresponding to a deflection of the vertical of 20 arcsec. For comparison and validation purposes, deflections of the vertical from astrogeodetic observations (Somieski, 2008), (Müller et al., 2006) are added in Fig. 11.1d. Further interpretation of the obtained geoid heights and gravity anomalies is carried out in the framework of the reduction of mass effects in Section 11.5.

11.2 Local Altimetric Geoid vs. Existing Models

To validate the marine geoid heights (Fig. 11.1a) obtained by shipborne altimetry (Section 11.1), they were compared to geoid heights from several gravity models. The analyzed global gravity models are EGM96 (Fig. 11.2a), EGM2008 (Fig. 11.2b), EIGEN-5S (Fig. 11.2c) and EIGEN-5C (Fig. 11.2d). All geoid heights were computed with respect to the WGS84 ellipsoid. Further details on the gravity models are given in Section 2.2.3. The different resolutions of the geoid models are

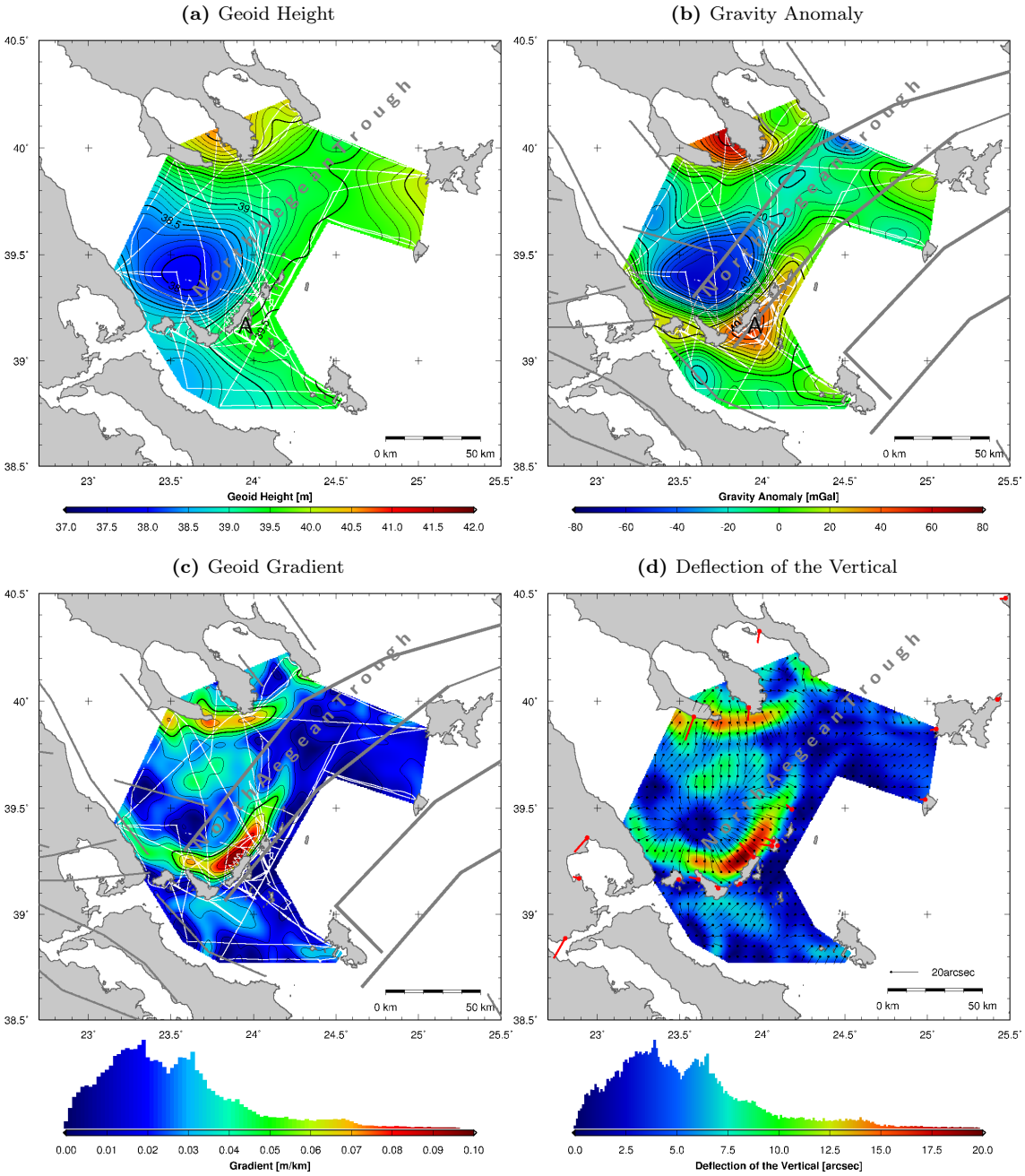

Figure 11.1: **(a)** Altimetric geoid heights with respect to the WGS84 reference ellipsoid, obtained by subtracting the RioMed mean dynamic topography (Fig. 2.6b) from sea surface heights determined by shipborne altimetry (Fig. 8.13). Contour interval: 0.1 m. White lines: ship tracks. A = Alonnisos. **(b)** Gravity anomalies derived from geoid heights in (a). Contour interval: 5 mGal. Gray lines: North Aegean fault system. **(c)** Horizontal gradients of the geoid heights in (a). Contour interval: 0.01 m/km. **(d)** Deflections of the vertical from geoid heights in (a). Red vectors: deflections of the vertical from astrogeodetic observations.

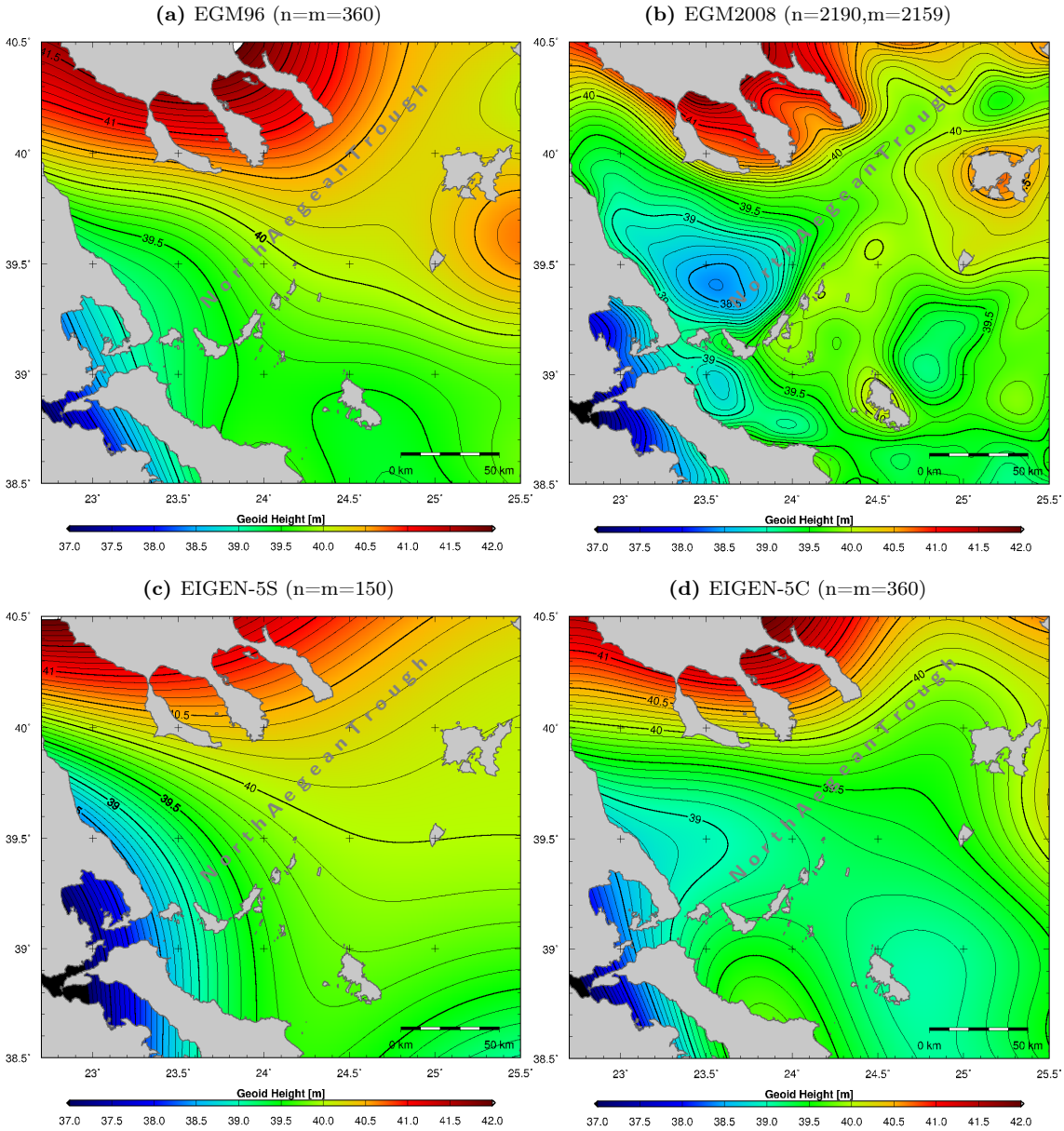

Figure 11.2: Geoid heights to degree n and order m with respect to the WGS84 reference ellipsoid, from **(a)** EGM96, **(b)** EGM2008, **(c)** EIGEN-5S and **(d)** EIGEN-5C. Contour intervals: 0.1 m.

seen (Fig. 11.2), e.g. by their capability of resolving the depression at the south-western end of the North Aegean Trough.

The residuals between the altimetric geoid (Fig. 11.1a) and the geoid models (Fig. 11.2) are shown in Fig. 11.3. Mean offsets and standard deviations are summarized in Tab. 11.1. In the ideal case of error-free sea surface heights, dynamic topography and geoid models, these residuals should be zero according to 2.27. The residuals with respect to EIGEN-5S have large values reaching 1.5 m, large gradients and a high standard deviation of 0.37 m (Fig. 11.3c). The poor agreement is due to the low resolution (approx. 130 km) of the EIGEN-5S. The two combined geoid solutions EGM96 and EIGEN-5C have a theoretical resolution of 55 km. The mean difference between

Table 11.1: Mean offsets and standard deviations (STD) between the altimetric geoid from shipborne altimetry and geoid models.

Geoid Model	(degree,order)	mean offset [m]	STD [m]
EIGEN-5S	(150,150)	-0.63	0.37
EIGEN-5C	(360,360)	-0.31	0.38
EGM96	(360,360)	-0.80	0.37
EGM2008	(360,360)	-0.42	0.25
EGM2008	(2190,2159)	-0.41	0.08
AUTH2008	-	-0.94	0.10

the altimetric geoid and EGM96 (Fig. 11.3a) and EIGEN-5C (Fig. 11.3d) are -0.80 m and -0.31 m, respectively, with similar standard deviations of 0.37 m and 0.38 m. As for EIGEN-5S, both models do not resolve the local negative anomaly at the south-western end of the North Aegean Trough, with residuals reaching -1.55 m and -1.05 m, respectively. The best agreement is obtained with EGM2008, with a mean difference of -0.41 m[1] and a standard deviation of 0.08 m (Fig. 11.3b). The good agreement is due to the high resolution of EGM2008. Its expansion to degree 2190 and order 2159 corresponds to a resolution of approx. 10 km.

The improved input data in terms of resolution and accuracy of the recent EIGEN-5C, as compared to EGM96, does not yield a significant improvement of the spatial resolution of EIGEN-5C. As already shown for the airborne data around Crete (Section 10.2), the limiting factor in terms of spatial resolution of the geoid models is their mathematical expansion of the spherical harmonics. Again, this is confirmed by computing an EGM2008 solution with a spherical harmonics expansion limited to degree and order 360 (Fig. 11.4a). The residuals with respect to the altimetric geoid have a standard deviation of 0.25 m (Fig. 11.5a), similar to those of EGM96 (Fig. 11.3a) and EIGEN-5C (Fig. 11.3d). The extension of the expansion of EGM2008, from degree and order 360 to degree 2190 and order 2159, yields an improvement of 0.17 m of the standard deviation with respect to the altimetric geoid, corresponding to an improvement of 68%. Additional residuals were computed between the altimetric geoid and the local gravimetric geoid model AUTH2008 (Fig. 11.4b) (Section 2.2.3). The residuals have a standard deviation of 0.10 m (Fig. 11.5b), similar to the one obtained with respect to EGM2008.

The mean offsets (Tab. 11.1) are different from the ones obtained with respect to the airborne altimetric geoid around Crete (Tab. 10.1), indicating discrepancies in the long wavelength geoid undulations between the two areas under investigation. Since the absolute geoid height is not of major interest, the offsets are not critical and were therefore not further investigated.

[1] It is a coincidence that this difference corresponds to the value of 0.41 m that has to be subtracted from EGM2008 geoid heights to make them correspond to the mean sea surface. By using the same method to compute residuals in the area around Crete, a mean difference of -0.14 m was obtained (Fig. 10.3b). Furthermore, without subtracting 0.41 m from EGM2008, the mean difference would be -0.82 m.

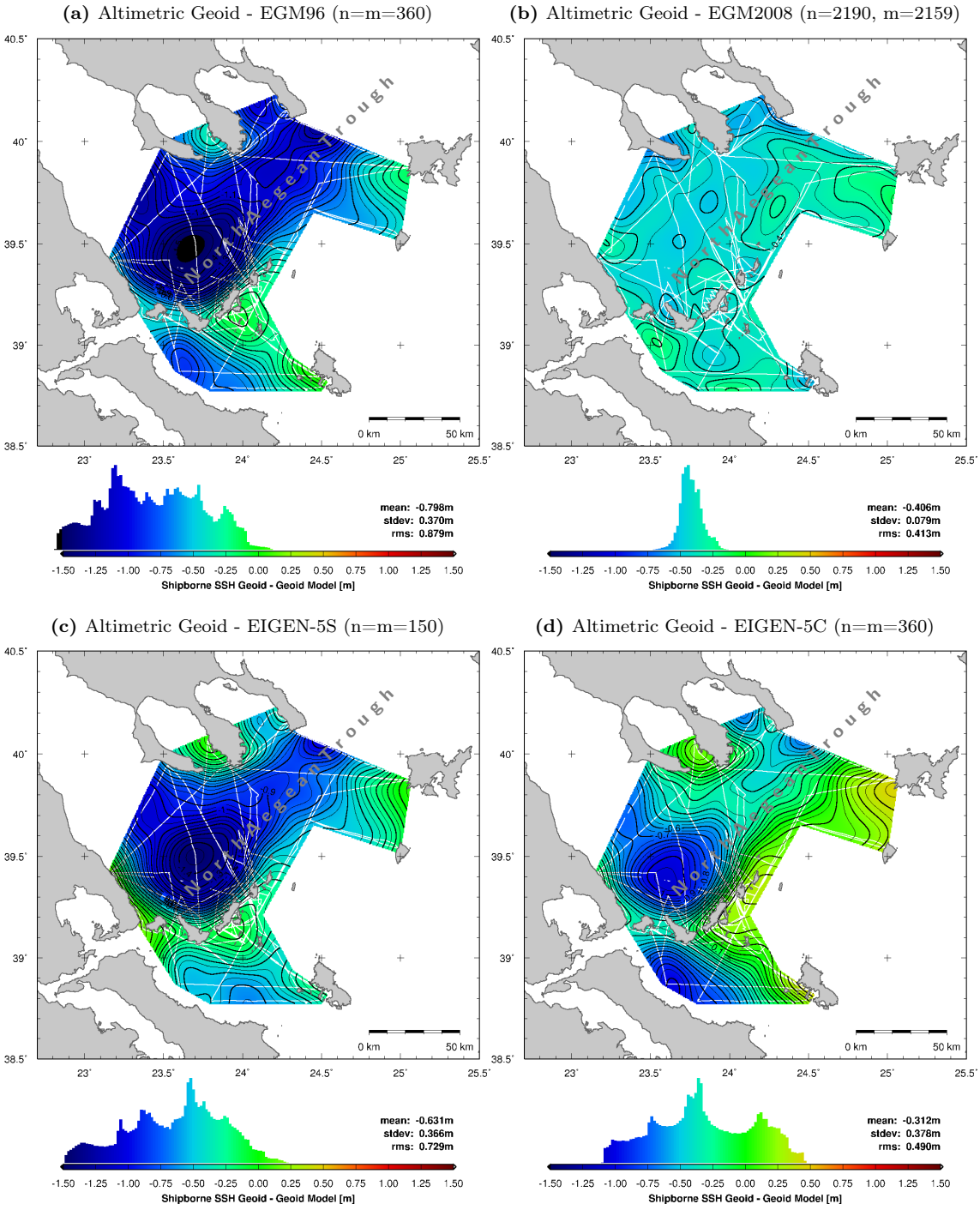

Figure 11.3: Difference between shipborne altimetric geoid (Fig. 11.1a) and geoid heights to degree n and order m from **(a)** EGM96, **(b)** EGM2008, **(c)** EIGEN-5S and **(d)** EIGEN-5C. White lines: ship tracks. Contour intervals: 0.05 m.

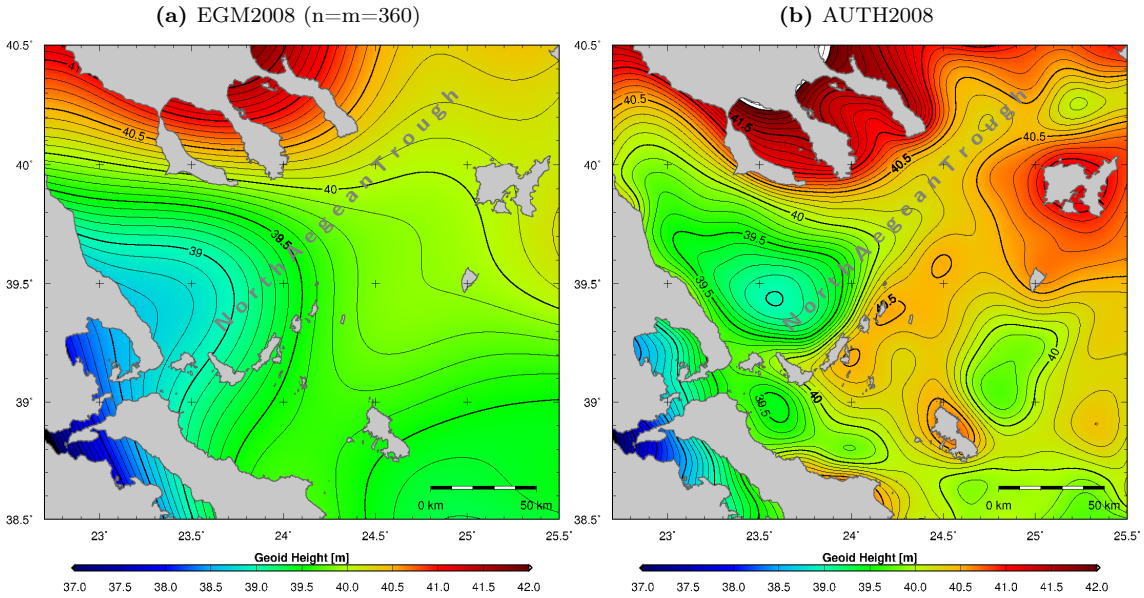

Figure 11.4: Geoid heights with respect to the WGS84 reference ellipsoid, from **(a)** EGM2008 with expansion limited to degree and order 360 and from **(b)** the gravimetric model AUTH2008 (b). Contour intervals: 0.1 m.

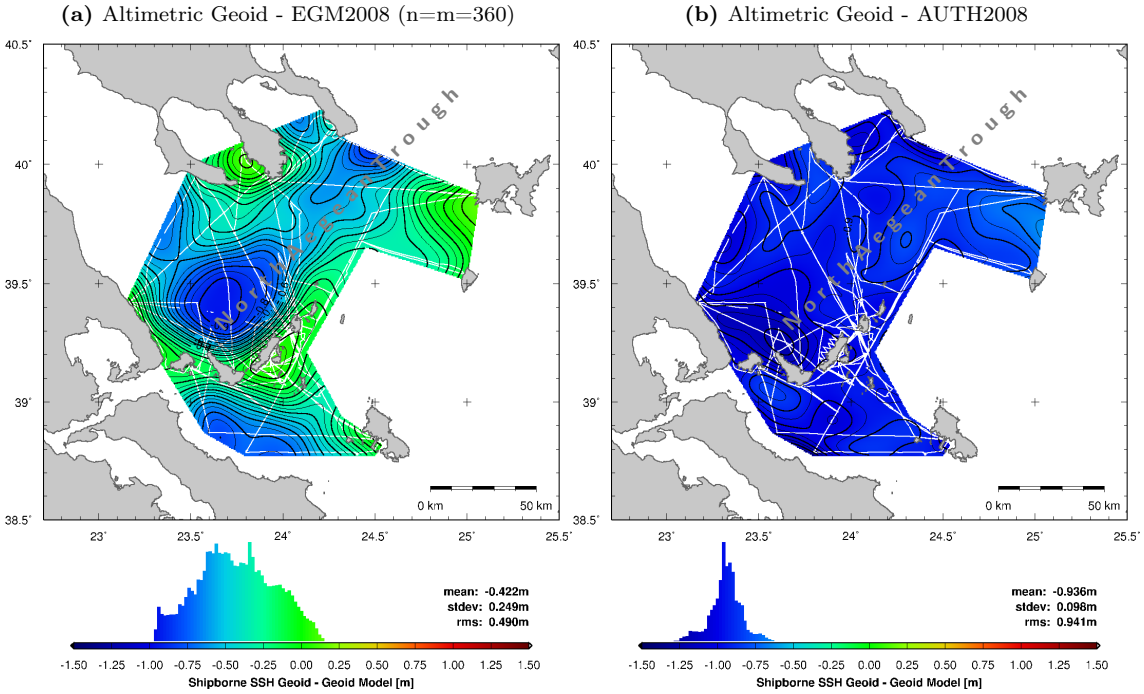

Figure 11.5: Difference between shipborne altimetric geoid (Fig. 11.1a) and geoid heights from **(a)** EGM2008 to degree and order 360 and **(b)** AUTH2008. White lines: ship tracks. Contour intervals: 0.05 m.

11.3 Mean Dynamic Topography Estimation

Among the geoid models used in Section 11.2, the satellite-only solution EIGEN-5S and the local gravimetric geoid model AUTH2008 are the only geoid solutions that are independent of altimetric sea surface height data. Hence, they would be the only appropriate models to determine the mean dynamic topography (MDT) using the direct method after (2.28) (Section 2.5). The pronounced residuals between the shipborne data and EIGEN-5S (Fig. 11.3c) are obviously making the EIGEN-5S unusable for realistic MDT determination at wavelengths below 130 km. The same remark holds for EGM96 and EIGEN-5C (Fig. 11.3a and Fig. 11.3d). Even if these models were independent of altimetric data, they would not be appropriate to determine the MDT at wavelengths below 55 km. Hypothetic MDT were computed from the residual fields of the sea surface heights from shipborne altimetry (Fig. 8.13) with respect to EGM2008 (Fig. 11.6a) and AUTH2008 (Fig. 11.6b) geoid heights. Geostrophic circulation fields were derived from the hypothetic MDT based on (2.30). Compared to the RioMed mean geostrophic circulation (Fig. 2.6b), the obtained circulations are unrealistic and spoiled by noisy eddies. By applying low-pass filters to both datasets, it was possible to eliminate the noisy eddies, but no significant circulation remained. Hence, it was not possible to derive a realistic circulation pattern based on the sea surface height observations and the used geoid models. The major reason lies in the fact that the presumed MDT, as e.g. given by RioMed (Fig. 2.6b), varies only within a range of 4 cm over the entire survey area. Furthermore, the gradients of the MDT associated with the circulation are below 0.5 cm/10 km. Hence, the MDT signal in the survey area is smaller or in the same order of magnitude as the accuracy of the shipborne sea surface heights and the used geoid models. It can be concluded that the sea surface height observations by shipborne altimetry and the considered geoid models are not accurate enough to resolve such small dynamic effects. In addition, EGM2008 is not independent of altimetric sea surface height data.

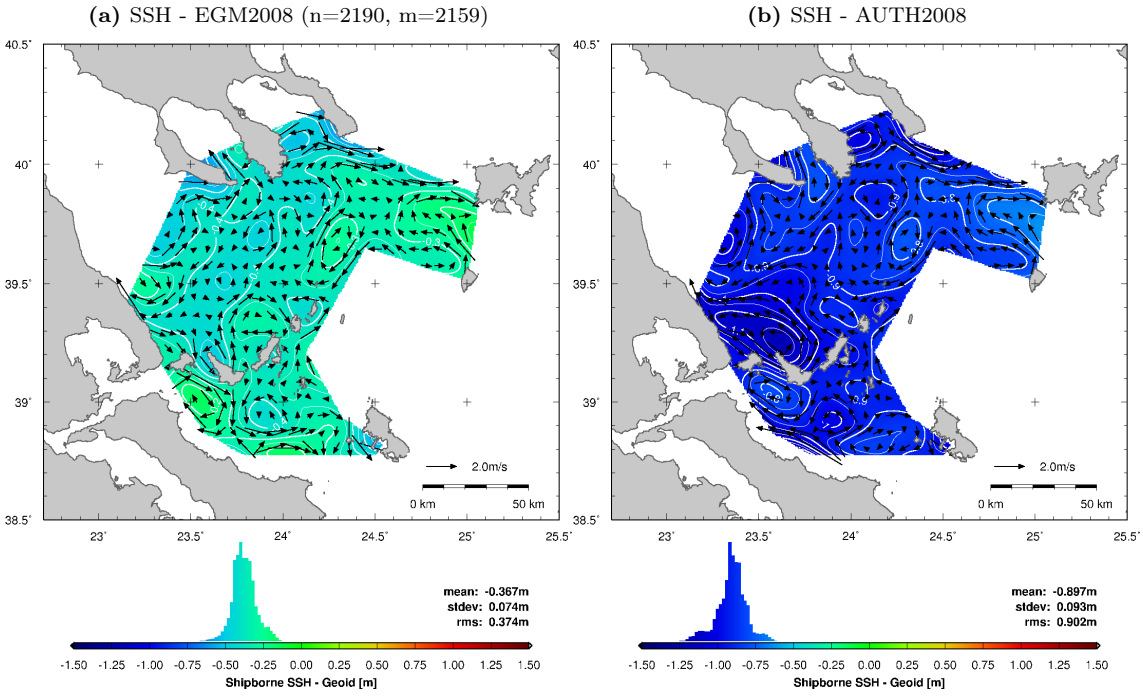

Figure 11.6: Hypothetic mean dynamic topography (background) and ocean circulation (arrows) from differences between sea surface heights from shipborne altimetry (Fig. 8.13) and geoid heights from **(a)** EGM2008 and **(b)** AUTH2008.

11.4 Modeled Mass Effects on Geoid Heights and Gravity

11.4.1 Introduction

The effects of mass anomalies on geoid heights were computed for the survey area in the North Aegean Sea, based on (2.22) and on cuboid masses (2.24). The grid spacing of the computation points and the mass elements was 30' × 30', corresponding to approx. 900 m. The distances between the mass elements and the computation points were computed using geocentric coordinates, in order to avoid effects of Earth's curvature. A maximum radius of influence of 275 km was considered for the masses effects. The area of influence extends from 19°E to 29°E and from 36°N to 43°N (Fig. 11.7a). The mass densities in Tab. 2.1 were used. Geoid heights are highly influenced by large-scale mass anomalies (Section 2.2.2). As compared to geoid heights, gravity anomalies are less affected by the long-wavelength part of the gravitational potential and are therefore better suited for the analysis of local gravity anomalies. Hence, the effects of mass anomalies on gravity were computed, based on (2.23) and (2.25), in order to obtain additional information on the local gravity field, although the major investigations were carried out on geoid heights. The gravity anomalies were computed at sea level, yielding e.g. exclusively negative effects of the topography on gravity anomalies. The mass effects are used in the Section 11.5 to reduce the geoid heights and gravity anomalies derived from shipborne altimetry. The theoretical background of the computation of mass effects on geoid heights and on gravity anomalies is given in Section 2.2.2.

11.4.2 Mass Effect of Topography and Bathymetry

The topography and bathymetry were taken from the SRTM30 (Shuttle Radar Topography Mission) digital terrain model, published by the United States Geological Survey (USGS). It has a resolution of 30'×30', corresponding to approx. 900 m. The topography and bathymetry of the area of influence are characterized by the topographic masses surrounding the North Aegean Sea and by the bathymetry of the North Aegean Trough (Fig. 11.7a). The topography and bathymetry (including water masses) have mainly positive effects on geoid heights (Fig. 11.8a), since the positive effect of the topographic mass excess predominates over the negative effect of the mass deficiency due to the water. The effect ranges between 18 m in the north-west and -4 m in the south of the survey area. A relative depression, associated with the bathymetric low of the North Aegean Trough, can hardly be depicted, due to the pronounced overall geoid gradient in north-west direction caused by the topographic mass excess in the north-west of the area of influence. Associated gravity anomalies are shown in Fig. 11.8b. Within the effect of topography and bathymetry, the water masses have positive effects between 0.7 m on the northern mainland of the survey area and 2.7 m at the North Aegean Trough (Fig. 11.9a). In the south-western part, the effect reaches 9 m, caused by the deep water of the Ionian Sea in the south-western part of the area of influence. Associated gravity anomalies are shown in Fig. 11.9b.

11.4.3 Mass Effect of Sediments

The survey area is characterized by two marine sediment spots reaching thicknesses of 6 km (Fig. 11.7b). The mass deficiency associated with the sediments has a negative effect on geoid heights, reaching -3 m (Fig. 11.10a). Associated gravity anomalies are shown in Fig. 11.10b.

11.4.4 Mass Effect of Moho Depths

For the computation of the effect of crust-mantle boundary (Moho) anomalies, Moho depths from the digital Moho depth map published by the ESC (European Seismological Commission) Working

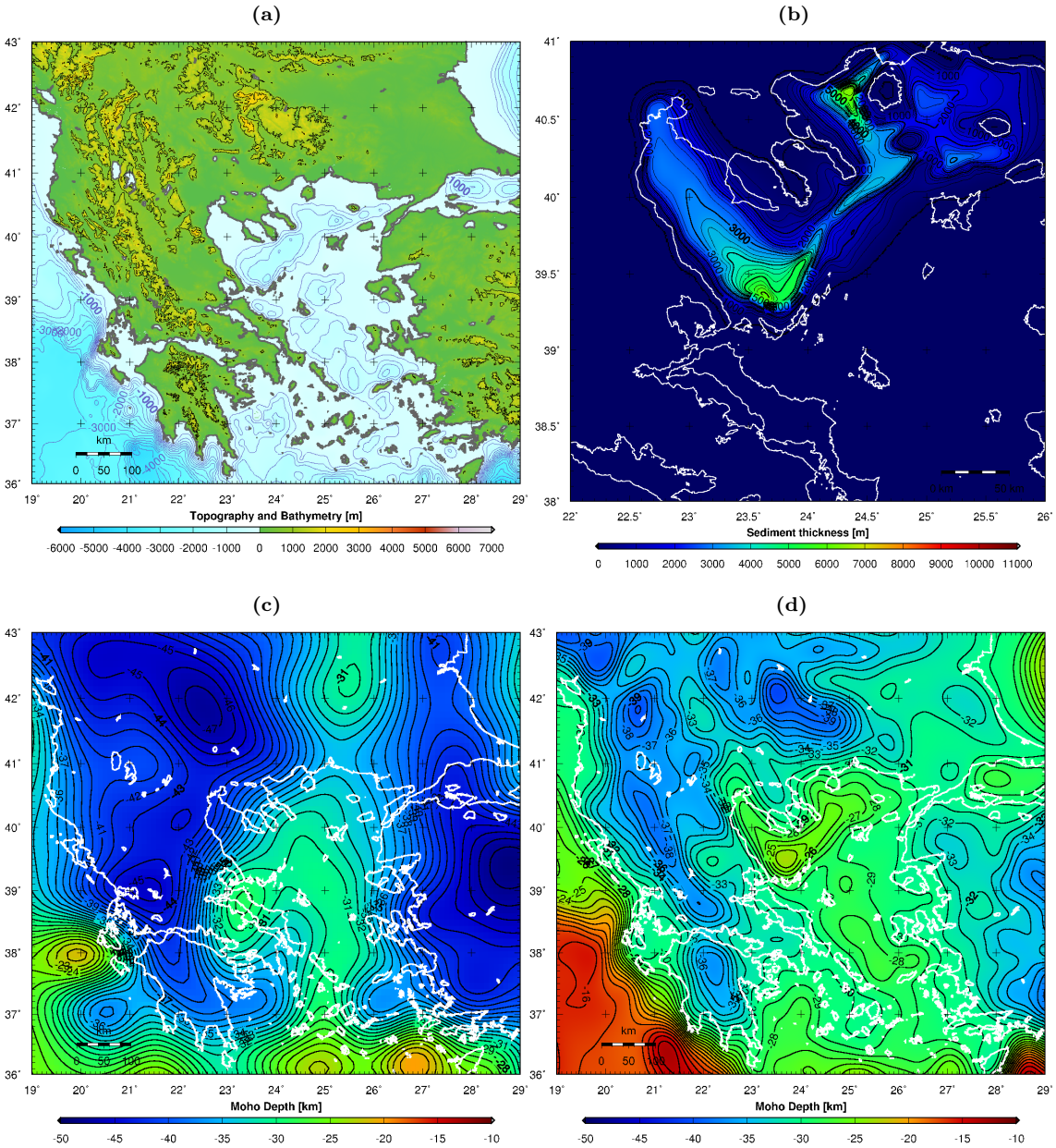

Figure 11.7: **(a)** Topography and bathymetry of the area of influence considered in the modeling of mass effects (contour interval topo: 1000 m, bathy: 250 m). **(b)** Light sediment thickness from unknown source (contour interval: 250 m). **(c)** Moho depth from ESC (Grad et al., 2009) (contour interval: 1 km). **(d)** Moho depth from isostatic compensation (reference depth: 30 km, contour interval: 1 km).

Group (Grad et al., 2009) (Fig. 11.7c) were used. Further details on the ESC Moho depths are given in Section 10.4.4. The Moho in the survey area is characterized by large-scale depressions over the Greek and Turkish mainland, locally reaching -47 km. The mass deficiency caused by the depression of the Moho in the north-west of the area of influence causes pronounced negative effects of more than -20 m on geoid heights, whereas the effect in the south reaches positive values of more than 10 m (Fig. 11.11a). Associated gravity anomalies are shown in Fig. 11.11b.

11.4.5 Mass Effect of Isostatic Moho Depths

As an alternative to the ESC Moho, Moho depths were computed based on isostatic compensation of the masses of topography, bathymetry, water and sediments, similar to the procedure in Section 10.4.5). A reference depth of -30 km was used. Since the model of isostatic compensation only reflects a theoretical correlation between the masses above the crust-mantle boundary (Moho) and the compensating depth of the boundary, it may sound more appropriate to use a Moho model predicted by real observations, like the ESC Moho (Section 11.4.4). In the present study, however, better reduction results were obtained with the isostatic Moho (Section 11.5).

The isostatic compensation has a weak uplift effect on the Moho in the marine areas of the Aegean Sea (Fig. 11.7d), due to mass deficiencies caused by water and sediments. The isostatic Moho rises up to a depth of -25 km at the North Aegean Trough. On the mainland, the Moho is characterized by large-scale depressions locally reaching -39 km, associated with a topographic mass excess. In the north of the survey area, the drop of the Moho is causing a mass deficiency that has a negative effect on geoid heights, reaching -15.5 m in the north-west (Fig. 11.12a). In the south, a positive effect of the Moho on geoid heights is obtained, reaching 7.5 m in the south-west. Associated gravity anomalies are shown in Fig. 11.12b.

11.4.6 Combined Mass Effects

The combination of the effects of topography and bathymetry (Fig. 11.8a) with the effects of sediments (Fig. 11.10a) yield mostly positive effects on geoid heights (Fig. 11.13a). They range between 17.5 m in the North-West and -4 m in the South. The introduction of the effects of sediments amplifies the local geoid depression at the North Aegean Trough. Associated gravity anomalies are shown in Fig. 11.13b.

The combination of the effects of topography, bathymetry and sediments (Fig. 11.13a) with the effects of the ESC Moho (Fig. 11.11a) reduces the effects on geoid heights (Fig. 11.14a). They reach a maximum of 8 m in the South and a minimum of -6 m in the North-West. By visually comparing the modeled geoid (Fig. 11.14a) to the observed geoid (Fig. 11.1a) and to EGM2008 (Fig. 11.2b), a poor agreement is observed. In particular, the modeled geoid (Fig. 11.14a) shows no distinct depression at the North Aegean Trough. Associated gravity anomalies are shown in Fig. 11.14b.

The combination of the effects of topography, bathymetry and sediments (Fig. 11.13a) with the effects of the isostatic Moho (Fig. 11.12a) yield small effects on geoid heights (Fig. 11.15a). They reach a maximum of 3 m in the West and North-West, associated with major topographic mass excesses, and a local minimum of -2.2 m at the North Aegean Trough. The introduction of the effect of the isostatic Moho removes the major geoid gradient in north-west direction observed in Fig. 11.8a and Fig. 11.13a. As a consequence, the shape of the modeled geoid becomes more realistic when compared to the observed geoid (Fig. 11.1a) and to EGM2008 (Fig. 11.2b). Associated gravity anomalies are shown in Fig. 11.15b.

11.4.7 Cuboids vs. Point Mass Modeling

The mass effects (Fig. 11.8 to Fig. 11.15) were computed based on cuboids masses using (2.24) and (2.25). Since the computation involving cuboid masses can be very CPU-intensive depending on the size and resolution of the data grids, a simplified method to compute mass effects on geoid heights and on gravity based on (2.22) and (2.23) consists in concentrating the mass of each cuboid at its center of mass. To assess the impact of this approximation, the effects computed by cuboid masses on geoid heights (Fig. 11.8a to Fig. 11.15a) were recomputed based on the center of mass (point mass) method. Differences between the cuboid and point mass methods are increased by the presence of elongated cuboids close to the computation point, typically produced by high

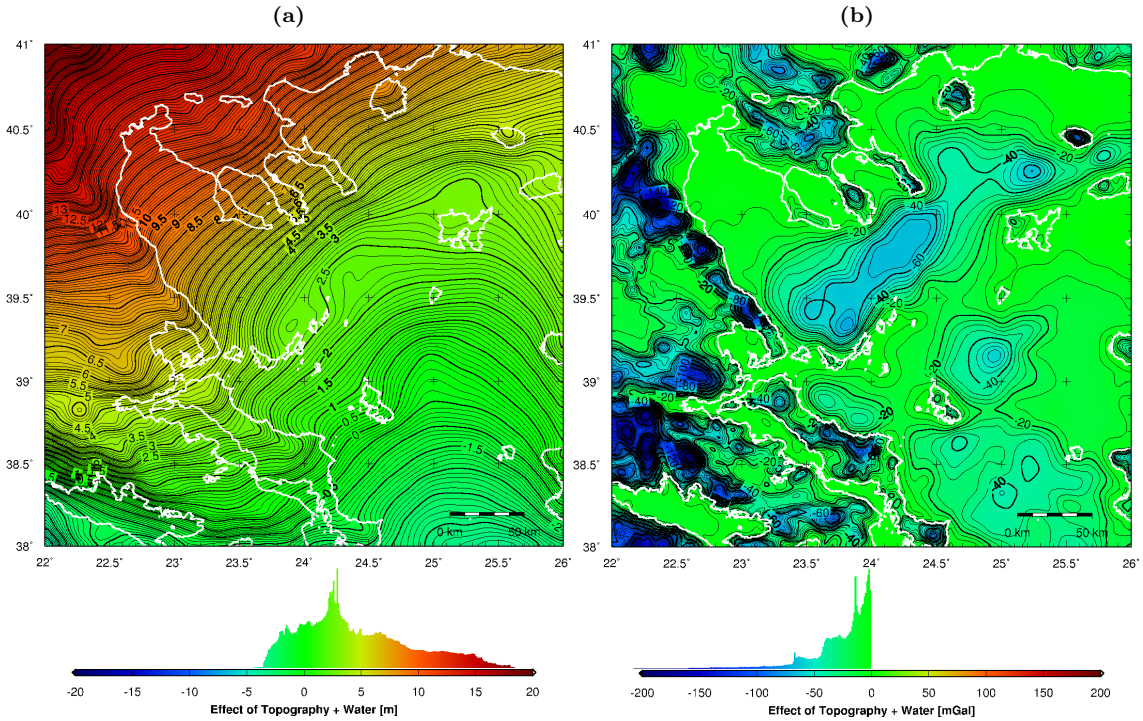

Figure 11.8: Effects of topography and bathymetry (including water masses) on **(a)** geoid heights (contour interval: 0.1 m) and **(b)** gravity (contour interval: 5 mGal).

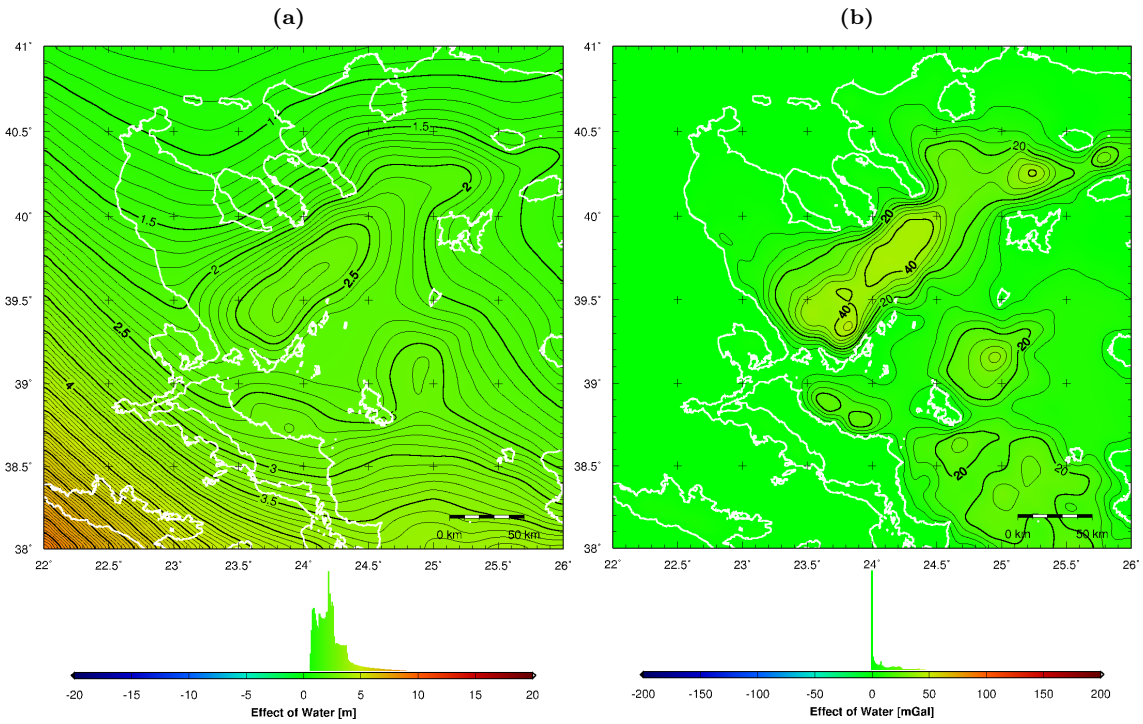

Figure 11.9: Effect of water masses on **(a)** geoid heights (contour interval: 0.1 m) and **(b)** gravity (contour interval: 5 mGal).

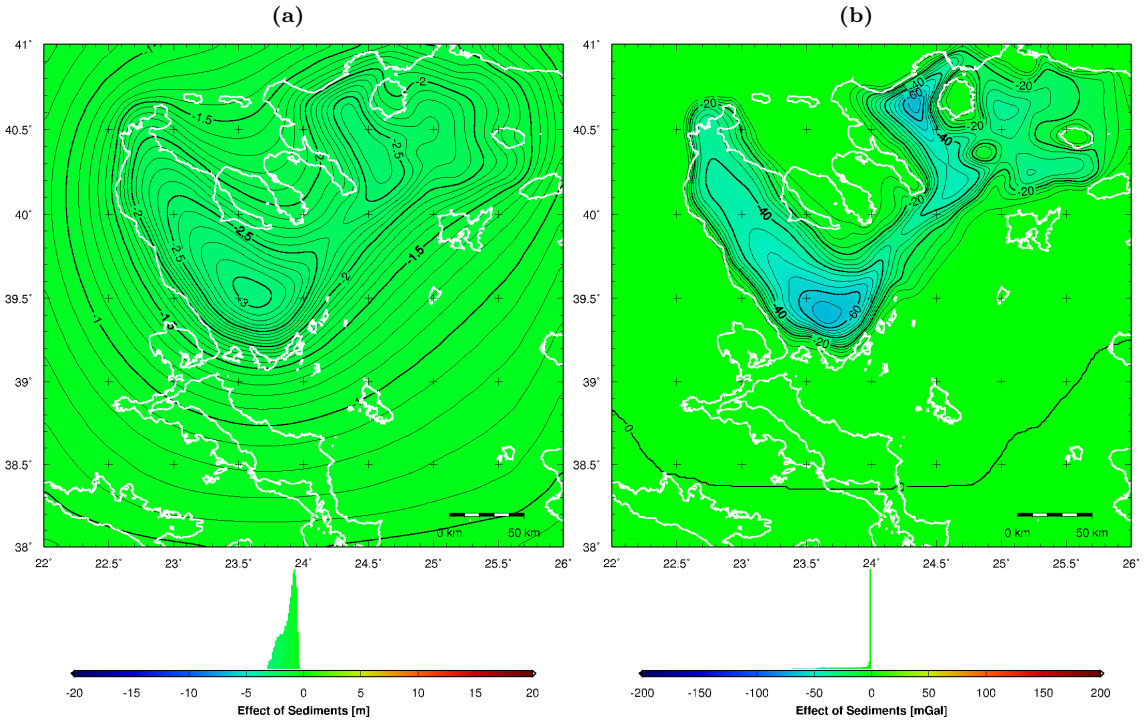

Figure 11.10: Effect of mass deficiency caused by sediments on **(a)** geoid heights (contour interval: 0.1 m) and **(b)** gravity (contour interval: 5 mGal).

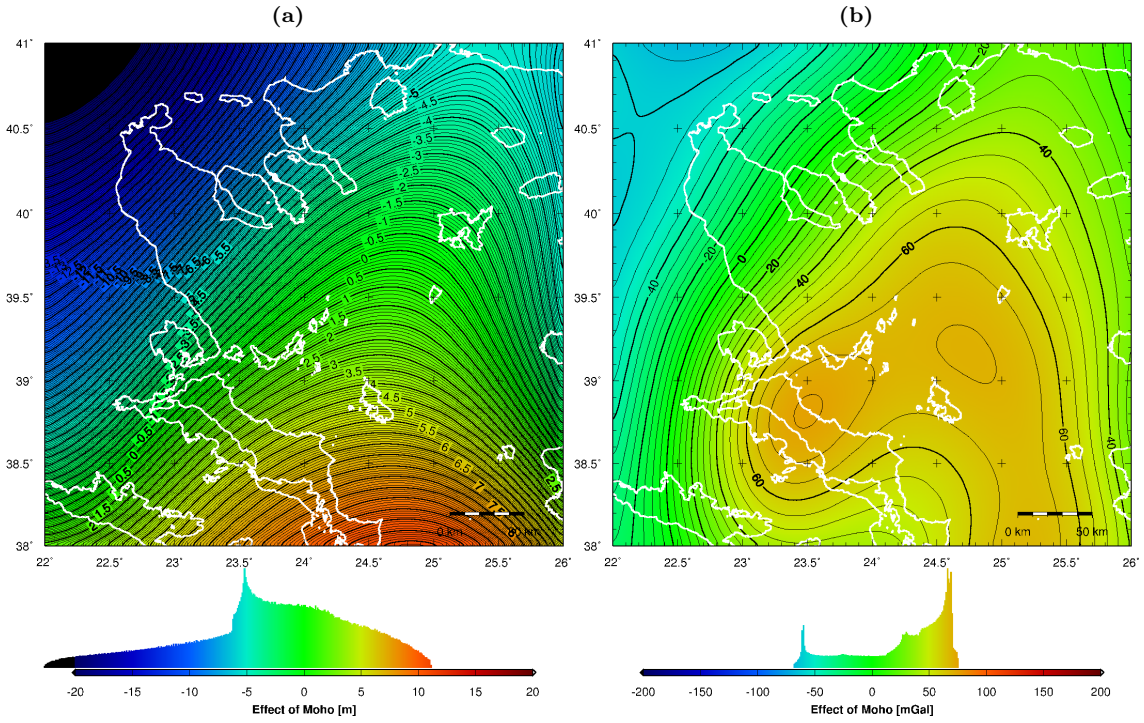

Figure 11.11: Effect of mass anomalies caused by Moho depths from ESC map (Fig. 11.7c) on **(a)** geoid heights (contour interval: 0.1 m) and **(b)** gravity (contour interval: 5 mGal).

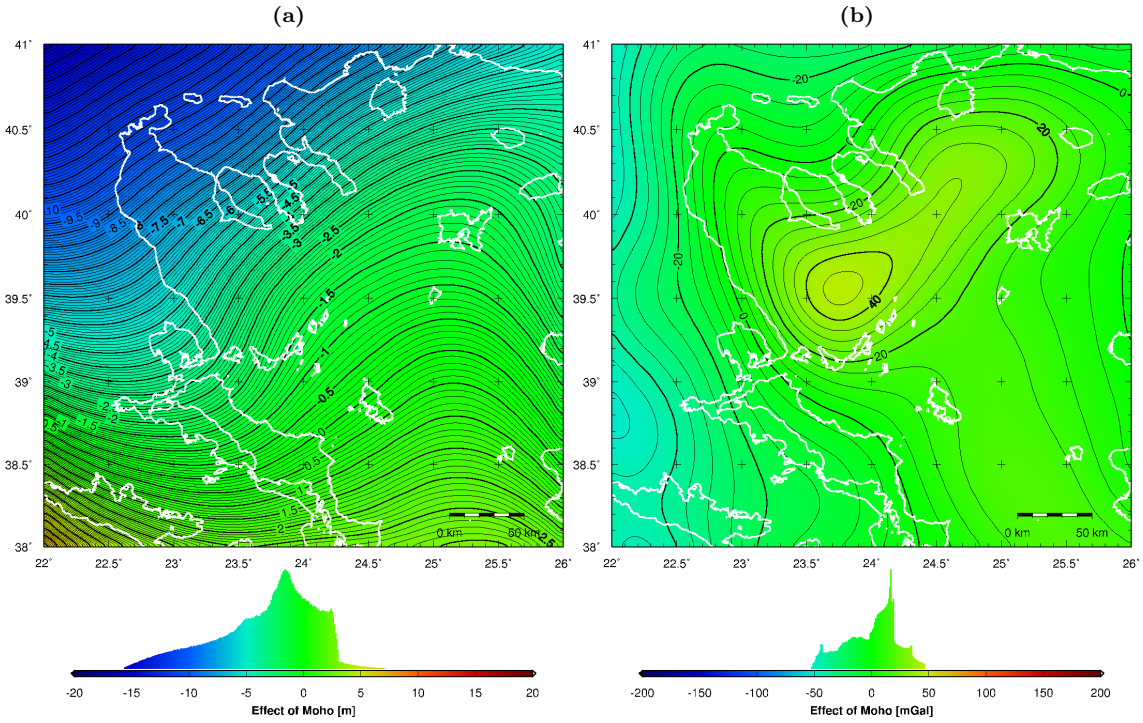

Figure 11.12: Effect of mass anomalies caused by Moho depths from isostatic compensation (Fig. 11.7d) on **(a)** geoid heights (contour interval: 0.1 m) and **(b)** gravity (contour interval: 5 mGal).

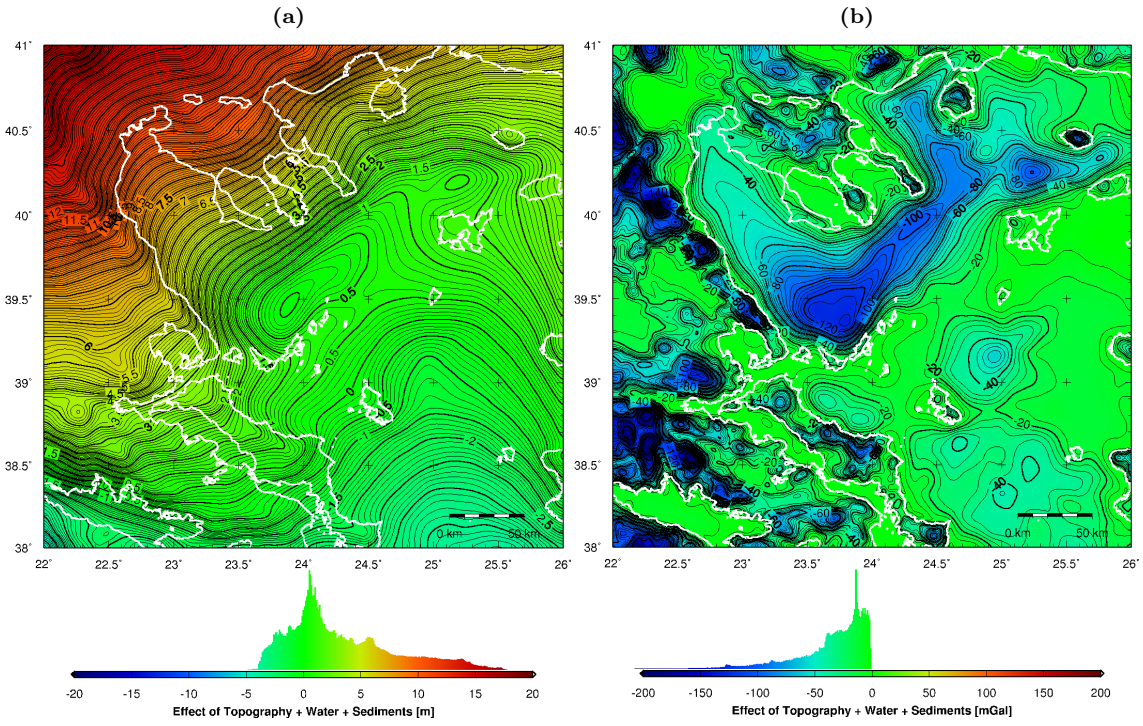

Figure 11.13: Sum of effects of topography, bathymetry (Fig. 11.8) and sediments (Fig. 11.10) on **(a)** geoid heights (contour interval: 0.1 m) and **(b)** gravity (contour interval: 5 mGal).

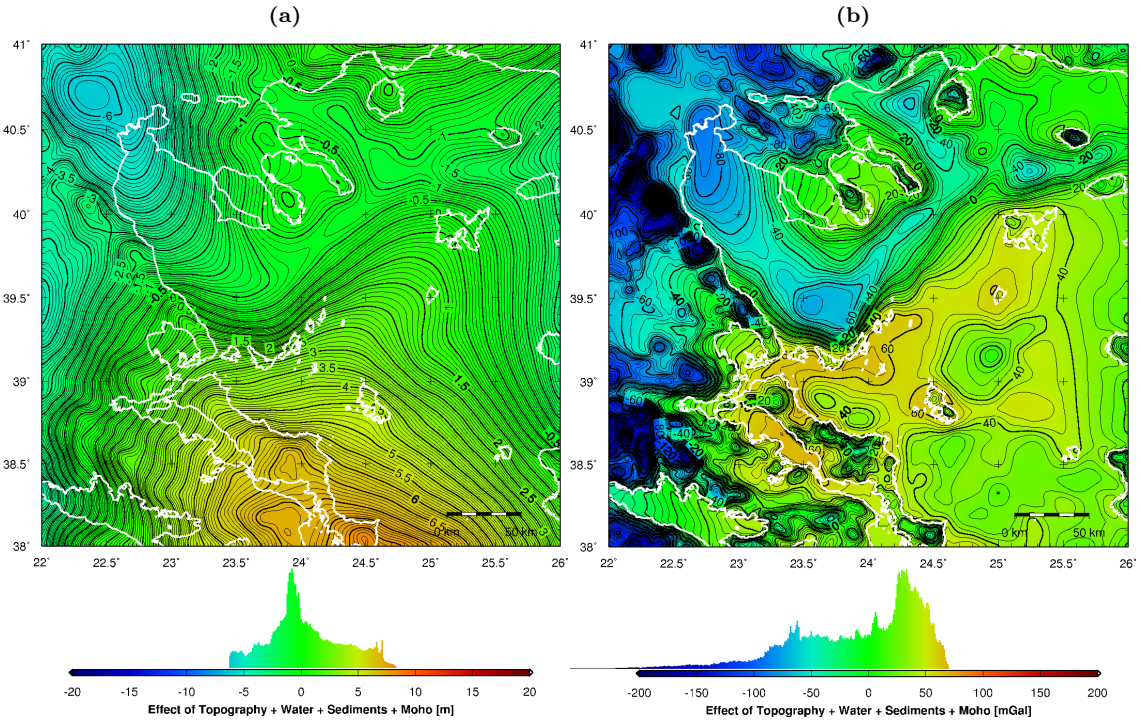

Figure 11.14: Sum of effects of topography, bathymetry, sediments (Fig. 11.13) and ESC Moho depths (Fig. 11.11) on **(a)** geoid heights (contour interval: 0.1 m) and **(b)** gravity (contour interval: 5 mGal).

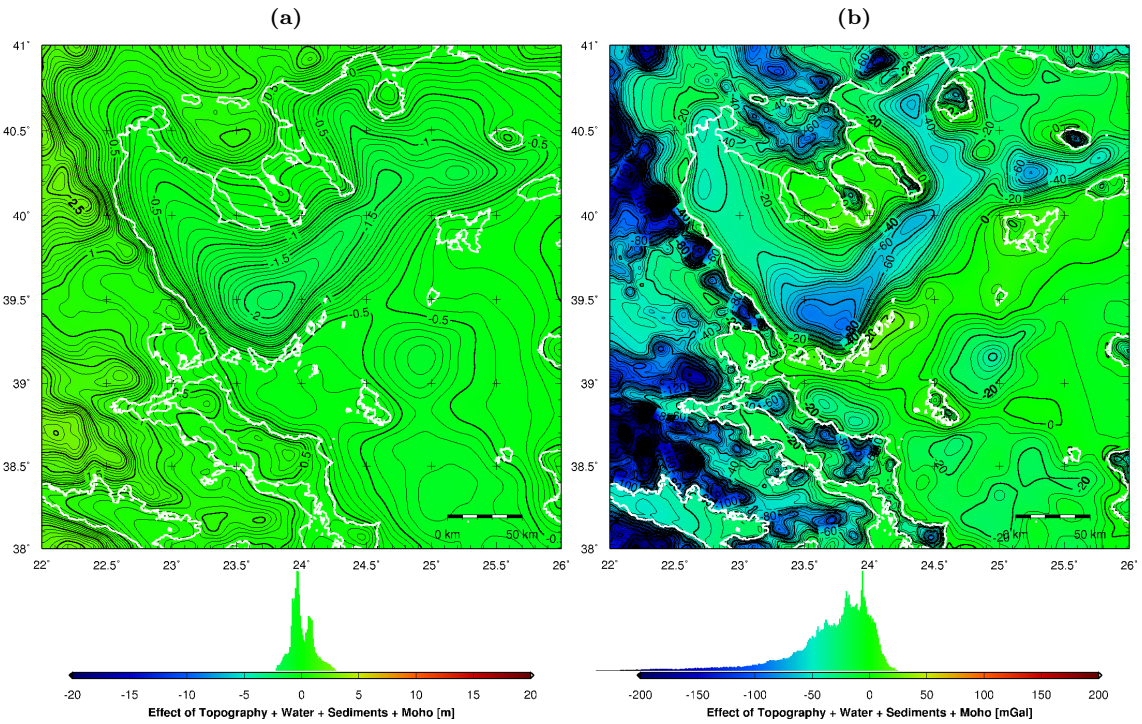

Figure 11.15: Sum of effects of topography, bathymetry, sediments (Fig. 11.13) and isostatic Moho depths (Fig. 11.12) on **(a)** geoid heights (contour interval: 0.1 m) and **(b)** gravity (contour interval: 5 mGal).

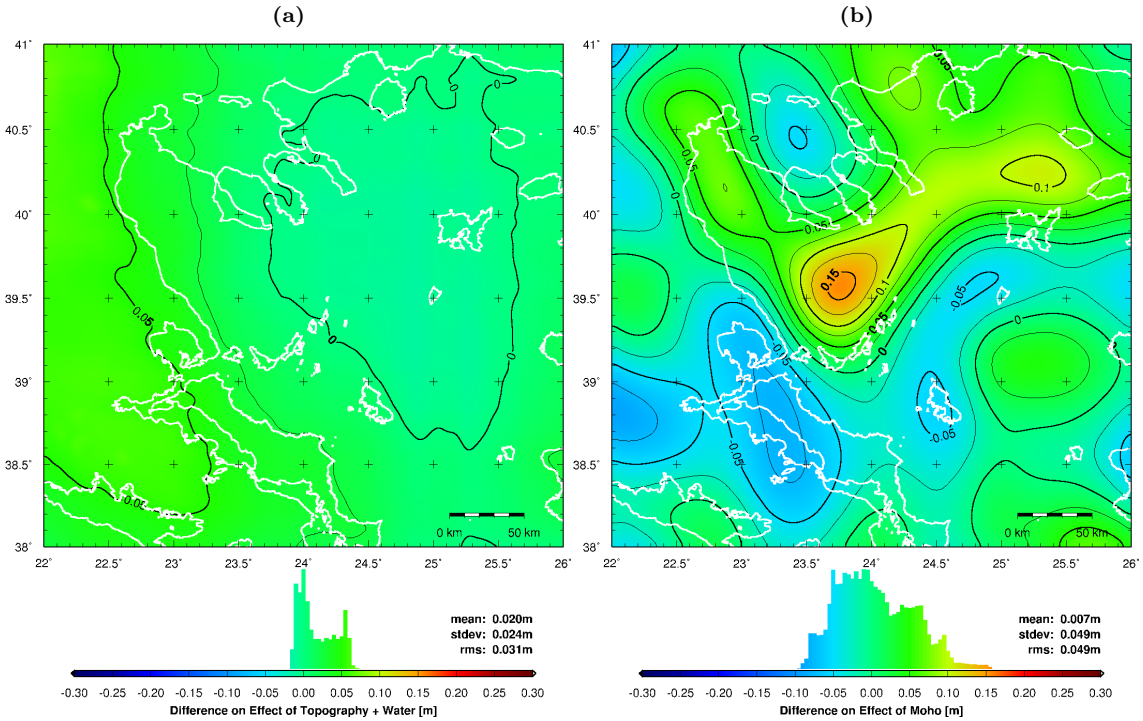

Figure 11.16: Differences on geoid heights between mass effects computed by cuboid masses and point masses from **(a)** topography/bathymetry and **(b)** Moho depths. Contour intervals: 0.025 m.

Table 11.2: Differences (mean offset, standard deviation (STD) and RMS) on geoid heights between mass effects computed by cuboid masses and point masses.

Effect	mean [cm]	STD [cm]	RMS [cm]
Topo/Bathy	2.0	2.4	3.1
Sediments	0.1	0.1	0.1
Moho	0.7	4.9	4.9
Topo/Bathy, Sediments, Moho	2.6	4.2	4.9

mountains, deep sea, large sediment layers and large Moho depth variations.

Small differences between the two methods are obtained for the sediments effects, while larger differences are obtained for the effect of topography and bathymetry and the effect of the Moho (Tab. 11.2). The differences of the effect of topography and bathymetry on the geoid are below 7 cm (Fig. 11.16a). The differences of Moho effects on the geoid reach 15 cm (Fig. 11.12a) and have a larger variation than the differences on the topography and bathymetry effect. The larger differences on the Moho effect are caused by the elongated shape of the Moho cuboids that can reach heights of more than 10 km. The differences on the final solution combining topography, bathymetry, sediments and Moho depths range between -5 cm and 15 cm, with an RMS of 4.9 cm. Hence, if an accuracy better than 5 - 10 cm is sought, the application of the cuboid model is mandatory. In the present case, regarding the sizes of the residual geoid heights after the reduction of mass effects (Section 11.5, Fig. 11.17a to Fig. 11.20a), the approximation of the point mass model has no significant effect on the size and spatial structure of the residuals. Uncertainties of the topography, sediments and Moho, as well as of the exact mass distribution inside the different layers, induce larger errors than the point mass approximation. The same conclusions were drawn from a similar investigation in the survey area of western Crete (Section 10.4.7).

11.5 Mass Reduction of Local Altimetric Geoid

11.5.1 Introduction

The mass effects computed in Section 11.4 were used to reduce the marine geoid heights obtained by shipborne altimetry (Fig. 11.1a). While geoid undulations are mainly affected by large-scale mass anomalies, gravity anomalies are better suited to describe the short-wavelength part of the gravity field, affected by local mass anomalies. Hence, marine gravity anomalies derived from shipborne altimetry (Fig. 11.1b) were also mass-reduced in order to obtain additional information on the local gravity field, although the major investigations were carried out on geoid heights. With the mass reduction, the mass effects are removed from the geoid heights or gravity anomalies. The residual geoid heights or gravity anomalies represent the effects caused by unmodeled masses. Hence, the mass reduction allows to detect anomalous mass distributions.

11.5.2 Topography-Bathymetry Cogeoid

In a first step, marine geoid heights from shipborne altimetry (Fig. 11.1a) were reduced for the mass effects of topography and bathymetry (including water masses) (Fig. 11.8a). The mass-reduced geoid heights (Fig. 11.17a) correspond to the topography-bathymetry cogeoid. Associated mass-reduced gravity anomalies are shown in Fig. 11.17b. After the removal of a mean offset, the mass-reduced geoid heights range between -3.9 m and 3.2 m, with pronounced gradients in north-west direction.

11.5.3 Topography-Bathymetry-Sediments Cogeoid

In a second step, marine geoid heights from shipborne altimetry (Fig. 11.1a) were reduced for the mass effects of topography, bathymetry and sediments (Fig. 11.13a). The mass-reduced geoid heights (Fig. 11.18a) correspond to the topography-bathymetry-sediments cogeoid. Associated mass-reduced gravity anomalies are shown in Fig. 11.18b. After the removal of a mean offset, the mass-reduced geoid heights range between -3.0 m and 2.1 m. Pronounced gradients in north-west direction remain after the reduction. The strong geoid gradients north of the island of Alonnisos, as well as the predominant geoid depression at the western end of the North Aegean Trough, are mainly removed by the reduction, indicating that these local features are mainly produced by the mass effects of the topography, bathymetry and sediments. Assuming the ideal case where the mass effects of topography, bathymetry and sediments were perfectly modeled and entirely removed by the reduction, and where no other mass anomalies except those produced by the Moho are present, the mass-reduced geoid heights (Fig. 11.18a) and gravity anomalies (Fig. 11.18b) would correspond to the mass effects produced by the real Moho. Under these assumptions, the pronounced local maximum of 1.3 m of the mass-reduced geoid in the North Aegean Trough region predicts a mass excess associated with a Moho uplift in this area. Another indication for a significant regional uplift of the Moho is given by the mass-reduced gravity anomalies, showing positive values between 60 mGal and 100 mGal across the entire area of the North Aegean Trough covered by the shipborne surveys (Fig. 11.18b). The predicted Moho uplift in the North Aegean Trough area is in accordance with the uplift of the modeled isostatic Moho (Fig. 11.7d).

11.5.4 Topography-Bathymetry-Sediments-Moho Cogeoid

In a third step, marine geoid heights from shipborne laser altimetry (Fig. 11.1a) were reduced for the mass effects of topography, bathymetry, sediments and ESC Moho (Fig. 11.14a). The mass-reduced geoid heights (Fig. 11.19a) correspond to the topography-bathymetry-sediments-Moho co-

geoid. Associated mass-reduced gravity anomalies are shown in Fig. 11.19b. After the removal of a mean offset, the mass-reduced geoid heights range between -4.0 m and 2.5 m, with pronounced gradients in north direction across the entire survey area. These gradients prevent a stringent interpretation of the topography-bathymetry-sediments-Moho cogeoid.

11.5.5 Topography-Bathymetry-Sediments-Isostasy Cogeoid

In a final step, marine geoid heights from shipborne altimetry (Fig. 11.1a) were reduced for the mass effects of topography, bathymetry, sediments and isostatic Moho (Fig. 11.15a). The mass-reduced geoid heights (Fig. 11.20a) correspond to the topography-bathymetry-sediments-isostasy cogeoid. Associated mass-reduced gravity anomalies are shown in Fig. 11.20b. After the removal of a mean offset, the mass-reduced geoid heights range between -1.5 m in the South-West to a local maximum of 1.0 m at the North Aegean Trough in the north-eastern part of the survey area. The pronounced gradients in north-west direction, observed in the topography-bathymetry-sediments cogeoid (Fig. 11.18a) have disappeared, indicating that they can be explained by the mass effects of the isostatic Moho. Weaker gradients in south-west direction appear instead. The origin of these gradients can be the large mass deficiencies in the Ionian Sea, associated with the Mediterranean Ridge, which are only partly considered within the area of influence in the computation of mass effects. A second hypothetic origin would be an anomalous Moho discontinuity with respect to the Moho modeled by isostatic compensation, characterized by a relative higher Moho at the local cogeoid maximum and an inclination in south-west direction.

The predominant geoid depression of 1.5 m at the south-western end of the North Aegean Trough (Fig. 11.1a) was eliminated by the reduction (Fig. 11.20a). Hence, this depression is not an anomaly, since it can be explained by the effects of the masses considered in the reduction. The geoid anomaly in the survey area is in fact the discontinuity of the depression towards the North-East along the North Aegean Trough (Fig. 11.1a), leading to the local maximum of 1.0 m of the mass-reduced geoid heights (Fig. 11.20a). This maximum is associated with mass-reduced gravity anomalies between 40 mGal and 60 mGal (Fig. 11.20b). The anomaly is caused by a local mass excess not considered in the modeled mass effects. The mass-reduced geoid heights and gravity anomalies do not allow to draw a conclusion whether the anomaly is caused by an anomalously dense crust, an overestimated sediment effect or an anomalous local Moho uplift. The gravity anomalies in the order of 40 mGal would correspond to an hypothetical local upwelling of the Moho by 4 km with respect to the isostatic Moho, yielding a theoretical Moho depth of 22 km. The local geoid anomaly lies on the northern fault bounding the North Aegean Trough. The area of the anomaly is identified as a major strike-slip boundary, characterized by high seismicity, separating the Anatolia-Aegean plate from Eurasia (McNeill et al., 2004). It is accompanied with dextral shear strain rates, combined with normal extension and isolated normal compression (Fig. 1.6) (Hollenstein, 2006). Furthermore, it is correlated with the epicenters of two recent strike-slip earthquakes of magnitude 6.9 and 5.4, in 1982 and 1992, respectively (McNeill et al., 2004). These considerations may be an indication that the observed geoid and gravity anomalies are caused by an anomalous upwelling of dense material linked to the geodynamic system of the North Aegean Trough.

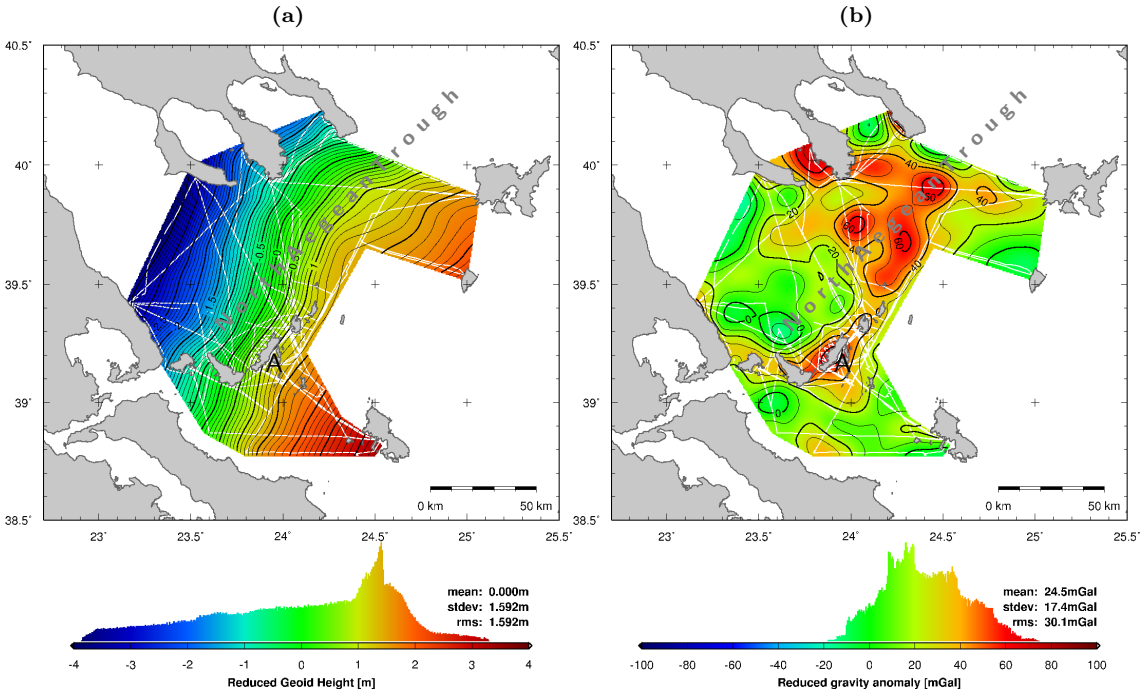

Figure 11.17: **(a)** Geoid heights from shipborne altimetry (Fig. 11.1a) reduced for mass effects of topography and bathymetry (Fig. 11.8a), with mean offset removed. **(b)** Associated gravity anomalies from reduction of Fig. 11.1b with Fig. 11.8b. Contour intervals: 0.1 m and 10 mGal. (A = Alonnisos).

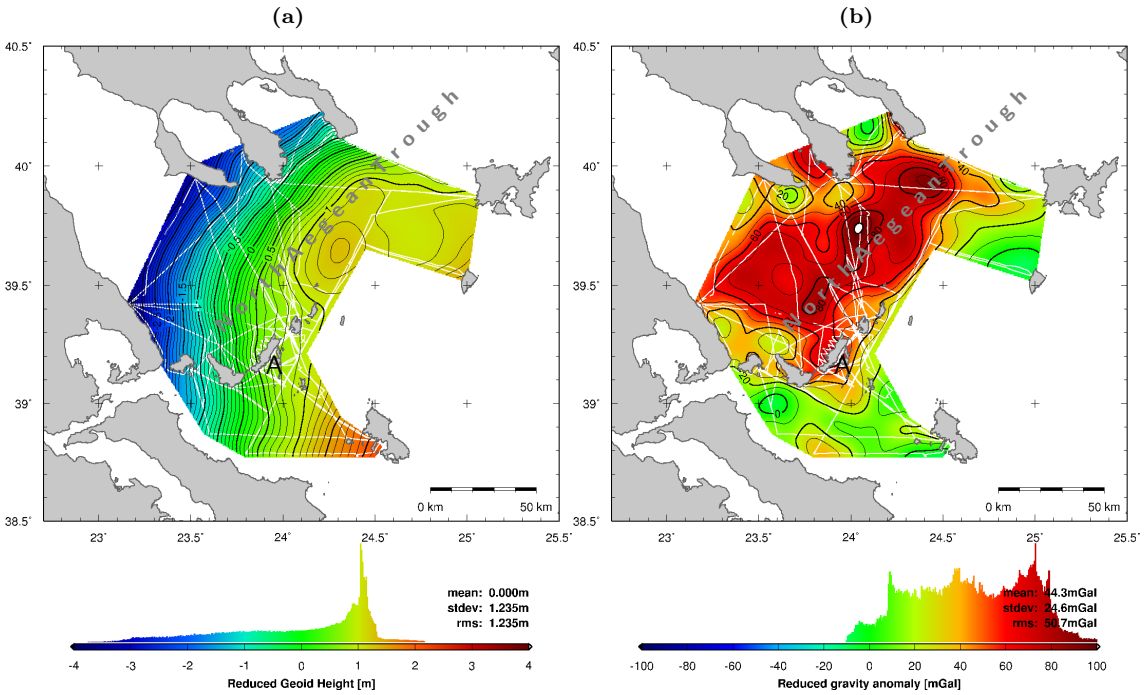

Figure 11.18: **(a)** Geoid heights from shipborne altimetry (Fig. 11.1a) reduced for mass effects of topography, bathymetry and sediments (Fig. 11.13a), with mean offset removed. **(b)** Associated gravity anomalies from reduction of Fig. 11.1b with Fig. 11.13b. Contour intervals: 0.1 m and 10 mGal. (A = Alonnisos).

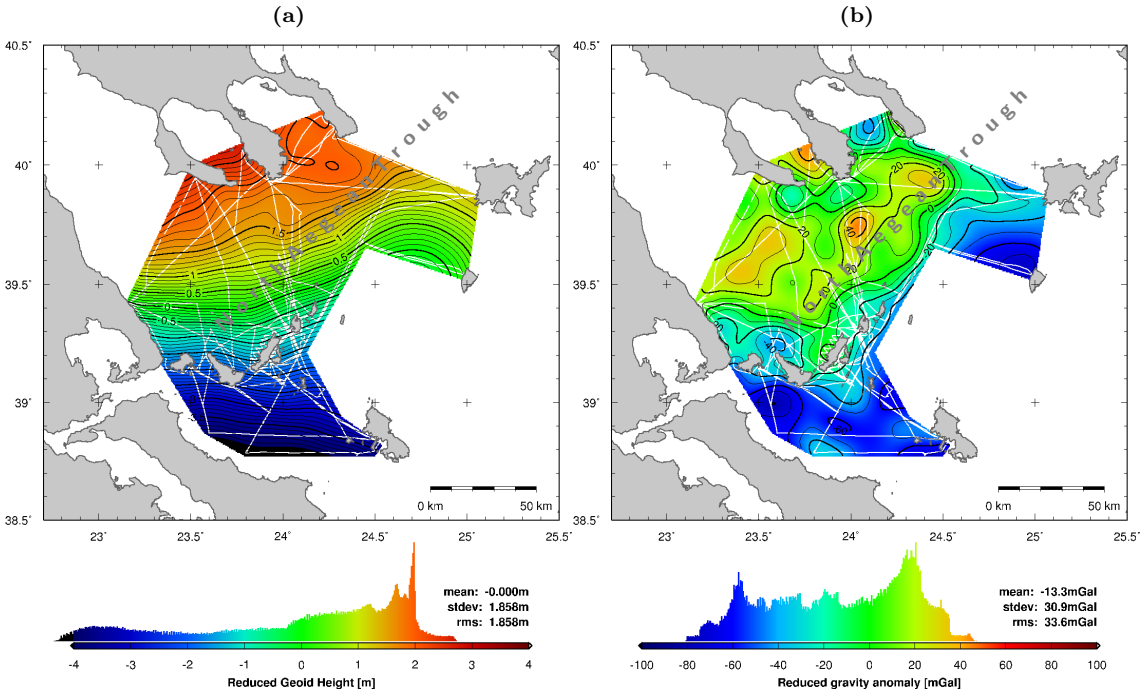

Figure 11.19: **(a)** Geoid heights from shipborne altimetry (Fig. 11.1a) reduced for mass effects of topography, bathymetry, sediments and ESC Moho (Fig. 11.14a), with mean offset removed. **(b)** Associated gravity anomalies from reduction of Fig. 11.1b with Fig. 11.14b. Contour intervals: 0.1 m and 10 mGal.

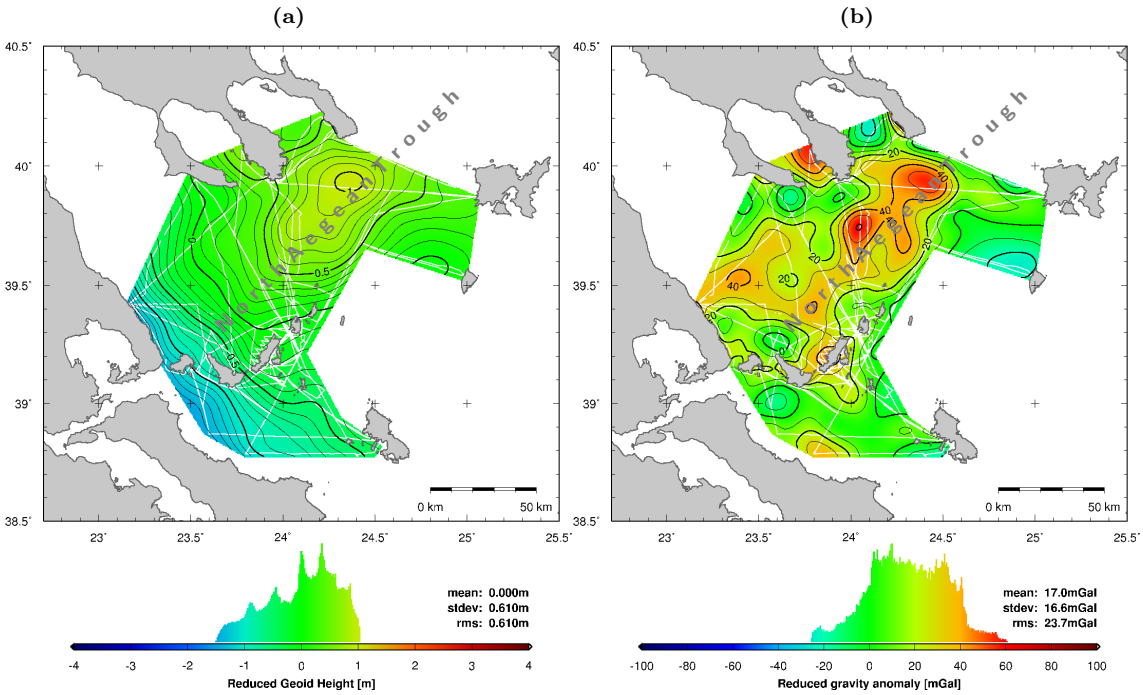

Figure 11.20: **(a)** Geoid heights from shipborne altimetry (Fig. 11.1a) reduced for mass effects of topography, bathymetry, sediments and isostatic Moho (Fig. 11.15a), with mean offset removed. **(b)** Associated gravity anomalies from reduction of Fig. 11.1b with Fig. 11.15b. Contour intervals: 0.1 m and 10 mGal.

12 Summary and Conclusions

The method of airborne laser altimetry was successfully developed and deployed for high-resolution sea surface height determination in the area of western Crete. Since airborne laser altimetry is very cost-intensive, a major aim of this project was the development of an alternative method for local-scale sea surface topography determination. A novel method of shipborne sea surface height observations was developed in the framework of this project. The method relies on one or more low-cost industrial ultrasonic distance sensors mounted on a boat, providing continuous information on the distance to the sea surface, in combination with a multi-antenna GPS system and a low-cost inertial measurement unit for position and attitude determination. Due to its analogy to airborne laser altimetry, the method is called shipborne ultrasound altimetry. The successful implementation of the new technique during several survey campaigns proved that shipborne ultrasound altimetry is a powerful method for providing offshore sea surface height observations, even under rough sea conditions. Hence, the method provides a low-cost alternative to airborne laser altimetry. In this work, the scientific potential of airborne laser altimetry and shipborne ultrasound altimetry for accurate sea surface height determination in local areas was demonstrated. The results are more than satisfying in terms of accuracy and repeatability, leading to high-resolution local sea surface topography solutions at sub-decimeter level, with some limitations stated below. In order to achieve best possible accuracies, a wide range of processing algorithms and corrections needs to be applied. On the instrumental level, they include precise kinematic GPS positioning, precise attitude retrieval and boresight misalignment calibration. On the sea surface level, they include correcctions for ocean waves, tides, atmospheric pressure forcing and wind forcing.

Differential kinematic GPS positions of the survey aircraft and boat were obtained at a vertical accuracy of better than 5 cm, even for baseline lengths of more than 100 km. However, it was seen in the airborne surveys that the vertical accuracy can be considerably degraded up to a level of 30 cm in case of extremely inhomogeneous atmospheric conditions. In this case, the inaccuracy of the corrections of GPS observations for tropospheric refraction and their impact on the vertical component of the GPS positions were found to be the limiting factor for the accuracy of the final sea surface topography by airborne and shipborne altimetry. Based on these conclusions, investigations were made to assess the kinematic potential of Bernese GPS Software Version 5 and its capability to estimate tropospheric path delays in kinematic mode. The source code of the Bernese software had to be adapted to the estimation of path delays in kinematic mode. Results similar to the classic solution with path delays predicted from an a priori model were obtained under homogeneous atmospheric conditions. Under extreme tropospheric conditions, differences between the two solutions could easily reach 0.5 m. The analysis showed that under such conditions, the Bernese solution including the estimation of tropospheric path delays was extremely sensitive to tropospheric parameter settings. The instability of the solution led to the conclusion that the algorithm used to model the troposphere is not sophisticated enough to provide a realistic representation of extremely inhomogeneous atmospheric conditions in kinematic mode. In order to improve the accuracy of kinematic GPS positioning, and hence of deduced sea surface heights, further research on modeling tropospheric influences in kinematic mode is needed.

Attitude determination using a multi-antenna GPS array produced reliable data for both the survey aircraft and sailing yacht. The good performance of the multi-antenna GPS attitude determination was demonstrated by comparing the solutions with the data of a high-precision INS platform, operated simultaneously aboard the aircraft. The comparisons showed a good correlation between the attitude data provided by the two systems, with standard deviations of the observed differences

in the order of 0.11° on the roll and pitch, and 0.06° on the yaw. The accuracy of the attitude derived from the multi-antenna GPS array was estimated to be in the order of 0.1°, given the specific antenna configurations. This value was found to meet the accuracy requirement established for sea surface height determination with airborne or shipborne altimetry. The achieved accuracy would further enable the use of the multi-antenna GPS method for attitude determination in a wide range of applications where high sampling rates are not required and where good GPS satellite visibility is warranted.

The boresight misalignment calibration method for airborne laser altimetry developed in this project is a truly self-calibrating technique, in the sense that it exclusively relies on the sea surface height observations themselves. There is no need for overflying special calibration surfaces. Additionally, the method relies directly on subsequent observations within the same flight line, with no need for overflying the same area more than once. Furthermore, the calibration algorithm is completely independent of any a priori information about the relief of the measured water surface, like e.g. geoid heights. The calibration method allowed to estimate boresight misalignment angles with an accuracy better than 0.1°, corresponding to the expected order of magnitude of boresight misalignment variations during flight operations, as well as to the estimated attitude accuracy. The boresight misalignment calibration allowed to mitigate systematic ground point height errors of up to 10 cm, due to a systematic aerodynamic pitch of the aircraft. Due to the small ranges of less than 3 m in shipborne ultrasound altimetry, and the large size of the ultrasound footprint, there was no need for boresight misalignment calibration in shipborne ultrasound altimetry.

Various ocean tide models, including FES2004 and POL (Proudman Oceanographic Laboratory) (Tsimplis et al., 1995), as well as local tide-gauge data, were analyzed for the correction of ocean tides. A significant contradiction among the models was observed in the survey areas around western Crete and in the North Aegean Sea. Around Crete, differences of up to 3 cm were observed between the models, as well as with respect to local tide-gauge data. The disagreement is significant, since tidal amplitudes in the area are only in the order of 2.5 cm. However, considering the small size of the encountered tidal amplitudes and of the differences between the models, the choice of the tide model is not crucial for the accuracy of the corrected sea surface heights. In the North Aegean Sea, tidal amplitudes are in the order of 15 - 20 cm, making the choice of the tidal model important. Significant differences of up to 20 cm were observed between the predictions of the global FES2004 model and the POL model. A validation with local tide-gauge data revealed large differences of up to 25 cm with respect to FES2004, while the differences with respect to the POL model were below 8 cm. Furthermore, the POL model showed a better agreement with the shipborne data. It allowed to significantly reduce the RMS of the sea surface height differences at crosspoints by 4.8 cm, and the maximum absolute difference by 8.0 cm. Applying tidal corrections directly from tide-gauge data produced a slightly worse agreement with the shipborne data, due to the fact that tide-gauge data is affected by local coastal effects. The remaining residuals of the tide-gauge observations with respect to the POL model are most likely due to local coastal effects, not resolved by the tidal model. It can be assumed that the model performs better offshore, in the absence of strong and hardly predictable coastal effects.

Corrections of sea surface heights for atmospheric pressure and wind forcing were applied using MOG2D dynamic atmospheric corrections. Corrections between -16 cm and 12 cm were obtained for the considered times and locations. In the case of the shipborne data, the MOG2D corrections allowed to reduce the RMS of height differences at crosspoints by 2.0 cm and the maximum absolute difference by 7.7 cm. Furthermore, they produced a significant improvement of the corrected sea surface heights, as compared to a classical inverse barometer correction. Sea level anomalies obtained from satellite radar altimetry were applied as additional correction to the airborne and shipborne observations. The beneficial effect of this correction, especially for the shipborne data collected over five years, was also demonstrated by the crosspoints analysis: the RMS of the sea surface height differences was reduced by 3.8 cm and the maximum absolute difference by 8.6 cm. This reveals the good compatibility of the airborne and shipborne observations with satellite radar altimetry data.

The accuracy and repeatability of the airborne and shipborne altimetry methods were estimated by analyzing sea surface height differences at crosspoints using the best-available combination of sea surface height corrections. The height differences at 100 crosspoints of the airborne campaign showed an RMS of 8.7 cm, while the five shipborne campaigns yielded a total of 1999 crosspoints with an RMS of 7.9 cm. After an LSQ adjustment of the height profiles based on the differences at crosspoints, the RMS values were further reduced to 4.5 cm and 5.5 cm, respectively. A standard deviation of only 3.1 cm was obtained for the residuals between the sea surface height profiles from airborne laser altimetry and the derived gridded and filtered sea surface topography. After an outlier removal based on the residuals, this standard deviation was reduced to 2.9 cm. The same procedure was applied to the shipborne data, yielding a standard deviation of 5.2 cm before and 3.6 cm after the outlier removal. The low RMS and standard deviation obtained for the height differences at crosspoints and the residuals underline the good accuracy and repeatability of the two methods. Furthermore, the agreement of better than 1 cm of these RMS and standard deviations between the airborne and shipborne altimetry methods shows that the performance of both methods is comparable in terms of accuracy and repeatability. It has to be noted that the instrumental accuracy of both methods is better than the RMS and standard deviations stated above, since these values include not only instrumental errors, but also errors of the geophysical sea surface height corrections. In order to further asses the accuracy of the methods, calibration measurements were performed with GPS buoys. The calibration of the airborne laser altimetry system, performed in calm nearshore conditions, as well as in harsh offshore conditions, provided excellent results, with sea surface heights fitting better than 5 cm.

Comparisons between airborne laser altimetry and nearly-simultaneous Jason-1 radar altimeter data along a dedicated profile of more than 100 km revealed variations of the height difference in the order of 10 cm. Additional comparisons were made between significant wave heights derived from airborne laser altimetry and from Jason-1 GDR data along the dedicated profile. A good agreement of better than 20 cm was obtained using Jason-1 Ku-band data.

In order to validate sea surface height products from satellite radar altimetry missions, the local sea surface topographies obtained by airborne and shipborne altimetry were compared to the CLS01 and DNSC08 mean sea surfaces (MSS) derived from multi-mission radar altimetry. Theoretically, the CLS01 and DNSC08 resolve wavelengths down to 10 - 20 km. The residuals between the sea surface topography from airborne laser altimetry around Crete and both CLS01 and DNSC08 show a good agreement with standard deviations in the order of 8 cm. However, local residuals of up to 50 cm are observed in a belt of 20 km around the coast of Crete, where strong geoid gradients of up to 0.22 m/km occur. In these coastal areas, CLS01 and DNSC08 sea surface heights suffer from a lack of satellite radar altimetry data. Since the coastline was not systematically covered by airborne laser altimetry, uncertainties also remain in the airborne sea surface topography regarding these areas. The residuals between the sea surface topography from shipborne altimetry and both CLS01 and DNSC08 show a good agreement, with standard deviations in the order of 6 cm. Thus, the agreement of both CLS01 and DNSC08 with the shipborne altimetry data in the North Aegean Sea is slightly better than with the airborne altimetry data around Crete. However, this is not a consequence of a better accuracy of the shipborne altimetry data, but rather related to the extreme sea surface height gradients encountered around Crete. Besides the validation of the MSS products, the good agreement with the MSS from CLS01 and DNSC08 allows to assess the good accuracy and resolution of the sea surface topographies determined by airborne and shipborne altimetry.

Two local high-resolution marine geoid solutions were derived from the sea surface heights obtained by airborne and shipborne altimetry, by subtraction of the RioMed mean dynamic ocean topography. In addition, geoid gradients, deflections of the vertical and gravity anomalies were derived from the altimetric geoid heights. The high accuracy of the two local altimetric geoid solutions was demonstrated by comparison with solution from the global gravity models EGM96, EGM2008, EIGEN-5S and EIGEN-5C. The spatial resolution of the local altimetric geoid solutions was found to be significantly higher than the resolution of existing geoid models with a spherical harmonics expansion limited to degree and order 360 (EGM96 and EIGEN-5C). The resolution of

these models corresponds to 55 km. Residuals between the local altimetric geoids and these models have standard deviations of 0.37 m to 0.40 m and maximum values of 1.5 m. It was shown that the resolution of these models is mainly limited by their mathematical expansion of spherical harmonics. Comparisons with the EIGEN-5S model, limited to degree and order 150, yielded even higher residuals, with standard deviations of up to 0.81 m and maximum values over 1.5 m. Comparisons between the two local altimetric geoids and the recently released EGM2008 revealed low residuals, with standard deviations of 0.08 m and 0.11 m. Additional comparisons with the local gravimetric geoid model AUTH2008 (Tziavos and Andritsanos, 1999; Vergos et al., 2004; Grigoriadis, 2009) produced similar standard deviations of 0.15 m and 0.10 m. Hence, all four geoid solutions have similar spatial resolutions. The EGM2008 is expanded to degree 2190 and order 2159, corresponding to a spatial resolution of 10 km. The original sea surface height observations from airborne and shipborne altimetry have an along-track resolution below 10 cm and 50 cm, respectively. However, the short-wavelength information contained in these observations is degraded by instrumental system noise and errors in geophysical sea surface height corrections (tides, inverse barometer) of at least the same order of magnitude as the geoid signal at these wavelengths. Hence, the short-wavelength geoid signal cannot be separated from the noise. In order to eliminate the noise and avoid associated unrealistic short-wavelength variations in the geoid heights, the sea surface height data has to be low-pass filtered with cut-off wavelengths around 10 km, similar to the resolution of EGM2008. In order to obtain reliable information on shorter-wavelength geoid signals by airborne or shipborne altimetry, both system noise and geophysical corrections need to be improved.

From an oceanographic perspective, the primary purpose of sea surface height observations is the determination of the dynamic ocean topography induced by ocean currents. Attempts were carried out to determine the mean dynamic topography (MDT) by subtracting geoid heights from the sea surface height obtained by airborne and shipborne altimetry (direct method). Among the geoid models used in this study, the satellite-only solution EIGEN-5S and the local gravimetric geoid model AUTH2008 are the only geoid solutions that are independent of altimetric sea surface height data. Hence, they would be the only appropriate models for MDT determination using the direct method. Due to the large residuals caused by its low spatial resolution of 130 km, satellite-only models like the EIGEN-5S are unusable for realistic MDT determination at wavelengths below 130 km. In closed seas with complex basin structures, like the Mediterranean, as well as in coastal areas, the resolution of scales shorter than 130 km is crucial for the determination of complex local-scale circulation. It is expected that shorter scales of the Earth's marine gravity field, independent of sea surface heights, will be provided by the GOCE mission scheduled for 2009. GOCE aims to provide geoid heights with cm accuracy at a resolution better than 100 km, constituting a major improvement of dynamic ocean topography determination and circulation studies. Hypothetic local MDT were nevertheless computed from the residual fields of the sea surface heights from airborne and shipborne altimetry with respect to EGM2008 and AUTH2008 geoid heights. The geostrophic circulation fields derived from the hypothetic MDT are unrealistic and spoiled by noisy eddies. Hence, it was not possible to derive a realistic circulation pattern based on the sea surface height observations and the used geoid models. The major reason lies in the fact that the presumed MDT only varies within a range below 10 cm in both survey areas. Furthermore, the gradients of the MDT associated with the circulation are below 1 cm/10 km. Hence, the MDT signal in these areas is in the same order of magnitude as the accuracy of the airborne and shipborne sea surface heights and the used geoid models. It can be concluded that the sea surface height observations by airborne and shipborne altimetry and the considered geoid models are not accurate enough to resolve such small dynamic effects. In addition, EGM2008 is not independent of altimetric sea surface height data.

In order to allow for a geophysical analysis and interpretation of the airborne and shipborne altimetric geoid solutions in the Aegean sea, various mass effects on geoid heights were modeled for the considered survey areas. Masses from topography, bathymetry, marine sedimentary deposits and crust-mantle boundary (Moho) depths were considered. It was shown that major parts of the geoid can be explained by the mass effects mentioned above. On the other hand, the residual geoid

also revealed distinct anomalies which can be related to up to now unrecognized mass distributions.

The region south of Crete is dominated by deep sea water reaching depths of 4000 m and sediment deposits with thicknesses of up to 10 km. The predominant geoid gradients, reaching 0.22 m/km and characterizing the geoid of the entire region, were completely reduced by the modeled mass effects. On the other hand, a strong gradient of the mass-reduced residual geoid appears north of Crete. It can, therefore, be concluded that the major geoid anomaly in the area is the relative geoid high north of Crete, rather than the depression south of Crete along the Hellenic Trench. The geoid anomaly north of Crete indicates a significant positive mass distribution beyond the northern border of the survey area, possibly linked to the Hellenic subduction zone. Density models based on seismic soundings are indicating an upwelling of the European mantle north of Crete, related to the subduction of the African oceanic lithosphere beneath the Eurasian continental lithosphere (Snopek et al., 2007; Makris and Yegorova, 2006; Casten and Snopek, 2006) and causing a significant positive mass anomaly.

In the North Aegean Sea, it was shown that the predominant geoid low of 1.5 m at the western end of the North Aegean Trough can be explained to a large extent by topographic, bathymetric, and known geologic effects, such as sediments and crust-mantle boundary. It is striking, however, that a widely-spread maximum of the residual geoid, reaching 1 m, is encountered north-east of the geoid low. This anomaly indicates the presence of a local mass excess. The mass-reduced geoid heights do not allow to draw a conclusion whether the anomaly is caused by an anomalously dense crust, an overestimated sediment effect or an anomalously high Moho. However, the geoid anomaly lies on the northern fault bounding the North Aegean Trough. The area is considered as a major strike-slip boundary, characterized by high seismicity, separating the Anatolia-Aegean plate from Eurasia (McNeill et al., 2004). It is accompanied with dextral shear strain rates, combined with normal extension and isolated normal compression (Hollenstein, 2006). It can, therefore, be assumed that the observed anomaly in the residual geoid is caused by an anomalous upwelling of dense material linked to the geodynamic system of the North Aegean Trough.

Preliminary attempts to geophysically interpret the obtained gravity field information based on mass modeling and mass reduction showed promising results and allowed to detect local mass anomalies. A future step in this direction would consist in a detailed and stringent geophysical interpretation of the obtained gravity field results, based on a thorough investigation of existing density models and the application of advanced inversion algorithms. With the inversion of the obtained local geoid, models of mass distribution can be further constrained, helping to better understand the dynamics of the Hellenic subduction zone and the westward continuation of the North-Anatolian Fault Zone.

Bibliography

Andersen, O. B. and Knudsen, P. (2008). The DNSC08 global Mean Sea Surface. Presentation at EGU-2008, Vienna, Austria, April, 2008.

Andersen, O. B., Knudsen, P., Toohey, J., Kenyon, S., and Pavlis, N. (2007). A new mean sea surface DNSC07. Poster at OSTST 2007.

AVISO (1996). *AVISO User Handbook for Merged TOPEX/POSEIDON Products*. AVI-NT-02-101, Edition 3.0.

AVISO (2008). *SSALTO/DUACS User Handbook: (M)SLA and (M)ADT Near-Real Time and Delayed Time Products*. CLS-DOS-NT-06.034, SALP-MU-P-EA-21065-CLS.

Barrell, H. (1951). The dispersion of air between 2500a and 6500a. *JOSA*, 41:295–299.

Barrell, H. and Sears, J. E. (1939). The refraction and dispersion of air for the visible spectrum. *Philosophical Transactions of the Royal Society of London*, A 238:1–64.

Baumann, H. (2003). *Absolute Airborne Gravimetry*. PhD thesis, ETH Zurich.

Becker, M., Zerbini, S., Baker, T., Bürki, B., Galanis, J., Garate, J., Georgiev, I., Kahle, H.-G., Kotzev, V., Lobazov, V., Marson, I., Negusini, M., Richter, B., Veis, G., and Yuzefovich, P. (2002). Assessment of height variations by GPS at Mediterranean and Black Sea coast tide gauges from the SELF projects. *Global and Planetary Change*, 34(1-2):5–35.

Berg, H. (1948). *Allgemeine Meteorologie*. Dümmler's Verlag, Bonn.

Beutler, G., Bock, H., Dach, R., Fridez, P., Gnäde, A., Hugentobler, U., Jäggi, A., Meind, M., Mervart, L., L.Prange, Schaer, S., Springer, T., Urschl, C., and Walser, P. (2007). Bernese GPS Software Version 5.0, edited by R. Dach, U. Hugentobler, P. Fridez and M. Meindl. Astronomical Institute, University of Berne.

Birch, K. P. and Downs, M. J. (1993). An updated Edlén equation for the refractive index of air. *Metrologia*, 30:155–162.

Birch, K. P. and Downs, M. J. (1994). Correction to the updated Edlén equation for the refractive index of air. *Metrologia*, 31:315–316.

Bonnefond, P., Exertier, P., Laurain, O., Ménard, Y., Orsini, A., Jan, G., and Jeansou, E. (2003). Absolute Calibration of Jason-1 and TOPEX/Poseidon Altimeters in Corsica. *Marine Geodesy*, 26(3-4):261–284.

Bufton, J. L., Hoge, F. E., and Swift, R. N. (1983). Airborne measurements of laser backscatter from the ocean surface. *Applied Optics*, 22(17):2603–2618.

Carrère, L. and Lyard, F. (2003). Modeling the barotropic response of the global ocean to atmospheric wind and pressure forcing - comparisons with observations. *Geophys. Res. Let.*, 30(6):1275.

Casten, U. and Snopek, K. (2006). Gravity modelling of the Hellenic subduction zone - a regional study. *Tectonophysics*, 417:183–200.

Chelton, D. B. (1988). WOCE/NASA Altimeter Algorithm Workshop. Technical Report No. 2, U.S. Planning Office for WOCE (World Ocean Circulation Experiment), College Station, TX.

Chelton, D. B., Ries, J. C., Haines, B. J., Fu, L.-L., and Callahan, P. S. (2001). *Satellite Altimetry and Earth Sciences*, chapter Satellite Altimetry, pages 1–131. Academic Press.

Ciddor, P. E. (1996). Refractive index of air: New equations for the visible and near infrared. *Applied Optics*, 35:1566–1573.

Ciddor, P. E. and Hill, R. J. (1999). Refractive index of air. 2. group index. *Applied Optics*, 38:1663–1667.

Cocard, M. (1995). *High Precision GPS Processing in kinematic mode.*, volume 52 of *Geodätisch-geophysikalische Arbeiten in der Schweiz*. Schweizerische Geodätische Kommission (ed.). 139p.

Cocard, M., Geiger, A., Kahle, H.-G., and Veis, G. (2002). Airborne laser altimetry in the Ionian Sea, Greece. *Global and Planetary Change*, 34(1-2):87–96.

Coulson, C. A. and Jeffrey, A. (1977). *Waves*. Longman Mathematical Texts.

Cox, C. and Munk, W. (1954). Measurement of the roughness of the sea surface from photographs of the sun's glitter. *Journal of the Optical Society of America*, 44(11):838–850.

Dobslaw, H. (2007). Modellierung der allgemeinen ozeanischen Dynamik zur Korrektur und Interpretation von Satellitendaten. Technical Report STR07/10, GeoForschungsZentrum Potsdam, Germany.

Dodson, A., Shardlow, P., Hubbard, L., Elgered, G., and Jarlemark, P. (1996). Wet tropospheric effects on precise relative GPS height determination. *Journal of Geodesy*, 70:188–202.

Dorandeu, J. and Le Traon, P. Y. (1999). Effects of Global Mean Atmospheric Pressure Variations on Mean Sea Level Changes from TOPEX/Poseidon. *Journal of Atmospheric and Oceanic Technology, American Meteorological Society*, 16(9):1279–1283.

Edlén, B. (1966). The refractive index of air. *Metrologia*, 2:71–80.

Ekman, M. (1989). Impacts of Geodynamic Phenomena on Systems for Height and Gravity. *Bulletin Geodesique*, 63(3):281–296.

Favey, E. (2001). *Investigation and Improvement of Airborne Laser Scanning Technique for Monitoring Surface Elevation Changes of Glaciers*. PhD thesis, ETH Zurich.

Favey, E. and Schlatter, A. (1998). Geoidbestimmung am Lac Léman. Technical Report 282, Institut of Geodesy and Photogrammetry, ETH Zurich. 130p.

Favey, E., Wehr, A., Geiger, A., and Kahle, H. G. (2002). Some examples of european activities in airborne laser techniques and an application in glaciology. *Journal of Geodynamics*, 34(3-4):347–355.

Fenoglio-Marc, L., Kusche, J., and Becker, M. (2006). Mass variation in the Mediterranean Sea from GRACE and its validation by altimetry, steric and hydrologic fields. *Geophys. Res. Lett.*, 33(L19606).

Foerste, C., Flechtner, F., Schmidt, R., Stubenvoll, R., Rothacher, M., Kusche, J., Neumayer, K.-H., Biancale, R., Lemoine, J.-M., Barthelmes, F., Bruinsma, J., Koenig, R., and Meyer, U. (2008). EIGEN-GL05C - A new global combined high-resolution GRACE-based gravity field model of the GFZ-GRGS cooperation. *General Assembly European Geosciences Union (Vienna, Austria 2008), Geophysical Research Abstracts*, 10(EGU2008-A-06944).

Fu, L.-L. and Chelton, D. B. (2001). *Satellite Altimetry and Earth Sciences*, chapter Large Scale Ocean Circulation, pages 133–169. Academic Press.

Geiger, A. (1987). Einfluss richtungsabhängiger Fehler bei Satellitenmessungen. Technical Report 130, Institute of Geodesy and Photogrammetry, ETHZ, Zürich. 40 p.

Geiger, A., Cocard, M., Peter, Y., and Kahle, H.-G. (1994). Precise DGPS and self calibrating laser altimetry for airborne marine geoid determination and detection of glacial fluctuation. In *Proceedings of 7th International Technical Meeting of The Satellite Division of The Institute of Navigation (ION), Salt Lake City, Utah, September 20-23*, pages 471–476.

Giacomo, P. (1982). Equation for the determination of the density of moist air. *Metrologia*, 18:33–40.

Gordon, H. R. (1977). One parameter characterization of the ocean's inherent optical properties from remote sensing. *Applied Optics*, 16(10):2627.

Goto, T., Miyakura, J., Umeda, K., Kadowaki, S., and Yanagi, K. (2005). A Robust Spline Filter on the basis of L2-norm. *Precision Engineering*, 29(2):157 – 161.

Grad, M., Tiira, T., and Group, E. W. (2009). IThe Moho depth map of the European Plate. *Geophys. J. Int.*, 176:279–292.

Grigoriadis, V. N. (2009). *Geodetic and geophysical approximation of the Earth's gravity field and applications in the Hellenic area*. PhD thesis, Aristotle University of Thessaloniki (AUTH), Department of Geodesy and Surveying, Greece.

Haines, B. J., Dong, D., Born, G. H., and Gill, S. K. (2003). The Harvest Experiment: Monitoring Jason-1 and TOPEX/Poseidon from a California Offshore Platform. *Marine Geodesy*, 26(3-4):239–259.

Hamad, N., Millot, C., and Taupier-Letage, I. (2005). A new hypothesis about the surface circulation in the eastern basin of the Mediterranean Sea. *Progress In Oceanography*, 66(2-4):287 – 298. Mediterranean physical oceanography and biogeochemical cycles: Mediterranean general circulation and climate variability.

Heiskanen, W. A. and Moritz, H. (1967). *Physical Geodesy*. W. H. Freeman and Company, San Fransisco.

Hernandez, F. and Schaeffer, P. (2000). Altimetric Mean Sea Surfaces and Gravity Anomaly maps inter-comparisons. Technical Report AVI-NT-011-5242-CLS, CLS, Ramonville St Agne.

Hernandez, F. and Schaeffer, P. (2001). The CLS01 Mean Sea Surface: A validation with the GSFC00.1 surface.

Hernla, M. (2000). Anwendung von Filtern bei der Auswertung gemessener Oberflächenprofile. *tm Technisches Messen, München*, 67(3):128–135.

Hofmann-Wellenhof, B. and Moritz, H. (2006). *Physical Geodesy*. Springer, Wien, New York, 2nd edition.

Hollenstein, C. (2006). *GPS deformation field and geodynamic implications for the Hellenic plate boundary region*. PhD thesis, ETH Zurich.

Hooper, W. P. and Gerber, A. (1983). Monte Carlo simulations of laser-generated sea surface aureole. *Applied Optics*, 27(24):2603–2618.

Hopfield, H. S. (1979). Improvements in the tropospheric refraction correction for range measurements. *Philosophical Transactions of the Royal Society of London*, A 294:341–352.

IUGG (1999). Resolution 3 of the International Association of Geodesy. Comptes Rendus of the XXII General Assembly. International Union of Geodesy and Geophysics (IUGG), 19–30 July 1999, Birmingham, 110–111.

Kahle, H.-G., Cocard, M., Peter, Y., Geiger, A., Reilinger, R., Barka, A., and Veis, G. (2000). GPS-derived strain rate field within the boundary zones of the Eurasian, African, and Arabian plates. *J. Geophys. Res.*, 105(B10):23353–23370.

Kahle, H.-G., Cocard, M., Peter, Y., Geiger, A., Reilinger, R., McClusky, S., King, R., Barka, A., and Veis, G. (1999). The GPS strain rate field in the Aegean Sea and western Anatolia. *Geophys. Res. Let.*, 26(16):2513–2516.

Kahle, H.-G. and Mueller, S. (1998). Structure and dynamics of the Eurasian-African/Arabian plate boundary system: Objectives, tasks and resources of the WEGENER group. *Journal of Geodynamics*, 25(3-4):303 – 325. WEGENER: Scientific Objectives and Methodological Challenges for the Application of Space-Geodetic Techniques to Earth Sciences.

Kayton, M. and Fried, W. R. (1997). *Avionics Navigation Systems*. John Wiley & Sons, Inc., 2nd edition.

Kourafalou, V. and Tsiaras, K. (2007). A nested circulation model for the North Aegean Sea. *Ocean Science*, 3(1):1–16.

Le Provost, C. (2001). *Satellite Altimetry and Earth Sciences*, chapter Ocean Tides, pages 267–303. Academic Press.

Le Traon, P. Y. and Morrow, R. (2001). *Satellite Altimetry and Earth Sciences*, chapter Ocean Currents and Eddies, pages 171–215. Academic Press.

Lemoine, F. G., Kenyon, S. C., Factor, J. K., Trimmer, R., Pavlis, N. K., Chinn, D. S., Cox, C. M., Klosko, S. M., Luthcke, S. B., Torrence, M. H., Wang, Y. M., Williamson, R. G., Pavlis, E. C., Rapp, R. H., and Olson, T. R. (1998). The Development of the Joint NASA GSFC and NIMA Geopotential Model EGM96. Technical Report NASA-TP-1998-206861, NASA Goddard Space Flight Center, Greenbelt, Maryland, USA.

Letellier, T. (2004). *Etudes des ondes de marée sur les plateaux continentaux*. PhD thesis, Université Paul Sabatier (Toulouse III, France.

Lighthill, J. (1978). *Waves in Fluids*. Cambridge University Press.

Luthcke, S., Blair, B., and Ekholm, S. (2002). Special issue on laser altimetry. *Journal of Geodynamics*, 34(3-4):343–594.

Lyard, F., Lefèvre, F., Letellier, T., and Francis, O. (2006). Modeling the global ocean tides: a modern insight from FES2004. *Ocean Dynamics*, 56:394–415.

Lynch, D. R. and Gray, W. G. (1979). A wave equation model for finite element tidal computations. *Computers and Fluids*, 7:207–228.

Mader, K. (1951). *Das Newtonsche Raumpotential prismatischer Körper und seine Ableitungen bis zur dritten Ordnung*. Sonderheft 11 der Österreichischen Zeitschrift für Vermessungswesen, Österreichische Kommission für International Erdmessung, Wien 1951.

Makris, J. and Yegorova, T. (2006). A 3-D density-velocity model between the Cretan Sea and Libya. *Tectonophysics*, 417:201–220.

Marini, J. W. and Murray, C. W. (1973). Correction of laser range tracking data for atmospheric refraction at elevations above 10 degrees. Technical Report NASA-TM-X-70555, NASA Goddard Space Flight Center, Greenbelt, Maryland, USA.

McCarthy, D. D. and Petit, G., editors (2004). *IERS Conventions (2003). IERS Technical Note No. 32*. International Earth Rotation and Reference Systems Service (IERS). Verlag des Bundesamts für Kartographie und Geodäsie. Frankfurt am Main.

McClusky, S., Balassian, S., Barka, A., Demir, C., Georgiev, I., Hamburger, M., Hurst, K., Kahle, H.-G., Kastens, K., Kekelidze, G., King, R., Kotzev, V., Lenk, O., Mahmoud, S., Mishin, A., Nadariya, M., Ouzounis, A., Paradissis, D., Peter, Y., Prilepin, M., Reilinger, R., Sanli, I., Seeger, H., Tealeb, A., Tokzoz, M., and Veis, G. (2000). GPS constraints on plate kinematics and dynamics in the eastern Mediterranean and Caucasus. *J. Geophys. Res.*, 105(B3):5695–5719.

McNeill, L. C., Mille, A., Minshull, T. A., Bull, J. M., Kenyon, N. H., and Ivanov, M. (2004). Extension of the North Anatolian Fault into the North Aegean Trough: Evidence for transtension, strain partitioning and analogues for Sea of Marmara basin models. *Tectonics*, 23(TC2016).

Millot, C. (1999). Circulation in the Western Mediterranean Sea. *Journal of Marine Systems*, 20(1-4):423 – 442.

Morel, A. and Prieur, L. (1977). Analysis of variations in ocean color. *Limnology and Oceanography*, 22:709–722.

Moritz, H. (1980). *Advanced Physical Geodesy*. H. Wichmann Verlag, Karlsruhe.

Mourre, B. (2004). *Etudes de configuration d'une constellation de satellites altimétriques pour l'observation de la dynamique océanique côtière*. PhD thesis, Université Paul Sabatier (Toulouse III, France.

Müller, A., Bürki, B., Limpach, P., Kahle, H.-G., Grigoriadis, V. N., Vergos, G. S., and Tziavos, I. N. (2006). Validation of Marine Geoid Models in the North Aegean Sea using Satellite Altimetry, Marine GPS Data and Astrogeodetic Measurements. In *Proceedings of the 1st International Symposium of the International Gravity Field Service (IGFS). Gravity Field of the Earth. August 2006, Istanbul, Turkey*, pages 90–95.

NGA (2004). *Handbook of Magnetic Compass Adjustment*. National Geospatial-Intelligence Agency (NGA), Bethesda, MD. Formely Pub.No. 226, as originally published by the Defense Mapping Agency, Hydrographic/Topographic Center, Washington, D.C., 1980.

NIMA (2000). Department of Defense World Geodetic System 1984—Its Definition and Relationships with Local Geodetic Systems. Technical Report 8350.2, National Imagery and Mapping Agency, USA. Third Edition, 172 p.

Numada, M., Nomura, T., Yanagi, K., Kamiya, K., and Tashiro, H. (2007). High-order spline filter and ideal low-pass filter at the limit of its order. *Precision Engineering*, 31(3):234 – 242.

Optech (1989). *Model 501SA Rangefinder Operator Manual*. Optech Systems Corporation, Toronto, Canada.

OSTM (2008). *OSTM/Jason-2 Products Handbook*. CNES:SALP-MU-M-OP-15815-CN, EUMETSAT:EUM/OPS-JAS/MAN/08/0041, JPL:OSTM-29-1237, NOAA:.

Pavlis, E., Mertikas, S., and the GAVDOS Team (2004). The GAVDOS mean sea level and altimeter calibration facility: Results for Jason–1. *Marine Geodesy*, 27(3-4):631–655. ISSN: 0149-0419.

Pavlis, N. K., Holmes, S. A., Kenyon, S. C., and Factor, J. K. (2008). An Earth Gravitational Model to Degree 2160: EGM2008. Presented at the 2008 General Assembly of the European Geosciences Union, Vienna, Austria, April 13-18, 2008.

Pepperl+Fuchs (2006). *Ultrasonic Sensors Catalogue, Factory Automation*. Pepperl+Fuchs, Mannheim, Germany.

Peter, Y. (1994). Aero-Laser-Profilierung zur Aufnahme von Geländeprofilen. Master's thesis, ETH Zurich.

Picot, N., Case, K., Desai, S., and Vincent, P. (2003). *AVISO and PODAAC User Handbook. IGDR and GDR Jason Products.* SMM-MU-M5-OP-13184-CN (AVISO), JPL D-21352 (PODAAC).

Plag, H.-P., Ambrosius, B., Baker, T., Beutler, G., Bianco, G., Blewitt, G., Boucher, C., Davis, J., Degnan, J., Johansson, J., Kahle, H.-G., Müller, S., and Zerbini, S. (1998). Scientific objectives of current and future WEGENER activities. *Tectonophysics*, 294:177–223.

POL (2009). Proudman Oceanographic Laboratory webdite: http://www.pol.ac.uk.

Rapp, R. H. (1989). The treatment of permanent tidal effects in the analysis of satellite altimeter data for sea surface topography. *manuscripta geodaetica*, 14(6):368–372.

Ray, R. D. (1999). A global ocean tide model from TOPEX/POSEIDON altimetry: GOT99.2. Technical Report NASA-TM-1999-209478, NASA Goddard Space Flight Center, Greenbelt, Maryland, USA.

Rio, M.-H. and Hernandez, F. (2004). A mean dynamic topography computed over the world ocean from altimetry, in situ measurements, and a geoid model. *J. Geophys. Res.*, 109(C12032).

Rio, M.-H., Poulain, P.-M., Pascal, A., Mauri, E., Larnicol, G., and Santoleri, R. (2007). A Mean Dynamic Topography of the Mediterranean Sea computed from altimetric data, in-situ measurements and a general circulation model. *Journal of Marine Systems*, 65:484–508.

Rio, M.-H., Schaeffer, P., Hernandez, F., and Lemoine, J.-M. (2006). From the Altimetric Sea Level Measurement to the Ocean Absolute Dynamic Topography: Mean Sea Surface, Geoid, Mean Dynamic Topography, a Three-Component Challenge. In *Proceedings of the Symposium on 15 Years of Progress in Radar Altimetry, 13-18 March 2006, Venice, Italy.* (ESA SP-614, July 2006).

Roblou, L. (2001). *Modélisation de la variation de la surface libre en mer Mediterranée, validation de MOG2D.* Université Toulouse III - Paul Sabatier.

Sandwell, D. T. and Smith, W. H. F. (1997). Marine gravity anomaly from Geosat and ERS 1 satellite altimetry. *Journal of Geophysical Research*, 102(B5):10039–10054.

Schöne, T. (2003). *GPS Water Level Measurements. Report of IAG Special Study Group 2.194.* IUGG General Assembly XXIII Sapporo, Japan, 30 June – 11 July 2003.

Snopek, K., Meier, T., Endrun, B., Bohnhoff, M., and Casten, U. (2007). Comparison of gravimetric and seismic constraints on the structure of the Aegean lithosphere in the forearc of the Hellenic subduction zone in the area of Crete. *Journal of Geodynamics*, 44(3-5):173–185.

Somieski, A. (2008). *Astrogeodetic Geoid and Isostatic Considerations in the North Aegean Sea, Greece.* PhD thesis, ETH Zurich.

Tratt, D. M., Menzies, R. T., and Cutten, D. R. (1996). Wind-driven angular dependence of sea surface reflectance measured with an airborne Doppler lidar. Technical report, Jet Propulsion Lab (JPL).

Tsimplis, M. N., Proctor, R., and Flather, R. A. (1995). A two dimensional tidal model for the Mediterranean Sea. *J. Geophys. Res.*, 100(C8):16223–16239.

Tziavos, I. N. and Andritsanos, V. (1999). Recent Geoid Computations for the Hellenic Area. *Phys. Chem. Earth (A)*, 24(1):91–96.

Tziavos, I. N., Andritsanos, V. D., Forsberg, R., and Olesen, A. (2004). Numerical investigation of downward continuation methods for airborne gravity data. In *Gravity, Geoid and Space Missions, GGSM 2004 IAG International Symposium*, volume 129 of *International Association of Geodesy Symposia*, pages 119–124. Springer Berlin Heidelberg.

Törnig, W. and Spellucci, P. (2000). *Numerische Mathematik für Ingenieure und Physiker, Band 2: Numerische Methoden der Analysis*. Springer-Verlag.

Verdun, J., Klingelé, E., Bayer, R., Cocard, M., Geiger, A., and Kahle, H.-G. (2003). The alpine Swiss-French airborne gravity survey. *Geophysical Journal International*, 152(1).

Vergos, G. S., Tziavos, I. N., and Andritsanos, V. D. (2004). Gravity data base generation and geoid model estimation using heterogeneous data. In *Gravity, Geoid and Space Missions, GGSM 2004 IAG International Symposium*, volume 129 of *International Association of Geodesy Symposia*, pages 155–160. Springer Berlin Heidelberg.

Škaloud, J. and Lichti, D. (2006). Rigorous approach to bore-sight self-calibration in airborne laser scanning. *ISPRS Journal of Photogrammetry and Remote Sensing*, 61(2006):47–59.

Škaloud, J. and Schaer, P. (2003). Towards a more rigorous boresight calibration. In *Proceedings ISPRS International Workshop on Theory Technology and Realities of Inertial/GPS/Sensor Orientation, Castelldefels, Spain, 22-23 September 2003*.

Wehr, A. and Lohr, U. (1999). Airborne laser scanning - an introduction and overview. *ISPRS Journal of Photogrammy and Remote Sensing*, 54:68–82.

Welch, A. J., Torres, J. H., and Cheong, W.-F. (1989). Laser Physics and Laser-Tissue Interactions. *Texas Heart Institute Journal*, 16:141–149.

Wessel, P. and Smith, W. H. F. (1998). New, Improved Version of Generic Mapping Tools Released. *EOS Trans., AGU*, 79(47):579.

Wessel, P. and Smith, W. H. F. (2005). *The Generic Mapping Tools (GMT) version 4.1 Technical Reference and Cookbook*. SOEST/NOAA.

WMO (1998). *Guide to Wave Analysis and Forecasting*. World Meteorological Organization (WMO), Geneva, Switzerland, 2nd edition. WMO-No.702.

Wunsch, C. (1972). Bermuda sea level in relation to tides, weather and baroclinic fluctuations. *Rev. Geophys. Sace Phys.*, 10:1–49.

Wunsch, C. and Stammer, D. (1997). Atmospheric Loading and the Oceanic "Inverted Barometer" Effect. *Rev. Geophys.*, 35(1):79–107.

Zerbini, S., Plag, H.-P., Baker, T., Becker, M., Billiris, H., Bürki, B., Kahle, H.-G., Marson, I., Pezzoli, L., Richter, B., Romagnoli, C., Sztrobryn, M., Tomasi, P., Tsimplis, N., Veis, G., and Verrone, G. (1996). Sea level in the Mediterranean: a first step towards separating crustal movements and absolute sea-level variations. *Global and Planetary Change*, 14(1-2):1–48.

Zissis, G. J., editor (1993). *The Infrared and Electro-Optical Systems Handbook, Vol. 1: Sources of Radiation*. Infrared Information Analysis Center, Environmental Research Institute of Michigan / SPIE Optical Engineering Press.

Zwally, H. J. and Brenner, A. C. (2001). *Satellite Altimetry and Earth Sciences*, chapter Ice Sheet Dynamics and Mass Balance, pages 351–369. Academic Press.

A Models of Atmospheric Refraction of Light

A.1 Barrell and Sears Model (1939)

In 1939, H. Barrell and J.E. Sears published one of the first equations for the refractive index as a function of the atmospheric parameters temperature, air pressure and water vapor pressure, derived from measurements on dry and moist air. The refractivity N (in ppm) of moist air is given by (Barrell and Sears, 1939):

$$\begin{aligned} N &= (n-1)\cdot 10^6 \\ &= \left[0.378125 + \frac{0.0021414}{\lambda^2} + \frac{0.00001793}{\lambda^4}\right] \frac{p\left(1+(1.049-0.0157t)\,p\cdot 10^{-6}\right)}{1+0.003661t} \\ &\quad - \left[0.0624 - \frac{0.00068}{\lambda^2}\right] \frac{e}{1+0.003661t} \end{aligned} \tag{A.1}$$

where

n	refractive index for atmospheric conditions t, p, e and wavelength λ
p	atmospheric pressure [Torr], with 1 Torr = 1.33322 hPa or 760 Torr = 1013.25 hPa
t	temperature [℃]
e	partial water vapor pressure [Torr]
λ	wavelength of light in the vacuum [μm]

According to (Barrell and Sears, 1939), (A.1) is applicable for the ranges $t = 10$℃ - 30℃ and $p = 720$ - 800 Torr (959.92 - 1066.58 hPa). Under standard atmospheric conditions ($t = 15$℃, $p = 1013.25$ hPa (760 Torr), $e = 0$), the standard refractivity N_s can be derived from (A.1):

$$N_s = (n_s - 1)\cdot 10^6 = 272.5837 + \frac{1.5437}{\lambda^2} + \frac{0.01293}{\lambda^4} \tag{A.2}$$

The refractivity N can be rewritten as a function of the refractivity N_s under standard conditions, by combining (A.1) and (A.2):

$$\begin{aligned} N &= (n-1)\cdot 10^6 \\ &= N_s\,\frac{p\left(1+(1.049-0.0157t)\,p\cdot 10^{-6}\right)}{720.88261\,(1+0.003661t)} - \left[0.0624 - \frac{0.00068}{\lambda^2}\right]\frac{e}{1+0.0003661t} \end{aligned} \tag{A.3}$$

In (A.3), N_s depends on the wavelength λ, following (A.2).

A.2 Barrell Model (1951)

In 1951, an update of the (Barrell and Sears, 1939) model was published, where the refractivity N (in ppm) of moist air is given by (Barrell, 1951):

$$\begin{aligned} N &= (n-1)\cdot 10^6 \\ &= N_s \, \frac{p\left(1+(1.049-0.0157t)\,p\cdot 10^{-6}\right)}{720.883\,(1+0.003661t)} - \left[0.0624 - \frac{0.00068}{\lambda^2}\right] \frac{e}{1+0.0003661t} \end{aligned} \tag{A.4}$$

with the refractivity N_s under standard conditions

$$N_s = (n_s-1)\cdot 10^6 = 272.729 + \frac{1.4823}{\lambda^2} + \frac{0.02041}{\lambda^4} \tag{A.5}$$

and

- n refractive index for atmospheric conditions t, p, e and wavelength λ
- n_s refractive index under standard conditions ($t = 15$°C, $p = 760$ Torr, $e = 0$)
- p atmospheric pressure [Torr]
- t temperature [°C]
- e partial water vapor pressure [Torr]
- λ wavelength of light in the vacuum [μm]

A.3 Edlén Model (1966)

The equations nowadays commonly used in physics and geodetic surveying to derive the refractive index from temperature, pressure and humidity are those published in (Edlén, 1966), where the refractivity N (in ppm) of moist air is given by:

$$\begin{aligned} N &= (n-1)\cdot 10^6 \\ &= N_s \, \frac{p\left(1+(0.817-0.0133t)\,p\cdot 10^{-6}\right)}{720.775\,(1+0.003661t)} - \left[0.057224 - \frac{0.000457}{\lambda^2}\right] e \end{aligned} \tag{A.6}$$

with the refractivity N_s under standard conditions

$$N_s = (n_s-1)\cdot 10^6 = 83.4213 + \frac{24060.30}{130-\lambda^{-2}} + \frac{159.97}{38.9-\lambda^{-2}} \tag{A.7}$$

and

- n refractive index for atmospheric conditions t, p, e and wavelength λ
- n_s refractive index under standard conditions ($t = 15$°C, $p = 760$ Torr, $e = 0$)
- p atmospheric pressure [Torr]
- t temperature [°C]
- e partial water vapor pressure [Torr]
- λ wavelength of light in the vacuum [μm]

A.4 Birch and Downs Model (1994)

Since the publication of (Edlén, 1966), several updates of the set of equations have been performed by several authors. One of these revised models was published in (Birch and Downs, 1993, 1994). The major difference with respect to the (Edlén, 1966) equations are the conversion to the SI units system and the change of the temperature scale from the International Practical Temperature Scale of 1948 (ITPS-1948) to the International Temperature Scale of 1990 (ITS-90). According to (Birch and Downs, 1994), the refractivity N (in ppm) of moist air is given by:

$$\begin{aligned} N &= (n-1)\cdot 10^6 \\ &= N_s\,\frac{p\left(1+(0.601-0.00972t)\,p\cdot 10^{-8}\right)}{96095.43\,(1+0.003661t)} - \left[0.00037345 - \frac{0.00000401}{\lambda^2}\right] e \end{aligned} \tag{A.8}$$

with the refractivity N_s under standard conditions

$$N_s = (n_s-1)\cdot 10^6 = 83.4254 + \frac{24061.47}{130-\lambda^{-2}} + \frac{159.98}{38.9-\lambda^{-2}} \tag{A.9}$$

and

n	refractive index for atmospheric conditions t, p, e and wavelength λ
n_s	refractive index under standard conditions ($t = 15$℃, $p = 101325$ Pa, $e = 0$)
p	atmospheric pressure [Pa]
t	temperature [℃]
e	partial water vapor pressure [Pa]
λ	wavelength of light in the vacuum [μm]

B Standard Atmosphere Model

Values for temperature, atmospheric pressure and water vapor pressure at an altitude h can be derived from a standard atmosphere model, as a function of altitude h and using reference values for a reference altitude h_0 (Berg, 1948):

$$\begin{aligned} T(h) &= T_0 - 0.0065\,(h - h_0) \\ p(h) &= p_0\ (1 - 0000226\,(h - h_0))^{5.225} \\ H(h) &= H_0\ \cdot e^{-0.0006396(h - h_0)} \end{aligned} \tag{B.1}$$

where T, p and H are the temperature [K], pressure [hPa] and relative humidity [%] at altitude h [m]. T_0, p_0 and H_0 are the corresponding values at the reference altitude h_0. Commonly used reference values for a standard atmosphere at sea level ($h_0 = 0$) are:

$$\begin{aligned} T_0 &= 288.15\,\text{K}\ (15°\text{C}) \text{ or } 291.15\,\text{K}\ (18°\text{C}) \\ p_0 &= 1013.25\,\text{hPa} \\ H_0 &= 50\% \\ e_0 &= 17\,\text{hPa} \end{aligned}$$

The water vapor pressure can be calculated from the relative humidity H by (Giacomo, 1982):

$$e(h) = \frac{H}{100} \cdot e_s \cdot f_w \tag{B.2}$$

with

$$e_s(h) = 0.01 \cdot e^{\left(1.2378847 \cdot 10^{-5}\ T^2\ -\ 1.9121316 \cdot 10^{-2}\ T\ +\ 33.93711047\ -\ 6.3431645 \cdot 10^{3}\ T^{-1}\right)} \tag{B.3}$$

and

$$f_w(h) = 1.00062\ +\ 3.14 \cdot 10^{-6}\ p\ +\ 5.6 \cdot 10^{-7}\ (T - 273.10)^2 \tag{B.4}$$

where e_s is the saturation water vapor pressure and f_w the enhancement factor.

C GPS-Equipped Buoys

C.1 Introduction

GPS-equipped buoys provide ground-truth information on the instantaneous sea surface height, enabling the determination of sea state parameters, the integration in early-warning systems for Tsunamis and the calibration of spaceborne, airborne and shipborne altimetry systems. Depending on the application, different types of buoys and concepts have been developed by different institutions. An overview of worldwide specialized buoy activities is given by (Schöne, 2003).

C.2 GPS-Equipped Buoys Developed by the GGL

For offshore hydrodynamic investigations and ground-truth observations of the sea surface height, the GGL has designed and constructed lightweight GPS buoys (Fig. C.1). The buoys weight 10 kg including the equipment and have a diameter of 0.40 m, facilitating their handling. The shell of the buoys is fabricated from microwave-transparent polycarbonate, so they can be waterproof sealed containing the GPS receiver, GPS antenna and power supply. The dimension of the buoys and the weight of the equipment were optimally chosen and designed in order to reach an exact floating balance. No ballast is needed to stabilize the buoy or to reach the foreseen floating line in the middle of the spherical buoy. Their small weight allows to follow the movements of the waves. The operation autonomy is about 24 hours. The buoys are equipped with Novatel DL–4 dual frequency GPS receivers.

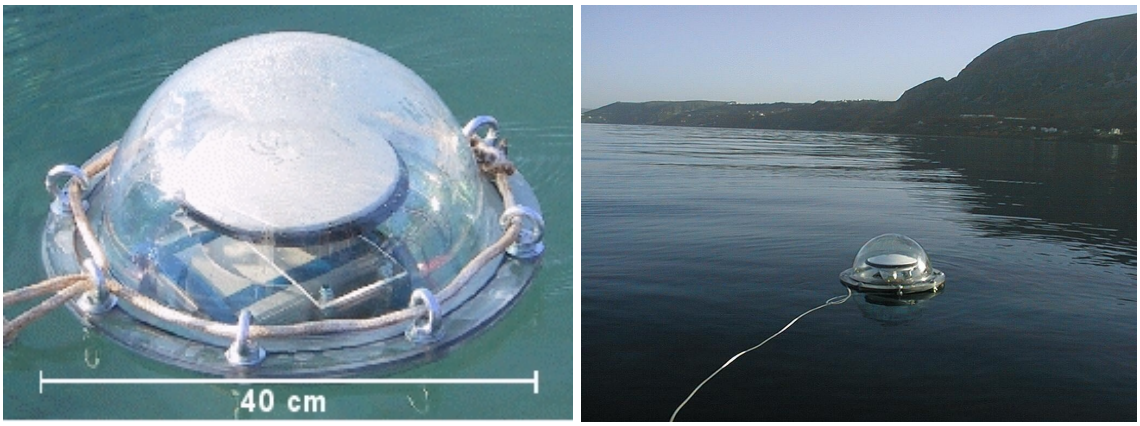

Figure C.1: GPS-equipped buoy deployed in coastal region, containing GPS receiver, GPS antenna and battery.

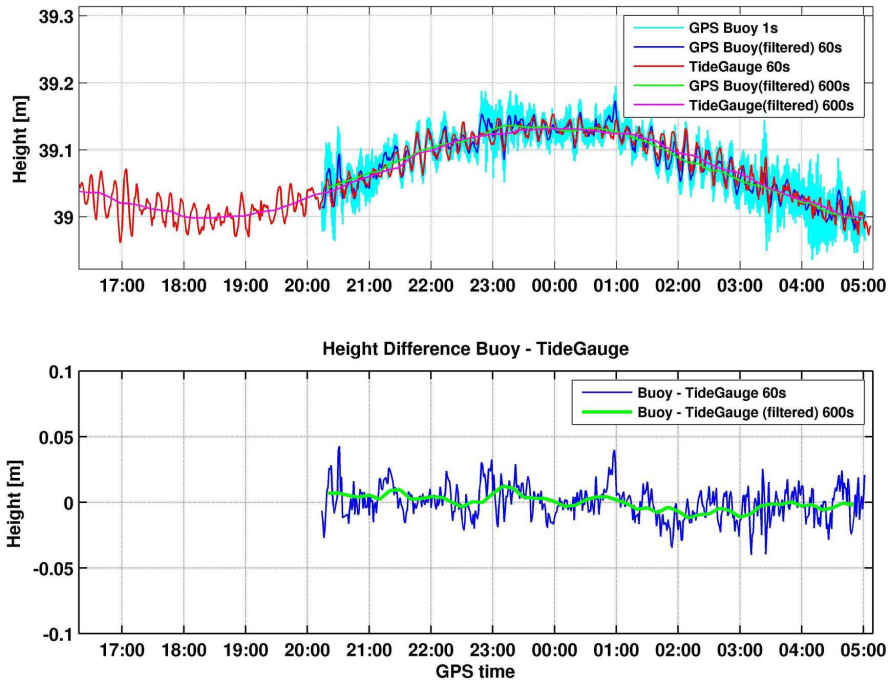

Figure C.2: Comparison between sea surface heights from GPS buoy and pressure tide-gauge in the same bay.

C.3 Case Study: Ocean Tide Observations with GPS Buoys

Apart from providing calibration data for spaceborne, airborne and shipborne altimetry systems, GPS buoys can be used to observe ocean tides. Onshore tide-gauges have the disadvantage to produce data only in coastal regions, whereas GPS buoys can be deployed offshore, thus providing accurate ground-truth ocean tide data for the open sea. Field observations with GPS buoys carried out in this project produced very promising results, as is shown by comparing them to pressure tide-gauge data. In this case study (Fig. C.2), both systems were operated in the same bay. The buoy data with an original sampling rate of 1 Hz (Fig. C.2 top, cyan line) were low-pass filtered and resampled to the 60 s sampling interval of the tide-gauge data (Fig. C.2 top, blue line). The difference between GPS and tide-gauge data (Fig. C.2 bottom, blue line) shows an RMS of 1.3 cm. Both methods have observed a special wave characterized by a period of about 11 minutes and an amplitude of about 2 cm, best distinguishable between 1:00 and 3:00 GPS time. For tidal analysis purposes, focusing on periods of 12 hours and above, both datasets were low-pass filtered and resampled to a sampling interval of 600 s (Fig. C.2 top, green and magenta lines). The filtered datasets show a good agreement (Fig. C.2 bottom, green line), with an RMS of their difference of only 0.5 cm.

D Rotation Matrices

D.1 General Formulation

A rotation in a three dimensional coordinate system of a vector $(x, y, z)^T$ is given by three consecutive rotations by the angles α_x, α_y and α_z around the three coordinate axes:

$$\begin{bmatrix} \bar{x} \\ \bar{y} \\ \bar{z} \end{bmatrix} = \boldsymbol{R}_3(\alpha_3) \cdot \boldsymbol{R}_2(\alpha_2) \cdot \boldsymbol{R}_1(\alpha_1) \cdot \begin{bmatrix} x \\ y \\ z \end{bmatrix} = \boldsymbol{R} \cdot \begin{bmatrix} x \\ y \\ z \end{bmatrix} \tag{D.1}$$

with

$$\boldsymbol{R}_1 = \begin{bmatrix} 1 & 0 & 0 \\ 0 & \cos\alpha_1 & \sin\alpha_1 \\ 0 & -\sin\alpha_1 & \cos\alpha_1 \end{bmatrix} \quad \boldsymbol{R}_2 = \begin{bmatrix} \cos\alpha_2 & 0 & -\sin\alpha_2 \\ 0 & 1 & 0 \\ \sin\alpha_2 & 0 & \cos\alpha_1 \end{bmatrix} \quad \boldsymbol{R}_3 = \begin{bmatrix} \cos\alpha_3 & \sin\alpha_3 & 0 \\ -\sin\alpha_3 & \cos\alpha_3 & 0 \\ 0 & 0 & 1 \end{bmatrix}$$

and

$$\boldsymbol{R} = \boldsymbol{R}_3(\alpha_3) \cdot \boldsymbol{R}_2(\alpha_2) \cdot \boldsymbol{R}_1(\alpha_1) \tag{D.2}$$

$$\boldsymbol{R} = \begin{bmatrix} \cos\alpha_2 \cos\alpha_3 & \cos\alpha_1 \sin\alpha_3 + \sin\alpha_1 \sin\alpha_2 \cos\alpha_3 & \sin\alpha_1 \sin\alpha_3 - \cos\alpha_1 \sin\alpha_2 \cos\alpha_3 \\ -\cos\alpha_2 \sin\alpha_3 & \cos\alpha_1 \cos\alpha_3 - \sin\alpha_1 \sin\alpha_2 \sin\alpha_3 & \sin\alpha_1 \cos\alpha_3 + \cos\alpha_1 \sin\alpha_2 \sin\alpha_3 \\ \sin\alpha_2 & -\sin\alpha_1 \cos\alpha_2 & \cos\alpha_1 \cos\alpha_2 \end{bmatrix}$$

The rotation matrix $\boldsymbol{R}$ is orthogonal and the transposed matrix is therefore equal to its inverse matrix. Additionally, the inverse of a rotation matrix is equal to three rotations in opposite order and around angles with opposite signs:

$$\boldsymbol{R}^{-1} = \boldsymbol{R}^T = \boldsymbol{R}_1(-\alpha_1) \cdot \boldsymbol{R}_2(-\alpha_2) \cdot \boldsymbol{R}_3(-\alpha_3) \tag{D.3}$$

$$\boldsymbol{R}^{-1} = \begin{bmatrix} \cos\alpha_2 \cos\alpha_3 & -\cos\alpha_2 \sin\alpha_3 & \sin\alpha_2 \\ \cos\alpha_1 \sin\alpha_3 + \sin\alpha_1 \sin\alpha_2 \cos\alpha_3 & \cos\alpha_1 \cos\alpha_3 - \sin\alpha_1 \sin\alpha_2 \sin\alpha_3 & -\sin\alpha_1 \cos\alpha_2 \\ \sin\alpha_1 \sin\alpha_3 - \cos\alpha_1 \sin\alpha_2 \cos\alpha_3 & \sin\alpha_1 \cos\alpha_3 + \cos\alpha_1 \sin\alpha_2 \sin\alpha_3 & \cos\alpha_1 \cos\alpha_2 \end{bmatrix}$$

In direct georeferencing, rotations are usually defined as:

$$\boldsymbol{R}_{\_} = \boldsymbol{R}_3(-\alpha_3) \cdot \boldsymbol{R}_2(-\alpha_2) \cdot \boldsymbol{R}_1(-\alpha_1) \tag{D.4}$$

$$\boldsymbol{R}_{\_} = \begin{bmatrix} \cos\alpha_2 \cos\alpha_3 & -\cos\alpha_1 \sin\alpha_3 + \sin\alpha_1 \sin\alpha_2 \cos\alpha_3 & \sin\alpha_1 \sin\alpha_3 + \cos\alpha_1 \sin\alpha_2 \cos\alpha_3 \\ \cos\alpha_2 \sin\alpha_3 & \cos\alpha_1 \cos\alpha_3 + \sin\alpha_1 \sin\alpha_2 \sin\alpha_3 & -\sin\alpha_1 \cos\alpha_3 + \cos\alpha_1 \sin\alpha_2 \sin\alpha_3 \\ -\sin\alpha_2 & \sin\alpha_1 \cos\alpha_2 & \cos\alpha_1 \cos\alpha_2 \end{bmatrix}$$

and the inverse matrix is:

$$\underset{\sim}{\boldsymbol{R}}^{-1} \;=\; \underset{\sim}{\boldsymbol{R}}^{T} = \boldsymbol{R}_1(\alpha_1) \cdot \boldsymbol{R}_2(\alpha_2) \cdot \boldsymbol{R}_3(\alpha_3) \tag{D.5}$$

$$\underset{\sim}{\boldsymbol{R}}^{-1} \;=\; \begin{bmatrix} \cos\alpha_2 \cos\alpha_3 & \cos\alpha_2 \sin\alpha_3 & -\sin\alpha_2 \\ -\cos\alpha_1 \sin\alpha_3 + \sin\alpha_1 \sin\alpha_2 \cos\alpha_3 & \cos\alpha_1 \cos\alpha_3 + \sin\alpha_1 \sin\alpha_2 \sin\alpha_3 & \sin\alpha_1 \cos\alpha_2 \\ \sin\alpha_1 \sin\alpha_3 + \cos\alpha_1 \sin\alpha_2 \cos\alpha_3 & -\sin\alpha_1 \cos\alpha_3 + \cos\alpha_1 \sin\alpha_2 \sin\alpha_3 & \cos\alpha_1 \cos\alpha_2 \end{bmatrix}$$

For small angles $d\alpha_i \simeq 0$, $\sin d\alpha_i \simeq d\alpha_i$ and $\cos d\alpha_i \simeq 1$, the rotation matrix $\boldsymbol{R}$ from (D.2) becomes:

$$\boldsymbol{R}(d\alpha) \;\simeq\; \begin{bmatrix} 1 & d\alpha_3 & -d\alpha_2 \\ -d\alpha_3 & 1 & d\alpha_1 \\ d\alpha_2 & -d\alpha_1 & 1 \end{bmatrix} \tag{D.6}$$

D.2 Rotation from Local Level to Geocentric System

The transformation of a vector $(X, Y, Z)^T$ from geocentric to topocentric $(E, N, U)^T$ (East, North, Up) coordinates is performed by a translation to the origin $(X_0, Y_0, Z_0)^T$ of the topocentric frame followed by two consecutive rotations:

$$\begin{bmatrix} E \\ N \\ U \end{bmatrix} = \boldsymbol{R}_1\left(\frac{\pi}{2} - \varphi\right) \cdot \boldsymbol{R}_3\left(\frac{\pi}{2} + \lambda\right) \cdot \left(\begin{bmatrix} X \\ Y \\ Z \end{bmatrix} - \begin{bmatrix} X_0 \\ Y_0 \\ Z_0 \end{bmatrix} \right) = \boldsymbol{R}_{ENU/G} \cdot \left(\begin{bmatrix} X \\ Y \\ Z \end{bmatrix} - \begin{bmatrix} X_0 \\ Y_0 \\ Z_0 \end{bmatrix} \right) \tag{D.7}$$

with

$$\boldsymbol{R}_{ENU/G} \;=\; \boldsymbol{R}_1\left(\frac{\pi}{2} - \varphi\right) \cdot \boldsymbol{R}_3\left(\frac{\pi}{2} + \lambda\right) \;=\; \begin{bmatrix} -\sin\lambda & \cos\lambda & 0 \\ -\sin\varphi\cos\lambda & -\sin\varphi\sin\lambda & \cos\varphi \\ \cos\varphi\cos\lambda & \cos\varphi\sin\lambda & \sin\varphi \end{bmatrix} \tag{D.8}$$

where φ and λ are the geographic latitude and longitude corresponding to $(X, Y, Z)^T$. The transformation from geocentric to topocentric $(N, E, D)^T$ (North, East, Down) coordinates is performed by a translation to the origin of the topocentric frame followed by two consecutive rotations:

$$\begin{bmatrix} N \\ E \\ D \end{bmatrix} = \boldsymbol{R}_2\left(-\frac{\pi}{2} - \varphi\right) \cdot \boldsymbol{R}_3(\lambda) \cdot \left(\begin{bmatrix} X \\ Y \\ Z \end{bmatrix} - \begin{bmatrix} X_0 \\ Y_0 \\ Z_0 \end{bmatrix} \right) = \boldsymbol{R}_{NED/G} \cdot \left(\begin{bmatrix} X \\ Y \\ Z \end{bmatrix} - \begin{bmatrix} X_0 \\ Y_0 \\ Z_0 \end{bmatrix} \right) \tag{D.9}$$

with

$$\boldsymbol{R}_{NED/G} \;=\; \boldsymbol{R}_2\left(-\frac{\pi}{2} - \varphi\right) \cdot \boldsymbol{R}_3(\lambda) \;=\; \begin{bmatrix} -\sin\varphi\cos\lambda & -\sin\varphi\sin\lambda & \cos\varphi \\ -\sin\lambda & \cos\lambda & 0 \\ -\cos\varphi\cos\lambda & -\cos\varphi\sin\lambda & -\sin\varphi \end{bmatrix} \tag{D.10}$$

The rotation matrix $\boldsymbol{R}_{G/L}^T$ from the topocentric NED frame to the geocentric system can be derived from (D.10), using (D.3):

$$\boldsymbol{R}_{G/L} \;=\; \boldsymbol{R}_{NED/G}^{-1} \;=\; \boldsymbol{R}_3(-\lambda) \cdot \boldsymbol{R}_2\left(\frac{\pi}{2} + \varphi\right) \;=\; \begin{bmatrix} -\sin\varphi\cos\lambda & -\sin\lambda & -\cos\varphi\cos\lambda \\ -\sin\varphi\sin\lambda & \cos\lambda & -\cos\varphi\sin\lambda \\ \cos\varphi & 0 & -\sin\varphi \end{bmatrix} \tag{D.11}$$

E Differential Clock Bias in Moving Baseline GPS Processing

Like in conventional differential GPS processing, the vector $\boldsymbol{dx}(t_R)$ obtained by moving baseline GPS processing is given by the difference between the position $\boldsymbol{x}_m(t_{Rm})$ of the remote receiver at its time of reception t_{Rm} and the position $\boldsymbol{x}_r(t_{Rr})$ of the reference receiver at its time of reception t_{Rr}:

$$\boldsymbol{dx}(t_R) \;=\; \boldsymbol{x}_m(t_{Rm}) \;-\; \boldsymbol{x}_r(t_{Rr}) \tag{E.1}$$

Due to the receiver-specific clock biases τ_i, the two times of reception t_{Rm} and t_{Rr} are not identical. In order to compute the attitude of a platform, vectors are needed at the nominal time t_N, that is the time at which the observations should have been taken. The nominal time t_N, as well as the position of the reference receiver $\boldsymbol{x}_r(t_N)$ and the remote receiver $\boldsymbol{x}_m(t_N)$ at nominal time are given by (Favey, 2001):

$$t_N \;=\; t_{Ri} \;+\; \tau_i \tag{E.2}$$
$$\boldsymbol{x}_r(t_N) \;=\; \boldsymbol{x}_r(t_{Rr}) \;+\; \tau_r\; \boldsymbol{v}_r(t_{Rr}) \tag{E.3}$$
$$\boldsymbol{x}_m(t_N) \;=\; \boldsymbol{x}_m(t_{Rm}) \;+\; \tau_m\; \boldsymbol{v}_m(t_{Rm}) \tag{E.4}$$

where $\boldsymbol{v}_r(t_{Rr})$ is the velocity of the reference receiver at its time of reception, $\boldsymbol{v}_m(t_{Rm})$ is the velocity of the remote receiver at its time of reception, τ_r is the clock bias of the reference receiver and τ_m is the clock bias of the remote receiver. Thus, the vector at nominal time t_N is obtained by subtracting (E.3) from (E.4), and using (E.1):

$$\begin{aligned} \boldsymbol{dx}(t_N) \;&=\; \boldsymbol{x}_m(t_N) \;-\; \boldsymbol{x}_r(t_N) \\ &=\; \boldsymbol{dx}(t_R) \;+\; \tau_m\; \boldsymbol{v}_m(t_{Rm}) \;-\; \tau_r\; \boldsymbol{v}_r(t_{Rr}) \end{aligned} \tag{E.5}$$

In the case of two static receivers, $\boldsymbol{v}_m(t_{Rm}) = \boldsymbol{v}_r(t_{Rr}) = 0$ and (E.5) becomes:

$$\boldsymbol{dx}(t_N) \;=\; \boldsymbol{dx}(t_R) \tag{E.6}$$

meaning that the difference between the two receiver clock biases has no effect. In the case of a static reference receiver and a moving remote receiver, $\boldsymbol{v}_r(t_{Rr}) = 0$ and (E.5) becomes:

$$\boldsymbol{dx}(t_N) \;=\; \boldsymbol{dx}(t_R) \;+\; \boldsymbol{\tau}_m\; \boldsymbol{v}_m(t_{Rm}) \tag{E.7}$$

meaning that the difference between the two receiver clock biases has no effect, considering (E.2). In the case of a moving baseline, with two moving receivers rigidly mounted on the same platform and with small rotational velocities, $\boldsymbol{v}_m(t_{Rm}) \simeq \boldsymbol{v}_r(t_{Rr})$ and (E.5) becomes:

$$\boldsymbol{dx}(t_N) \;=\; \boldsymbol{dx}(t_R) \;+\; (\tau_m - \tau_r)\; \boldsymbol{v} \tag{E.8}$$

where $\boldsymbol{v} \simeq \boldsymbol{v}_m(t_{Rm}) \simeq \boldsymbol{v}_r(t_{Rr})$ is the velocity of the platform. Thus, the vector deformation is given by the difference between the two receiver clock biases multiplied by the velocity of the platform. With a differential clock bias in the order of 1 ms and an aircraft velocity of 70 m/s, the vector distortion due to asynchronous receiver clocks would be 7 cm. For this reason, it is not advisable to introduce the known vector lengths in the GPS baseline processing as additional information in the case of highly-dynamic applications like airborne laser altimetry. The approach for differential clock bias correction described above is based on (Favey, 2001).

F ECMWF Atmospheric Pressure

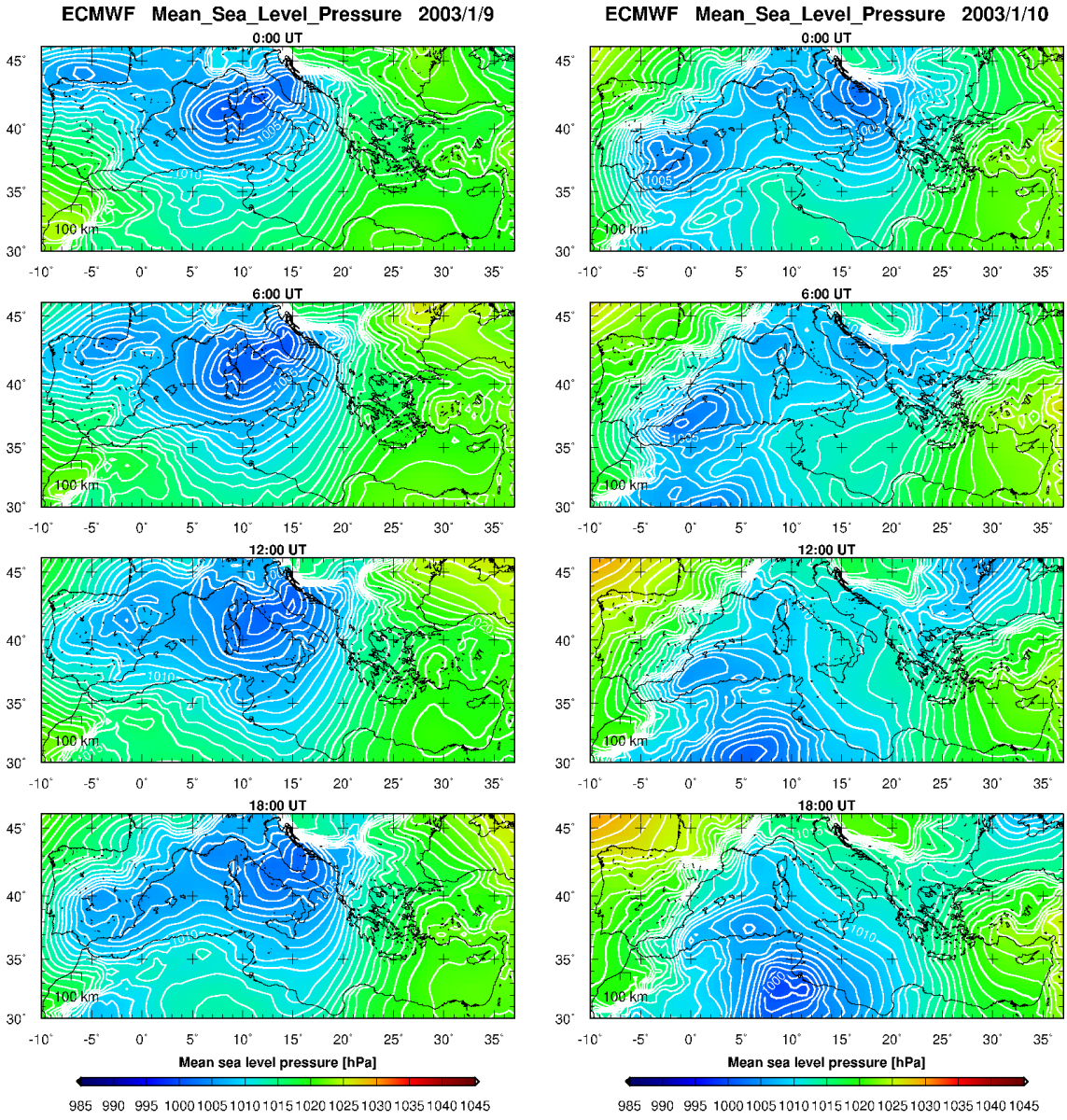

Figure F.1: ECMWF six hours atmospheric pressure at mean sea level over the Mediterranean Sea on 09/01/2003 and 10/01/2003. Contour interval: 1 hPa.

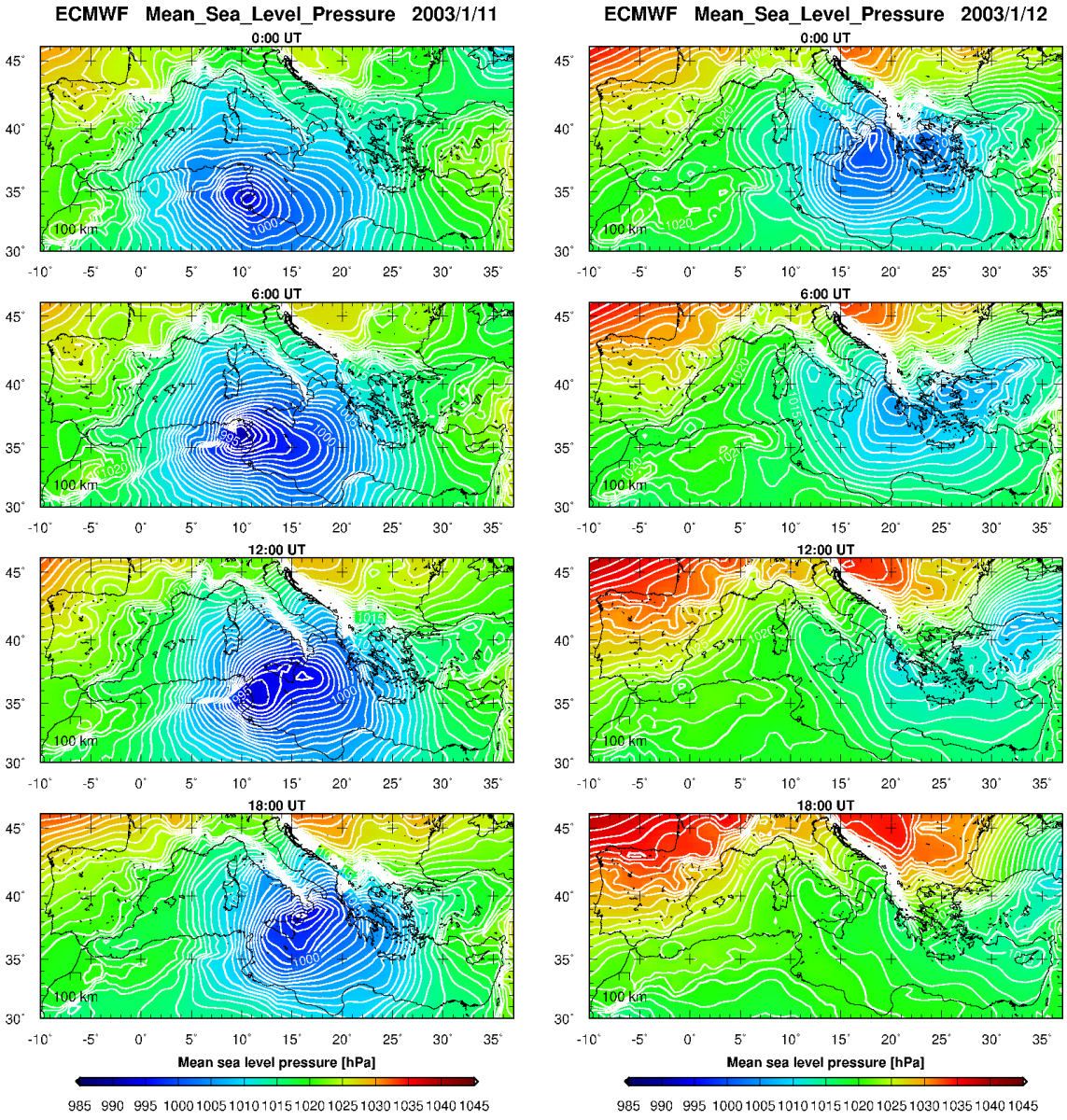

Figure F.2: ECMWF six hours atmospheric pressure at mean sea level over the Mediterranean Sea on 11/01/2003 and 12/01/2003. Contour interval: 1 hPa.

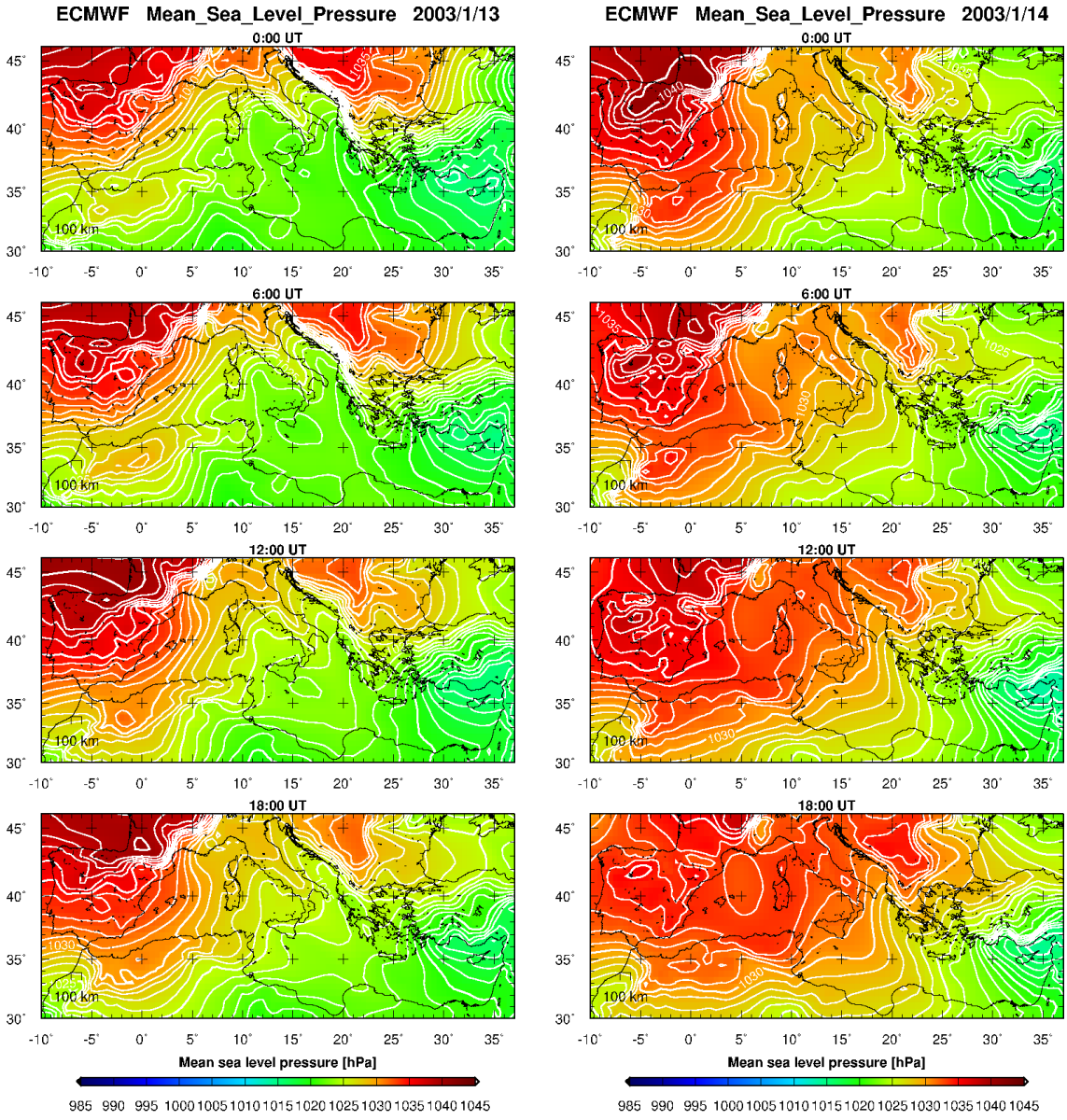

Figure F.3: ECMWF six hours atmospheric pressure at mean sea level over the Mediterranean Sea on 13/01/2003 and 14/01/2003. Contour interval: 1 hPa.

G Dynamic Atmospheric Correction over the Mediterranean Sea

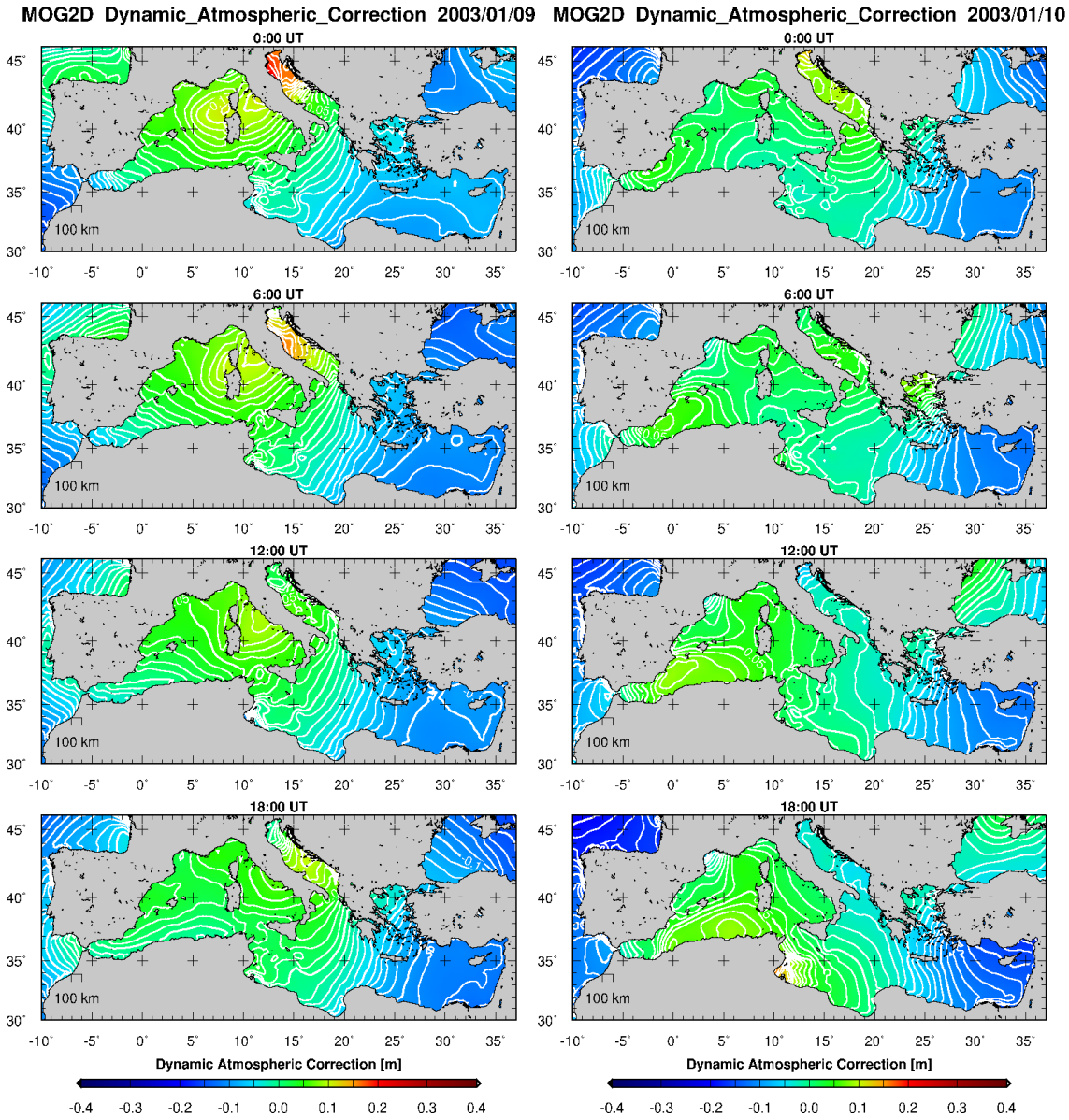

Figure G.1: MOG2D dynamic atmospheric correction grids over the Mediterranean Sea on 09/01/2003 and 10/01/2003, for the effect of pressure and wind forcing on sea surface height. Contour interval: 0.01 m. Corresponding ECMWF atmospheric pressure grids at sea level are shown in Appendix F, Fig. F.1.

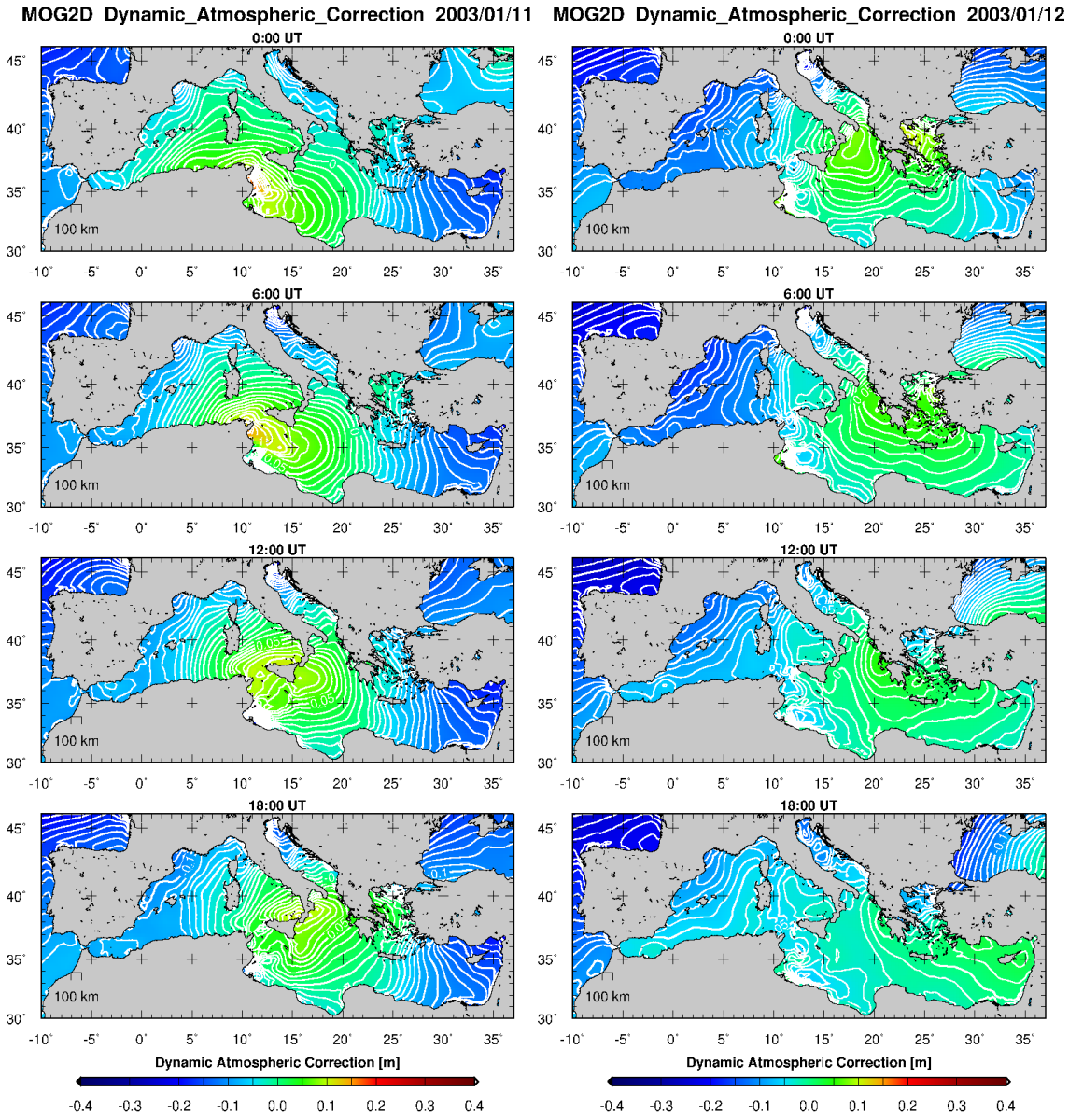

Figure G.2: MOG2D dynamic atmospheric correction grids over the Mediterranean Sea on 11/01/2003 and 12/01/2003, for the effect of pressure and wind forcing on sea surface height. Contour interval: 0.01 m. Corresponding ECMWF atmospheric pressure grids at sea level are shown in Appendix F, Fig. F.2.

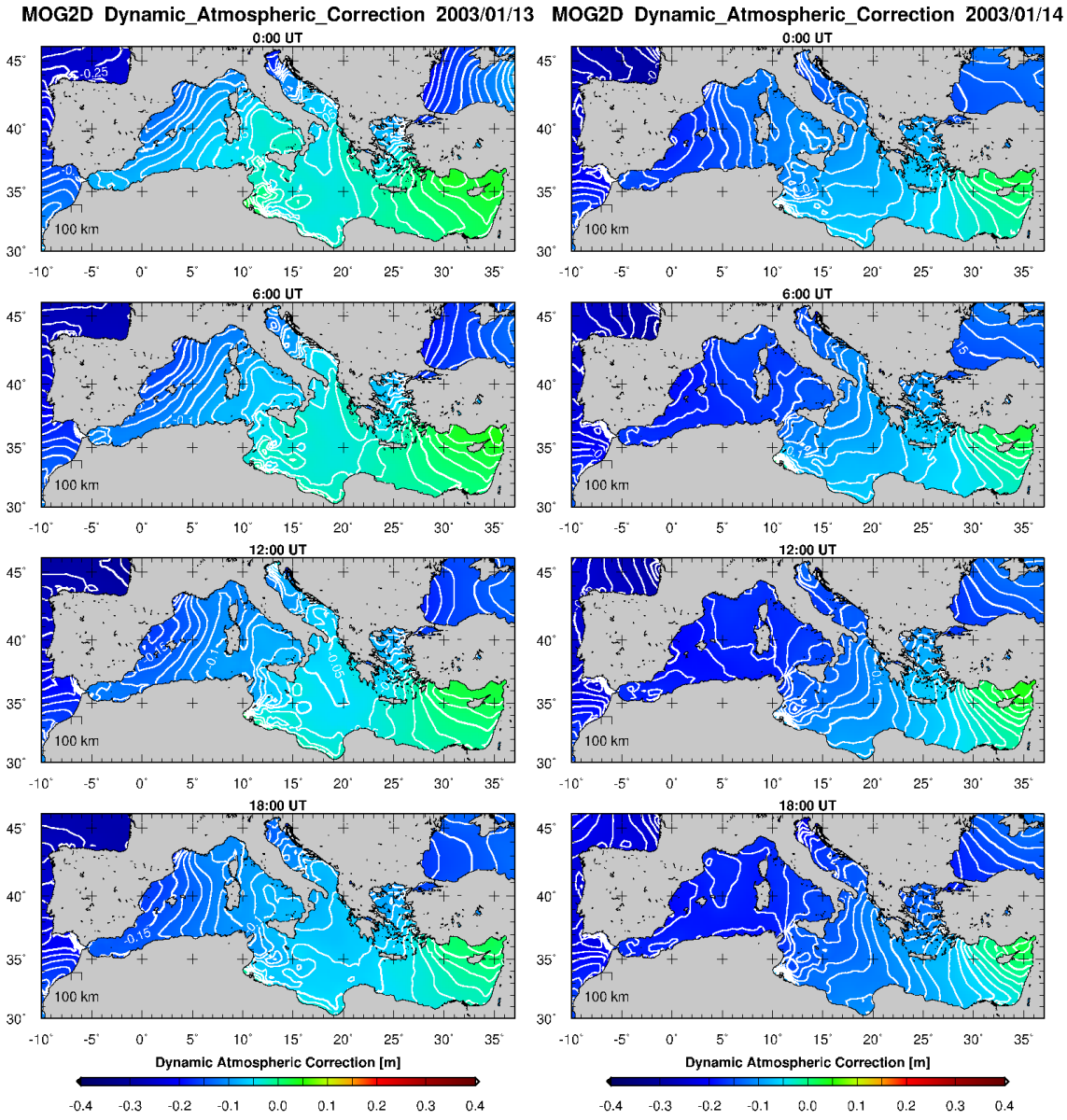

Figure G.3: MOG2D dynamic atmospheric correction grids over the Mediterranean Sea on 13/01/2003 and 14/01/2003, for the effect of pressure and wind forcing on sea surface height. Contour interval: 0.01 m. Corresponding ECMWF atmospheric pressure grids at sea level are shown in Appendix F, Fig. F.3.